Plasma Physics Reports, Vol. 30, No. 1, 2004, pp. 1–8. Translated from Fizika Plazmy, Vol. 30, No. 1, 2004, pp. 3–10.

TOKAMAKS

Application of the Canonical Profile Theory to the Problems of Heat Transport in Tokamaks

Yu. N. Dnestrovskij*, A. Yu. Dnestrovskij*, S. E. Lysenko*, S. V. Cherkasov*, and M. J. Walsh**

**Nuclear Fusion Institute, Russian Research Centre Kurchatov Institute, Moscow, 123182 Russia*

***Walsh Scientific Ltd., Abingdon, Oxon, OX14 3DB, UK*

Received February 20, 2003

Abstract—A transport model for describing electron and ion plasma temperatures is developed on the basis of the canonical profile theory for a tokamak with an arbitrary cross section. A comparison with the data from experiments on eight different tokamaks shows that the model is capable of adequately simulating plasma discharges. A scaling for the behavior of the relative temperature gradient at half the plasma minor radius is constructed based on both an analysis of the experimental data and the results of numerical calculations. © *2004 MAIK "Nauka/Interperiodica".*

1. INTRODUCTION

In order to describe relaxed plasma states in tokamaks, Kadomtsev [1] and other authors [2, 3] proposed to use the following two principles: (i) at a given total plasma current, the free plasma energy in the relaxed state is minimum, and (ii) the profiles of the plasma current and plasma pressure are self-consistent. In [1–3], the relaxed states of a plasma cylinder with a circular cross section were studied. More recently, solutions minimizing the free energy functional were called canonical profiles. The problem of canonical profiles in a tokamak with an arbitrary cross section was considered in our earlier paper [4]. In the present study, we develop a transport model with critical gradients by using the canonical profiles obtained in that paper. The model proposed here is tested by comparing the computed results with experimental data from different tokamaks. By analyzing the experimental results and those calculated with our model, we also construct a scaling for the relative temperature gradients [5].

2. CANONICAL PROFILE FOR A TOKAMAK WITH AN ARBITRARY CROSS SECTION OF THE PLASMA COLUMN

First, we present a brief derivation of the equation for the canonical profile [4]. We assume that the equilibrium problem (i.e., the Grad–Shafranov equation for the poloidal magnetic flux function ψ) is solved for given distributions of the plasma current and plasma pressure. The equation ψ = const determines the magnetic surfaces. We parameterize the magnetic surfaces by the variable ρ defined in terms of the toroidal magnetic flux as follows:

$$\pi\rho^2 B_0 = \Phi, \quad \Phi = \int_S \mathbf{B}\cdot d\mathbf{S}, \tag{1}$$

where B_0 is the vacuum toroidal magnetic field at the center of the chamber. At the plasma surface, we have $\rho = \rho_{max} = a_{eff}$, where a_{eff} is the effective plasma radius. For a large-aspect-ratio tokamak, the effective plasma radius at a low pressure is equal to $a_{eff} = \sqrt{k}a$, where a is the plasma minor radius and k is the plasma elongation.

Under the condition that the total plasma current is conserved, the free energy functional has the form

$$F = \int_V (B_{pol}^2/8\pi + p/(\gamma-1))d^3x + \lambda_1\int_S j_\varphi dS. \tag{2}$$

Here, B_{pol} is the poloidal magnetic field, p is the plasma pressure, λ_1 is a Lagrange multiplier, and V is the plasma volume. The last term on the right-hand side of expression (2), $\int_S j_\varphi dS = I_p$, describes the conservation of the total plasma current.

In order to eliminate the plasma pressure from functional (2) and reduce the problem of minimizing this functional to a one-dimensional one, we use the profile consistency conditions [1]

$$p = p(\mu), \quad j_\varphi = j_\varphi(\mu), \quad j_\varphi(\mu) = Ap(\mu), \tag{3}$$

where $\mu = 1/q = 1/(2\pi B_0\rho)\partial\psi/\partial\rho$ and $A = \text{const}(\mu)$ is a proportionality coefficient. Minimizing functional (2)

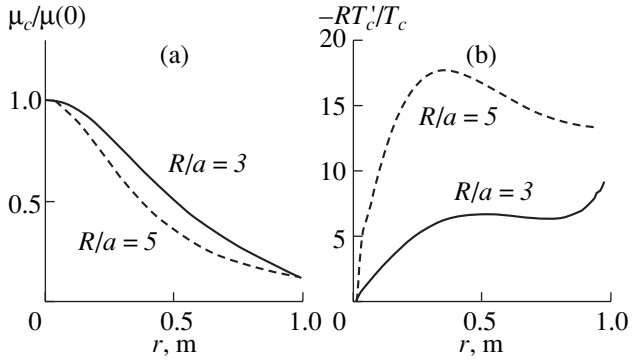

Fig. 1. (a) Canonical profiles $\mu_c/\mu(0)$ and (b) critical gradients RT_c'/T_c for two tokamaks with a large and a moderate aspect ratio, $R/a = 5$ and $R/a = 3$, respectively, and for $a = 1$ m and $q_a = 7$.

under conditions (3) yields the following Euler equation for the function $\mu(\rho)$ [4]:

$$\rho^2 G\partial\mu_c^2/\partial\rho + (\lambda/2)\partial/\partial\rho((1/V')\partial/\partial\rho(V'G\rho\mu_c)) = C\rho\partial\mu_c/\partial\rho/V'. \quad (4)$$

Here, V' and $G = R^2\langle(\nabla\rho)^2/r^2\rangle$ are metric coefficients that can be determined by solving the equilibrium problem, the prime denotes the derivative with respect to ρ, the integration constant C and parameter λ are to be determined from the boundary conditions, and the subscript c stands for the canonical profile.

Kadomtsev [1] implicitly employed the following boundary conditions for a tokamak with a circular cross section—the so-called circular cylinder approximation (CCA):

$$\mu_c(0) = \mu_0, \quad \mu_c'(0) = 0, \quad \mu_c(a) = \mu(a) \equiv \mu_a, \quad \lim\mu_c(\rho \longrightarrow \infty) = 0, \quad (5)$$

where $\mu_0 \sim 1$ and μ_a is the boundary value of the function $\mu(\rho)$, which is a solution to the set of transport equations. In the CCA, we have $\mu_a = RB_\theta/aB_0 = 0.2RI_p/a^2B_0$. The last of the boundary conditions (5) implies that the canonical profile can be chosen with no regard for the actual physical circumstances at the plasma boundary. Such boundary conditions will be referred to as "soft" conditions. Also, Eq. (4) with boundary conditions (5) in the CCA will be referred to as the Kadomtsev problem and the corresponding solutions will be marked by the superscript ^{K}. The solution to the Kadomtsev problem has the form [1]

$$\mu_c = \mu_c^K = \mu_0/(1 + \rho^2/a_j^2), \quad a_j^2 = a^2 q_0/(q_a - q_0). \quad (6)$$

For a toroidal plasma that is bounded by the separatrix it is impossible to impose the boundary condition at infinity. In this case, it is convenient to formulate the boundary conditions at the plasma surface using the first-order impedance:

$$X \equiv i(a_{\text{eff}})/(2G(a_{\text{eff}})\mu(a_{\text{eff}})), \quad (7)$$

where $i = (\mu_{00}R/B_0)j_\varphi = (1/V')\partial/\partial\rho(GV'\rho\mu)$ is the dimensionless current. For the Kadomtsev problem, the impedance has the form $X^K = \mu(a_{\text{eff}})/\mu(0)$.

The boundary conditions for a circular plasma cylinder,

$$\mu_c(0) = \mu(0), \quad \mu_c'(0) = 0, \quad \mu_c(a) = \mu(a), \quad X_c = X^K = \mu(a)/\mu(0) \quad (8)$$

are equivalent to conditions (5). In what follows, we will assume that, in the general case of a toroidal plasma column, boundary conditions (8) single out the special "Kadomtsev" solutions of interest to us. These solutions for the canonical profiles $\mu_c(\rho)$ are weakly sensitive to variations in the physical parameters of the plasma at its boundary (such as changes in the boundary temperature, radiative losses, and impurity seeding).

To determine canonical profiles of the temperature and density, $T_c(\rho)$ and $n_c(\rho)$, we recall that, in a steady state, the current and temperature profiles should deviate only slightly from being canonical. That is why the canonical profiles of the current and temperature should approximately satisfy Ohm's law, $j_c(\rho) \sim T_c^{2/3}$. This law and conditions (3) yield the relationships

$$T_c \sim j_c^{2/3}, \quad n_c \sim T_c^{1/2} \sim j_c^{1/3}. \quad (9)$$

In transport models, the expressions for the fluxes contain critical gradients. Canonical profiles determine the target of relaxation. When the profiles of the plasma parameters are canonical, the fluxes should be small. As a consequence, the dimensionless critical gradients Ω_{Tc} are determined by the canonical profiles of the current and, by virtue of relationships (9), have the form:

$$\Omega_{Tc} \equiv R/L_{Te} \equiv -RT_c'/T_c = -(2/3)Rj_c'/j_c, \quad \Omega_{nc} \equiv -Rn_c'/n_c = -(1/3)Rj_c'/j_c. \quad (10)$$

Calculations show that canonical profiles become flatter as the aspect ratio $A = R/a$ decreases and/or the elongation k and triangularity δ increase [4]. This flattening is illustrated by Fig. 1, which shows the normalized profiles $\mu_c(\rho)/\mu_c(0)$ for two different aspect ratios $A = 3$ and 5 (Fig. 1a) and the profiles of the critical gradients, $-RT_c'/T_c$, for the same parameters (Fig. 1b). The results of calculating the canonical profiles are discussed in more detail in [4].

3. MODIFIED CANONICAL PROFILE TRANSPORT MODEL

The set of transport equations in question consists of equations for the poloidal magnetic field and the electron and ion temperatures, T_i and T_e. For simplicity, we do not consider here the equation for the density. The equilibrium is found by solving the Grad–Shafranov equation. In contrast to our earlier works in which canonical profiles were calculated from Kadomtsev solution (6), the canonical profiles are now obtained by solving Eq. (4) with boundary conditions (8). The sequence of operations in the canonical profile transport model (CPTM) is shown in Fig. 2.

We assume that the critical gradients of the ion and electron temperatures are the same, $\Omega_{Tci} = \Omega_{Tce} = \Omega_{Tc}$, where Ω_{Tc} is given by the first of formulas (10), and choose the heat flux in the L mode in the form

$$Q_k = Q_k^l + Q_k^{PC} \quad (k = i, e), \tag{11}$$

$$Q_k^l = -\kappa_k^l \frac{\partial T_k}{\partial \rho}, \quad \kappa_k^l = n\chi_k^l, \tag{12}$$

$$Q_k^{PC} = \kappa_k^{PC}(T_k/R)(\Omega_{Tk} - \Omega_{Tc})H(\Omega_{Tk} - \Omega_{Tc}). \tag{13}$$

Here, $H(x)$ is the Heaviside step function defined as $H(x) = 1$ for $x \geq 0$ and $H(x) = 0$ for $x < 0$ and

$$\Omega_{Tk} = -RT_k'/T_k \tag{14}$$

are the relative gradients of the electron and ion temperatures. Heat fluxes (12), which are labeled by the superscript l, are proportional to the temperature gradients. Heat fluxes (13), which are labeled by the superscript PC, are proportional to the difference between the relative and critical temperature gradients. In tokamaks, the stiffness κ_k^{PC} is usually much larger than the thermal conductivity κ_k^l. The transport coefficients are chosen in the form [6–10]

$$\kappa_k^{PC} = \alpha_k^{PC}(1/M)(a/R)^{0.75} q(a_{\text{eff}}/2) q_{cyl} \times (T_k(a_{\text{eff}}/4))^{0.5} \bar{n}(3/R)^{1/4}/B_0 = \text{const}(\rho), \tag{15}$$

$$\chi_k^l = \text{const}(\rho) = \tilde{\alpha}_e \frac{(T_e(a_{\text{eff}}/2))^{1/2}}{n(a_{\text{eff}}/2)Rq(a_{\text{eff}})}, \quad \chi_k^l = \chi_i^{neo}, \quad q_{cyl} = \frac{5a^2 B_0}{I_p R}, \tag{16}$$

with $\alpha_e^{PC} = 3.5$, $\alpha_i^{PC} = 5$, and $\tilde{\alpha}_e \approx 2$. Here, M is the ion-to-proton mass ratio and the physical quantities are expressed in the following units: T in keV, B_0 in T, a and R in m, n in 10^{19} m^{-3}, χ_k in m^2 s^{-1}, and κ_k in 10^{19} m^{-1} s^{-1}.

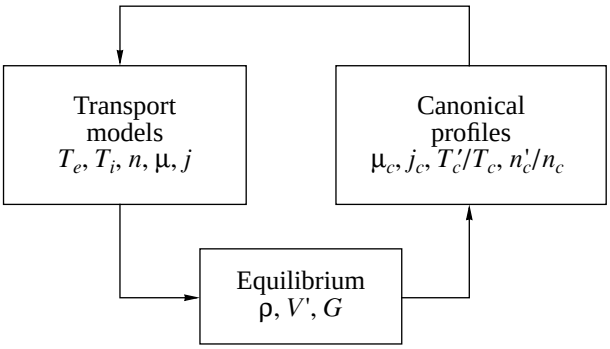

Fig. 2. Flow chart of the modified transport model.

4. VALIDATION OF THE CANONICAL PROFILE TRANSPORT MODEL

The transport model was validated by using the data from 45 tokamak discharges. Specifically, we used the published data on seven discharges with off-axis ECRH in ASDEX-U [11–13] and the data on six discharges from the MAST tokamak database. We also used the data on 32 discharges in DIII-D, JET, JT-60U, TFTR, ASDEX-U, T-10, and TEXTOR from the ITER Profile Database [14]. We tried to choose data on OH- and L-mode discharges; however, in some of the DIII-D and JET discharges and in most of the MAST discharges, the plasma was apparently in the H mode. In making the choice, we discarded several (about five) H-mode discharges in DIII-D since the electron temperature profiles for them were very flat and thus disagreed with fairly sharply peaked ion temperature profiles. The discharges that were used to test the model are listed in the table. Almost all of them were simulated using the

List of the selected discharges

Tokamak	Shot number
DIII-D	69627, 69648, 71378a, 71378b, 71384, 78106, 78109, 78281, 78283, 78316, 78328, 81499, 90105, 90118
ASDEX-U	6136, 6905, 13558oh, 13558a, 13558b, 13654oh, 13654, 15600oh, 15600
JET	19649oh, 19649, 19691oh, 19691, 26087, 26095, 32745
MAST	4505-H, 6252-H, 6326-H, 6762-H, 6952-H, 9005-L
JT-60U	21795, 21796, 21810, 21811
TEXTOR	68812
T-10	47379, 47405
TFTR	103648, 103808

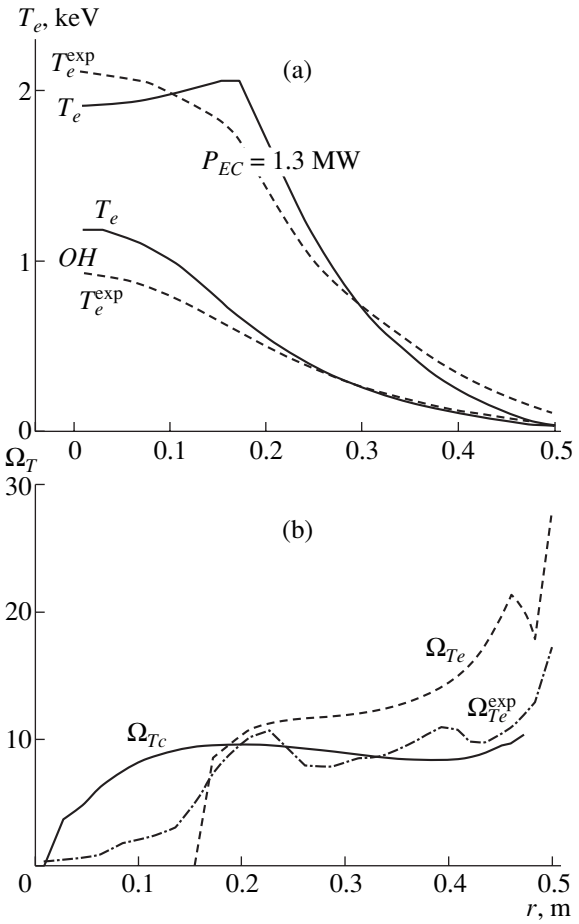

Fig. 3. (a) Temperature profiles and (b) relative and critical gradients during Ohmic (OH) and off-axis ECRH in shot no. 15 600 in ASDEX-U.

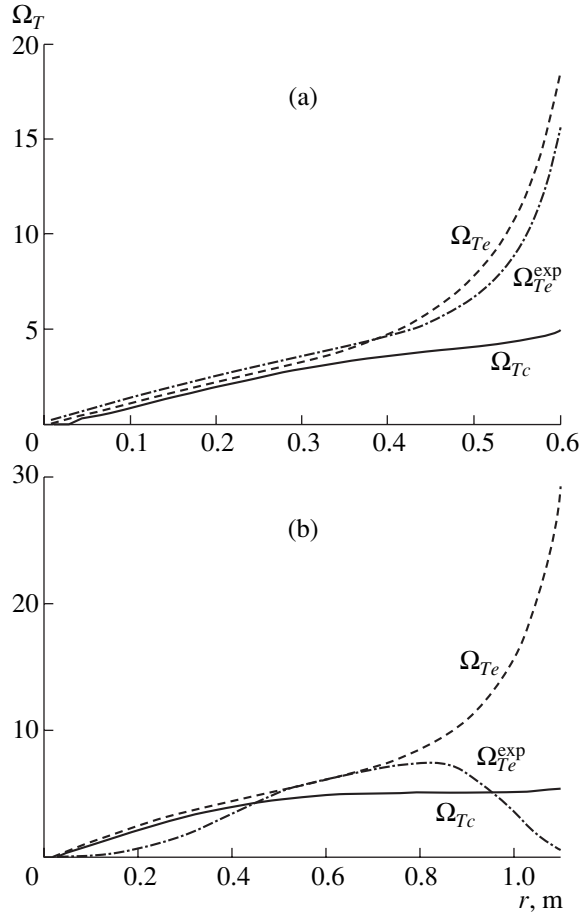

Fig. 4. Profiles of the relative and critical gradients in (a) shot no. 69 648 in DIII-D and (b) shot no. 19 691 in JET.

CPTM by means of the ASTRA code [15]. The plasma density profiles were taken from experiments. The H-mode pedestals were described by artificially increasing the electron and ion temperatures at the boundary.

Here, we analyze only the electron temperature profiles and do not consider data on the ions. We compare the calculated electron temperature profiles $T_e(\rho)$ with the experimental profiles $T_e^{exp}(\rho)$. We also compare the calculated and experimental relative temperature gradients, $\Omega_{Te} = -RT_e'/T_e$ and $\Omega_{T_e^{exp}} = -RT_e^{exp\prime}/T_e^{exp}$, and present the profiles of the critical gradient $\Omega_{Tc} = -RT_c'/T_c$ (for brevity, a_{eff} is replaced with a).

The calculations were compared with experiments by using the following two types of metrics that characterize the deviation of the calculated results from the experimental data:

$$dt2 = \sum_{0.2a}^{a} \left| T_e - T_e^{exp} \right| / \sum_{0.2a}^{a} T_e^{exp}, \qquad (17)$$

$$dtn2 = \sum_{0.2a}^{a} \left| T_e/T_e(0.2a) - T_e^{exp}/T_e^{exp}(0.2a) \right| / \sum_{0.2a}^{a} T_e^{exp}/T_e^{exp}(0.2a). \qquad (18)$$

Here, the summation is performed starting from the point $\rho = 0.2a$ in order to avoid errors introduced by the sawtooth oscillations, which were ignored in calculations. Metric (18) compares the profiles normalized to the temperature values at the radius $\rho = 0.2a$. In fact, this indicates that we compare the averaged temperature gradients.

Figures 3–5 show a comparison between the calculated and experimental results for ASDEX-U, DIII-D, JET, and MAST. The accuracy of modeling the T_e profiles is illustrated in Figs. 3a and 5a. The relative gradients $\Omega_{Te} = -RT_e'/T_e$, $\Omega_{T_e^{exp}} = -RT_e^{exp\prime}/T_e^{exp}$ and the critical gradients $\Omega_{Tc} = -RT_c'/T_c$ for these four tokamaks are presented in Figs. 3b, 4a, 4b, and 5b. The pro-

files are seen to be flat in the gradient region; consequently, the gradients can be characterized by their mid-radius values. The temperature gradients were calculated in natural coordinates determined from the solution to the equilibrium Grad–Shafranov equation; this indicates that, for a toroidal plasma with a noncircular cross section, the gradients are averaged over the magnetic surfaces.

5. SCALINGS FOR THE TEMPERATURE GRADIENTS

A comparison between the calculated and experimental relative temperature gradients, Ω_{Te} and $\Omega_{T_e^{\exp}}$, is shown in Fig. 6. We can see that the calculated and experimental relative temperature gradients are in reasonably good agreement with one another. The error bar (about ±15–20%) in determining $\Omega_{T_e^{\exp}}$ for one ASDEX-U discharge is also shown. According to this figure, the dimensionless gradients Ω_{Te} change over a broad range—from $\Omega_{Te} \sim 2$ for MAST to $\Omega_{Te} \sim 10$–12 for T-10. In [4], it was shown that the larger the aspect ratio $A = R/a$ and/or the quantity q, the more peaked the canonical profile (or, equivalently, the larger the relative gradient Ω_{Te}). It can also be seen that the peakedness of the canonical profile increases with decreasing the elongation k and/or triangularity δ. Consequently, the parameter $\zeta = qA^2/k$ can serve as a scaling (self-similar) parameter for the relative temperature gradient. The scaling parameter can also depend on the triangularity; however, this dependence is not considered here because it is weaker than the dependence on the elongation [4]. The aspect ratio in the parameter ζ is raised to the second power because the gradient is normalized to the plasma major radius. The expression for the scaling parameter can be refined by using the asymptote of the critical gradient Ω_c in the Kadomtsev case (6),

$$\Omega_c = \frac{16}{3}\frac{Aq}{q+4}, \qquad (19)$$

where $A \gg 1$. This implies, in particular, that it would be better to use a weaker dependence on q, $\xi = qA^2/(k(q+4))$, for the scaling parameter. Of course, the above considerations help merely to estimate which of the scaling parameters is most suitable for describing the calculated and experimental relative temperature gradients, Ω_{Te} and $\Omega_{T_e^{\exp}}$. A search for a more realistic scaling requires substantial computational work aimed at the statistical analysis of the deviations of the calculated results from the experimental data. This is why only a few examples will be discussed here.

Figure 7 shows the dependence of the experimental relative gradients $\Omega_{T_e^{\exp}}$ at mid-radius, $\rho = a/2$, on the scaling parameter $\xi = qA^2/(k(q+4))$ for all of the chosen discharges in the eight tokamaks. We emphasize that Fig. 7 presents only experimental data. The theory of canonical profiles merely helps to choose the form of the scaling parameter ξ. All the experimental points are

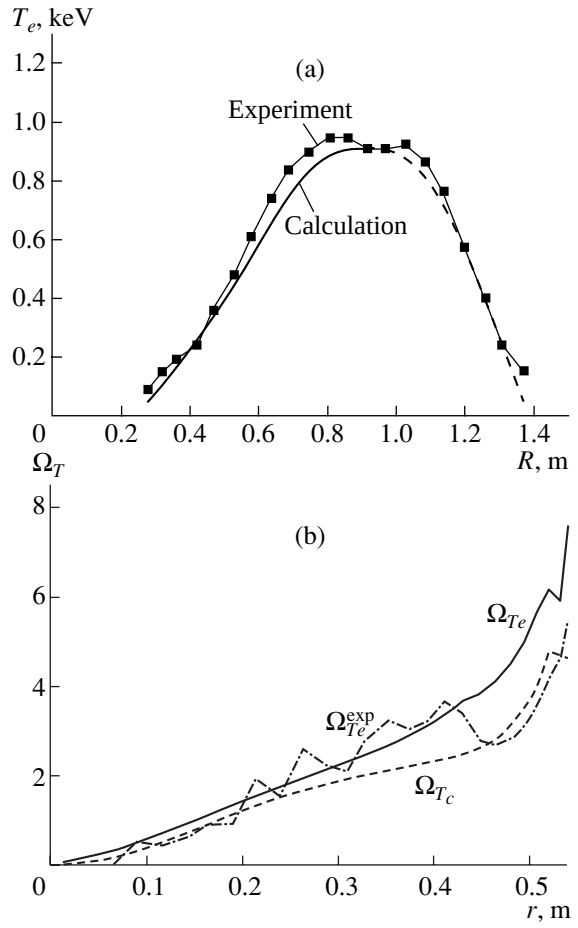

Fig. 5. (a) Temperature profiles and (b) critical gradients at t = 265 ms in shot no. 6252 in MAST.

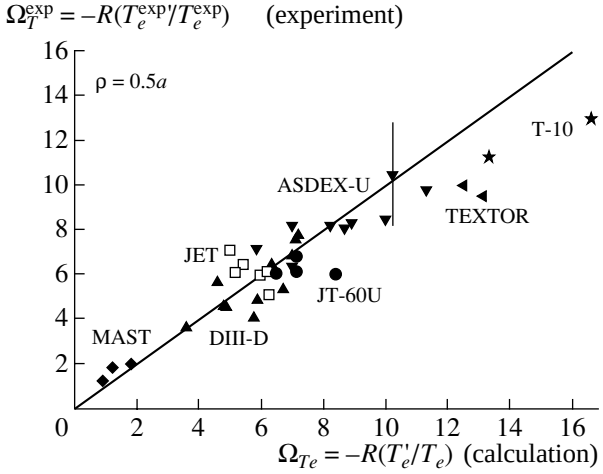

Fig. 6. Comparison between the measured and calculated relative gradients.

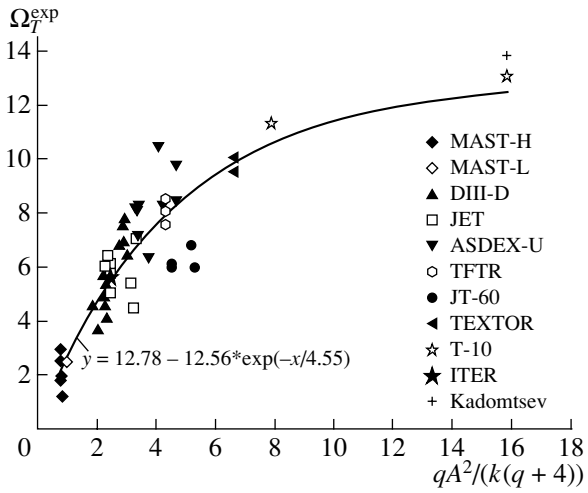

Fig. 7. Dependence of the measured relative gradient of the electron temperature on the scaling parameter $\xi = qA^2/(k(q+4))$. The cross indicates the value of the critical gradient calculated from Kadomtsev asymptotic formula (19) for the corresponding T-10 shot.

seen to lie near a certain smooth convex curve. On the one hand, the scatter of the points around the curve is fairly large; on the other hand, the experimental errors in calculating $\Omega_{T_e^{exp}}$ are also large. As the aspect ratio increases, critical gradient (19) in the case of the Kadomtsev solution increases without saturation. The rightmost experimental point in Fig. 7 refers to a discharge in T-10 with an aspect ratio of $A = 6$ and a minor radius of $a = 25$ cm. Since this radius value is not typical of the T-10 tokamak, the reliability of the measurements of the temperature profile during the discharge was low. Nevertheless, this experimental point is close to the point predicted by formula (19) and is marked by the cross in Fig. 7.

Based on the results shown in Fig. 7, we can try to predict Ω_{Te} values for the ITER-FEAT project. For a discharge with the parameters $R = 6$ m, $a_m = 2$ m, $A = 3$, $k = 1.7$, and $q = 3.5$, we obtain $\xi = 2.45$, in which case the results of Fig. 7 yield $\Omega_{Te} = 5.6$. Since this is an interpolation problem (rather than an extrapolation one, as is the case with the problem of predicting the energy confinement time), the prediction should be sufficiently reliable.

Figure 8 shows the relative temperature gradient Ω_{Te} calculated at mid-radius as a function of the parameter ξ for the same discharges. Also shown in the figure is the approximating curve, which is seen to differ slightly in shape from that in Fig. 7. However, the value $\Omega_{Te} \approx 6$ predicted for ITER-FEAT remains almost the same.

The dependence of the critical gradient Ω_c on the parameter ξ is displayed in Fig. 9. The approximating curve is also similar in shape to those in Figs. 7 and 8. Figure 10 shows how the calculated relative temperature gradient Ω_{Te} depends on the calculated critical gradient Ω_c. The elevation of the points above the diagonal corresponds to the deviation of the temperature profile from a canonical. The mean deviation is seen to be about 10%. The deviation itself depends on the power input to the plasma and also on the stiffness $\chi_k = \kappa_k^{PC}/n$ in heat flux (13). Our model has a moderate stiffness. For typical JET parameters, the stiffness is about $\chi_i \sim 7.5$ and $\chi_e \sim 5$ m^2/s. In stiff models, like the IFS/PPPL model [16], the stiffness is about $\chi_i \sim 20$ m^2/s, so that the deviation of the calculated gradients from the critical ones should be smaller.

The accuracy of predictions derived from the CPTM is illustrated in Fig. 11, which shows the correlation

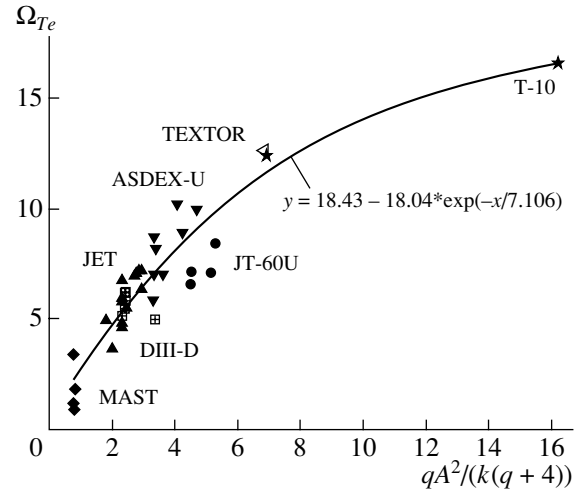

Fig. 8. Dependence of the calculated relative gradient of the electron temperature on the scaling parameter $\xi = qA^2/(k(q+4))$.

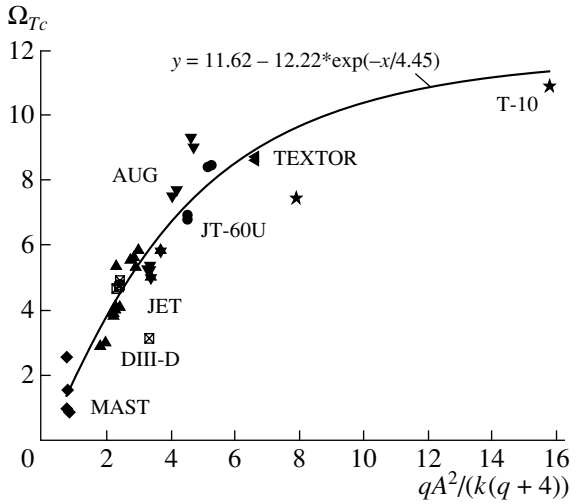

Fig. 9. Dependence of the critical temperature gradient on the scaling parameter $\xi = qA^2/(k(q+4))$.

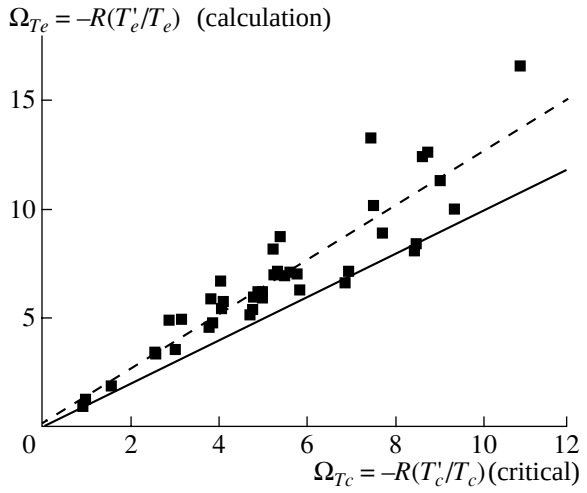

Fig. 10. Dependence of the calculated relative gradient Ω_{Te} on the critical gradient Ω_c. The dashed line shows the linear approximation, while the solid line is the diagonal.

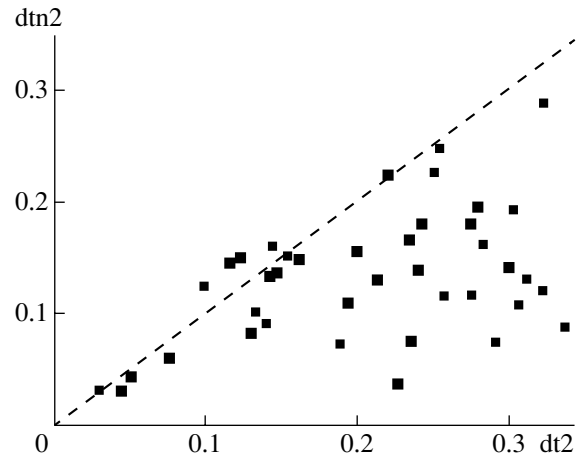

Fig. 11. Normalized deviation of T_e from $T_e^{\exp}$ vs. the linear deviation of T_e from $T_e^{\exp}$.

between the normalized and linear deviations for the discharges chosen above. First, we can see that the mean linear deviation is about 20–22%. Such a large mean deviation can be partially explained by the fact that, in simulations, we neglected some important physical processes, such as sawtooth oscillations and plasma emission. From Fig. 11, we also see that normalized deviations (18) are about two times smaller than linear deviations (17). This indicates that, in describing the temperature gradients, the processes ignored in the analysis are of minor importance. As a result, with the model proposed here, the description of the gradients is less sensitive to various types of error than the description of the absolute values of the electron temperature.

6. CONCLUSIONS

Based on the canonical profile theory developed for tokamak plasmas with arbitrary cross sections, we have proposed a modified transport model in which the critical temperature gradient $\Omega_c = R/L_T$ in the expressions for the heat flux is determined in terms of the calculated canonical profile. The model was validated by comparing the computed results with experimental data from eight different tokamaks. Modeling of a set of 45 discharges yields good agreement between the experimental and calculated temperature profiles. An analysis of the measured and calculated relative temperature gradients $\Omega_{Te} = -RT_e'/T_e$ makes it possible to determine a reasonable scaling parameter, $qA^2/(k(q + 4))$, for the temperature gradient. The scaling obtained here can be used to predict the shapes of the electron and ion temperature profiles in present-day and future tokamaks.

ACKNOWLEDGMENTS

We are grateful to G.V. Pereverzev for providing us with a new version of the ASTRA code. This work was supported in part by the Russian Foundation for Basic Research (project no. 00-15-96536), Ministry of Atomic Energy of the Russian Federation, and Consulting Agreement no. QS06588 with UKAEA (United Kingdom).

REFERENCES

1. B. B. Kadomtsev, Fiz. Plazmy **13**, 443 (1987) [Sov. J. Plasma Phys. **13**, 443 (1987)].
2. D. Biskamp, Comm. Plasma Phys. Control. Fusion **10**, 165 (1986).
3. J. Y. Hsu and M. S. Chu, Phys. Fluids **30**, 1221 (1987).
4. Yu. N. Dnestrovskij, A. Yu. Dnestrovskij, S. E. Lysenko, and S. V. Cherkasov, Fiz. Plazmy **28**, 963 (2002) [Plasma Phys. Rep. **28**, 887 (2002)].
5. Yu. N. Dnestrovskij, A. Yu. Dnestrovskij, S. E. Lysenko, and S. V. Cherkasov, in *Proceedings of the 19th IAEA Fusion Energy Conference, Lyon, 2002*, Paper TH/P1-04.
6. Yu. N. Dnestrovskij and G. V. Pereverzev, Plasma Phys. Controlled Fusion **30**, 47 (1988).
7. Yu. N. Dnestrovskij, E. L. Berezovskij, S. E. Lysenko, *et al.*, Nucl. Fusion **31**, 1877 (1991).
8. Yu. N. Dnestrovskij, Yu. V. Esipchuk, N. A. Kirneva, *et al.*, Fiz. Plazmy **23**, 614 (1997) [Plasma Phys. Rep. **23**, 566 (1997)].
9. Yu. N. Dnestrovskij, S. V. Cherkasov, S. E. Lysenko, *et al.*, Nucl. Fusion **38**, 373 (1998).

10. Yu. N. Dnestrovskij, M. P. Gryaznevich, A. Yu. Dnestrovskij, *et al.*, Fiz. Plazmy **26**, 579 (2000) [Plasma Phys. Rep. **26**, 539 (2000)].

11. F. Ryter, C. Angioni, M. Beurskens, *et al.*, Plasma Phys. Controlled Fusion **43**, A323 (2001).

12. F. Ryter, G. Tardini, H.-U. Fahrbach, *et al.*, in *Proceedings of the 29th EPS International Conference on Plasma Physics and Controlled Fusion, Montreux, 2002*, ECA **26B**, Paper P-1.048.

13. F. Leuterer, R. Dux, G. Gantenbein, *et al.*, in *Proceedings of the 12th International Workshop on ECE and ECRH, Aix-en-Provence, 2002*; http://wshop.free.fr/ec12/.

14. D. Boucher, J. W. Connor, W. A. Houlberg, *et al.*, Nucl. Fusion **40**, 1955 (2000); http://tokamak-profiledb.ukaea.org.uk/.

15. G. V. Pereverzev and P. N. Yushmanov, Tech. Rep. IPP 5/98 (Max-Planck Institut für Plasmaphysik, Garching, 2002).

16. M. Kotschenreuther, W. Dorland, M. A. Beer, and G. W. Hammett, Phys. Plasmas **2**, 2381 (1995).

Translated by O.E. Khadin

Plasma Physics Reports, Vol. 30, No. 1, 2004, pp. 18–29. Translated from Fizika Plazmy, Vol. 30, No. 1, 2004, pp. 21–32.

PLASMA DYNAMICS

Concerning the Maximum Energy of Ions Accelerated at the Front of a Relativistic Electron Cloud Expanding into Vacuum

S. V. Bulanov[1], T. Zh. Esirkepov[2, 3], J. Koga[2], T. Tajima[2], and D. Farina[4]

[1] *Prokhorov Institute of General Physics, ul. Vavilova 38, Moscow, 119991 Russia*

[2] *APRC, JAERI, Kizu, Kyoto, Japan*

[3] *Moscow Institute of Physics and Technology, Institutskiĭ pr. 9, Dolgoprudnyĭ, 141700 Russia*

[4] *Institute for Plasma Physics–CNR, Milan, Italy*

Received May 22, 2003

Abstract—Results of particle-in-cell simulations are presented that demonstrate characteristic interaction regimes of high-power laser radiation with plasma. It is shown that the maximum energy of fast ions can substantially exceed the electron energy. A theoretical model is proposed of ion acceleration at the front of a relativistic electron cloud expanding into vacuum in the regime of strong charge separation. The model describes the electric field structure and the dynamics of fast ions inside the electron cloud. The maximum energy the ions can gain at the front of the expanding electron cloud is found. © *2004 MAIK "Nauka/Interperiodica"*.

1. INTRODUCTION

Over the past few decades, the problem of the generation of charged particle beams in the interaction of high-power electromagnetic radiation with plasma have attracted great interest [1]. This interest stems from the fact that the interaction of a high-power laser pulse with a collisionless plasma results in the generation of large-scale collective electric fields in which electrons and ions can be accelerated up to extremely high energies. The high ion-acceleration efficiency observed in experiments [2–10] has stimulated discussion about the possibility of using laser-accelerated ions in various applications. Among them, we note the use of such ions in controlled fusion research (with in the framework of the concept of fast ignition of preliminary compressed thermonuclear targets [11, 12]), the hadron therapy of oncological diseases [13–16], and the diagnostics of ultrafast plasma processes [17, 18].

Numerous experimental studies (see, e.g., [2–10]) have been devoted to the investigation of different regimes of fast-ion generation in the interaction of multiterawatt and petawatt laser radiation with thin solid targets (foils). In some papers, it was asserted that both the ions initially located at the front side and those located at the rear side of the target are involved in the acceleration process. We note that such acceleration was previously observed in computer simulations [19, 20]. Computer simulations have also demonstrated the high efficiency of ion acceleration in the interaction of high-power laser radiation with plasma [21–27]. Moreover, 3D simulations have demonstrated that the transverse and longitudinal emittances of the ion beam can be controlled by varying the target parameters [28–33].

The interpretation of the results of the above experiments and of computer simulations demands the development of a theory of such acceleration. In particular, the theoretical models should be able to describe the maximum ion energy and the shape of the energy spectrum of fast ions as functions of the laser-pulse and target parameters. Although various mechanisms of ion acceleration (see, e.g., [1, 19–36]) have been discussed in the literature, two of them traditionally attract the greatest interest. According to the first mechanism, the ions are accelerated in a target surface layer in which the strong electric field is localized. The field amplitude and the width of the surface layer are such that the electric potential drop is on the order of the electron thermal energy and, accordingly, the ion energy is on the order of the electron thermal energy times the ion charge number. The second mechanism assumes that the ions are accelerated at the front of a plasma expanding into vacuum [37–45]. In this model, the accelerating electric field is assumed to be generated due to space charge separation in a narrow layer at the front of the plasma cloud, which, on the whole, is electrically neutral. In this case, the energy of fast ions does not depend on their charge and can substantially exceed the electron energy, as was observed experimentally in [46].

A transition to electromagnetic radiation powers corresponding to relativistically strong fields radically changes the acceleration regime. In particular, computer simulations [21, 25, 28, 29] show that the interaction of petawatt laser radiation with foils results in the formation of extended regions with a strong electric field. In these regions, the plasma quasineutrality is strongly violated, which should necessarily be taken

1063-780X/04/3001-0018$26.00

into account when describing ion acceleration theoretically.

One well-known example of efficient ion acceleration under conditions of strong charge separation is the Coulomb explosion of a cluster [34, 47–49]. In this case, the electrons escape from the cluster under the action of strong electromagnetic radiation and the collective electric field of the expanding ion component plays a key role in the acceleration process. In other situations (e.g., in the regime considered in [31–33]), a small number of light ions gain energy in a time-independent electric field near the target surface and their dynamics can be described in the test-particle approximation.

In the next section, we describe the results of particle-in-cell (PIC) simulations demonstrating laser–plasma interaction regimes in which the energy of fast ions substantially exceeds the electron energy. In Section 3, we present a theoretical model of the acceleration of a relatively small group of ions at the front of a relativistic electron cloud expanding into vacuum in the regime of strong charge separation. The model explains the acceleration of fast ions up to energies higher than the electron energy. The results obtained within this model describe the electric-field structure and the dynamics of fast ions inside the electron cloud. The maximum energy the ions can gain at the front of the expanding electron cloud is found.

2. RESULTS OF COMPUTER SIMULATIONS OF ION ACCELERATION UP TO ENERGIES SUBSTANTIALLY EXCEEDING ELECTRON ENERGY

Numerical simulations of charged particle acceleration in the interaction of ultrashort laser pulses with thin targets were performed with a 2D version of the REMP code [50]. This is a relativistic electromagnetic code based on the PIC method [51–53]. It is well known that PIC simulations allow one to take into account various nonlinear and kinetic processes occurring in the interaction of high-power laser radiation with targets. On the other hand, such simulations make it possible to reveal the distinctive features of particle acceleration in one- and multidimensional models. Here, we consider the acceleration of protons and pions (π^+) in the interaction of laser radiation with two-layer targets. In both cases, the target is an aluminum foil with a thin hydrogen or pion-containing layer on its rear side. The efficiency of pion generation in laser plasma was calculated in [54]. We note that ultrashort laser pulses are considered to be a very promising means for accelerating short-lived particles (see [1]) because the characteristic time needed to accelerate such particles to relativistic energies can be substantially shorter than their decay time. For example, the decay time of a pion is 2.6×10^{-8} s, whereas the characteristic acceleration time can be shorter than several hundred femtoseconds.

In the case of proton acceleration, simulations were performed in a $120\lambda \times 60\lambda$ region with a mesh size of $0.1\lambda \times 0.1\lambda$, where $\lambda = 2\pi c/\omega$ is the laser wavelength, with ω being the laser frequency. The total number of particles was about 10^7. The particles and electromagnetic radiation were absorbed at the boundaries of the simulation region; however, the influence of the boundary conditions was negligible because of the sufficiently large dimensions of the simulation region. The target was a 3λ-thick aluminum foil with a 0.25λ-thick hydrogen layer on its rear side. The aluminum ions were assumed to be triply ionized. The electron density inside the aluminum foil was equal to $n_0 = 4n_{cr}$, where $n_{cr} = m_e\omega^2/4\pi e^2$ is the critical density. The proton density in the hydrogen layer was $n_0 = 1.33n_{cr}$. The proton-to-electron mass ratio was $m_p/m_e = 1836$, and the aluminum-to-proton nuclear mass ratio was $m_{Al}/m_p = 26.98$. The target was located near the $x = 40\lambda$ plane. The laser pulse entered the simulation region from the left boundary, which was located at $x = 0$. The electric field of incident radiation was directed along the y axis (p-polarized radiation). The dimensionless amplitude of the laser pulse was $a_0 = eE_0/m_e\omega c = 3$, which corresponded to an intensity of $I \approx 1.2 \times 10^{19}$ W/cm^2 for a laser wavelength of $\lambda = 1$ μm. The width and length of the laser pulse were 30λ and 90λ, respectively, which corresponded approximately to 350-TW laser power.

The simulation results are shown in Figs. 1–3. Here and below, the units of length and time are the laser wavelength and period, respectively. Figure 1 shows the energy spectra of (a) electrons, (b) protons, and (c) aluminum ions at $t = 650$ (the instant by which the maximum energies of protons and electrons have already reached their quasi-steady values). It can be seen that the maximum proton energy (15 MeV) is approximately three times the maximum electron energy (5 MeV) and thirty times the aluminum-ion energy per nucleon. The protons are accelerated in the electric field produced by fast electrons, which gain energy in the interaction with laser radiation and then get into the region behind the target. Figure 2 shows the distributions of the (a) x and (b) y components of the electric field in the (x, y) plane at $t = 100$ (the instant at which the proton energy spectrum varies most rapidly). It can be seen that the transverse component of the electromagnetic field does not penetrate to the rear side of the target and that the longitudinal electric field (it is this field that accelerates protons) occupies an extended region behind the target. Figure 3 shows the distributions of the (a) electron, (b) proton, and (c) aluminum-ion densities in the (x, y) plane at $t = 300$.

In the case of pion acceleration, simulations were performed in the $160\lambda \times 60\lambda$ region. The target was a 3λ-thick aluminum foil with a 0.25λ-thick pion-containing layer on its rear side. The pion-to-electron mass ratio was $m_\pi/m_e \approx 279$. The other simulation parameters were the same as in the case of proton acceleration. The simulation results are shown in Figs. 4–6. Figure 4

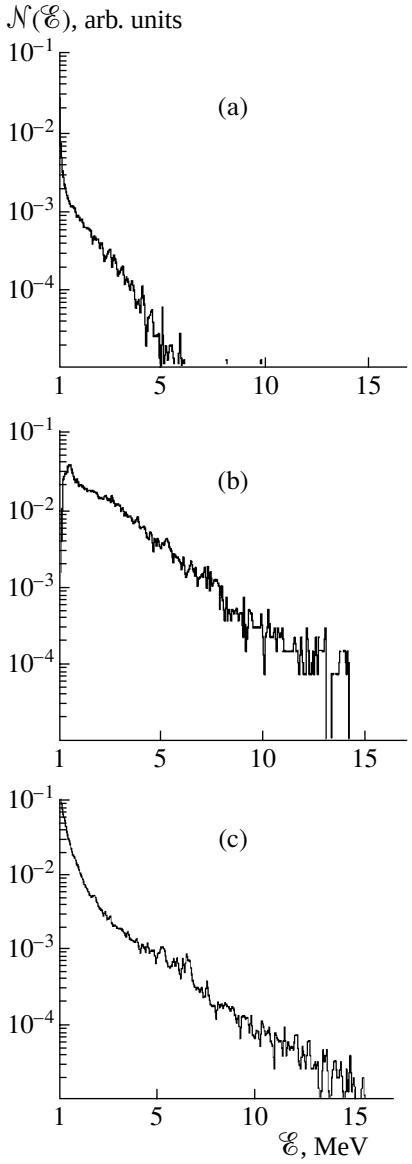

Fig. 1. Energy spectra of (a) electrons, (b) protons, and (c) aluminum ions at $t = 650$.

shows the energy spectra of (a) electrons, (b) pions, and (c) aluminum ions at $t = 250$ (the instant by which the maximum energies of pions and electrons have already reached their quasi-steady values). It can be seen that the maximum pion energy (12 MeV) is approximately two-and-a-half times the maximum electron energy (5 MeV) and is much higher than the aluminum-ion energy per one nucleon. As in the previous case, the pions are also accelerated in a quasistatic electric field produced by fast electrons on the rear side of the target. Figure 5 shows the distributions of the (a) x and (b) y components of the electric field at $t = 87.5$, while Fig. 6 shows the distributions of the (a) electron, (b) pion, (c) and aluminum-ion densities in the (x, y) plane at $t = 212.5$.

3. INTERACTION OF IONS WITH A COLLECTIVE ELECTRIC FIELD GENERATED DURING THE EXPANSION OF A RELATIVISTIC ELECTRON CLOUD INTO VACUUM

3.1. Electric Field Structure near the Front of the Electron Cloud

Let us consider the acceleration of ions during the "vacuum heating" of electrons. We assume that the first (heavy-ion) layer of a two-layer target of width l remains at rest during the interaction. The light ions are described in the test-particle approximation. The lower indices i, α, and e stand for heavy ions, light ions, and electrons, respectively.

We assume that the electrons are initially located inside the target (in the interval $-l/2 < x < l/2$). Under the action of a short laser pulse, the electrons gain a momentum $p_{e,0}$ directed along the x axis. The expansion of the electron cloud into vacuum is determined by the self-consistent electric field, which also accelerates light ions. This acceleration mechanism can be regarded as an extension of the well-known mechanism of ion acceleration during the expansion of plasma into vacuum [37, 38] to the case in which plasma quasineutrality is strongly violated and the particles have relativistic energies.

To describe the expansion of an electron cloud into a vacuum, we will use one-dimensional equations of electron hydrodynamics:

$$\frac{\partial n_e}{\partial t} + \frac{\partial (n_e v_e)}{\partial x} = 0, \tag{1}$$

$$\frac{\partial p_e}{\partial t} + v_e \frac{\partial p_e}{\partial x} = -eE, \tag{2}$$

$$\frac{\partial E}{\partial x} = 4\pi e(Z_i n_i(x) - n_e), \tag{3}$$

where n_e is the electron density, the electron velocity and momentum are related to each other by the expression $v_e = cp_e/(m_e^2c^2 + p_e^2)^{1/2}$, and the ion density $n_i(x)$ is assumed to be uniform inside the interval $-l/2 < x < l/2$ and equal to zero outside of it.

To find the solution to Eqs. (1)–(3), we switch from the Euler variables x and t to the Lagrange variables x_0 and t. Here, x_0 is the coordinate of an element of the electron fluid at the initial instant $t = 0$ ($-l/2 < x_0 < l/2$). The Euler and Lagrange variables are related to each other by the expression

$$x = x_0 + \xi_e(x_0, t), \tag{4}$$

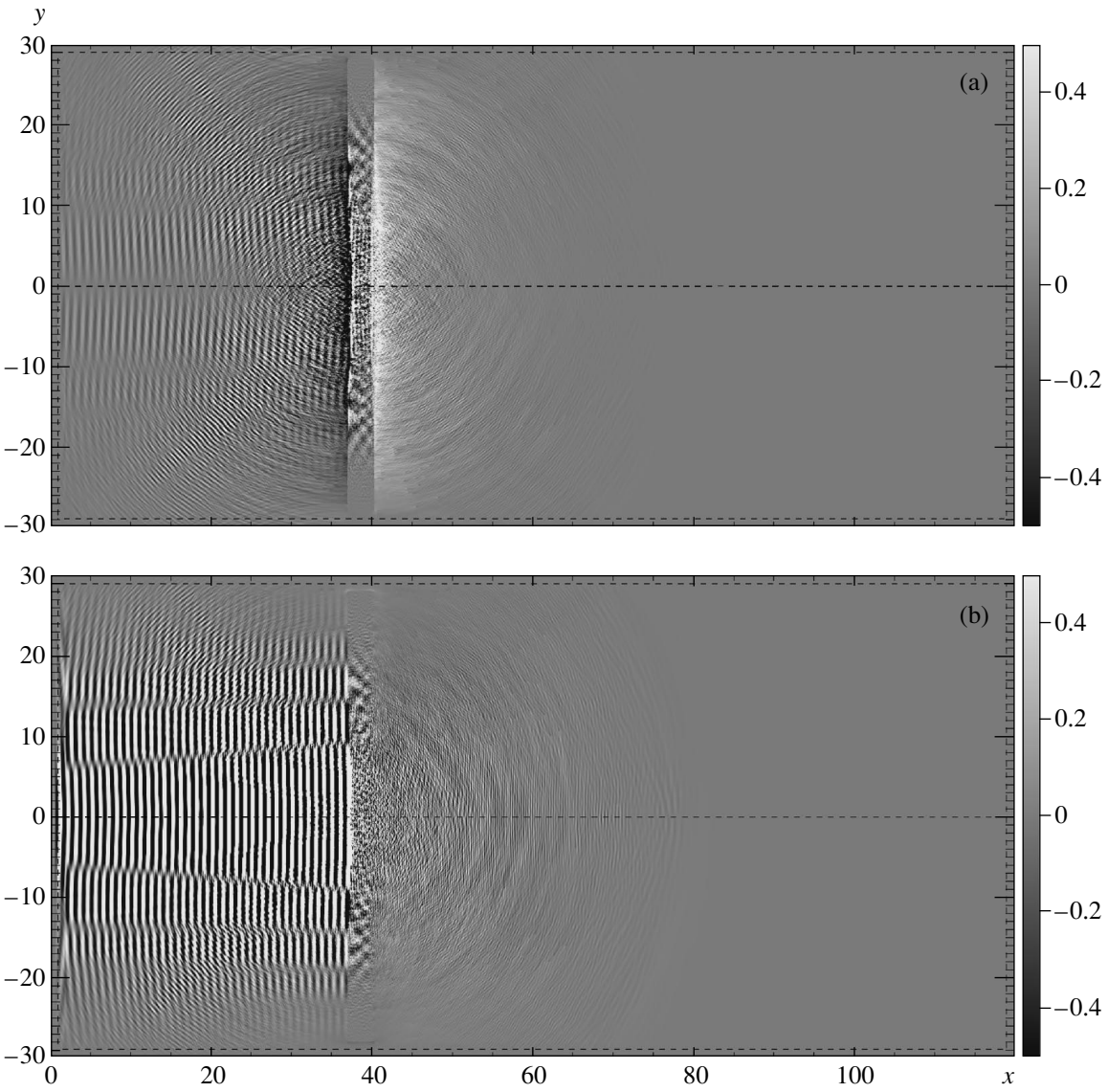

Fig. 2. Distributions of the (a) x and (b) y components of the electric field in the (x, y) plane at $t = 100$.

where $\xi_e(x_0, t)$ is the distance by which an element of the electron fluid is displaced from its initial position over the time t. At the initial instant, we have $\xi_e(x_0, 0) = 0$. In the Lagrange variables, Eqs. (1)–(3) become (see [55–57])

$$\frac{\partial p_e}{\partial t} = -4\pi Z_i e^2 \int_0^{\xi_e(x_0, t)} n_i(x_0 + s)ds, \quad (5)$$

$$\frac{\partial \xi_e}{\partial t} = c\frac{p_e}{(m_e^2c^2 + p_e^2)^{1/2}}. \quad (6)$$

In our case, the density profile of heavy ions $n_i(x)$ is given by the expression $n_i(x) = n_0\theta(l/2 - x)$, where $\theta(x)$ is the Heaviside step function: $\theta(x = 0$ at $x < 0$ and $\theta(x) = 1$ at $x > 0$. As a result, the right-hand side of Eq. (5) takes the form

$$eE(x_0, t) = -4\pi Z_i n_0 e^2 \begin{cases} l/2 - x_0, & l/2 < x_0 + \xi_e(x_0, t) \\ \xi_e(x_0, t), & -l/2 < x_0 + \xi_e(x_0, t) < l/2 \\ -l/2 - x_0, & x_0 + \xi_e(x_0, t) < -l/2. \end{cases} \quad (7)$$

We are first of all interested in the dependence of the electric field on the coordinate and time near the front of the electron cloud. It follows from Eq. (7) that, in the Lagrange variables, the electric field has the form $E(x_0, t) = -4\pi n_0 Z_i e(l/2 - x_0)$. To find the electric field profile

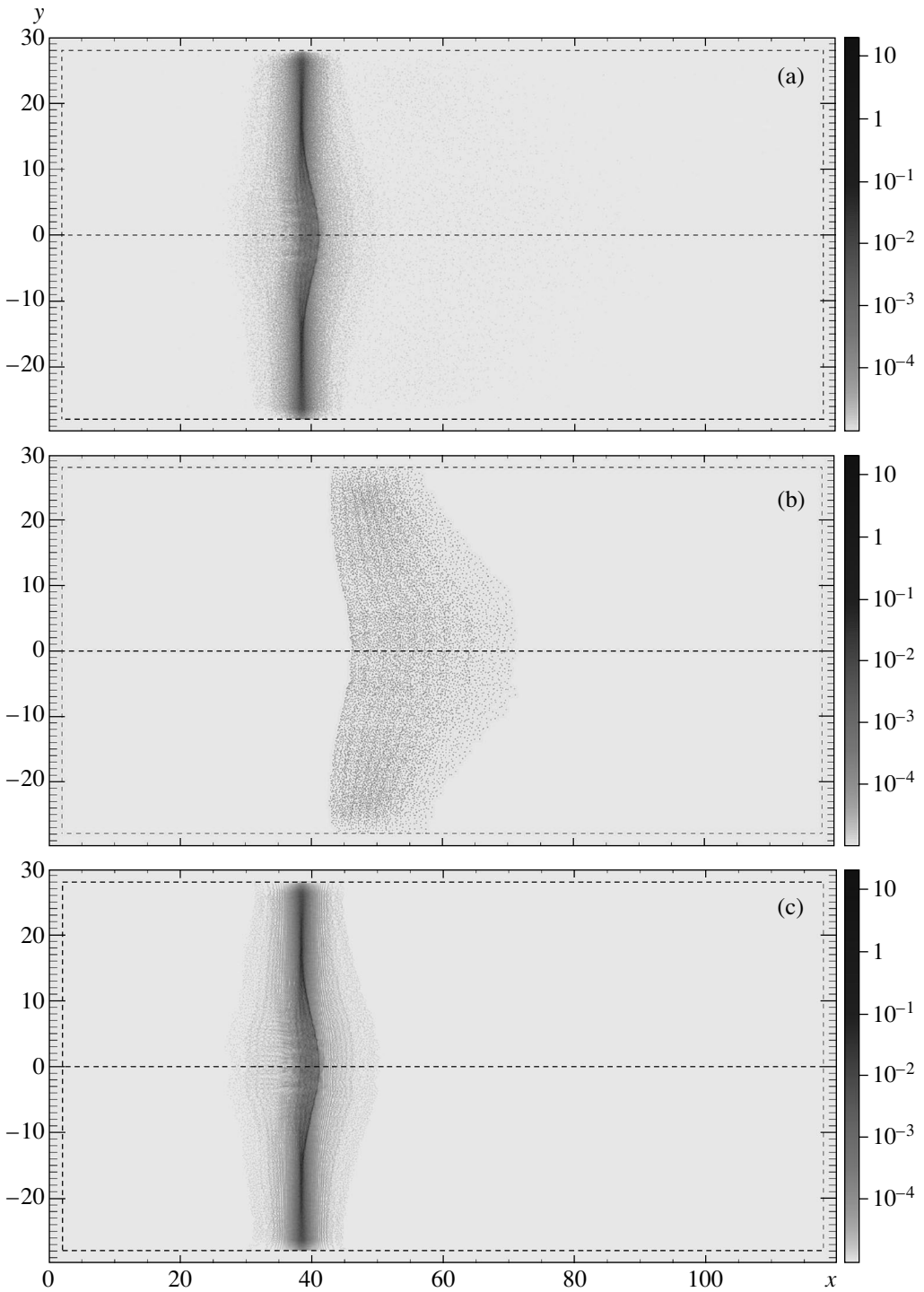

Fig. 3. Distributions of the (a) electron, (b) proton, and (c) aluminum-ion densities in the (x, y) plane at $t = 300$.

as a function of the Euler coordinate x, it is necessary to use the solutions to Eqs. (5) and (6):

$$p_e(x_0, t) = p_{e,0}(x_0) - 2\pi Z_i n_0 e^2 (l - 2x_0)t, \qquad (8)$$

$$\xi_e(x_0, t) = \frac{c}{\kappa(x_0)}\{[m_e^2c^2 + p_{e,0}^2(x_0)]^{1/2} - [m_e^2c^2 + (p_{e,0}(x_0) - \kappa(x_0)t)^2]^{1/2}\}, \qquad (9)$$

where the function $p_{e,0}(x_0)$ describes the initial distribution of the electron momentum in the cloud and

$$\kappa(x_0) = 2\pi n_0 Z_i e^2 (l - 2x_0). \quad (10)$$

It can be seen that the displacement of an electron from its initial position ($\xi_e(x_0, 0) = 0$) first increases as $\xi_e(x_0, 0) \approx v_{e,0}t$, where $v_{e,0} = cp_{e,0}/(m_e^2c^2 + p_{e,0}^2)^{1/2}$ is the initial electron velocity. In a time of $t_m = p_{e,0}(x_0)/[\pi n_0 Z_i e(2l - x_0)]$, the displacement reaches its maximum value $\xi_{e,m}(x_0) = c\{[m_e^2c^2 + p_{e,0}^2(x_0)]^{1/2} - m_e c\}/\kappa(x_0)$ and then decreases. It follows from the expressions obtained that the closer the Lagrange coordinate x_0 of an element of the electron fluid to the boundary of the plasma layer, the longer the time required for the element to return to its initial position ($\approx t_m$). For $x_0 \longrightarrow l/2$ (which corresponds to the particles located at the front of the electron cloud), the return time tends to infinity. Near the front of the electron cloud, where $\kappa(x_0) \longrightarrow 0$, we have

$$\xi_e(x_0, t) \approx c\frac{p_{e,0}(x_0)t}{(m_e^2c^2 + p_{e,0}^2(x_0))^{1/2}} - 2\pi n_0 Z_i e^2\left(\frac{l}{2} - x_0\right)\frac{m_e^2c^3t^2}{(m_e^2c^2 + p_{e,0}^2(x_0))^{3/2}}. \quad (11)$$

We assume that, near the front of the cloud, the initial distribution of the electron momentum $p_{e,0}(x_0)$ is uniform; i.e., $p_{e,0}$ does not depend on the coordinate x_0. Using Eqs. (4) and (10), we find the relation between the Lagrange and Euler coordinates:

$$x_0 = \frac{4(x - v_{e,0}t) + blt^2}{2(2 + bt^2)}, \quad (12)$$

where

$$b = \frac{4\pi n_0 Z_i e^2 m_e^2 c^3}{(m_e^2c^2 + p_{e,0}^2(x_0))^{3/2}}. \quad (13)$$

It follows from this that the electric field profile near the front of the electron cloud is described by the expression

$$E(x, t) = -4\pi n_0 Z_i e\frac{2(x - v_{e,0}t) - l}{2 + bt^2}\theta\left(v_{e,0}t + \frac{l}{2} - x\right). \quad (14)$$

It can be seen that the electric field vanishes at the front of the cloud (i.e., at $x = l/2 + v_{e,0}t$). The gradient of the electric field is proportional to the electron density and depends on time as

$$\frac{\partial E}{\partial x} = -8\pi Z_i e\frac{n_0}{2 + bt^2}. \quad (15)$$

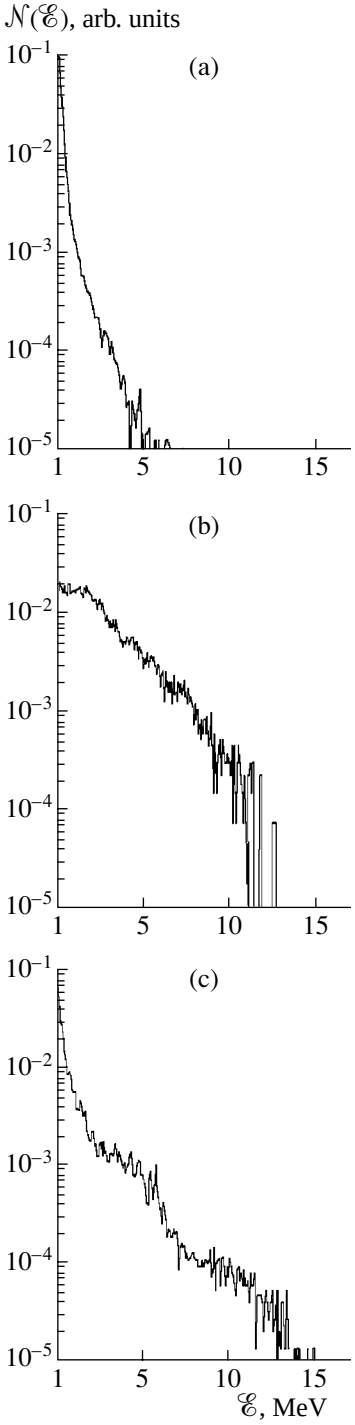

Fig. 4. Energy spectra of (a) electrons, (b) pions, and (c) aluminum ions at $t = 250$.

3.2. Acceleration of Ions at the Front of the Electron Cloud

Let us consider the acceleration of ions with a mass m_a and charge $Z_a e$ in the electric field described by

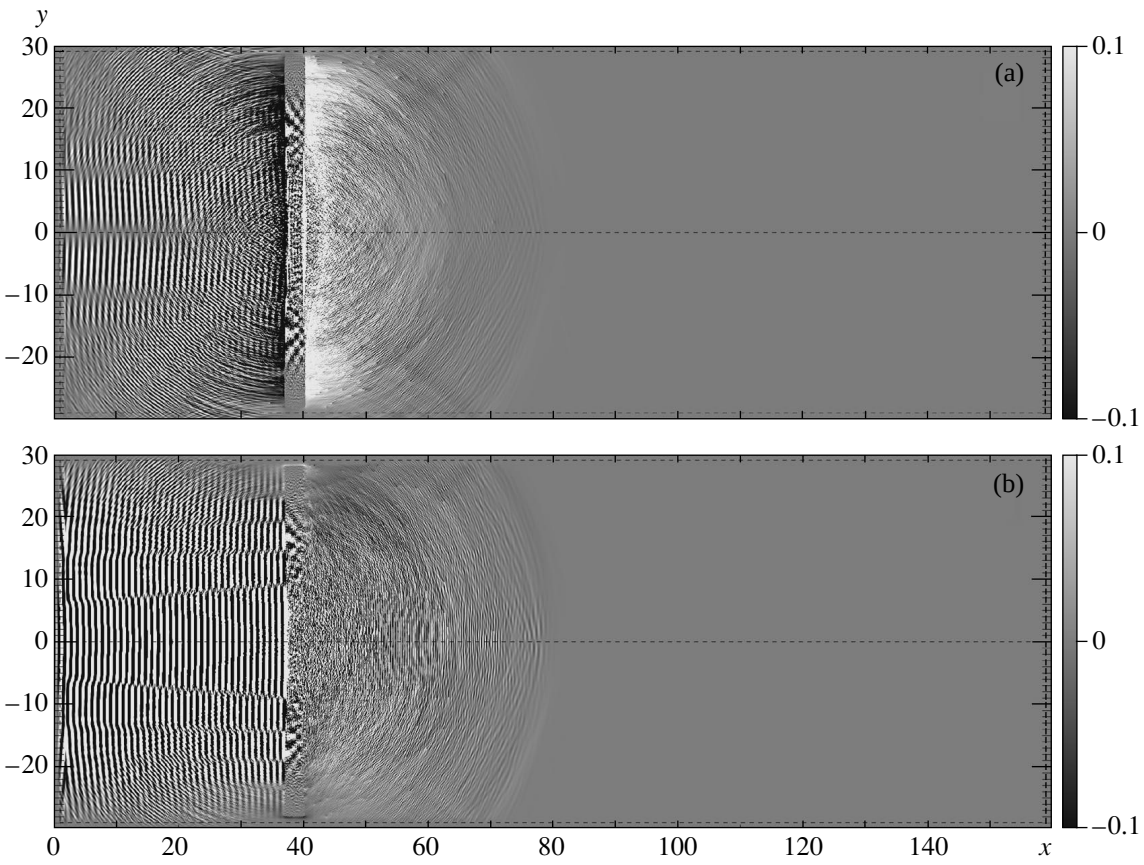

Fig. 5. Distributions of the (a) x and (b) y components of the electric field in the (x, y) plane at $t = 87.5$.

expression (15). The equation of motion of an ion in this field has the form

$$\dot{p}_a = -4\pi n_0 Z_i Z_a e^2 \frac{x_a - v_{e,0}t - l/2}{1 + bt^2/2}\theta\left(v_{e,0}t + \frac{l}{2} - x_a\right), \quad (16)$$

$$\dot{x}_a = c\frac{p_a}{(m_a^2c^2 + p_a^2)^{1/2}}, \quad (17)$$

where the superior dot stands for the time derivative and p_a and x_a are the momentum and coordinate of an ion, respectively.

3.2.1. Nonrelativistic limit. In the case of nonrelativistic ion energies, Eqs. (16) and (17) can be transformed into one equation for x_a:

$$\ddot{x}_a + b\left(\frac{2\mu}{2 + bt^2}\right)x_a = \mu b\frac{2v_{e,0}t + l}{2 + bt^2}, \quad (18)$$

where

$$\mu = \frac{Z_a m_e}{m_a}\left[1 + \left(\frac{p_{e,0}}{m_e c}\right)^2\right]^{3/2}. \quad (19)$$

The solution to Eq. (18) can be expressed in terms of hypergeometric functions:

$$x_a(t) = \frac{l}{2} + \left(x_{a,0} - \frac{l}{2}\right)F\left(\alpha, \beta; \gamma; -\frac{bt^2}{2}\right) + t\left[v_{e,0} + (\dot{x}_{a,0} - v_{e,0})F\left(-\beta, -\alpha; \gamma + 1; -\frac{bt^2}{2}\right)\right]. \quad (20)$$

Here, $x_{a,0}$ and $\dot{x}_{a,0}$ are the initial coordinate and velocity of an ion and $F(\alpha, \beta; \gamma; z)$ is the hypergeometric function [58], whose parameters α, β, and γ are related to μ by the expressions

$$\alpha = -\frac{1}{4} - i\frac{(8\mu - 1)^{1/2}}{4}, \quad \beta = -\frac{1}{4} + i\frac{(8\mu - 1)^{1/2}}{4}, \quad \gamma = \frac{1}{2}. \quad (21)$$

Let, at the initial instant $t = 0$, an ion be at rest and located at the point $x_{a,0} = l/2$ (i.e., at the front of the electron cloud). In this case, we should set $x_{a,0} = l/2$ and

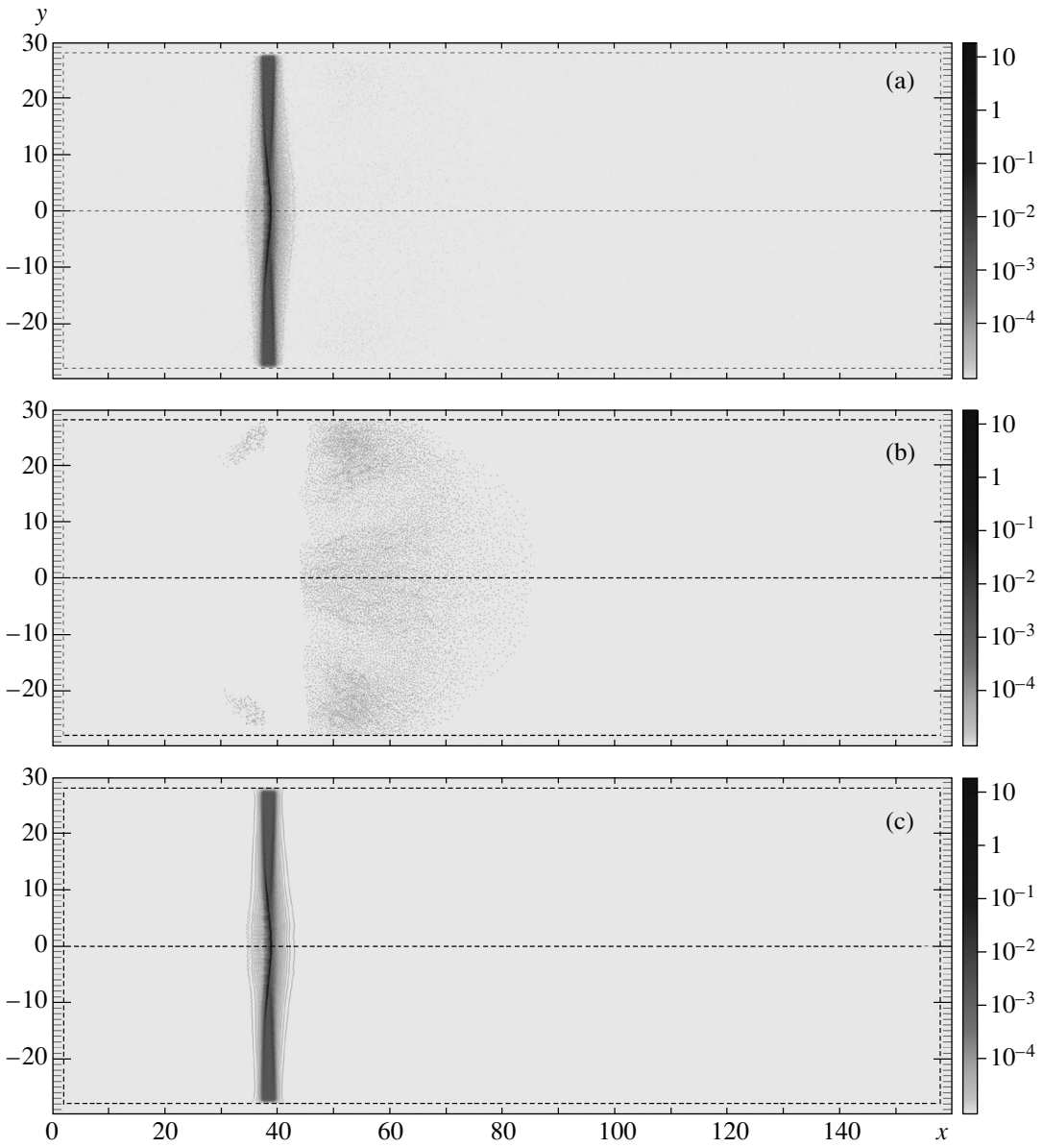

Fig. 6. Distributions of the (a) electron, (b) pion, and (c) aluminum-ion densities in the (x, y) plane at $t = 212.5$.

$x_{a,0} = 0$ in Eq. (20). It then follows from Eq. (20) that the ion coordinate depends on time as

$$x_a(t) = \frac{l}{2} + v_{e,0}t\left[1 - F\left(\frac{1-(1-8\mu)^{1/2}}{4}, \frac{1+(1-8\mu)^{1/2}}{4}; \frac{3}{2}; -\frac{bt^2}{2}\right)\right]. \quad (22)$$

It can be seen that the second term on the right-hand side of this expression increases with time. At the instant $t = t^*$, which is determined by the equation

$$F\left(\frac{1-(1-8\mu)^{1/2}}{4}, \frac{1+(1-8\mu)^{1/2}}{4}; \frac{3}{2}; -\frac{b(t^*)^2}{2}\right) = 0, \quad (23)$$

the ion coordinate becomes $x_{a,0}(t^*) = l/2 + v_{e,0}t^*$; i.e., in the course of acceleration, the ion crosses the front of the electron cloud and leaves it behind. As a result, the ion gains the velocity

$$\dot{x}_a(t^*) = v_{e,0} + v_{e,0}\frac{\mu b(t^*)^2}{24}F\left(\frac{5-(1-8\mu)^{1/2}}{4}, \frac{5+(1-8\mu)^{1/2}}{4}; \frac{5}{2}; -\frac{b(t^*)^2}{2}\right). \quad (24)$$

Since, after crossing the front of the electron cloud, the ion velocity becomes higher than the maximum

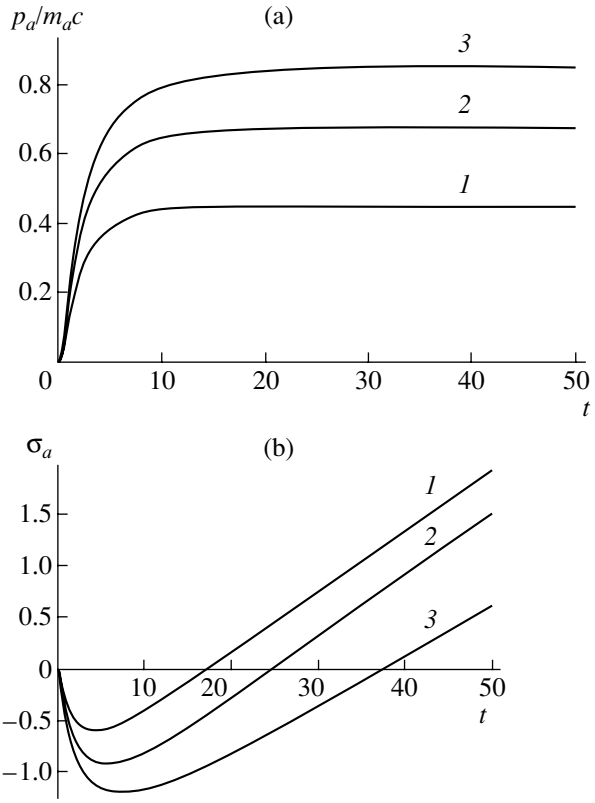

Fig. 7. Time dependence of (a) the ion momentum and (b) the distance between the accelerated ion and the front of the electron cloud for $\beta_{e,0}$ = (*1*) 0.35, (*2*) 0.5, and (*3*) 0.6.

electron velocity, which is, in turn, assumed to be nonrelativistic, the ion energy should be no higher than m_ac^2. Using the asymptotic of the hypergeometric function at $z \longrightarrow \infty$,

$$F(\alpha, \beta; \gamma; z) \approx \frac{\Gamma(\gamma)\Gamma(\beta-\alpha)}{\Gamma(\beta)\Gamma(\gamma-\alpha)}(-z)^{-\alpha} + \frac{\Gamma(\gamma)\Gamma(\alpha-\beta)}{\Gamma(\alpha)\Gamma(\gamma-\beta)}(-z)^{-\beta}, \quad (25)$$

we find from Eq. (23) that, in the limit $t^* \longrightarrow \infty$, the ion gains the velocity

$$\dot{x}_a(t^*) \approx v_{e,0}\left\{1 + \frac{\pi^{1/2}2^{1/4}}{8}\mu\left(\frac{2}{b}\right)^{(1-\sqrt{1-8\mu})/4} \times \frac{\Gamma(\sqrt{1-8\mu}/2)}{\Gamma[(5+\sqrt{1-8\mu})/4]^2}(t^*)^{(\sqrt{1-8\mu}-1)/2}\right\}. \quad (26)$$

It can be seen that, at $t^* \gg 1$, the ion velocity is approximately equal to the expansion velocity of the electron cloud. Therefore, in the nonrelativistic limit, the characteristic energy of fast ions is equal to

$$\mathcal{E}_a = \frac{m_a v_{e,0}^2}{2} \equiv \frac{m_a}{m_e}\mathcal{E}_e. \quad (27)$$

As in the approach of [38], this energy does not depend on the ion charge; this fact, in both cases, reflects the kinematic relationship corresponding to a situation in which the ion overtakes the front of the electron cloud.

3.2.2. Ultrarelativistic limit. Let us consider ion acceleration at the front of the electron cloud in the case of relativistic ion energies. We rewrite Eqs. (16) and (17) in the form

$$\dot{p}_a = -\varepsilon\frac{\sigma_a}{1+t^2}\theta(-\sigma_a), \quad (28)$$

$$\dot{\sigma}_a = \frac{p_a}{(1+p_a^2)^{1/2}} - \beta_{e,0}. \quad (29)$$

Here, $\varepsilon = \mu/8$, $\beta_{e,0} = v_{e,0}/c$, the time is in units of $\tau = 2^{1/2}(1 + (p_{e,0}/m_ec)^2)^{3/4}\omega_{pe}^{-1}$, and the momentum is in units of m_ac. In passing over from Eqs. (16) and (17) to Eqs. (28) and (29), we switched from the coordinate x_a to the new coordinate

$$\sigma_a = (x_a - v_{e,0}t - l/2)/c\tau, \quad (30)$$

which is the distance between the current ion position and the front of the electron cloud. Figure 7 presents the results of the numerical integration of Eqs. (28) and (29). Figure 7a shows the time dependence of the ion momentum $p_a(t)$, while Fig. 7b shows the time dependence of the distance between the ion and the front of the electron cloud $\sigma_a(t) = x_a(t) - \beta_{e,0}t - l/2$. Curves *1*, *2*, and *3* correspond to $\beta_{e,0}$ values of 0.35, 0.5, and 0.6, respectively. The initial conditions are chosen so that $p_a(0) = 0$ and $\sigma_a(0) = 0$. Such initial conditions correspond to a situation in which, at $t = 0$, an ion with a zero velocity is located at the front of the electron cloud. It can be seen that, in the initial stage of acceleration, the function $\sigma_a(t)$ is negative and increases in absolute value. This corresponds to the increase in the distance between the current position of the accelerated ion and the front of the electron cloud. This distance then starts to decrease until the ion overtakes the front. At the instant the ion crosses the front, the ion velocity is higher than the electron velocity; i.e., the higher the expansion velocity of the cloud, the higher the ion energy. The ion energy satisfies the inequality

$$\mathcal{E}_a \geq \frac{m_ac^2}{(1-\beta_{e,0}^2)^{1/2}} = \frac{m_a}{m_e}\mathcal{E}_e. \quad (31)$$

which gives a lower estimate of the maximum energy of the ions accelerated in the course of expansion of a relativistic electron cloud into a vacuum. Obviously, this is a generalization of expression (27) to the case of relativistic ion energies.

Let us now analyze a situation in which an ion gets into the acceleration regime at the instant $t_0 \gg 1$, by which the electron cloud has already substantially expanded. We consider the case in which the characteristic acceleration time $t_{acc} \approx [(1 + t_0^2)/\varepsilon]^{1/2}$ is much less than t_0. This condition can be satisfied only when the parameter ε is large enough. The inequality $\varepsilon \gg 1$ is equivalent to the condition that the electron energy is ultrarelativistic. In this limit, the right-hand side of Eq. (28) can be approximated by the expression $-\varepsilon[\sigma_a/(1 + t_0^2)]\theta(-\sigma_a)$. As a result, the set of Eqs. (28) and (29) takes a Hamiltonian form with the Hamiltonian

$$\mathcal{H}(p_a, \sigma_a) = (1 + p_a^2)^{1/2} - p_a\beta_{e,0} + \varepsilon\frac{\sigma_a^2}{2(1 + t_0^2)}\theta(-\sigma_a). \quad (32)$$

The fact that Hamiltonian (31) does not depend explicitly on time ($\mathcal{H}(p_a, \sigma_a) = h$) allows us to calculate the momentum the ion gains due to the interaction with the expanding electron cloud. We note that the instant at which the ion crosses the front of the electron cloud corresponds to a zero value of $\sigma_a(t)$. At $t = t_0$, the ion crosses the front of the electron cloud for the first time. From here, we find that $h = (1 + p_{a,0}^2)^{1/2} - p_{a,0}\beta_{e,0}$, where $p_{a,0}$ is the initial value of the ion momentum. At the instant $t = t^*$, the accelerated ion catches up with the front of the cloud and crosses it. This instant also corresponds to a zero value of $\sigma_a(t)$: $\sigma_a(t) = 0$. It follows from Eq. (32) that the resulting ion momentum is

$$p_a = \frac{\beta_{e,0}h + [\beta_{e,0}^2h^2 - (1 - h^2)(1 - \beta_{e,0}^2)]^{1/2}}{1 - \beta_{e,0}^2}. \quad (33)$$

Let the ion be initially at rest; i.e., $p_{a,0} = 0$. We then have $h = 1$ and

$$p_a \approx \frac{2\beta_{e,0}h}{1 - \beta_{e,0}^2}, \quad (34)$$

which is equal to the momentum the particle gains due to an elastic reflection from a wall moving with a velocity $c\beta_{e,0}$ close to the speed of light. In dimensional units, formula (34) can be rewritten in the form

$$\mathcal{E}_\alpha \approx \frac{m_\alpha c^2}{1 - \beta_{e,0}} \approx 2m_\alpha c^2\left(\frac{\mathcal{E}_e}{m_e c^2}\right)^2. \quad (35)$$

3.2.3. Simple particle acceleration model. The basic features of the above mechanism of charged particle acceleration can be illustrated using the following simple model. A similar model was used in [59] to analyze the problem of the charge neutralization of an ion beam interacting with a plasma slab. We assume that the relativistic electrons form a thin bunch oriented perpendicularly to the x axis. We also assume that the bunch propagates with a constant velocity $c\beta_{e,0}$ and that its shape does not change with time. Between the electron bunch and the target, there is a homogeneous electric field $E = 2\pi e n_0 \Delta x$, where $n_0\Delta x$ is the number of electrons per unit area of the bunch. In this electric field, the momentum and coordinate of an ion of species α with a charge of $Z_\alpha e$ depend on time as

$$p_\alpha(t) = Z_\alpha eEt, \quad (36)$$

$$x_\alpha(t) = \frac{[m_\alpha^2c^4 + (Z_\alpha eEct)^2]^{1/2} - m_\alpha c^2}{Z_\alpha eE}. \quad (37)$$

We assume that the initial coordinate of an ion is zero. At the instant $t = t^*$, the ion catches up with an electron bunch. The acceleration time t^*, which can be found from the condition $x_\alpha(t^*) = c\beta_{e,0}t^*$ is equal to

$$t^* = \frac{2m_\alpha c\beta_{e,0}}{(1 - \beta_{e,0}^2)Z_\alpha eE}. \quad (38)$$

We find from here that the energy of the accelerated ion is $\mathcal{E}_\alpha = 2m_\alpha c^2\beta_{e,0}(\mathcal{E}_e/m_e c^2)^2$, which agrees with formula (35).

4. DISCUSSION OF THE RESULTS OBTAINED

In this paper, we have found the maximum energy of the fast ions accelerated at the front of an electron cloud expanding into a vacuum. The energy of the fast electrons generated in the interaction of high-power laser radiation with a target can be estimated from below as $a_0 m_e c^2$, which corresponds to the kinetic energy of electrons oscillating in the field of an electromagnetic wave with a dimensionless amplitude of $a_0 = eE/m_e c\omega \gg 1$ [60]. Then, using Eqs. (33) and (34), we find that the maximum energy of fast ions is on the order of $2m_\alpha c^2 a_0^2$. For example, at $a_0 \approx 1$ (which corresponds to a laser intensity of about 10^{18} W/cm^2), the plasma electrons can gain an energy of a few megaelectronvolts. In this case, according to Eqs. (33) and (34), the energy of fast ions can reach a few gigaelectronvolts. Obviously, under real experimental conditions, there are some factors (such as the finite transverse dimensions of the laser pulse and the target) that violate the one-dimensional approximation used in deducing Eqs. (33) and (34). As a result, the energy of fast ions will be somewhat lower. This also concerns the results of computer simulations presented in Section 2, in which the finite

dimensions of the simulation region were an additional factor limiting the ion energy. Nevertheless, the conclusion that moderate-power laser pulses can, in principle, be used to generate high-energy ions seems to be important when considering methods for optimizing the parameters of laser accelerators.

ACKNOWLEDGMENTS

This study was supported in part by the Russian Foundation for Basic Research (project no. 02-02-16756) and INTAS (grant no. 01-0233).

REFERENCES

1. T. Tajima and G. Mourou, Phys. Rev. ST Accel. Beams **5**, 031301 (2002).
2. E. L. Clark, K. Krushelnick, M. Zepf, *et al.*, Phys. Rev. Lett. **85**, 1654 (2000).
3. R. A. Snavely, M. H. Key, S. P. Hatchett, *et al.*, Phys. Rev. Lett. **85**, 2945 (2000).
4. A. Maksimchuk, S. Gu, K. Flippo, *et al.*, Phys. Rev. Lett. **84**, 4108 (2000).
5. A. J. Mackinnon, M. Borghesi, S. Hatchett, *et al.*, Phys. Rev. Lett. **86**, 1769 (2001).
6. A. J. Mackinnon, Y. Sentoku, P. K. Patel, *et al.*, Phys. Rev. Lett. **88**, 215006 (2002).
7. P. McKenna, K. W. D. Ledingham, I. Spencer, *et al.*, Rev. Sci. Instrum. **73**, 4176 (2002).
8. I. Spencer, K. W. D. Ledingham, P. McKenna, *et al.*, Phys. Rev. E **67**, 046402 (2003).
9. K. Matsukado, T. Esirkepov, H. Daido, *et al.*, Phys. Rev. Lett. (in press).
10. M. Zepf, E. Clark, F. Beg, *et al.*, Phys. Rev. Lett. **90**, 64801 (2003).
11. M. Roth, T. E. Cowan, M. H. Key, *et al.*, Phys. Rev. Lett. **86**, 436 (2001).
12. V. Yu. Bychenkov, V. Rozmus, A. Maksimchuk, *et al.*, Fiz. Plazmy **27**, 1076 (2001) [Plasma Phys. Rep. **27**, 1017 (2001)].
13. S. V. Bulanov and V. S. Khoroshkov, Fiz. Plazmy **28**, 493 (2002) [Plasma Phys. Rep. **28**, 453 (2002)].
14. S. V. Bulanov and V. S. Khoroshkov, Med. Fiz. **1** (13), 50 (2002).
15. S. V. Bulanov, T. Zh. Esirkepov, V. S. Khoroshkov, *et al.*, Phys. Lett. A **299**, 240 (2002).
16. E. Fourkal, B. Shahine, M. Ding, *et al.*, Med. Phys. **29**, 2788 (2002).
17. M. Borghesi, D. H. Campbell, A. Schiavi, *et al.*, Phys. Plasmas **9**, 2214 (2002).
18. M. Borghesi, S. V. Bulanov, D. H. Campbell, *et al.*, Phys. Rev. Lett. **88**, 135002 (2002).
19. J. Denavit, Phys. Rev. Lett. **69**, 3052 (1992).
20. W. S. Lawson, P. W. Palumbo, and D. J. Larson, Phys. Plasmas **4**, 788 (1997).
21. T. Zh. Esirkepov, I. Sentoku, K. Mima, *et al.*, Pis'ma Zh. Éksp. Teor. Fiz. **70**, 80 (1999) [JETP Lett. **70**, 82 (1999)].
22. A. G. Zhidkov, A. Sasaki, T. Tajima, *et al.*, Phys. Rev. E **60**, 3273 (1999).
23. Y. Ueshima, Y. Sentoku, and Y. Kishimoto, Nucl. Instrum. Methods Phys. Res. A **455**, 181 (2000).
24. A. Pukhov, Phys. Rev. Lett. **86**, 3562 (2001).
25. A. V. Kuznetsov, T. Zh. Esirkepov, F. F. Kamenets, and S. V. Bulanov, Fiz. Plazmy **27**, 225 (2001) [Plasma Phys. Rep. **27**, 211 (2001)].
26. Y. Sentoku, V. Yu. Bychenkov, K. Flippo, *et al.*, Appl. Phys. B **74**, 207 (2002).
27. A. Zhidkov, M. Uesaka, A. Sasaki, and H. Daido, Phys. Rev. Lett. **89**, 215002 (2002).
28. S. V. Bulanov, N. M. Naumova, T. Zh. Esirkepov, *et al.*, Pis'ma Zh. Éksp. Teor. Fiz. **71**, 593 (2000) [JETP Lett. **71**, 407 (2000)].
29. Y. Sentoku, T. V. Lisseikina, T. Zh. Esirkepov, *et al.*, Phys. Rev. E **62**, 7271 (2000).
30. S. Wilks, A. B. Langdon, T. E. Cowan, *et al.*, Phys. Plasmas **8**, 542 (2001).
31. H. Ruhl, S. V. Bulanov, T. E. Cowan, *et al.*, Fiz. Plazmy **27**, 387 (2001) [Plasma Phys. Rep. **27**, 363 (2001)].
32. T. Esirkepov, S. Bulanov, H. Daido, *et al.*, Phys. Rev. Lett. **89**, 175003 (2002).
33. S. V. Bulanov, T. Zh. Esirkepov, F. F. Kamenets, *et al.*, Fiz. Plazmy **28**, 1059 (2002) [Plasma Phys. Rep. **28**, 975 (2002)].
34. S. V. Bulanov, F. Califano, G. I. Dudnikova, *et al.*, in *Reviews of Plasma Physics*, Ed. by V. D. Shafranov (Kluwer Academic, New York, 2001), Vol. 22, p. 227.
35. J. Mendonca, J. Davies, and M. Eloy, Meas. Sci. Technol. **12**, 1801 (2001).
36. G. Mourou, T. Tajima, and S. V. Bulanov, Rev. Mod. Phys. (in press).
37. A. V. Gurevich, L. V. Pariĭskaya, and L. P. Pitaevskiĭ, Zh. Éksp. Teor. Fiz. **49**, 647 (1966) [Sov. Phys. JETP **22**, 449 (1966)].
38. A. V. Gurevich, L. V. Pariĭskaya, and L. P. Pitaevskiĭ, Zh. Éksp. Teor. Fiz. **63**, 516 (1972) [Sov. Phys. JETP **36**, 274 (1972)].
39. A. V. Gurevich and A. P. Meshcherkin, Zh. Éksp. Teor. Fiz. **80**, 1810 (1981) [Sov. Phys. JETP **53**, 937 (1981)].
40. P. Mora and R. Pellat, Phys. Fluids **22**, 2300 (1979).
41. S. G. Gitomer, R. D. Jones, F. Begay, *et al.*, Phys. Fluids **29**, 2679 (1986).
42. D. S. Dorozhkina and V. E. Semenov, Fiz. Plazmy **24**, 481 (1998) [Plasma Phys. Rep. **24**, 440 (1998)].
43. V. E. Kovalev, V. Yu. Bychenkov, and V. T. Tikhonchuk, Pis'ma Zh. Éksp. Teor. Fiz. **74**, 12 (2001) [JETP Lett. **74**, 10 (2001)].
44. V. E. Kovalev and V. Yu. Bychenkov, Phys. Rev. Lett. **90**, 185004 (2003).
45. P. Mora, Phys. Rev. Lett. **90**, 185002 (2003).
46. G. Hairapetian and R. L. Stenzel, Phys. Rev. Lett. **65**, 175 (1990).
47. I. Last, I. Schek, and J. Jortner, J. Chem. Phys. **107**, 6685 (1997).
48. K. Nishihara, H. Amitani, M. Murakami, *et al.*, Nucl. Instrum. Methods Phys. Res. A **464**, 98 (2001).
49. Y. Kishimoto, T. Masaki, and T. Tajima, Phys. Plasmas **9**, 589 (2002).

50. T. Zh. Esirkepov, Comput. Phys. Commun. **135**, 144 (2001).
51. J. M. Dawson, Rev. Mod. Phys. **55**, 403 (1983).
52. Yu. A. Berezin and V. A. Vshivkov, *Particle Method in the Dynamics of Tenuous Plasmas* (Nauka, Novosibirsk, 1980).
53. R. W. Hockney and J. W. Eastwood, *Computer Simulations Using Particles* (McGraw-Hill, New York, 1981; Mir, Moscow, 1987).
54. V. Yu. Bychenkov, I. Sentoku, S. V. Bulanov, *et al.*, Pis'ma Zh. Éksp. Teor. Fiz. **74**, 664 (2001) [JETP Lett. **74**, 586 (2001)].
55. A. I. Akhiezer and G. A. Lyubarskiĭ, Dokl. Akad. Nauk SSSR **80**, 193 (1951).
56. J. M. Dawson, Phys. Rev. **113**, 383 (1959).
57. S. V. Bulanov, L. M. Kovrizhnykh, and A. S. Sakharov, Phys. Rep. **186**, 1 (1990).
58. I. S. Gradshteyn and I. M. Ryzhik, *Table of Integrals, Series, and Products* (Nauka, Moscow, 1971; Academic, New York, 1980).
59. F. Califano, F. Pegoraro, and S. V. Bulanov, Phys. Rev. E (in press).
60. A. I. Akhiezer and R. V. Polovin, Zh. Éksp. Teor. Fiz. **30**, 915 (1956) [Sov. Phys. JETP **3**, 696 (1956)].

Translated by A.S. Sakharov

Plasma Physics Reports, Vol. 30, No. 1, 2004, pp. 30–37. Translated from Fizika Plazmy, Vol. 30, No. 1, 2004, pp. 33–40.

PLASMA DYNAMICS

Roentgenographic Investigations of the Dynamics and Spatial Structure of Wire-Array Z-Pinches

E. V. Grabovskiĭ, G. G. Zukakishvili, S. L. Nedoseev, G. M. Oleĭnik, and I. Yu. Porofeev

Troitsk Institute for Innovation and Fusion Research, Troitsk, Moscow oblast, 142190 Russia

Received March 20, 2003; in final form, July 21, 2003

Abstract—The implosion of wire arrays is studied at the Angara-5-1 facility with the help of an X-ray pinhole camera. It is shown that the drift of the plasma toward the axis occurs in the form of a "plasma rainstorm." The data constituting a part of the experimental database are presented. Based on these data, it is established that the spatial structure of an imploding plasma is highly inhomogeneous, so that it makes no sense to talk about a plasma shell that implodes as a single entity. In this case, plasma inhomogeneities arising due to a "cold start" and prolonged plasma production have a decisive impact on the final parameters of a hyper-terawatt Z-pinch.

1. INTRODUCTION

At present, the implosion of wire arrays (liners) is being studied extensively [1–3]. In the stage of the maximum liner compression, a high-power soft X-ray (SXR) pulse is generated that can be used in inertial confinement fusion (ICF) research.

According to the concept of prolonged plasma production [4], the implosion of wire arrays proceeds as follows: Just after the current begins to flow through the wire array, a plasma is produced on the wire surface and the discharge current switches from the wires to this low-density plasma corona. The wire cores, which remain in their initial positions over most of the discharge phase, play the role of stationary plasma sources. The plasma corona, through which most of the current flows, drifts toward the array axis under the action of the Ampére force.

It was shown in [5] that, at a current of ~1 MA, the mass of the dense wire cores 70 ns after the beginning of the current pulse is ~70% of their initial mass. Originally, the wire array is a set of wires equally spaced along a cylindrical surface. Therefore, the plasma flows produced at the wires are azimuthally nonuniform from the very beginning of the discharge. Moreover, the plasma produced from an individual wire is also nonuniform in the axial direction.

The azimuthal and axial inhomogeneities of the plasma produced from the liner wires give rise to plasma jets that can merge and undergo self-focusing under the action of their magnetic self-field. In [6], this phenomenon was called "the radial plasma rainstorm."

In the present paper, we will show that the inhomogeneities of the imploding plasma that appear due to both the "cold start" of the Z-pinch and the subsequent prolonged plasma production decisively affect the final parameters of an emitting hyper-terawatt Z-pinch.

In this paper, the data constituting a part of the experimental database are presented. It is on the basis of these data that the main conclusions of [6] were formulated.

2. EXPERIMENTAL AND DIAGNOSTIC TECHNIQUES

The experiments were performed at the Angara-5-1 facility [7]. As a load, we used arrays assembled of 30 to 120 tungsten wires 5–8 μm in diameter. The array diameter was varied in the range of 8–20 mm, and the length was varied in the range of 1–1.5 cm. We also used composite liners consisting of two coaxial wire arrays and a low-density solid agar-agar cylinder on the liner axis.

The main diagnostics used in this study was the high-resolution imaging of the Z-pinch with the help of time-integrating X-ray pinhole cameras. Time-integrating pinhole cameras are widely used as a simple, reliable, and informative diagnostic tool in experiments with fast Z-pinches (see, e.g., [8]). To image the imploding liner in different spectral ranges, the pinhole cameras were equipped with filters. The spatial resolution of the images in the 1-keV photon energy range was 30 μm. The high spatial resolution of time-integrating pinhole cameras allowed us to obtain information on extremely short-duration implosion phases. Indeed, for one to obtain a sharp image of an emitting object having a characteristic size Δx and moving with a velocity v, the object should emit no longer than a time $\Delta t \sim \Delta x/v$. Assuming that the velocity of the imploding plasma is about the Alfvén velocity, $v \sim 3 \times 10^7$ cm/s, we find that the lifetime of an emitting object with a size of $\Delta x \sim 100$ μm should be a fraction of a nanosecond; otherwise the object image will be smeared out. To obtain the more complete information on pinch inhomogeneities, we sometime used two pinhole cameras

1063-780X/04/3001-0030$26.00 © 2004 MAIK "Nauka/Interperiodica"

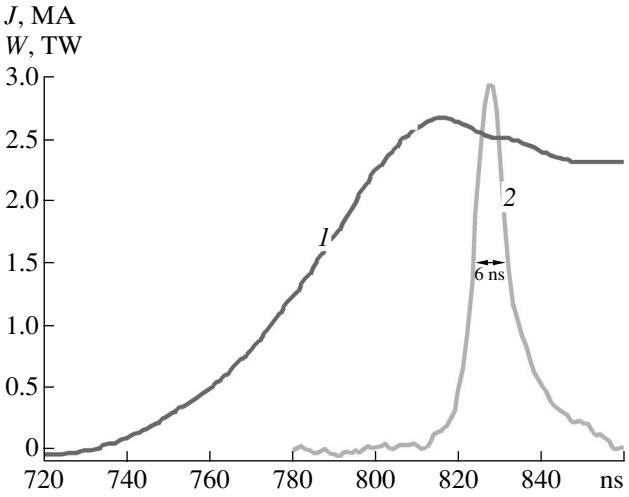

Fig. 1. Typical waveforms of the (*1*) current *J* and (*2*) SXR (~200 eV) emission power *W*.

that produced X-ray images in two perpendicular directions. Having two such mutually orthogonal projections, we were able to determine the spatial structure of the object.

Besides pinhole cameras, we also used other diagnostics. Here, we list only the diagnostics from which the results presented in this paper were obtained:

(i) magnetic probes installed at a distance of 55 mm from the liner axis for measuring the liner current;

(ii) a frame X-ray image tube (XRIT) based on a microchannel (MCP) camera;

(iii) frame laser shadowgraphy; and

(iv) SXR diagnostics based on four vacuum X-ray diodes (XRD) with different absorbent filters for recording the waveforms of the emission power in a photon energy range of 0.1–2 keV.

3. EXPERIMENTAL RESULTS

The experiments carried out at the Angara-5-1 facility showed that the implosion of wire arrays 10–15 mm in length and 8–20 mm in diameter resulted in the formation of a pinch on the liner axis. The pinch length was equal to the length of the array, and the pinch diameter was less than 1 mm. The pinch mainly emitted in the photon energy range 0.05–1.5 keV. Figure 1 shows typical waveforms of the load current and SXR signals. The ratio of the initial liner radius R to the minimum Z-pinch radius r (recorded by the pinhole camera) allows us to evaluate the compression ratio of the load. In our experiments, this ratio is $R/r \approx 10$. The SXR emission power is ~5 TW, the duration of the SXR pulse is about 6 ns, and the total emission energy is about 40 kJ. Figure 2 shows typical SXR images of Z-pinches.

3.1. Structure of the Emitting Plasma Generated on the Wires

In time-integrated pinhole images (Fig. 3), one can see a plasma that leaves the wires in the form of indi-

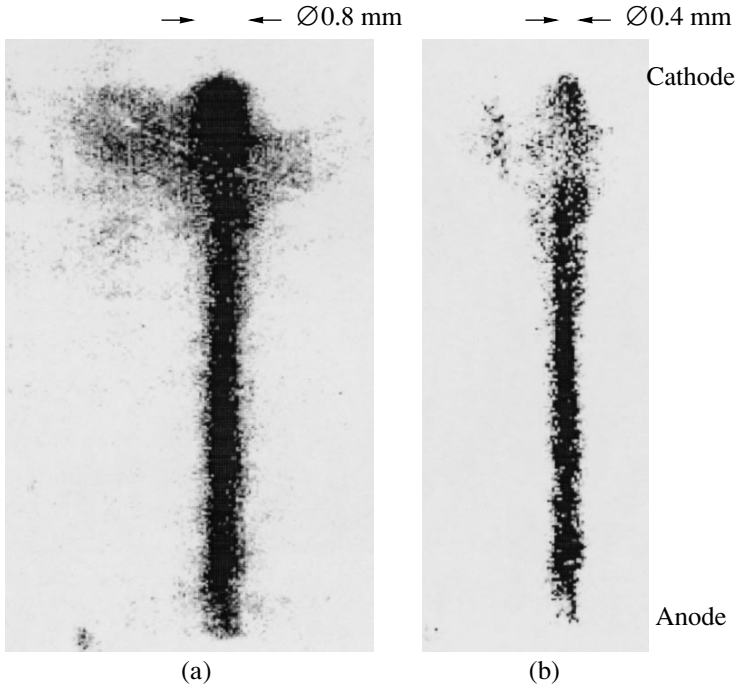

Fig. 2. Time-integrated X-ray pinhole images of an emitting Z-pinch: (a) $h\nu > 200$ eV and (b) $h\nu > 600$ eV (the pinch length is 1 cm).

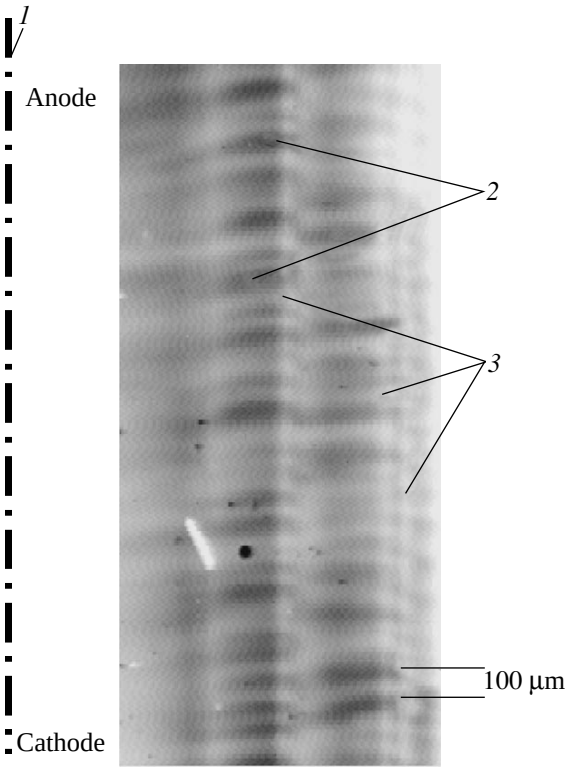

Fig. 3. Time-integrated X-ray pinhole image ($h\nu > 50$ eV) of the outer part of the liner: (*1*) liner axis, (*2*) plasma leaving the wires in the form of jets, and (*3*) wire shadows against the background plasma.

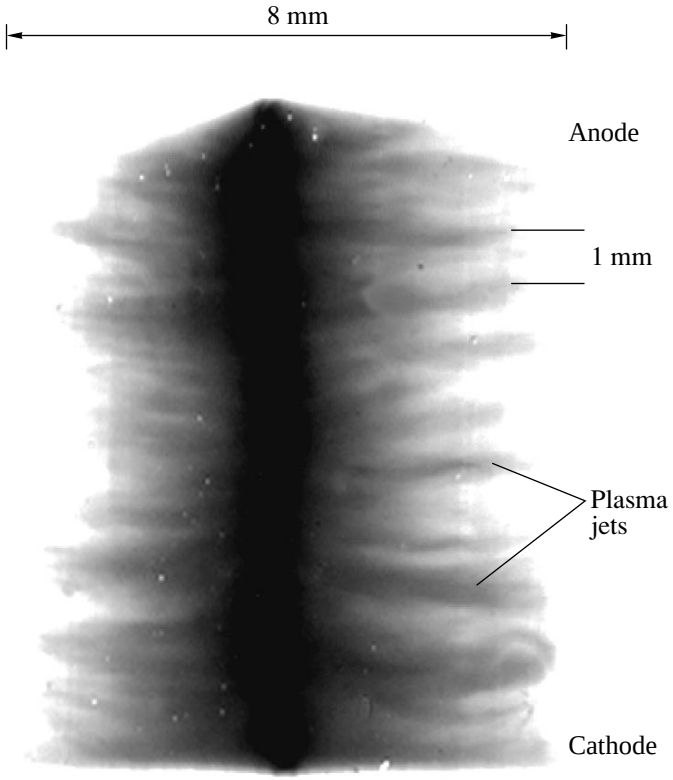

Fig. 4. Time-integrated X-ray pinhole image ($h\nu > 150$ eV) of an 8-mm-diameter liner: the plasma in the form of jets drifts from the periphery toward the axis.

vidual jets and then drifts toward the axis. The mean axial distance between the plasma jets generated from a single wire is 150 μm. Further, the primary jets merge into larger jets (see Fig. 4). The axial distance between the secondary jets is about 1 mm. These jets fill the liner cavity with plasma and produce a plasma precursor near the axis (the so-called "prepinch"), which emits in the photon energy range 100–300 eV.

The nonuniformity of the produced plasma is also seen in both the laser shadow image and XRIT frame images taken with a time resolution of ~2 ns in the ~200-eV photon energy range (Fig. 5). It can be seen

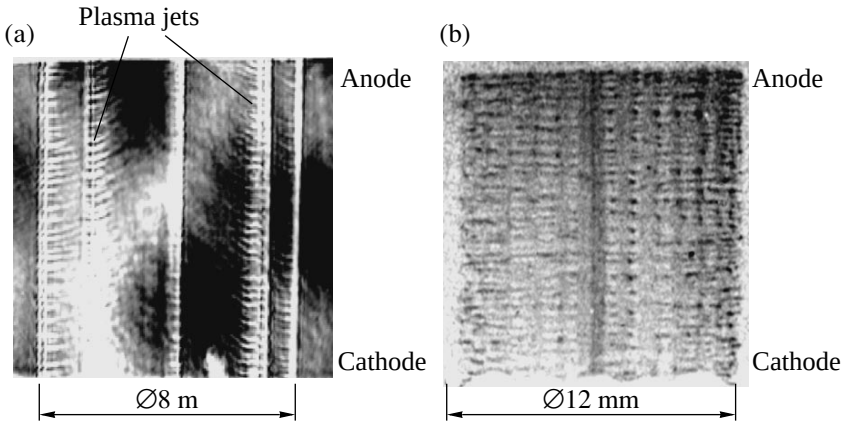

Fig. 5. Plasma jets leaving the array wires: (a) laser shadow image taken 54 ns after the beginning of the current pulse (25 kA per wire) and (b) frame X-ray pinhole image ($h\nu \sim 200$ eV) taken 77 ns after the beginning of the current pulse (50–55 kA per pulse).

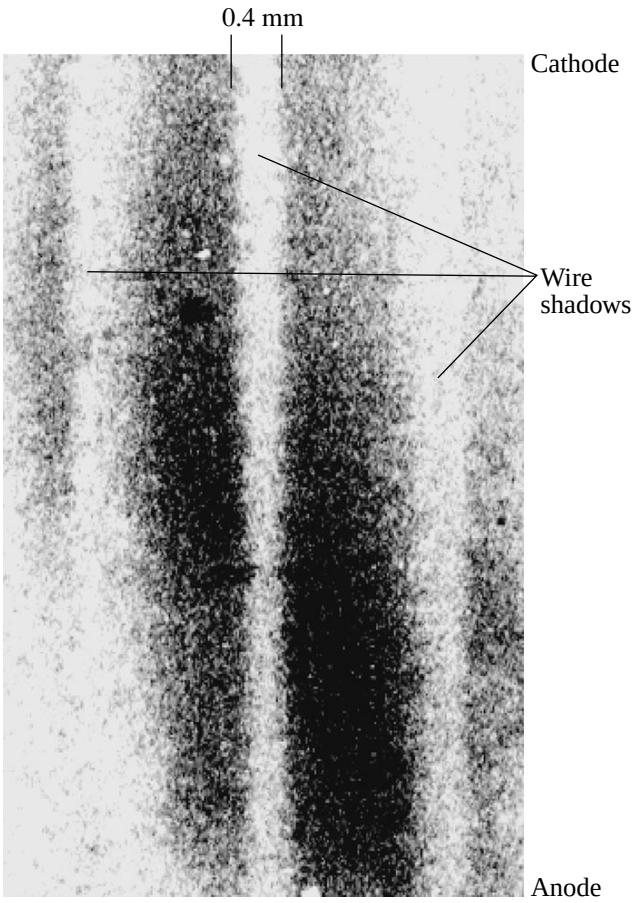

Fig. 6. Frame X-ray pinhole image ($h\nu$ > 150 eV) of the liner wire shadows against the background of the prepinch plasma at 70 ns after the beginning of the current pulse.

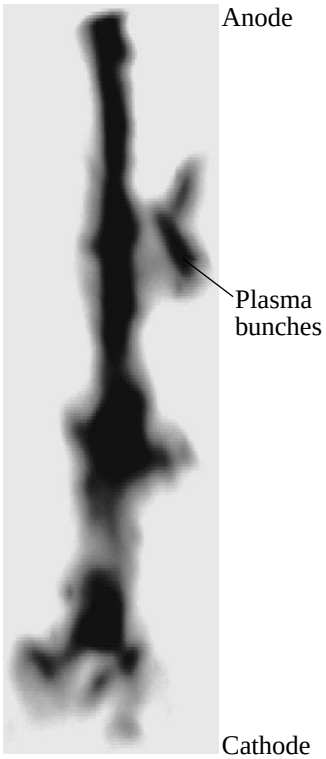

Fig. 7. Time-integrated frame X-ray pinhole image ($h\nu$ > 1 keV) of a pinch segment of length ~5 mm with off-axis plasma bunches.

that the characteristic scale length of the plasma nonuniformity along each wire is 100–200 μm. The plasma leaves the wires in the form of jets ~1 mm in length and then drifts toward the axis. Thus, time-resolved measurements, as well as the time-integrated pinhole camera images, demonstrate the existence of extended plasma jets starting from each wire.

The cores of the liner wires in pinhole images (Figs. 3, 4) are seen as light vertical lines against the background of radiation emitted by the plasma leaving the wires. This means that the wires are opaque to plasma emission and produce shadows in the images. The wire diameter that is reached during the expansion of the dense core is estimated at 50 μm. Since the described pinhole image is integrated over time, it is obvious that the core shadows can be seen against the background of the emitting jets only if the wires disappear after (or simultaneously with) the jets.

The wire shadows in SXR emission were also observed in XRIT frame images taken with an exposure of 2 ns (Fig. 6). The XRIT shutter operated 70 ns after the beginning of the current pulse. At that instant, the wire shadows and the plasma leaving the wires can be seen against the background of the plasma filling the liner interior. We note that the plasma generation on the liner wires is nonuniform in the axial direction. The characteristic scale length of the plasma nonuniformity is 100–200 μm, and the width of the wire shadow varies from 200 to 400 μm. This size is one order of magnitude larger than the wire diameter estimated from the time-integrated pinhole images. The reason for this is that the time-integrating pinhole camera records the minimum shadow width of a wire surrounded by the plasma corona over the entire implosion process, whereas the XRIT records the shadow width of a wire surrounded by the plasma against the background of the prepinch plasma at the instant of the MCP shutter operation.

3.2. Off-Axis Plasma Bunches

The drift of the plasma leaving the wires and the merging of the primary jets into larger ones result in the self-focusing of some of the jets near the liner axis. We also observed the collision of the plasma jets heated to a few tens of electronvolts near the axis. This results in the generation of plasma bunches, one of which can be seen in the pinhole image shown in Fig. 7.

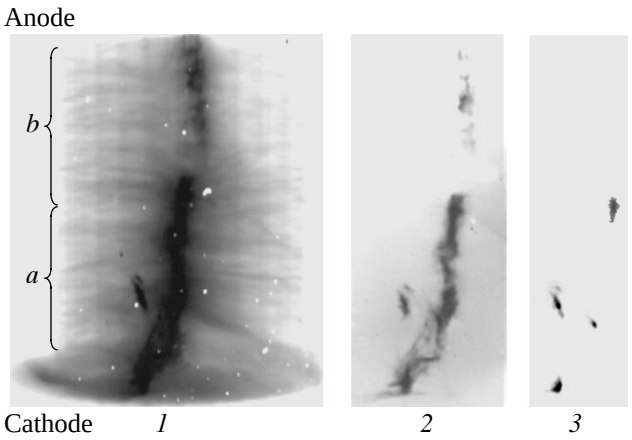

Fig. 8. Time-integrated X-ray pinhole images of the (*a*) cathode and (*b*) anode regions of a 1.5-cm-long pinch: (*1*) $h\nu > 150$ eV, (*2*) $h\nu > 1$ keV, and (*3*) $h\nu > 2$ keV.

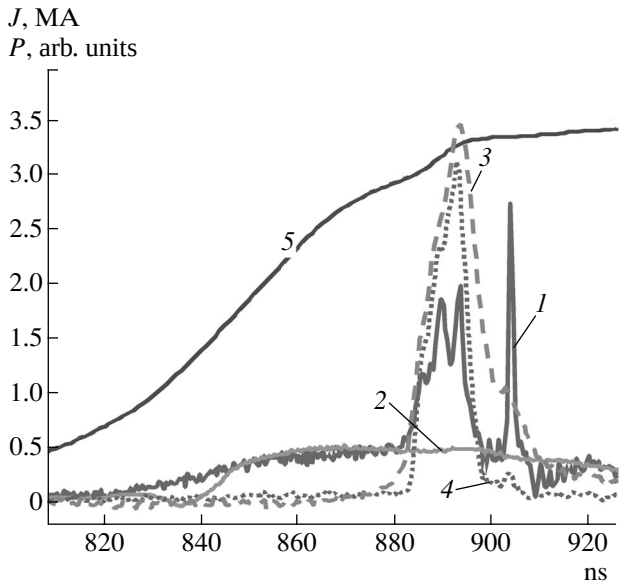

Fig. 9. Waveforms of the (*5*) current *J* and signals *P* from XRD detectors sensitive in the energy ranges (*1*) $h\nu > 1$ keV (cathode region), (*2*) $h\nu > 1$ keV (anode region), (*3*) $h\nu$ = 200–400 eV, and (*4*) $h\nu$ = 400–1000 eV for the shot presented in Fig. 8.

The bunches emit in the photon energy range of 0.2–2 keV and higher. The emission power of these sources is comparable to the emission power of the plasma column of the Z-pinch in the energy range 0.2–1 keV and is even higher at higher photon energies. The instant of the maximum pinch emission does not coincide with the instant of emission from the off-axis plasma bunches. As a result, the SXR pulse turns out to be protracted, which leads to a decrease in the emission power. The emission peaks corresponding to the plasma bunches lag behind the peak of the pinch emission by 5–15 ns. In most of the shots, up to three plasma bunches were produced in the cathode region of the pinch. This can be seen in pinhole images recorded with the use of different filters (Fig. 8). In this case, a wire array consisting of thirty 6-μm tungsten wires arranged on a circle 12 mm in diameter was used as a load. A 5-mm-diameter tube made of agar-agar foam with a mass per unit length of 400 μg/cm was placed at the axis on the anode side. The tube length was one-half the liner length.

In the cathode region of the pinch, one can see bright spots that emit over a wide photon energy range (including photon energies above 2 keV).

Figure 9 shows XRD signals obtained with different filters and cathodes and the waveform of the liner current for the shot presented in Fig. 8. Signal *1* was taken from an XRD that was sensitive to photons with energies above 1 keV and was aimed at the cathode region of the pinch. Signal *2* was taken from an identical detector aimed at the anode region. The difference between the signals shows that the cathode plasma bunches emit in the harder spectral range. In the images shown in Fig. 8, one can see four plasma bunches corresponding to four peaks in signal *1*. Such bunches result in the widening of the SXR pulse (signals *3* and *4*). Signal *3* reflects all the SXR bursts seen in signal *1*. The time spread of the emission bursts from different plasma bunches (which is seen in signal *1*) results in a protracted SXR pulse integrated over the entire spectrum.

3.3. Studies of the Cathode Plasma

In the early stage of implosion, a so-called cathode plasma that has an axial velocity component is generated at the cathode surface and also in the region where the liner wires contact with the cathode. It can be seen in the pinhole image presented in Fig. 10 that this plasma is conical in shape.

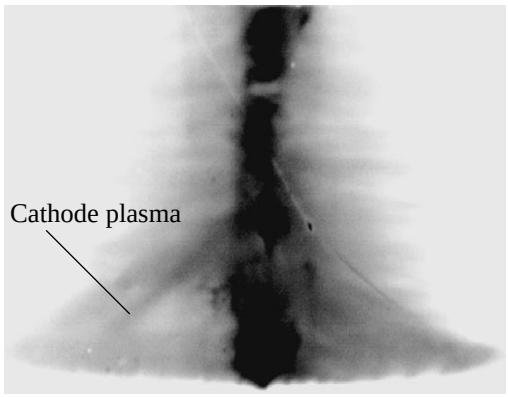

Fig. 10. X-ray pinhole image ($h\nu > 50$ eV) of the conical cathode plasma. The size of the cone base (12 mm) corresponds to the array diameter.

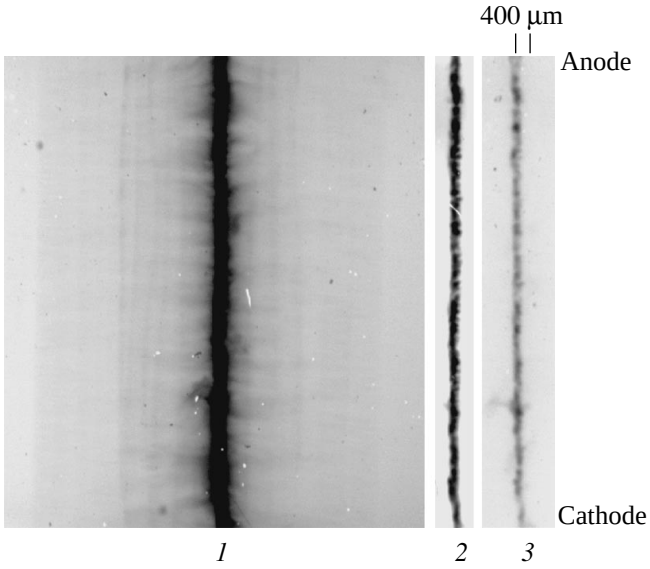

Fig. 11. X-ray pinhole image of a 15-mm-long composite pinch: (*1*) $h\nu > 50$ eV, (*2*) $h\nu > 1$ keV, and (*3*) $h\nu > 2$ keV. The outer 12-mm-diameter liner consists of thirty 5-μm tungsten wires, while the inner 6-mm-diameter liner consists of twenty 6-μm tungsten wires.

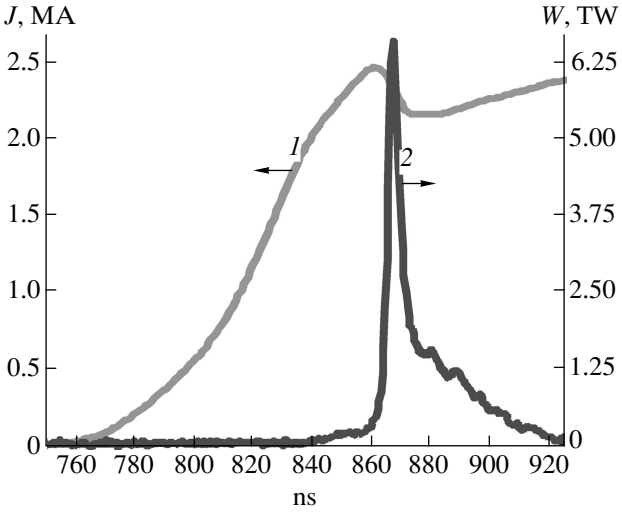

Fig. 12. Waveforms of the (*1*) current and (*2*) SXR ($h\nu$ ~200 eV) emission power for the shot presented in Fig. 11.

The cone is formed due to the high axial velocity of the cathode plasma. The generation of plasma bunches is probably provoked by an uncontrolled increase in the plasma mass due to cathode phenomena. When the liner length was increased from 1 to 1.5 cm, the effect of the cathode plasma became less pronounced.

The pinch compression ratio also increased when, instead of single arrays, we used composite liners consisting of two coaxial wire arrays (see Fig. 11). Figure 12 shows the waveforms of the SXR emission power and the liner current. For composite arrays, the compression ratio was $R/r \approx 30$ and plasma bunches leading to an increase in the SXR pulse duration almost disappeared.

3.4. Plasma Nonuniformity inside the Z-Pinch

Figure 13 shows pinhole images taken in two perpendicular directions. One can see regions with a low emission intensity inside the Z-pinch. The low-intensity regions are present in all images and correlate with one another, which means that these structures are three-dimensional. It is possible that the presence of such structures inside the pinch hinders further pinch compression.

The appearance of such regions can be explained as follows. During a prolonged plasma production, as was described above, plasma jets are generated that are directed toward the liner axis by the Ampère force. Near the axis, the jets collide. Extending along the axis, the jets form current filaments that are independent of one another; intertwining, these filaments form the pinch body. The chaotic character of this process results in the appearance of regions with a higher magnetic

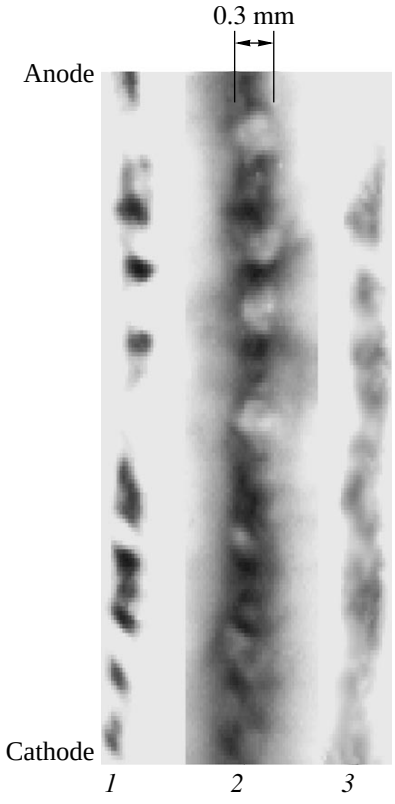

Fig. 13. Fragments of X-ray pinhole images of a Z-pinch: (*1*) $h\nu > 1$ keV, (*2*) $h\nu > 150$ eV, and (*3*) $h\nu > 1$ keV. Images *1* and *2* are taken in one direction, while image *3* is taken in a perpendicular direction.

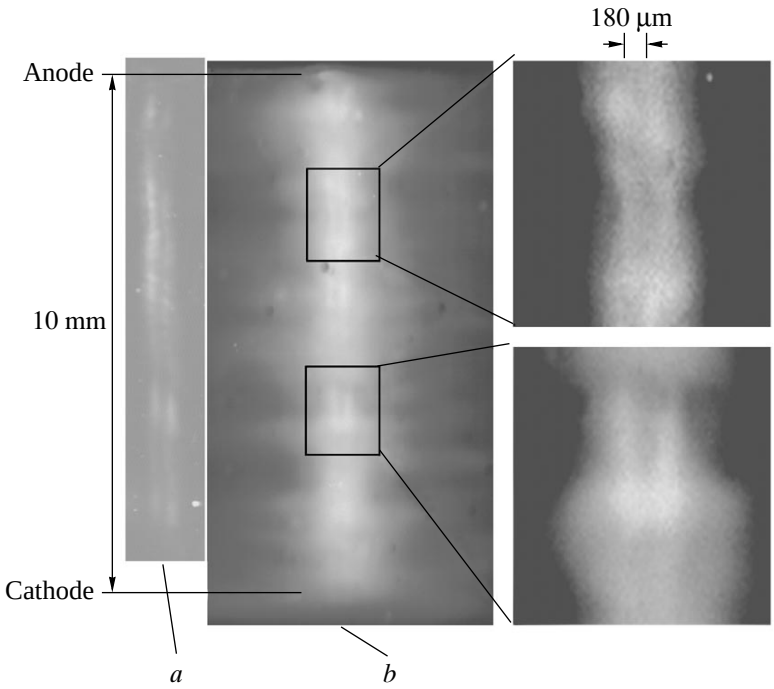

Fig. 14. X-ray pinhole images of the pinch structure: (*a*) $h\nu > 1$ keV and (*b*) $h\nu > 150$ eV. The enlarged fragments of the pinch structure taken at $h\nu > 150$ eV are shown on the right.

field. Inside these regions, the plasma density is low in comparison to the density in the jets; hence, the emission intensity from these regions is low.

In the experiments described below, arrays made of wires spaced a distance of 0.2 to 0.6 mm from each other were used as loads. This distance is slightly smaller than the interwire distance in liners in which the highest SXR emission power (>3 TW) was obtained.

Regions with low emission intensity can extend along the liner axis under the action of the pressure of the imploding shell. In the pinhole images presented in Fig. 14, one can clearly see a complicated, spatially periodic structure with a characteristic scale length of 180 μm. Such a pinch structure can adversely affect the final compression ratio and, consequently, the SXR emission power, which, in this case, turned out to be ~1 TW.

We note again that the low-intensity regions inside the pinch were observed during the implosion of liners with an interwire distance of less than 0.6 mm. Similar structures with smaller characteristic scale lengths were probably produced in liners with interwire distances larger than 0.6 mm. In this case, they, however, could not be detected because of an insufficiently high spatial resolution of the pinhole camera.

4. SUMMARY

Based on the acquired experimental data on the implosion of wire arrays, the following scenario of an implosion may be inferred.

When the electric current flows through the liner wires, they generate a plasma that is nonuniform in the axial direction, the characteristic scale length of the nonuniformity being 100–200 μm. In the azimuthal direction, the nonuniformity scale length is determined by the distance between the wires. The plasma leaving the wires drifts toward the axis under the action of the Ampére force. Due to axial and azimuthal modulation, the plasma flow acquires the form of individual plasma jets. The initial asymmetry and self-focusing of the jets lead to the formation of bright plasma bunches in the axial region (at a distance of 0.5–2.0 mm from the pinch axis). This results in the generation of a protracted SXR pulse. The off-axis plasma bunches are more often produced in the cathode region of the liner and emit in a photon energy range above 2 keV. As the liner implodes toward the array axis, the radii of the plasma bunches decrease and the bunches can merge into individual current-carrying plasma filaments extended along the discharge axis.

5. CONCLUSIONS

The spatial structure of the imploding plasma is so nonuniform that it makes no sense to talk about a plasma shell that implodes as a single entity. Under these conditions, a description of the Z-pinch implosion in terms of the Rayleigh–Taylor instability or the classical “snow plow” model is certainly incorrect.

The cathode plasma generated in the early stage of implosion has been investigated. In pinhole images,

this plasma is seen to be conical in shape. When the liner length was increased from 1 to 1.5 cm, the cathode plasma became less pronounced. The presence of the cathode plasma and the generation of plasma bunches located mainly in the cathode region of the liner are probably interrelated and are caused by the uniformity of the liner current.

The plasma bunches produced near the Z-pinch axis decrease the SXR emission power.

1.5-cm-long double arrays provide a higher compression ratio ($R/r \approx 30$) as compared to simple wire arrays.

The complicated, spatially periodic structure of a Z-pinch with a characteristic scale length of ~200 μm has been observed. In some cases, the pinch looks like a system of two (or more) independent plasma filaments located near the axis.

ACKNOWLEDGMENTS

This study was supported in part by the Russian Foundation for Basic Research, project nos. 01-02-17319, 01-02-17526, and 02-02-17200.

REFERENCES

1. M. B. Bekhtev, V. D. Vikharev, S. V. Zakharov, *et al.*, Zh. Éksp. Teor. Fiz. **95**, 1653 (1989) [Sov. Phys. JETP **68**, 955 (1989)].
2. I. K. Aĭvazov, M. B. Bekhtev, V. V. Bulan, *et al.*, Fiz. Plazmy **16**, 645 (1990) [Sov. J. Plasma Phys. **16**, 373 (1990)].
3. T. W. L. Sanford, G. O. Allshouse, B. M. Marder, *et al.*, Phys. Rev. Lett. **77**, 5063 (1996).
4. V. V. Aleksandrov, A. V. Branitskiĭ, G. S. Volkov, *et al.*, Fiz. Plazmy **27**, 99 (2001) [Plasma Phys. Rep. **27**, 89 (2001)].
5. V. V. Alexandrov, M. V. Fedulov, I. N. Frolov, *et al.*, in *Proceedings of the 5th International Conference on Dense Z-Pinches, Albuquerque, 2002*, Ed. by J. Davis, Cr. Deeney, and N. R. Pereira, p. 87.
6. V. V. Aleksandrov, E. V. Grabovskiĭ, G. G. Zukakishvili, *et al.*, Zh. Éksp. Teor. Fiz. **124**, 829 (2003).
7. Z. A. Al'bikov, E. P. Velikhov, A. I. Veretennikov, *et al.*, At. Energ. **68** (1), 26 (1990) [Sov. At. Energy **68** (1), 34 (1990)].
8. M. G. Haines, IEEE Trans. Plasma Sci. **30**, 588 (2002).

Translated by E.L. Satunina

Plasma Physics Reports, Vol. 30, No. 1, 2004, pp. 38–43. Translated from Fizika Plazmy, Vol. 30, No. 1, 2004, pp. 41–46.

PLASMA DYNAMICS

Correlation between the Parameters of Ion and X-ray Emissions from the Plasma of a Micropinch Discharge

A. E. Gureĭ*, A. N. Dolgov, D. E. Prokhorovich**, A. S. Savjolov**, and A. A. Tikhomirov***

** Lebedev Physical Institute, Russian Academy of Sciences, Leninskiĭ pr. 53, Moscow, 119991 Russia*

*** Moscow Engineering Physics Institute, Kashirskoe sh. 31, Moscow, 115409 Russia*

Received January 30, 2003; in final form, April 22, 2003

Abstract—Ion emission from the plasma of a micropinch discharge is studied by analyzing the plasma flow from the discharge region with the help of time-of-flight technique and probe diagnostics. Concurrently, soft X-ray emission from the micropinch is recorded. The experimental data are interpreted using the radiative contraction model. © *2004 MAIK "Nauka/Interperiodica".*

In [1, 2], passive particle diagnostics were shown to be applicable to studying the plasma of a micropinch discharge. In [2], the energy spectra of neutrals and single-charged ions leaving the discharge region were recorded using a time-of-flight technique in the particle energy range from 10 eV to 100 keV. The particle groups that were formed in different stages of the discharge were distinguished. In [1], the energy spectra of high-energy (~50 keV) single- and multicharged ions emitted from the plasma of a micropinch discharge were studied using the Thomson technique. The results of these studies provided information on the mechanisms for the ion flow formation and other processes in micropinch plasma. A characteristic feature of these studies (as compared to the earlier papers [3, 4], in which ion emission from the plasma of fast Z-pinches produced in plasmas of high-Z elements was also investigated) is the close examination of the discharge operation.

To increase the reliability and informativeness of the experimental results, it is of interest to perform simultaneous measurements of the ion emission parameters and other characteristics of the discharge plasma, as well as to widen the range of the particle diagnostics employed. In the present study, we used passive particle diagnostics concurrently with the measurements of soft X-ray emission. A schematic of the experiment is shown in Fig. 1. A micropinch discharge was produced in a low-inductive vacuum spark device. The cylindrical cathode and conical anode (both made of iron) were placed into a vacuum chamber with a residual pressure of no higher than 10^{-4} torr. The working medium was the vapor of the electrode material. The discharge was ignited with the help of an auxiliary erosion discharge produced near the cathode surface. A bank of high-voltage low-inductance capacitors served as a power supply of the main discharge. The discharge current reached its maximum 1 μs after the beginning of the discharge.

The discharges were observed with the help of an X-ray pinhole camera that produced images of the discharge plasma in the photon energy range $h\nu \geq 3$ keV. The spatial resolution was no worse than 100 μm. The temporal characteristics of the discharge were determined using a magnetic probe recording the time derivative of the current.

The ion emission was studied using time-of-flight diagnostics with a path base length of 0.5–1.6 m. The

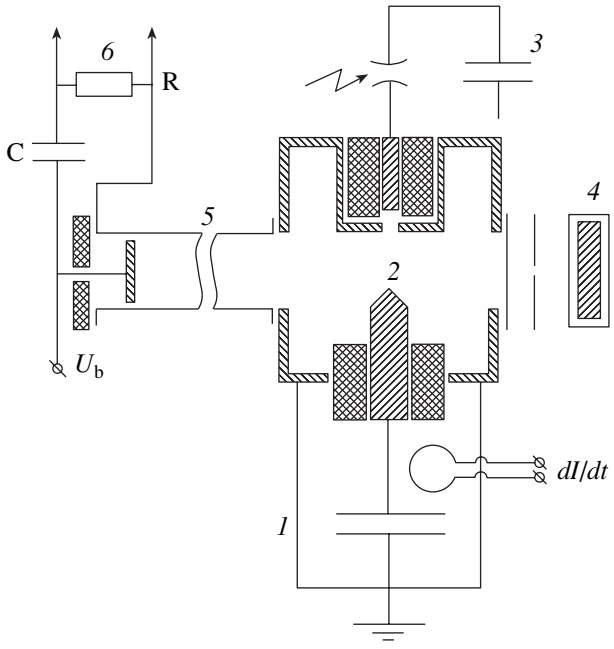

Fig. 1. Schematic of the experiment: (*1*) main discharge circuit, (*2*) electrode system, (*3*) auxiliary (trigger) discharge circuit, (*4*) X-ray recording system, (*5*) ion recording system, and (*6*) input of an oscilloscope or analog-to-digital converter.

1063-780X/04/3001-0038$26.00 © 2004 MAIK "Nauka/Interperiodica"

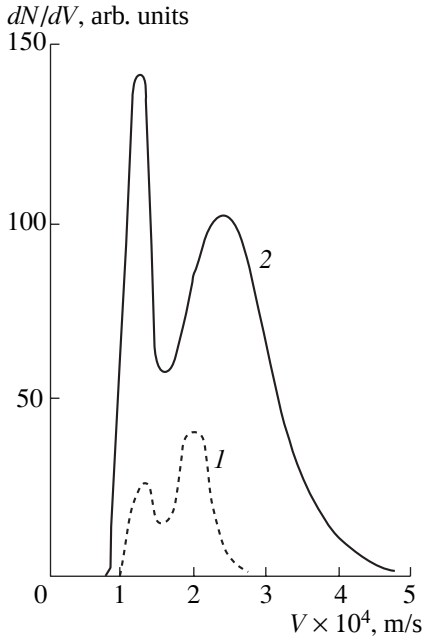

Fig. 2. Typical ion spectra emitted from the discharge plasma in the axial direction at $I_{max} < I_{cr}$ (curve *1*) and $I_{max} > I_{cr}$ (curve *2*).

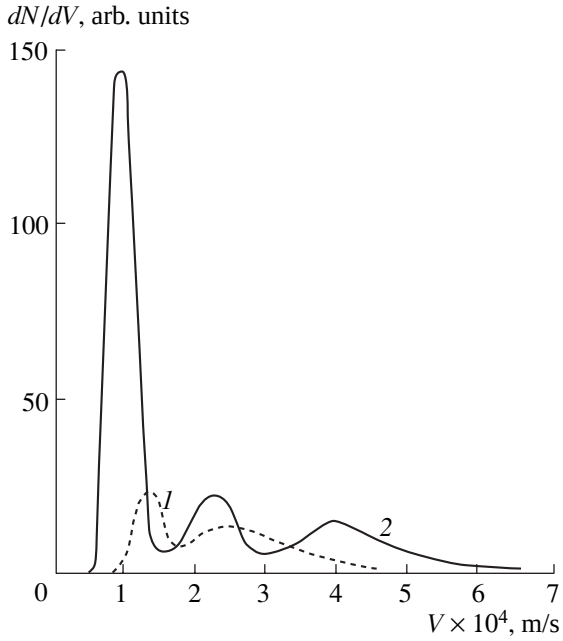

Fig. 3. Typical ion spectra emitted from the discharge plasma in the radial direction at $I_{max} < I_{cr}$ (curve *1*) and $I_{max} > I_{cr}$ (curve *2*).

ion flow was intercepted by a passive collector, which was biased with respect to the grounded discharge chamber, and was recorded with either a storage oscilloscope or a high-speed analog-to-digital converter connected to a PC. The results of [1, 2] show that the recorded ion flow consists mainly of single-charged Fe ions. The ion spectrum dN/dV was derived from the recorded dependence of the ion current I_i on the flight time:

$$I_i = e\frac{dN}{dt} = e\frac{dN}{dV}\left|\frac{d}{dt}\left(\frac{l}{t}\right)\right|, \quad (1)$$

where e is the electron charge, l is the path base length, and $V = l/t$ is the ion velocity. Expression (1) yields

$$\frac{dN}{dV} = \frac{I_i t^2}{el}. \quad (2)$$

The zero time (i.e., the instant at which the recorded ion flow was generated) was determined by the photocurrent pulse caused in the collector circuit by short-wavelength plasma emission.

The integral soft X-ray (SXR) yield from the discharge was measured with a dosimeter based on a photomultiplier operating in the integrating regime. A 0.5-mm-thick organic scintillator was used for the down-conversion of X-ray photons. The scintillator and photomultiplier were prevented from long-wavelength radiation by a 100-μm-thick absorbing Be filter. The dosimeter was calibrated using synchrotron radiation from a circular electron accelerator. The calibration showed that the dosimeter efficiently recorded radiation in the photon energy range of 1–3 keV.

According to the radiative contraction model [5], which most adequately describes most of the experimental data, the plasma column constriction narrows to a micron size (i.e., a micropinch forms) at currents higher than the critical current determined by the balance between the radiative losses and Joule heating in the discharge channel. For a Fe plasma, the critical current is $I_{cr} \sim 50$ kA.

Figures 2 and 3 present characteristic ion spectra obtained with a collector that was negatively biased with respect to the ground in order to cut off the electron component. The spectra were recorded in the axial and radial directions at discharge currents of 40 kA ($I_{max} < I_{cr}$) and 150 kA ($I_{max} > I_{cr}$). To record the particle flows in the axial direction, we used a cathode with an axial hole 3 mm in diameter and four auxiliary erosion-type sources located symmetrically about the discharge axis. In a regime with $I_{max} < I_{cr}$, when there was no micropinch in the discharge plasma, the spectra exhibited pronounced maxima corresponding to particle velocities of $(1–1.5) \times 10^4$ m/s and $(2–2.5) \times 10^4$ m/s. In a regime with $I_{max} > I_{cr}$, when a micropinch formed in each discharge, another maximum corresponding to a particle velocity of 4×10^4 m/s appeared in the spectrum.

A comparative analysis of the spectra obtained by recording the particle flows in the axial and radial directions allows us to identify the first of the above veloci-

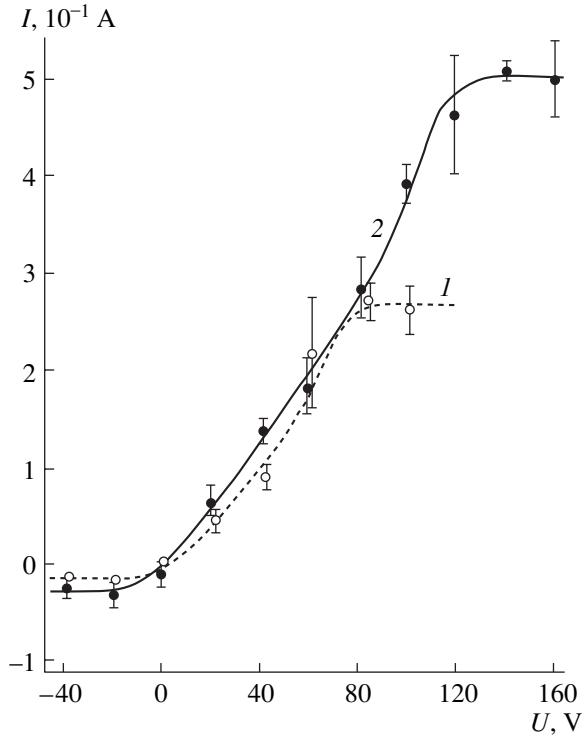

Fig. 4. Current–voltage characteristics of the plasma flow emitted from the discharge region at $I_{max} < I_{cr}$ (curve *1*) and $I_{max} > I_{cr}$ (curve *2*).

ties with an average ion thermal velocity in the stage of a steady-state plasma column [6]. The second velocity can be attributed to the velocity of the axial plasma flow that is generated when the current-carrying plasma shell converges toward the discharge axis in the course of the implosion of the ionized vapor of the electrode material and the formation of the plasma column. The third of the observed maxima probably corresponds to the group of particles that are generated when the pinching process converts into radiative contraction [2].

Apparently, the reason why the third maximum occurs when the ions are recorded in the radial direction and does not occur when they are recorded in the axial direction is that the relatively fast particles emitted from the micropinch region are scattered by the slower particles of the peripheral plasma. The scattering reduces the velocities of fast particles and result in their departure from the recording area. This mechanism of deforming the initial spectrum is most efficient when the ions are recorded in the axial direction because, in this case, the parameter $\sigma\langle n\rangle L$ (where σ is the scattering cross section, $\langle n\rangle$ is the average density of slow particles, and L is the length of the peripheral plasma) is much higher and the solid angle within which the ions can reach the collector is much smaller than in the case when the ions are recorded in the radial direction.

Particles with velocities of lower than 0.5×10^4 m/s remain virtually undetected by the apparatus employed. This may be explained by their charge neutrality [2]. Particles with velocities of higher than 7×10^4 m/s are not present in the spectra because of insufficient resistance of the recording system to the high-frequency interferences induced in the recording apparatus in the initial stage of the discharge.

We note that the shape of the collector signals showed good reproducibility from shot to shot regardless of the bias magnitude and polarity. This hinted that we should use the collector as a plane electric probe in the plasma flow. We measured the current–voltage characteristics in which, at a given bias potential, the current averaged over the signal duration was taken as a collector current. Evidently, these collector current–voltage characteristics are averaged over both space (the collector area) and time (the duration of the recorded signal). Hence, the electron temperature of the plasma flow obtained from the slope of the electron branch of the characteristic can only be regarded as an estimate (Fig. 4). For both recording directions (axial and radial), the electron temperature was found to be $T_e = 25 \pm 5$ eV for a subcritical discharge current (I_{max} = 40 kA) and $T_e = 18 \pm 5$ eV for a supercritical current (I_{max} = 150 kA). This result agrees with the model prediction because, in the radiative contraction model of Fe plasma, the temperature $T_e \cong 20$ eV corresponds to the stage of plasma column formation. The fact that the electron temperature recorded at $I_{max} < I_{cr}$ exceeds that recorded at $I_{max} > I_{cr}$ is confirmed by observations of the structure of the discharge plasma emitting in the photon energy range $h\nu > 1$ keV (Fig. 5). In the former case, the radiation source is the plasma column as a whole, whereas in the latter case, the radiation source in the above spectral range is only the constriction region, i.e., the micropinch. As the constriction narrows, which is possible at discharge currents higher than the critical current, the particle density per unit length sharply decreases and the specific plasma resistance in the constriction increases due to the matter outflow in the axial direction. As a result, the discharge current decreases, whereas the Joule heating power in the micropinch increases [5].

To increase the reliability of the experimental results, we also employed probe diagnostics. Two identical 3-mm-diameter plane probes located symmetrically about the discharge chamber axis within the 1.3-m-long axially oriented path base were used (because of the design features of the facility, it was impossible to orient the probes radially). Shifting the probes in the radial direction at a fixed distance from the discharge region allowed us to trace the radial profile of the electron density. We obtained the waveforms of the probe current in different discharges at a fixed probe potential with respect to the chamber. In this way, we acquired the statistics of the waveforms at a fixed

probe potential. According to [13], such an approach is quite justified.

As in the case of collector measurements, when plotting the probe current–voltage characteristics, the average current was taken as a probe current.

Within the measurement accuracy, the electron temperature is nearly independent of the probe location and is different for subcritical and supercritical discharge currents. As is the case with collector measurements, the average electron temperature in the former case is higher than in the latter; however, the statistical scatter in the T_e value actually overlaps both ranges. In our opinion, it is reasonable to determine the most probable T_e value over a set of the measurement results (Fig. 6). For the supercritical discharge current, we obtain $T_e = 17 \pm 2$ eV, whereas for the subcritical discharge current, we obtain $T_e = 27 \pm 4$ eV.

In some cases, it was also possible to monitor the time evolution of T_e in the plasma flow. When treating the time-resolved current–voltage characteristics, we did not observe any significant deviation of T_e from its time-averaged value.

The determination of T_e by the slope of the electron branch of the current–voltage characteristics is based on the fact that the obtained temperature corresponds to the r.m.s. electron thermal velocity, which is $V_e \cong 3 \times 10^6$ m/s, whereas the mean velocity of the plasma flow is $V \sim 10^4$ m/s. Thus, in view of the fact that $V \ll V_e$, the electron branch of the characteristic is nearly the same as for a plasma that is at rest with respect to the collector [7].

Simultaneous measurements of the parameters of ion emission in the radial direction and the SXR yield in a photon energy range of 1–3 keV were performed when the discharge current exceeded the critical value. A comparative analysis of the dosimeter readings and pinhole images unambiguously shows that a micropinch is present in a pinhole image (the so-called "hot spot") only if the energy recorded by the dosimeter exceeds a certain threshold level E_{thr}. The ion emission parameters were measured in a discharge regime such that the recorded energy was high enough (namely, $E = (1.5–4.5)E_{thr}$) and the process of plasma pinching led to the formation of a micropinch in each discharge.

The spectra recorded at different E diverge at high particle velocities (higher than 4×10^4 m/s): the higher E, the larger the contribution of the fast particles to the ion spectrum. Simultaneous measurements of the ion velocity distribution and SXR yield enable a more reliable interpretation of the distribution character as compared to the previous studies, in which such interpretation was based on the comparison of the recorded characteristic ion velocities with theoretical predictions.

According to the model predictions [8], which are confirmed by the experimental results [9], the first contraction can be considered as a transition to an equilib-

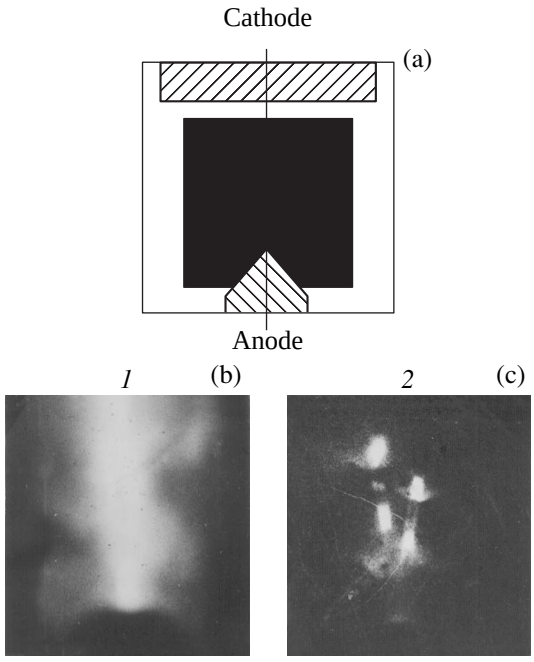

Fig. 5. (a) Area of pinhole measurements (dark rectangle) and (b, c) characteristic pinhole images of the discharge area in the photon energy range $h\nu > 1$ keV for (b) $I_{max} < I_{cr}$ and (c) $I_{max} > I_{cr}$.

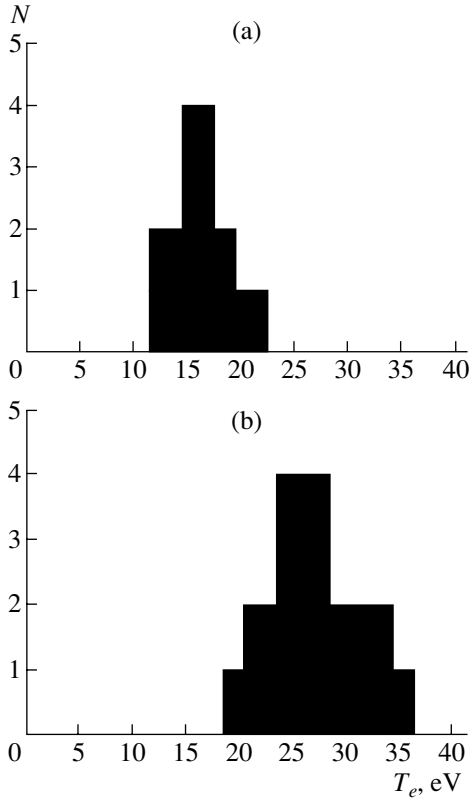

Fig. 6. Number of measurements N vs. electron temperature T_e of the plasma emitted from the discharge at currents of (a) 150 and (b) 50 kA.

rium state whose parameters are governed by the discharge current. This circumstance accounts for good reproducibility of the pinch plasma parameters during the first contraction. After the first contraction is completed, energy balance is established between Joule heating, radiative losses, and energy loss due to the plasma outflow from the constriction. The plasma temperature in the constriction is determined by the relation

$$T_e = \frac{\mu_0 I^2}{8\pi k(1+z)N_i}, \quad (3)$$

where I is the current through the constriction, N_i is the plasma ion density per unit length, z is the average charge number, and k is the Boltzmann constant. In this stage, the electron and ion temperatures are equalized, $T_i = T_e$ [2].

The second contraction begins due to the violation of the energy balance, when the plasma density per unit length decreases substantially and the temperature increases to 0.5 keV, so that the ionization from the L shell of Fe ions begins, which leads to a sharp increase in radiative losses. The second contraction stops because of the onset of the plasma anomalous resistivity [5]. Hence, this contraction can be regarded as a transition to a thermodynamically nonequilibrium state, via which the Z-pinch converts into an arc discharge operating in a slightly inhomogeneous cold plasma. For this reason, the reproducibility of the plasma parameters from shot to shot is poor during the second contraction.

The spectral range of radiation recorded by the X-ray dosimeter corresponds to that of the photorecombination emission from FeXVII–FeXXIV ions that arise as a result of the ionization from the L shell. The emission accompanying the ionization from the K shell is almost absent [10]. The heating of the plasma to a temperature that is sufficient for the efficient ionization from the K shell of Fe ions occurs in the stage of anomalous resistivity, i.e., when the pinching process terminates because of the decrease in the plasma density per unit length and the increase in the current density [8]. However, the situation can even be more complicated if one takes into account a small amount of the plasma laying beyond the micropinch region. In this case, the current is intercepted (at least partially) by the outer plasma, which leads to a change in the Z-pinch dynamics [11].

The correlation between the X-ray yield from the micropinch plasma in the spectral range corresponding to the photorecombination emission from the L-shell ions and the spectrum of ion emission in the velocity range $V_i \geq 4 \times 10^4$ m/s can be explained as follows. It is reasonable to suggest that the onset of the anomalous plasma resistivity in different discharges interrupts the pinching process at its different stages, depending on certain situational factors. According to model predictions, this interruption occurs almost instantaneously [5]. The main fraction of the radiant energy should be emitted after the plasma becomes transparent to its intrinsic emission (L-shell emission). The fact that we observe a hot spot (an image of a micropinch emitting in the K-shell spectrum of Fe ions) in each discharge means that the plasma also becomes transparent in each discharge. Consequently, the high plasma density is achieved that is necessary for the efficient conversion of the plasma thermal energy into the energy of K-shell emission when the plasma resistivity becomes anomalous. An additional confirmation of the fact that the micropinch plasma becomes transparent is the magnitude of the measured level of the X-ray yield: on the average, $E = (2–3)E_{\text{thr}}$. The higher the plasma density during the transparency stage, the higher the effective temperature of the micropinch plasma in the stage of anomalous resistivity and expansion, which is recorded by means of diffraction spectroscopy. Typically, this temperature is $T_e \sim 2–3$ keV [12], which corresponds to a Fe ion thermal velocity of $V_i \cong (8–10) \times 10^4$ m/s. According to the model predictions, the temperature of the micropinch plasma at the end of the second contraction phase is $T_e \cong 0.8–1$ keV, which, under the conditions of quasi-equilibrium, corresponds to a Fe ion thermal velocity of $V_i \cong (5–6) \times 10^4$ m/s [8].

The observed ion spectra differ in the energy range corresponding to the ion emission in the contraction stage, which allows one to assume that there are certain situational factors that affect the micropinch dynamics in this stage. Such a factor can be the degree to which the current flowing through a micropinch is shunted by the peripheral plasma. This degree definitely impacts the rate of implosion and heating of the micropinch plasma and, consequently, the ion emission spectrum and the intensity of the emitted radiation.

ACKNOWLEDGMENTS

We are grateful to the staffs of the Plasma Physics Department at the Moscow Engineering Physics Institute and the Dense Plasma Laboratory at the Lebedev Physical Institute for their help and cooperation.

REFERENCES

1. V. A. Veretennikov, A. E. Gureĭ, A. N. Dolgov, *et al.*, Pis'ma Zh. Tekh. Fiz. **21**, 78 (1995) [Tech. Phys. Lett. **21**, 940 (1995)].
2. A. N. Dolgov, Fiz. Plazmy **22**, 629 (1996) [Plasma Phys. Rep. **22**, 569 (1996)].
3. Yu. A. Bykovskiĭ, V. B. Lagoda, and G. A. Sheroziya, Pis'ma Zh. Éksp. Teor. Fiz. **30**, 489 (1979) [JETP Lett. **30**, 458 (1979)].
4. Yu. A. Bykovskiĭ, V. B. Lagoda, and G. A. Sheroziya, Zh. Tekh. Fiz. **50**, 1357 (1980) [Sov. Phys. Tech. Phys. **25**, 785 (1980)].

5. V. V. Vikhrev, V. V. Ivanov, and K. N. Koshelev, Fiz. Plazmy **8**, 1211 (1982) [Sov. J. Plasma Phys. **8**, 688 (1982)].
6. M. A. Gulin, A. N. Dolgov, O. V. Nikolaev, and A. S. Savjolov, Fiz. Plazmy **16**, 1015 (1990) [Sov. J. Plasma Phys. **16**, 590 (1990)].
7. O. V. Kozlov, *Electric Probe in Plasma* (Atomizdat, Moscow, 1969).
8. K. N. Koshelev, Yu. V. Sidel'nikov, V. V. Vikhrev, and V. V. Ivanov, *Spectroscopy of Multicharged Ions in Hot Plasmas* (Nauka, Moscow, 1991).
9. V. A. Veretennikov, Candidate's Dissertation (Moscow, 1987).
10. W. Lotz, J. Opt. Soc. Am. **57**, 873 (1967).
11. V. S. Imshennik and N. A. Bobrova, *Collisional Plasma Dynamics* (Énergoatomizdat, Moscow, 1997).
12. V. V. Vikhrev, V. V. Ivanov, K. N. Koshelev, and Yu. V. Sidel'nikov, Dokl. Akad. Nauk SSSR **282**, 1361 (1982) [Sov. Phys. Dokl. **27**, 153 (1982)].
13. *High Speed Physics*, Ed. by K. von Vollrath and G. Thomer (Springer-Verlag, Vienna, 1967; Mir, Moscow, 1971), Vol. 3.

Translated by N.N. Ustinovskiĭ

Plasma Physics Reports, Vol. 30, No. 1, 2004, pp. 44–55. Translated from Fizika Plazmy, Vol. 30, No. 1, 2004, pp. 47–59.

PLASMA KINETICS

Vlasov Equation in Terms of Canonical Variables

A. M. Ignatov

Prokhorov Institute of General Physics, ul. Vavilova 38, Moscow, 119991 Russia

Received April 17, 2003

Abstract—A new approach to the perturbation theory for the Vlasov equation is discussed. The approach is based on the expansion of the Hamiltonian in powers of the canonical variables about their equilibrium values. Unlike the traditional approach, the proposed perturbation theory provides energy conservation in every order. In particular, solutions to linearized equations are constructed that carry certain energy and momentum. The influence of decay processes on the kinetic beam–plasma instability is also discussed. © *2004 MAIK "Nauka/Interperiodica".*

1. INTRODUCTION

The present paper deals with the Vlasov equation—the simplest kinetic equation implemented in plasma theory:

$$\frac{\partial f(t, \mathbf{r}, \mathbf{v})}{\partial t} + \mathbf{v}\frac{\partial f(t, \mathbf{r}, \mathbf{v})}{\partial \mathbf{r}} - \frac{e}{m}\frac{\partial \phi(t, \mathbf{r})}{\partial \mathbf{r}}\frac{\partial f(t, \mathbf{r}, \mathbf{v})}{\partial \mathbf{v}} = 0. \quad (1)$$

Here, the potential $\phi(\mathbf{r})$ satisfies Poisson's equation

$$\Delta\phi(t, \mathbf{r}) = -4\pi e(n(t, \mathbf{r}) - n_0) \quad (2)$$

where

$$n(t, \mathbf{r}) = \int d\mathbf{v} f(t, \mathbf{r}, \mathbf{v}) \quad (3)$$

is the particle number density and n_0 is the density of the neutralizing background. Traditionally, the dynamics of collisionless plasma is studied in terms of the perturbation theory; i.e., the distribution function is written as $f(t, \mathbf{r}, \mathbf{v}) = f_0(\mathbf{v}) + f_1(t, \mathbf{r}, \mathbf{v})$, where the deviation $f_1(t, \mathbf{r}, \mathbf{v})$ is on the order of the $\phi(t, \mathbf{r})$, and the expansion in powers of $\phi(t, \mathbf{r})$ is then performed. As the first step of this procedure, we have the linearized Vlasov equation

$$\frac{\partial f_1(t, \mathbf{r}, \mathbf{v})}{\partial t} + \mathbf{v}\frac{\partial f_1(t, \mathbf{r}, \mathbf{v})}{\partial \mathbf{r}} - \frac{e}{m}\frac{\partial \phi(t, \mathbf{r})}{\partial \mathbf{r}}\frac{\partial f_0(\mathbf{v})}{\partial \mathbf{v}} = 0. \quad (4)$$

It is well known that there are various ways of solving the initial problem for this equation. The Landau method based on the Laplace transform is widely spread. There is also the Van Kampen approach using the representation in terms of the eigenfunction of the linearized Vlasov equation. Of course, both methods are mathematically equivalent and yield the same results.

At first sight, what are the reasons to describe all this again? There is not enough space here to list all textbooks and monographs discussing the Vlasov equation. The problem of ballistic modes (or quasi-waves) arising in Van Kampen approach, as well as relations between various methods, is also well illuminated in the literature [1–6].

However, there are questions concerning Eq. (1) that have no satisfactory (at least from the methodological viewpoint) answers. One of them is the problem of energy balance. With a distribution function being a solution to Eq. (1), the net energy

$$H = \int d\mathbf{r}d\mathbf{v}\frac{mv^2}{2} f(t, \mathbf{r}, \mathbf{v}) + \int d\mathbf{r}\frac{1}{8\pi}\left(\frac{\partial \phi(t, \mathbf{r})}{\partial \mathbf{r}}\right)^2 \quad (5)$$

remains constant. This is easy to check by differentiating Eq. (5) with respect to time, integrating the second term by parts, and taking into account the Vlasov equation (1) and Poisson's equation (2). Inserting $f(t, \mathbf{r}, \mathbf{v}) = f_0(\mathbf{v}) + f_1(t, \mathbf{r}, \mathbf{v})$ into Eq. (5) and assuming that $f_1 \sim \phi$, the energy takes the form of an expansion in powers of the potential, $H = H_0 + H_1 + H_2$, where $H_i \sim \phi^i$. If the deviation f_1 satisfies linearized Vlasov equation (4), then the first two terms of the energy expansion are constant, but the time derivative of the electric field energy H_2 is nonzero.

On the other hand, with an isotropic equilibrium distribution $f_0(\mathbf{v}) = f_0(v^2)$, the following quadratic expression is constant:

$$H_L = -\frac{m}{4}\int d\mathbf{r}d\mathbf{v}\frac{f_1(t, \mathbf{r}, \mathbf{v})^2}{f_0'(v^2)} + \int d\mathbf{r}\frac{1}{8\pi}\left(\frac{\partial \phi(t, \mathbf{r})}{\partial \mathbf{r}}\right)^2. \quad (6)$$

At first sight, it is impossible to get this quantity with the help of the straightforward expansion of energy (5). In fact, how did it occur that the unperturbed distribution function appeared in the denominator? However, expression (6) is entirely meaningful, as will be discussed below.

1063-780X/04/3001-0044$26.00

The linearized Vlasov equation meets with one more adversity. There are many exact solutions to nonlinear equation (1), e.g., the Bernstein–Green–Kruskal (BGK) waves and their various generalizations. One can evaluate energy (5) of a BGK wave. With the amplitude of a BGK wave going to zero, it transforms to a linear Van Kampen wave, but for the latter, energy (5) is not defined. Since Van Kampen waves form a complete set, every nonlinear wave may be represented as their combination. A periodic nonlinear wave with a period L is expressed in terms of all harmonics with the wave vectors $k_n = 2\pi n/L$ ($n = 0, \pm 1, \pm 2, \ldots$). It was found that, even for small-amplitude BGK waves, the convergence of corresponding series is very slow and one must take into account all harmonics [7].

Thus, the traditional perturbation theory used in plasma physics violates energy conservation at its first step, which cannot help but annoy a physicist. They usually reconcile this nuisance by assuming that the problem of energy balance may be resolved by the nonlinear theory. The well-known physical reason for the violation of energy conservation is the resonant interaction between particles and waves, which is described, e.g., by the quasilinear theory.[1]

In this respect, plasma physics differs radically from other areas of physics. Dealing with a conservative system we are, as a rule, able to use the perturbation expansion that conserves energy in every order. Studying, e.g., oscillations of a crystalline lattice, one starts from introducing normal modes, each of them carrying a certain energy. One then takes into account anharmonicity, electron–phonon interaction, and a great many other processes; however, in every order of perturbation theory, a conserving quantity (which may be identified with energy) is found. There is a fairly regular algorithm called the classical or canonical perturbation theory, which is based on the expansion of the Hamiltonian in powers of deviation from an equilibrium state and the consequent elimination of the nonresonant terms. This approach is successful in various areas of physics (see, e.g., [8, 9]).

The procedure of classical perturbation theory may be briefly outlined as follows. Let us suppose that we are dealing with a physical system described by Hamilton's equations:

$$\frac{\partial q_i}{\partial t} = \frac{\delta H}{\delta p_i}, \quad \frac{\partial p_i}{\partial t} = -\frac{\delta H}{\delta q_i}, \tag{7}$$

where the generalized momentum p_i and the generalized coordinate q_i are distributed quantities that depend on the configuration space coordinates and, possibly, some additional variables. The Hamiltonian $H(p_i, q_i)$ is a functional of p_i and q_i, and $\delta H/\delta p_i$ stands for the functional derivative. The temporal evolution of any quantity g depending on p_i and q_i is described with the help of the Poisson bracket: $\dot{g} = \{g, H\}$.

Expanding the Hamiltonian H in powers of the deviations Δp_i and Δq_i of the canonical variables from their steady-state values, we obtain quadratic (H_2), cubic (H_3), etc., terms. A linear change of variables reduces a quadratic Hamiltonian of a stable homogeneous medium to the form

$$H_2 = \sum_j \int d\mathbf{k}\, \omega_j(\mathbf{k}) a_{j\mathbf{k}} a^*_{j\mathbf{k}}, \tag{8}$$

where $\omega_j(\mathbf{k})$ are the eigenfrequencies of a medium and $a_{j\mathbf{k}}$ are the corresponding complex amplitudes. The next terms of the expansion (H_3, H_4, etc.) are also written in terms of the complex amplitudes. Then, an appropriate canonical transform eliminates nonresonant parts of the interaction Hamiltonians. For example, the only nonzero terms remaining in H_3 are such that $\omega_{j_1}(\mathbf{k}_1) = \omega_{j_2}(\mathbf{k}_2) + \omega_{j_3}(\mathbf{k}_3)$ and $\mathbf{k}_1 = \mathbf{k}_2 + \mathbf{k}_3$. The details of this procedure in application to many physical problems may be found in the reviews [8, 9].

As a rule, relations between natural physical quantities and the generalized coordinates and momenta are fairly involved. The most complicated part of the problem is for the search an appropriate change of variables. However, the problem is solved for seemingly all of the hydrodynamic plasma models (see, e.g., [8–10]). As for the Vlasov equation, the situation is more sophisticated. Below, we will discuss this problem in more detail. It should be also pointed out that the Hamiltonian approach to evolutionary equations (in particular, to the Vlasov equation) is closely related to various variational principles. There are many (at least six) such principles known for the Vlasov equation [11, 12].

The natural impulse arises to attempt applying the Hamiltonian mechanics to kinetic phenomena in collisionless plasmas—the problem on which the present paper is focused. The first step in using the canonical perturbation theory is to rewrite Eq. (1) in the Hamiltonian form. This is discussed in Section 2. Various ways of introducing the canonical variables are briefly reviewed in Section 3. One particular way is used in Section 4 to derive linearized equations resulting from the expansion of the Hamiltonian in powers of deviations of the canonical variables. Unlike the solutions to the linearized Vlasov equation, one may attribute energy to the obtained linear eigenmodes. The influence of the three-wave decay on the evolution of the beam instability is studied in Section 5 as an example of a nonlinear process. The relation between some versions of the perturbation theory is discussed in Section 6.

[1] It should be noted however that, although the quasilinear theory was formulated more than forty years ago, its applicability range is still under discussion.

2. THE HAMILTONIAN FORM OF THE VLASOV EQUATION

One may identically rewrite Eq. (1) as

$$\frac{\partial f}{\partial t} = [f, E]_{\mathbf{r},\mathbf{v}}, \tag{9}$$

where $E(\mathbf{v}, \mathbf{r}) = mv^2/2 + e\phi(\mathbf{r})$ is the energy per particle and $[,]_{\mathbf{r},\mathbf{v}}$ is the familiar mechanical Poisson bracket

$$[A, B]_{\mathbf{r},\mathbf{v}} = \frac{1}{m}\left(\frac{\partial A}{\partial \mathbf{v}}\frac{\partial B}{\partial \mathbf{r}} - \frac{\partial A}{\partial \mathbf{r}}\frac{\partial B}{\partial \mathbf{v}}\right). \tag{10}$$

In contrast to what is written in many textbooks, representation (9) is not the Hamiltonian form yet. The phase space now is infinite-dimensional and is composed of all distribution functions $f(\mathbf{r}, \mathbf{v})$. An appropriate form of the Vlasov equation should look as follows:

$$\frac{\partial f(t, \mathbf{r}, \mathbf{v})}{\partial t} = \{f(t, \mathbf{r}, \mathbf{v}), H\}, \tag{11}$$

where H is Hamiltonian (5). The Poisson bracket $\{A, B\}$ in Eq. (11) should be a bilinear antisymmetric operation acting on arbitrary functionals of the distribution function, $A(f)$ and $B(f)$, and must satisfy the Jacobi identity. It is easy to verify that the following operation:

$$\{A, B\} = \int d\mathbf{v}d\mathbf{r} f(\mathbf{r}, \mathbf{v})\left[\frac{\delta A}{\delta f(\mathbf{r}, \mathbf{v})}, \frac{\delta B}{\delta f(\mathbf{r}, \mathbf{v})}\right]_{\mathbf{r},\mathbf{v}}, \tag{12}$$

which is called the Lie–Poisson bracket, meets all the above requirements and Vlasov equation (9) indeed takes form (11). Here, the potential $\phi(\mathbf{r})$ is considered to be a functional of $f(\mathbf{r}, \mathbf{v})$ defined by the solution to Poisson's equation (2). For completeness, it useful to write down the evaluation of the electric energy variation:

$$\begin{aligned}\delta\frac{1}{8\pi}\int d\mathbf{r}(\nabla\phi(\mathbf{r}))^2 &= \frac{1}{4\pi}\int d\mathbf{r}\nabla\phi(\mathbf{r})\cdot\nabla\delta\phi(\mathbf{r}) \\ &= -\frac{1}{4\pi}\int d\mathbf{r}\phi(\mathbf{r})\Delta\delta\phi(\mathbf{r}) = e\int d\mathbf{r}d\mathbf{v}\phi(\mathbf{r})\delta f(\mathbf{r}, \mathbf{v}).\end{aligned} \tag{13}$$

This form of the Vlasov equation was first proposed by Morrison [13]. A more complete set of the Vlasov–Maxwell equations is also written in the Hamiltonian form [13], and a similar representation is known for the Klimontovich equation [14]. The physical meaning of representation (11) and braces (12) is fairly arcane. It is clear that net energy (5) is the averaged single-particle energy, but it is not so clear why Poisson bracket (10) should be averaged.

Besides the energy, there are other integrals of motion associated with the Vlasov equation. First, there is the net momentum related to the translational symmetry:

$$\mathbf{P} = \int d\mathbf{v}d\mathbf{r} m\mathbf{v} f(\mathbf{r}, \mathbf{v}). \tag{14}$$

Then, there is the infinite set of the so-called Casimir invariants

$$C_F = \int d\mathbf{v}d\mathbf{r} F(f(\mathbf{r}, \mathbf{v})), \tag{15}$$

where $F(f)$ is an arbitrary function of its argument. The Casimir invariants are related to the specific structure of bracket (12): they commute not only with the Hamiltonian but also with an arbitrary functional $A(f)$ ($\{C_F, A(f)\} = 0$). An infinite number of conservation laws arise because Eq. (1) describes the motion of an incompressible fluid in the single-particle phase space $(\mathbf{r}, \mathbf{v})$. For example, this may be illustrated by the following reasoning: If we choose an arbitrary function as $F(f) = \theta(g - f)$, then the invariability of integral (15) means that, in the course of evolution, the phase space volume surrounded by the surface $f(\mathbf{r}, \mathbf{v}) = g$ remains constant. There are only two macroscopic observable quantities among Casimir invariants: the net number of particles ($F(f) = f$) and the entropy ($F(f) = -f\ln f$).

Operation (12) is an example of a noncanonical Poisson bracket. Its main distinction from ordinary mechanical bracket (10) is that it explicitly depends on the phase-space coordinates, i.e., in our particular case, on the distribution function. Such structures (which often appear in physics) have been intensively studied in recent years. The simplest and best-known example is the motion of a rigid body described by Euler's equations. Further details about noncanonical brackets may be found in the reviews [9, 10] (see also the references cited therein).

The origin of the problems of the traditional perturbation theory discussed in the introduction is clear from representation (11). Besides the energy and the momentum, integrals (15) should remain constant in the course of evolution. In other words, the phase-space point $f(t)$ always belongs to a manifold $C_F = \text{const}$, which is called a symplectic leaf. In solving an initial problem, we choose an initial distribution function $f_0(\mathbf{r}, \mathbf{v})$ and, therefore, a certain symplectic leaf. As a result, the net phase space is foliated into a set of symplectic leaves. When we perform the straightforward expansion of Eqs. (1) and (2) in powers of the distribution function deviations f_1, we ignore the additional integrals of motion. Moreover, besides the energy, Lie–Poisson bracket (12) should be also expanded in powers of f_1 due to its explicit dependence on f. Although it is a feasible procedure (see below, Section 3.4), the linear dynamics was only described in this way, while the investigation of wave interactions with the help of the classical perturbation theory seems to be a difficult task. In order to use the classical perturbation theory, one should find canonical variables for Eq. (11), i.e., change the phase-space coordinates in such a way that the Poisson bracket is independent of coordinates. Various ways of achieving this goal are discussed in the next section.

3. CANONICAL VARIABLES

3.1. Multiflow Hydrodynamics

It was known long ago [15] that, instead of Vlasov equation (1), collisionless kinetics may be described by the infinite set of hydrodynamic equations:

$$\frac{\partial n(t, \mathbf{r}, \mathbf{w})}{\partial t} + \nabla \cdot (n(t, \mathbf{r}, \mathbf{w})\mathbf{V}(t, \mathbf{r}, \mathbf{v})) = 0, \quad (16)$$

$$\frac{\partial \mathbf{V}(t, \mathbf{r}, \mathbf{w})}{\partial t} + (\mathbf{V}(t, \mathbf{r}, \mathbf{w}) \cdot \nabla)\mathbf{V}(t, \mathbf{r}, \mathbf{w}) = -\frac{e}{m}\nabla\phi(t, \mathbf{r}). \quad (17)$$

Here, $\mathbf{w}$ is a Lagrangian label distinguishing various flows in phase space ($\mathbf{r}$, $\mathbf{v}$). For example, one may assume that there are no perturbations at $r \longrightarrow \infty$ and $\mathbf{V}(t, \mathbf{r}, \mathbf{w}) = \mathbf{w}$. These hydrodynamic variables are linked with the distribution function by the relation

$$f(t, \mathbf{r}, \mathbf{v}) = \int d\mathbf{w} n(t, \mathbf{r}, \mathbf{w})\delta(\mathbf{v} - \mathbf{V}(t, \mathbf{r}, \mathbf{w})), \quad (18)$$

i.e., the net particle number density is

$$n(t, \mathbf{r}) = \int d\mathbf{w} n(t, \mathbf{r}, \mathbf{w}). \quad (19)$$

It is easily verified by straightforward substitution that with $n(t, \mathbf{r}, \mathbf{w})$ and $\mathbf{V}(t, \mathbf{r}, \mathbf{w})$ satisfying Eqs. (16) and (17) the distribution function $f(t, \mathbf{r}, \mathbf{v})$ satisfies Vlasov equation (1).

The net energy in terms of the hydrodynamic variables appears thus:

$$H = \int d\mathbf{r} d\mathbf{w} \frac{m}{2} n(t, \mathbf{r}, \mathbf{w}) V^2(t, \mathbf{r}, \mathbf{w}) + \frac{1}{8\pi}\int d\mathbf{r}(\nabla\phi(t, \mathbf{r}))^2, \quad (20)$$

where the potential is considered as a functional of the densities, $n(t, \mathbf{r}, \mathbf{w})$.

Canonical variables for hydrodynamics are well known. In particular, limiting ourselves to vortex-free solutions to Eqs. (16) and (17) and introducing the mass density $\rho(t, \mathbf{r}, \mathbf{w}) = mn(t, \mathbf{r}, \mathbf{w})$ and the velocity potential $\mathbf{V}(t, \mathbf{r}, \mathbf{w}) = \nabla\psi(t, \mathbf{r}, \mathbf{w})$, Eqs. (16) and (17) are written as

$$\frac{\partial \rho}{\partial t} = \frac{\delta H}{\delta \psi}, \quad \frac{\partial \psi}{\partial t} = -\frac{\delta H}{\delta \rho}. \quad (21)$$

It was pointed out in review [9] that this way of writing yields the Hamiltonian form of Vlasov equation (11) with the Poisson bracket given by Eq. (12). In principle, writing the kinetic equation in form (21) allows one to implement classical perturbation theory.

It is important to note the following. From the viewpoint of physics, hydrodynamic equations (16) and (17) and the Vlasov equation describe the same system. However, they are in no way equivalent mathematically: this is clear from just counting down the number of degrees of freedom. With a given distribution function it is impossible to reconstruct the densities $n(t, \mathbf{r}, \mathbf{w})$ and the velocities $\mathbf{V}(t, \mathbf{r}, \mathbf{w})$ of each flow. For example, one can always make a change of variables $\mathbf{w} = \mathbf{u}(t, \mathbf{r}, \mathbf{w}')$ in Eq. (18), where $\mathbf{u}$ are some functions and $\mathbf{w}'$ is a new Lagrangian label. The functions $n(t, \mathbf{r}, \mathbf{w})$ and $\mathbf{V}(t, \mathbf{r}, \mathbf{w})$ will then alter, but the form of Eqs. (16) and (17) will not change; this gives us reason to speak about the gauge invariance of hydrodynamics [9]. The hydrodynamic variables contain more information than the distribution function. Meanwhile, they are observable, at least, in a computational experiment. To reconstruct the hydrodynamic variables from the computational results, one has to monitor the motion of every particle; this is one of the most often used diagnostics. Mean while, to determine the distribution function, the instant snapshot of the particle positions in phase space is enough. Finally, there is one more circumstance: Eqs. (16) and (17) are able to describe rotational motions, which results in reasonable solutions to the Vlasov equation. Thus, the assertion of [9], according to which representation (21) introduces the canonical variables to the Vlasov equation, is hardly well-based. However, Eqs. (16) and (17) are a reasonable alternative that may be used as a starting point for classical perturbation theory. Beware: one can foresee that unphysical ghost linear waves will appear along this route.

3.2. Symplectic Leaf Parametrization

Another way is to introduce a special coordinate system in phase space. In a very simplified and lapidary paraphrase, the procedure, which has been discussed in a number of papers (e.g., [16–18][2]), consists in the following. It is well known that the formal solution to the Vlasov equation with the initial distribution $f(0, \mathbf{r}, \mathbf{v}) = f_0(\mathbf{r}, \mathbf{v})$ is $f(t, \mathbf{r}, \mathbf{v}) = f_0(\mathbf{r}_0, \mathbf{v}_0)$, where the initial coordinates and velocities of particles, $\mathbf{r}_0$ and $\mathbf{v}_0$, are linked with their current values $\mathbf{r}$ and $\mathbf{v}$ by Newton's equations, i.e., by some canonical transform Λ. In shorthand notation, this is written as $f(t) = f_0 \circ \Lambda$. Since the canonical transforms preserve the phase-space volume, Casimir invariants (15) remain constant under the action of a canonical transform. The symplectic leaf passing through a given initial point f_0 in the functional phase space is parameterized by a group of canonical transforms connected with a unity. Thus, one may look for a canonical transform such that $f(t) = f_0 \circ \Lambda(t)$ is a solution to the Vlasov equation and $\Lambda(0) = 1$.

Canonical transforms are defined by generating functions. The action of the canonical transform with the generating function S on the initial distribution function is written symbolically as

$$f(t) = e^{\mathcal{L}_S} f_0, \quad (22)$$

[2] To familiarize oneself with the mathematics used in these papers, the books [19–21], listed in order of growing size and complexity, are recommended.

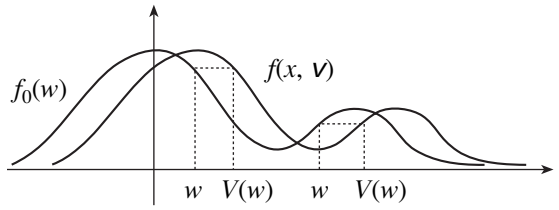

Fig. 1. Construction of a function $V(t, x, w)$.

where the action of the operator $\mathcal{L}_S$ (called the Lie derivative) on an arbitrary function $g(\mathbf{r}, \mathbf{v})$ is defined by the rule $\mathcal{L}_{Sg} = [S, g]$ and $[,]$ is Poisson bracket (10). It is readily seen from Eq. (22) that the generating function S plays the role of the coordinates at the symplectic leaf. Distribution functions given by Eq. (22) are dynamically accessible; i.e., only such functions may appear as a result of continuous evolution of the initial distribution f_0.

An equation for the generating function S equivalent to the Vlasov equation was derived in [16–18] in the form of infinite series. It was proved that this equation is Hamiltonian and that the Poisson bracket is independent of the coordinates at the symplectic leaf. Regardless of all the elegance of the geometric approach, this way can hardly yield concrete results that are interesting from the viewpoint of physics.

3.3. One-Dimensional Vlasov Equation

In one important particular case, the arbitrariness of the Lagrangian label **W**, mentioned in Section 3.1, may be utilized to get rid of the redundant degrees of freedom in Eqs. (16) and (17) and to designate the explicit parametrization of the symplectic leaf (see Section 3.2). Let us consider one-dimensional solutions to the Vlasov equation. Let all variables depend on one spatial coordinate x only. Dependence on the transverse velocity is irrelevant, and we can rid of it by integration. The hydrodynamic velocities are conveniently introduced in the following way [22]: We consider a solution $V(t, x, w)$ to the equation

$$f(t, x, V(t, x, w)) = f_0(w), \tag{23}$$

where $f_0(w)$ is a distribution function; e.g., $f_0(w) = f(t, x, w)|_{x \to \infty}$. The solution to Eq. (23) is unique if both functions $f(t, x, w)$ and $f_0(w)$ have the same number of maxima and minima with respect to w and their values at extremal points coincide (Fig. 1).

Let $f(t, x, v)$ be a solution to Eq. (1), velocities $u_i(t, x)$ correspond to the extremal points of the distribution $(\partial f(t, x, v)/\partial v|_{v = u_i} = 0)$ and $f_i = f(t, x, u_i)$. Then, as follows from Eq. (1), $\partial f_i/\partial t + u_i \partial f_i/\partial x = 0$; i.e., there exist solutions with $f_i = \text{const}$. If we restrict ourselves to functions of this kind only, then the solution to Eq. (23) is single-valued, with $\partial V(t, x, w)/\partial w > 0$ and $V(t, x, w)|_{w \to \pm\infty} \longrightarrow \pm\infty$. The introduced hydrodynamic variables $V(t, x, w)$ are the level lines of the distribution function and each of them is equipped with its own label w. The same representation is actually implemented in the well-known "waterbag" method, which is sometimes used to numerically solve the Vlasov equation [23].

The equation for $V(t, x, w)$ immediately follows from Eq. (1):

$$\frac{\partial V(t, x, w)}{\partial t} + V(t, x, w)\frac{\partial V(t, x, w)}{\partial x} = -\frac{e}{m}\frac{\partial \phi(t, x)}{\partial x}, \tag{24}$$

where the potential still satisfies Poisson's equation (2), while the density is expressed in terms of the hydrodynamic velocities

$$n(t, x) = -\int dw\, f_0'(w) V(t, x, w). \tag{25}$$

Therefore, the Lagrangian description introduced by Eq. (23) yields constant hydrodynamic densities reducing Eq. (16) to an identity, and the dynamics is described with Euler equation (24). The integrals of the Vlasov equation are also easily expressed in terms of the velocities $V(t, x, w)$. Energy (5) and momentum (14) are

$$H = -\frac{m}{6}\int dx dw\, f_0'(w) V^3(t, x, w) + \frac{1}{8\pi}\int dx \left(\frac{\partial \phi(t, x)}{\partial x}\right)^2, \tag{26}$$

$$P = -\frac{m}{2}\int dx dw\, f_0'(w) V^2(t, x, w), \tag{27}$$

and Casimir invariants (15) are written as

$$C_F = -\int dx dw V(t, x, w)\frac{\partial F(f_0(w))}{\partial w}. \tag{28}$$

Finally, the Hamiltonian form of Vlasov equation (11) is reduced to

$$\frac{\partial V(t, x, w)}{\partial t} = \{V(t, x, w), H\}_V = \frac{1}{m f_0'(w)}\frac{\partial}{\partial x}\left(\frac{\delta H}{\delta V(t, x, w)}\right), \tag{29}$$

where Poisson bracket (12) in terms of $V(t, x, w)$ is

$$\{A, B\}_V = \int dx dw \frac{1}{m f_0'(w)}\frac{\delta A}{\delta V(t, x, w)}\frac{\delta}{\delta x}\frac{\delta B}{\delta V(t, x, w)}. \tag{30}$$

This is easy to verify, considering that the variational derivative of Hamiltonian (26) is

$$\frac{\delta H}{\delta V(t, x, w)} = -f_0'(w)\left[\frac{m}{2}V^2(t, x, w) + e\phi(t, x)\right]. \tag{31}$$

The zeros $f_0'(w)$ in the denominators of Eqs. (29) and (30) are harmless, because they always cancel out. In fact, one might get rid of them by redefining $V(t, x, w)$, but this results in inconvenient bulky expressions.

The advantages and disadvantages of the chosen way are readily seen from Eqs. (24)–(29). As it has been already pointed out, condition (15) defines a manifold in phase space. Using Eq. (23), we change from the distribution function to the velocities and introduce a special coordinate system in phase space in the vicinity of a point $f_0(w)$ in which the symplectic leaf C_F = const takes a very simple form. Introducing in Eq. (28) velocity perturbations $V(t, x, w) = w + U(t, x, w)$ the corresponding constraint defining the symplectic leaf is reduced to the condition

$$\int dx U(t, x, w) = 0, \tag{32}$$

which is easily met in every order of the perturbation theory.

Hamiltonian (26) now contains terms that are quadratic and cubic in U and are associated with the energy of the system eigenmodes and, correspondingly, with the interaction energy. The Poisson bracket given by Eq. (30) is now independent of the coordinate $V(t, x, w)$. Thus, Eq. (24) is a good starting point for classical perturbation theory.

On the other hand, solutions to Eq. (24) may exist for a certain limited time period; sooner or later, the wavebreaking resulting in singularities may occur, after which Eq. (24) fails to hold. In terms of the distribution function, this corresponds to the formation of phase-space vortices; however, the Vlasov equation is applicable even in this stage of evolution. This means that the introduced functions $V(t, x, w)$ form an appropriate coordinate system in a finite phase-space area. This is fairly natural from the viewpoint of topology because one can hardly hope to cover the net manifold C_F = const with a single coordinate chart.

However, as the amplitude of perturbations decreases, the time during which singularities are formed tends to infinity. That is why, in using the perturbation theory, the temporal limitations do not manifest themselves. Below (see Sections 4 and 5), the linear eigenmodes and their interactions are studied with the help of Eq. (24).

3.4. "Free Energy" of Collisionless Plasma

Prior to investigating specific processes, we will discuss one more approach to the linearized Vlasov equation. Integral (6) of the one-dimensional linearized Vlasov equation has the form

$$H_L = -\frac{m}{2}\int dx dv \frac{v}{f_0'(v)} f_1(t, x, v)^2 + \frac{1}{8\pi}\int dx \phi'(t, x)^2. \tag{33}$$

In [24, 25], this expression was obtained according to the following reasoning: Suppose we are interested in the stability of a steady state with a distribution function $f_0(v)$. The stability may be studied with the help of a corresponding Lyapunov function and its dependence on small perturbations. It has already been pointed out that the straightforward expansion of the Hamiltonian, which is often used to investigate conservative systems, takes us nowhere. In [24, 25], this expansion was performed for perturbations satisfying the dynamical accessibility constraint C_F = const [see Eq. (15)], rather than for arbitrary perturbations f_1. This resulted in expression (33), which was rather conventionally called "free energy."

It was also shown that the linearized Vlasov equation is written in the canonical form with Hamiltonian (33) if one takes the zero-order term in the expansion of Lie–Poisson bracket (12) in powers of f_1, i.e., replaces $f(\mathbf{r}, \mathbf{v})$ with $f_0(v)$. The Van Kampen eigenfunctions of Eq. (4) reduce Hamiltonian (33) to form (8). Therefore, every Van Kampen wave is attributed with free energy, which may be either positive or negative. It should be noted that the expansion procedure used in [23, 24] is rather cumbersome and it is unclear whether it may be used to investigate the next orders of the perturbation theory and wave interactions.

4. LINEAR EIGENMODES

Here, we sketch the perturbation theory [22] based on the parametrization of the symplectic leaf discussed in Section 3.3. Introducing the small deviations from the equilibrium, $V(t, x, w) = w + U(t, x, w)$, we expand Hamiltonian (26) in powers of U. Assuming that the function $f_0(w)$ in Eq. (23) is normalized as $\int dw f_0(w) = n_0$ and the perturbations meet constraint (32), the linear term of expansion is identically zero and the quadratic term is

$$H_2 = -\frac{m}{2}\int dx dw w f_0'(w) U^2(t, x, w) + \frac{1}{8\pi}\int dx \left(\frac{\partial \phi(t, x)}{\partial x}\right)^2, \tag{34}$$

where the potential obeys Poisson's equation

$$\frac{\partial^2 \phi(t, x)}{\partial x^2} = 4\pi e \int dw f_0'(w) U(t, x, w). \tag{35}$$

The problem is to find a linear change of variables $U(t, x, w)$ that transforms Hamiltonian (34) into some simple form similar to Eq. (8). Evidently, the problem is reduced to the solution of linearized Euler equation (24)

$$\frac{\partial U(t, x, w)}{\partial t} + w\frac{\partial U(t, x, w)}{\partial x} = -\frac{e}{m}\frac{\partial \phi(t, x)}{\partial x} \quad (36)$$

and may be solved in a standard fashion similar to the Van Kampen method. First, we perform the Fourier transformation

$$U(t, x, w) = \int \frac{dk}{\sqrt{2\pi}} e^{ikx} U_k(t, w)$$

and represent the time dependence of a perturbation as $U_k(t, w) = \exp(-ik\lambda t)g_k(w, \lambda)$. Then, taking into account Eq. (35), Eq. (36) is rewritten as

$$(w - \lambda)g_k(w, \lambda) = \frac{4\pi e^2}{mk^2}\int dw_1 f_0(w_1)g_k(w_1, \lambda). \quad (37)$$

One can easily recognize in this expression the adjoint Vlasov equation, which appears in the framework of the Van Kampen approach to Eq. (4) [1, 2]. It is of interest that the implementation of the adjoint Vlasov equation is traditionally regarded as a formal trick without any physical sense. In fact, as follows from Eq. (37), the adjoint Vlasov equation describes the oscillations of the level lines of the distribution function.

The solutions to Eq. (37) are called the adjoint Van Kampen functions. As is well-known, there are two types of solutions. First, there are the solutions corresponding to an arbitrary real value of the phase velocity λ. The corresponding eigenmodes belonging to the continuous spectrum are written as

$$g_k(w, \lambda) = \frac{\varepsilon_{2k}(\lambda)}{\pi}\frac{P}{w - \lambda} + \varepsilon_{1k}(\lambda)\delta(w - \lambda), \quad (38)$$

where the sign P denotes principal-value integration. The functions $\varepsilon_{1, 2k}(\lambda)$ are the real and imaginary parts of the ordinary dielectric permittivity

$$\varepsilon_{1k}(\lambda) = 1 - \frac{4\pi e^2}{mk^2}\int dw \frac{P}{w - \lambda} f_0'(w), \quad (39)$$

$$\varepsilon_{2k}(\lambda) = \frac{4\pi^2 e^2}{mk^2} f_0'(\lambda). \quad (40)$$

Here, it is convenient to treat the dielectric permittivity as a function of the phase velocity $\lambda = \omega/k$, rather than the frequency ω.

Solutions to adjoint Vlasov equation (37) of the second kind appear if the eigenvalue λ is complex. These solutions exist under the condition

$$\varepsilon_k^{(\pm)}(\lambda) = 0, \quad (41)$$

where

$$\varepsilon_k^{(\pm)}(\lambda) = 1 - \frac{4\pi e^2}{mk^2}\int dw \frac{dw}{w - \lambda} f_0'(w) \quad (42)$$

are the analytic continuations of the complex dielectric permittivity to the upper, $\mathrm{Im}\lambda > 0$ ($\varepsilon_k^{(+)}(\lambda)$), and correspondingly, to the lower, $\mathrm{Im}\lambda < 0$ ($\varepsilon_k^{(-)}(\lambda)$) half-planes. The existence of the roots of dispersion relation (41) indicates the medium is unstable. We denote the roots of $\varepsilon_k^{(+)}(\lambda)$ from the upper half-plane as $\lambda_s(k)$, where $s = 1, 2, \ldots$, and the roots of $\varepsilon_k^{(-)}(\lambda)$ from the lower half-plane are equipped with the indices $\lambda_s = -1, -2, \ldots$. It is evident from Eq. (42) that $\lambda_s(k)$ are even functions of k. Moreover, since the roots of $\varepsilon^{(-)}(\lambda)$ are obtained from the roots of $\varepsilon^{(+)}(\lambda)$ by complex conjugation, we can always number the eigenvalues in such a way that $\lambda_{-s}(k) = \lambda_s(k)^*$. The solutions to Eq. (37) corresponding to the eigenvalues $\lambda_s(k)$ are very simple:

$$g_k^s(w) = \frac{1}{w - \lambda_s(k)}. \quad (43)$$

Thus, an arbitrary solution to Eq. (36) may be written as

$$U_k(t, w) = \int d\lambda g_k(w, \lambda)a_k(t, \lambda) + \sum_{s = \pm 1, \pm 2\ldots} g_k^s(w)a_k^s(t), \quad (44)$$

where the complex amplitudes obey equations

$$\dot{a}_k(t, \lambda) = -ik\lambda a_k(t, \lambda) \quad (45)$$

and

$$\dot{a}_k^s(t) = -ik\lambda_s(k)a_k^s(t). \quad (46)$$

Since $U_k(t, w)$ is the Fourier transform of a real quantity; i.e., $U_{-k}(t, w) = U_k^*(t, w)$, Van Kampen functions (38) and (43) and the roots of dispersion relation (41) are even functions of k, and the complex amplitudes satisfy the conjugation conditions

$$a_{-k}(\lambda) = a_k^*(\lambda), \quad a_{-k}^{-s} = a_k^{s*}. \quad (47)$$

The introduced complex amplitudes describe two types of oscillations. The amplitudes $a_k(\lambda)$ correspond to the oscillations of the continuous spectrum, or quasi-waves. The spectral parameter λ is an arbitrary real number; consequently, the oscillation frequency is arbitrary. The second type of oscillations described by the amplitudes a_k^s is characterized by a certain dependence of the phase velocity on the wavenumber. The number of these modes coincides with the number of roots of dispersion relation (41); in particular, there are no such modes in a stable medium. According to the accepted

numeration, the modes with $s > 0$ describe growing oscillations, while those with $s < 0$ correspond to the decaying oscillations. When the unperturbed distribution $f_0(w)$ is varied, the number of discrete spectrum modes may change; however, the wave branches always appear and disappear by pairs.

Relation (44) is an integral transform, which allows one to reconstruct the hydrodynamic velocities from the given complex amplitudes. Using this relation, one may easily express various velocity-averaged quantities in terms of the complex amplitudes, e.g., density perturbation (25) and the electric field potential

$$\phi_k = \int d\lambda \frac{\varepsilon_{2k}(\lambda)}{\pi} a_k(\lambda) + \sum_s a_k^s. \quad (48)$$

Using the known properties of the Van Kampen functions, transform (44) can be inverted,

$$a_k(\lambda) = \frac{1}{\varepsilon_{2k}(\lambda) R_k(\lambda)} \int dw \varepsilon_{2k}(w) g_k(w, \lambda) U_k(w), \quad (49)$$

$$a_k^s = \frac{1}{\pi R_s(k)} \int \frac{dw}{w - \lambda_s(k)} \varepsilon_{2k}(w) U_k(w), \quad (50)$$

where $R_k(\lambda) = \varepsilon_{1k}(\lambda)^2 + \varepsilon_{2k}(\lambda)^2 = \left|\varepsilon_k^{(\pm)}(\lambda)\right|^2$, $R_s(k) = \varepsilon_k^{(\pm)'}(\lambda_s(k))$, and the plus or minus sign in the latter expression corresponds to the sign of s.

Thus, the oscillations described by Eq. (36) are very similar to the Van Kampen waves. At first sight, there is only one minor distinction: the dependence of the eigenmodes on w is given by the adjoint Van Kampen functions. There is, however, one extremely important consideration: we can assign the energy and the momentum to the modes characterized by the amplitudes $a_k(\lambda)$ and a_k^s, while this is impossible to do with Van Kampen waves. With the help of transform (44), quadratic Hamiltonian (34) may be written as

$$H_2 = \frac{1}{2} \int dk k^2 \left\{ -\int d\lambda \lambda \frac{\varepsilon_{2k}(\lambda)}{\pi} R_k(\lambda) |a_k(\lambda)|^2 + \sum_s \lambda_s(k) R_s(k) a_k^s a_k^{-s*} \right\}. \quad (51)$$

It may be also shown that transform (44) converts general equation (29) to the set of equations for the complex amplitudes,

$$\frac{\partial a_k(\lambda)}{\partial t} = \frac{\pi i}{k \varepsilon_{2k}(\lambda) R_k(\lambda)} \frac{\delta H}{\delta a_{-k}(\lambda)}, \quad (52)$$

$$\frac{\partial a_k^s}{\partial t} = -\frac{i}{k R_s(k)} \frac{\delta H}{\delta a_{-k}^s}. \quad (53)$$

Substituting the quadratic Hamiltonian (51) to these expressions, we again obtain linearized equations (45) and (46). Finally, the difference between net momentum (27) and Hamiltonian (51) is in the absence of the factors λ and $\lambda_s(k)$ only:

$$P = \frac{1}{2} \int dk k^2 \left\{ -\int d\lambda \frac{\varepsilon_{2k}(\lambda)}{\pi} R_k(\lambda) |a_k(\lambda)|^2 + \sum_s R_s(k) a_k^s a_k^{-s*} \right\}. \quad (54)$$

It is clear from Eq. (51) that the posed problem of reducing Hamiltonian (34) to the diagonal form is nearly solved. In order to write the contribution of the continuous spectrum in the form of Eq. (8), it is sufficient to renormalize the amplitudes $a_k(\lambda)$ with the appropriate factors. However, we avoid this because we otherwise have to watch out for possible changes in the sign of $\varepsilon_{2k}(\lambda)$ [see Eq. (40)], which results in fairly complicated expressions.

It follows from Eqs. (51) and (54) that we can attribute every oscillation with the amplitude $a_k(\lambda)$ to the definite energy and momentum, which are conserved in the absence of dissipation and nonlinear interactions. In this sense, the quasi-particles we are dealing with are well-defined physical objects. This is the cause of the evanescence of the usual Van Kampen waves: if we are unable to characterize something by conserving quantities, there are no reasons to regard this as a physical object. As in the case of the Van Kampen waves, every quasi-particle described by the solution to Eq. (36) consist of an additional beam of particles and a corresponding perturbation of the electric field. One may say, by analogy with quantum mechanics, that the amplitudes $a_k(\lambda)$ correspond to the dressed states of particles.

Besides the continuous spectrum, there are also discrete spectrum modes with the amplitudes a_k^s in an unstable medium. It was already pointed out that they always appear in pairs: for every growing wave $a_k^s \sim \exp(\gamma t - i\omega t)$, there is a decaying wave $a_k^{-s} \sim \exp(-\gamma t - i\omega t)$, and the only time-independent combination of the complex amplitudes is $a_k^s a_k^{-s*}$. It is according to this rule that the growing and decaying waves are arranged in integrals of motion (51) and (54). In contrast to the continuous spectrum, the quasi-particles are characterized by two amplitudes instead of one. One may attribute the energy and the momentum only to such an object. This quite general conclusion also follows from the analysis of the energy and momentum balance in the electrodynamics of continuous media [26].

We must also discuss the sign of the energy of linear waves: In a stable medium, $f_0'(w) < 0$ at $w > 0$ and the

integrand in Eq. (51) is always positive. Therefore, the energy of a wave in the continuous spectrum is also positive. Evidence of the instability is the fact that the imaginary part of dielectric permittivity (40) changes its sign; continuous spectrum waves with the corresponding value of the phase velocity λ carry negative energy. Since the last term in the integrand of Eq. (51) is not sign-definite, the question of the sign of the energy of discrete spectrum modes is meaningless. This viewpoint differs from that accepted in [24, 25], where growing or decaying solutions were attributed to zero energy. As was pointed out in [26], there are no physical objects with identically zero energy because an infinitesimal interaction (e.g., in the course of measurement) would convert such an object to something else.

The initial problem for Eq. (36) is solved like the initial problem for the Vlasov equation in a framework of the Van Kampen approach [1, 2]. The initial values of amplitudes $a_k(0, \lambda)$ and $a_k^s(0)$ are evaluated from the initial value of $U_k(w)|_{t=0}$ with the help of Eqs. (49) and (50). Then, using Eqs. (45) and (46), one can reproduce the temporal evolution of any averaged quantity, e.g., potential (48). In a stable medium, the asymptotic expansion of potential (48) at $t \longrightarrow \infty$ accounts for Langmuir oscillations and Landau damping. Evidently, the leading term of the expansion is determined by the values of λ corresponding to the minimum of the function $R_k(\lambda)$ in Eq. (49), i.e., by the zero of the complex dielectric permittivity $\varepsilon_k^{(+)}(\lambda)$ nearest to the real axis.

5. NONLINEAR INTERACTION

The wave interaction energy is given by the cubic term of expanded Hamiltonian (26):

$$H_3 = -\frac{m}{6}\int dx dw\, f_0'(w) U^3(x, w). \tag{55}$$

Using Eq. (44), one can easily express the interaction Hamiltonian in terms of the complex amplitudes. For example, the interaction of one unstable mode that consists of two complex amplitudes a_k^s ($s = \pm 1$) with two continuous spectrum waves is described by the Hamiltonian

$$H_3 = \sum_s \int dk dk_1 dk_2 d\lambda_1 d\lambda_2 \frac{1}{\sqrt{2\pi}} \delta(k + k_1 + k_2) \times T^s_{k;\, k_1 k_2}(\lambda_1, \lambda_2) a_k^s a_{k_1}(\lambda_1) a_{k_2}(\lambda_2), \tag{56}$$

where the element of the interaction matrix is given by the integral

$$T^s_{k;\, k_1 k_2}(\lambda_1, \lambda_2) = -\frac{m}{2}\int dw\, f_0'(w) g_k^s(w) g_{k_1}(w, \lambda_1) g_{k_2}(w, \lambda_2). \tag{57}$$

All other terms of the interaction Hamiltonian (e.g., those describing the interaction of three continuous spectrum waves) are arranged in a similar way. One may express integrals like those in Eq. (57) in terms of the Van Kampen functions (38), (43); however, instead of writing down general bulky expressions, we would rather consider a particular example.

Suppose we are dealing with the kinetic beam instability near its threshold. There is then a single root of Eq. (41), $\varepsilon_k^{(+)}(\lambda_0 + i\gamma) = 0$, in the upper half-plane ($\gamma > 0$). Let $k = k_0$ be the wave vector corresponding to the maximum growth rate, which is assumed to be small, $\gamma \ll \lambda_0$. We consider the resonant three-wave interaction of this single unstable mode with continuous spectrum waves.

If the wave vectors of two other waves are $k_{1,2}$, then we have $k_0 \approx k_1 + k_2$. The condition of the tree-wave synchronism for the continuous spectrum waves with the phase velocities $\lambda_{1,2}$ is written as $k_0\lambda_0 \approx k_1\lambda_1 + k_2\lambda_2$. In particular, waves with $\lambda_{1,2} \approx \lambda_0$ satisfy this condition; i.e., all waves with $\lambda_{1,2} - \lambda_0 \sim \gamma$ can take part in the three-wave interaction. Taking into account Eq. (47), the complex amplitudes of the interacting oscillations are represented as

$$a_k^s = \frac{1}{\sqrt{|kR_s(k)|}}(e^{-ik_0\lambda_0 t} b^s_{k-k_0} + e^{ik_0\lambda_0 t} b^{-s*}_{-k-k_0}), \tag{58}$$

$$a_k(\lambda) = \sqrt{\frac{\pi}{|k\varepsilon_{2k}(\lambda) R_k(\lambda)|}} \times \sum_{\alpha = 1, 2} [e^{-ik_\alpha\lambda_0 t} b_{\alpha k - k_\alpha}(\lambda - \lambda_0) + e^{ik_\alpha\lambda_0 t} b^*_{\alpha - k - k_\alpha}(\lambda - \lambda_0)]. \tag{59}$$

It is assumed here that the envelope amplitudes b_q^s and $b_{1,2q}(\lambda)$ are sharp functions of q of vanishing width and, in addition, $b_{1,2q}(\lambda)$ are localized at $\lambda \le \gamma$.

In evaluating matrix element (57), it should be remembered that, in the first order of the expansion in powers of γ, the real part of the dielectric permittivity vanishes, $\varepsilon_{1k_0}(\lambda_0) = 0$; hence, $\varepsilon_{1k_{1,2}}(\lambda_0) \sim 1$ and $\varepsilon_{2k_{1,2}}(\lambda_0) \sim \gamma/\lambda_0$. Therefore, the first term in Van Kampen functions (38) is small. Moreover, in the vicinity of the resonance, we ignore the dependence of matrix element (57) on the wave vectors, which results in

$$T^s_{k;\, k_1 k_2}(\lambda_1, \lambda_2) = \frac{1}{2} m f_0'(\lambda_0) \delta(\lambda_1 - \lambda_2) \frac{\varepsilon_{1k_1}(\lambda_0)\varepsilon_{1k_2}(\lambda_0)}{\lambda_1 - \lambda_0 - is\gamma}. \tag{60}$$

Then, we discard the dependence of all the coefficients in Eq. (51) on q and perform the Fourier transformation $b_q^s(t) \longrightarrow b^s(x)$, $b_{\alpha q}(\lambda) \longrightarrow b_\alpha(\lambda, x)$. Equa-

tions (52) and (53) are now written in the truncated form

$$\dot{b}^s = -i\frac{\partial H}{\partial b^{-s*}} = s\gamma b^s - i\beta\int d\lambda \frac{b_1(\lambda)b_2(\lambda)}{\lambda - is\gamma}, \quad s = \pm 1, \tag{61}$$

$$\dot{b}_1(\lambda) = i\frac{\delta H}{\delta b_1^*(\lambda)} = -ik_1\lambda b_1(\lambda) + i\beta b_2^*(\lambda)\sum_{s=\pm 1}\frac{b^s}{\lambda - is\gamma}, \tag{62}$$

$$\dot{b}_2(\lambda) = i\frac{\delta H}{\delta b_2^*(\lambda)} = -ik_2\lambda b_2(\lambda) + i\beta b_1^*(\lambda)\sum_{s=\pm 1}\frac{b^s}{\lambda - is\gamma}, \tag{63}$$

where the Hamiltonian is the energy density

$$H = \gamma\sum_{s=\pm 1} isb^s b^{-s*} - \int d\lambda \sum_{\alpha = 1,2}\lambda k_\alpha |b_\alpha(\lambda)|^2 + 2\beta\,\mathrm{Re}\sum_{s=\pm 1}\int d\lambda \frac{b^s b_1^*(\lambda)b_2^*(\lambda)}{\lambda - is\gamma}, \tag{64}$$

and the dimensional coefficient β is

$$\beta = \frac{m^2}{4\pi e^2}\sqrt{\frac{k_1 k_2}{k_0\varepsilon'_{1k_0}(\lambda_0)}}.$$

Equations (61)–(63) describe the influence of plasma echo on the development of the beam instability. Their structure resembles usual three-wave equations. There are two basic distinctions. First, as has already been pointed out, the high-frequency mode is described by two complex amplitudes (61); the energy of this mode is given by the first term in Hamiltonian (64). Second, the low-frequency modes are wave packets with a phase velocity spread. Due to phase mixing, the spread yields the Landau damping of the Fourier components of the electric field with the wave vectors $k_{1,2}$.

In studying wave interactions with allowance for Landau damping, the damping is often approximated as dissipation. For example, a wave is described by an equation like $\dot{a} = -\gamma_L a$ + nonlinear terms. Strictly speaking, this approximation is absolutely unjustified. Landau damping arises as an asymptotic expansion of a solution to a linear problem, which is valid at long enough times, $t \gg \gamma_L^{-1}$. If we ignore the nonlinear term in Eq. (62), then the potential $\phi_{k_1} \sim \int d\lambda b_1(0, \lambda)\exp(-ik_1\lambda t)$ behaves asymptotically like $\phi_{k_1} \sim \exp(-k_1\Delta\lambda t)$, where $\Delta\lambda$ is the width of the wave packet. However, all the experience of nonlinear physics demonstrates that the most interesting things happen when the time scales of two different processes coincide. Here, we are focused on the coinciding time scales of phase mixing ($t_{ph} = 1/k_{1,2}\Delta\lambda$) and nonlinear interaction ($t_{nl} \sim \beta|b^s|/\Delta\lambda$). It is evident that, in this case, Landau damping should be explicitly described as a result of phase mixing and the possible nonlinear correlations between various waves must be taken into account.

Besides energy (64), Eqs. (61)–(63) preserve additional integrals of motion that are analogous to the Manley–Row integrals. One can easily verify that

$$\frac{d}{dt}(|b_1(\lambda)|^2 - |b_2(\lambda)|^2) = 0, \tag{65}$$

$$\frac{d}{dt}\left(\sum_{s=\pm 1} b^s b^{-s*} - \int d\lambda |b_1(\lambda)|^2\right) = 0. \tag{66}$$

One may treat these relations as the balance of the number of quasi-particles in the three-wave interaction. In particular, implying the condition $k_0 = k_1 + k_2$, we obtain the conservation of the net momentum.

Despite the additional integrals of motion, it is impossible to solve Eqs. (61)–(63) analytically. Qualitatively, one may conjecture that the three-wave interaction accelerates the kinetic instability, making it explosive. Energy conservation condition (64) combined with Manley–Row integrals (65) and (66) allow an unlimited growth of the amplitude, which is typical of explosive-type instabilities.

The numeric solution to Eqs. (61)–(63) depicted in Figs. 2–4 confirm this qualitative reasoning. For numeric solutions, the scales of the amplitude, time, and phase velocity were chosen to make all the dimensional parameters equal to unity ($k_0 = 1$, $\gamma = 1$, and $\beta = 1$). The continuous distribution over λ was approximated by a discrete one (500 points). The figures demonstrate a particular case with $k_1 = k_2 = 0.5$ and $b_1(\lambda) = b_2(\lambda)$. The initial conditions were $b^{+1}(0) = 0.01$, $b^{-1}(0) = 0.01i$, and $b_1(0, \lambda) = 0.01/(\lambda^2 + 0.5)$ ($|\lambda| < 5$).

The function $|b_1(t, \lambda)|$ for different instants is depicted in Fig. 2. At $t = t_0 \approx 4$, the central part of the distribution starts to reduce; some later, lateral satellites appear, which become visible at $t = 4.5$. At approximately the same time, the phase $\arg b_1(t, \lambda)$ begins to deviate strongly from the linear dependence $0.5\lambda t$. The dependence of the energy of the unstable mode (i.e., the first term in Hamiltonian (64)) is shown in Fig. 3. This value is initially zero and the well-marked energy exchange starts simultaneously with the distortion of the low-frequency spectrum at $t = t_0$.

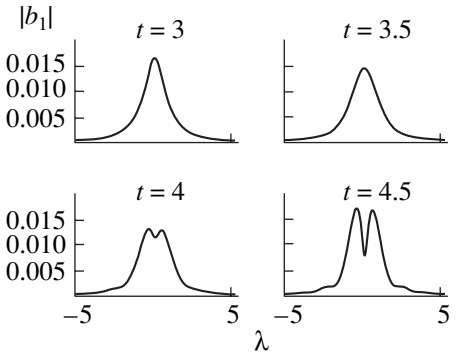

Fig. 2. Continuous spectrum evolution.

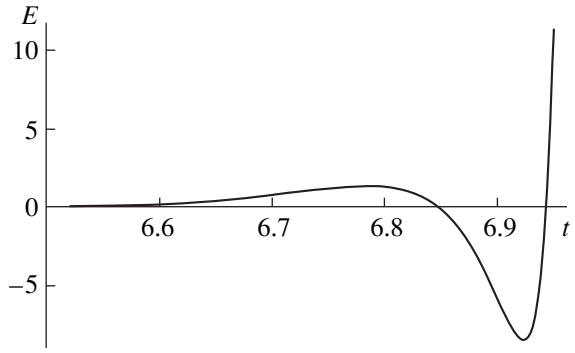

Fig. 3. Unstable mode energy vs. time.

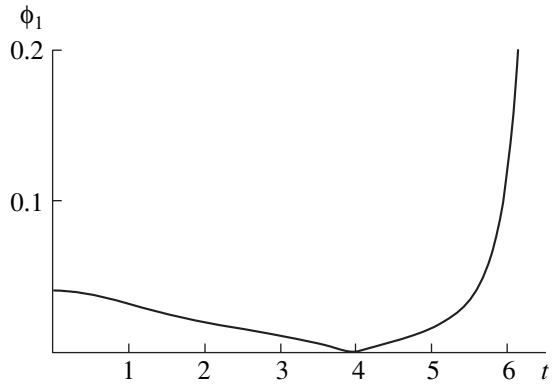

Fig. 4. Low-frequency potential vs. time.

Figure 4 shows the evolution of the potential of the low-frequency subharmonic, i.e., the integral $\phi_1(t) = \int d\lambda b_1(t, \lambda)$. In the linear stage ($t < t_0$), Landau damping provided by phase mixing is observed.

In the nonlinear stage ($t > t_0$), all the variables demonstrate fast growth (faster than in the exponential one). The numerical results show that the amplitudes behave like $1/(t - t_1)^2$, where the time of explosion is $t_1 \approx 7$. A reduction in the initial amplitude results in an increase in the time t_0, while over the time interval $t_0 < t < t_1$, the evolution remains qualitatively the same.

One may say that the evolution of the low-frequency potential (Fig. 4) demonstrates the competition between Landau damping and parametric decay instability in the field of the high-frequency wave. In the initial stage, Landau damping dominates; however, later decay instability overpowers.

The explosive character of the instability does not necessarily mean that we are here faced with the abovementioned inapplicability of Eq. (24) at long times. Getting rid of the non-resonant terms in the cubic Hamiltonian results in corrections to the energy that are proportional to the amplitudes in the forth power. In particular, these corrections provide a nonlinear frequency shift. How these effects influence beam instability is still unknown.

6. CONCLUSIONS

The main thesis of this paper may be formulated as follows: If we describe the collisionless kinetics in terms of some new variable instead of the distribution function, we are able to construct a perturbation theory that preserves energy in its every order. In particular, one can speak of the energy of linear waves and introduce well-defined quasi-particles, while in the framework of the traditional approach, the definition of the energy of Langmuir waves is rather conventional. The theory formulated here uses the expansion of the Hamiltonian and, to a great extent, is analogous to the classical perturbation theory known from mechanics. However, compared to the familiar procedures of plasma electrodynamics, it is more complicated. It should be stressed that two versions of the perturbation theory are in no way equivalent.

The relation between the distribution function and the velocity used here, $V(t, x, w) = w + U(t, x, w)$, is the nonlinear functional transform (23). Exact equations (1) and (24) are equivalent but there is no simple correspondence between their expansions in the powers of small deviations. For example, using Eq. (23), we may expand the distribution function into a series in powers of $U(t, x, w)$:

$$f(t, x, v) = f_0(v) - U(t, x, v) f_0'(v) + \frac{1}{2}\frac{\partial}{\partial v}(U^2(t, x, v) f_0'(v)) + \ldots. \quad (67)$$

If we represent the correction to the distribution as the second term in Eq. (67), $f_1(t, x, v) = -U(t, x, v) f_0'(v)$, then we obtain linearized Euler equation (36) from linearized Vlasov equation (4). However, the result would be different if we expand Eq. (1) in powers of the potential and Eq. (24) in powers of $U(t, x, v)$ up to the higher orders.

If we take the solution to linearized equation (36) corresponding to a Langmuir wave, substitute it in

transform (67), and then average over the oscillation period, we obtain an equation for the averaged distribution that is analogous to the quasilinear equation. Therefore, the linear equations discussed above and the quasilinear theory are of the same asymptotic accuracy.

It should be noted that the author is not calling for a complete revision of traditional plasma electrodynamics, or to have it rewritten in new terms and concepts. It is sometimes just useful to have a look at very familiar things from a new viewpoint.

REFERENCES

1. R. Balescu, *Statistical Mechanics of Charges Particles* (London, 1963; Mir, Moscow, 1967).
2. G. Ecker, *Theory of Fully Ionized Plasmas* (McGraw-Hill, New York, 1972; Mir, Moscow, 1974).
3. B. B. Kadomtsev, *Collective Phenomena in Plasma* (Nauka, Moscow, 1988).
4. V. N. Pavlenko and A. G. Sitenko, *Echo Phenomena in Plasma and Plasma-like Media* (Nauka, Moscow, 1988).
5. A. S. Kingsep, *Introduction in Nonlinear Plasma Physics* (Mosk. Fiz.-Tekh. Inst., Moscow, 1996).
6. A. V. Timofeev, *Resonance Phenomena in Plasma Oscillations* (Fizmatlit, Moscow, 2000).
7. H. Schamel, Phys. Plasmas **12**, 4831 (2000).
8. V. E. Zakharov, S. L. Musher, and A. M. Rubenchic, Phys. Rep. **129**, 285 (1985).
9. V. E. Zakharov and E. A. Kuznetsov, Usp. Fiz. Nauk **167**, 1137 (1997) [Phys. Usp. **40**, 1087 (1997)].
10. P. J. Morrison, Rev. Mod. Phys. **70**, 467 (1998).
11. H. Ye and P. J. Morrison, Phys. Fluids B **4**, 771 (1992).
12. A. J. Blizard, Phys. Rev. Lett. **84**, 5768 (2000).
13. P. J. Morrison, Phys. Lett. A **80**, 383 (1980).
14. O. A. Grechannyi, Teor. Mat. Fiz. **43**, 273 (1980).
15. D. Bohm, *General Theory of Collective Coordinates* (London, 1959; Mir, Moscow, 1958).
16. J. D. Crawford and P. D. Hislop, Phys. Lett. A **134**, 19 (1988).
17. H. Ye, P. J. Morrison, and J. D. Crawford, Phys. Lett. A **156**, 96 (1991).
18. T. Flå, Phys. Plasmas **1**, 2409 (1994).
19. B. F. Schutz, *Geometrical Methods of Mathematical Physics* (Cambridge Univ., Cambridge, 1980; Mir, Moscow, 1984).
20. V. I. Arnold, *Mathematical Methods of Classical Mechanics* (Nauka, Moscow, 1978; Springer-Verlag, New York, 1989).
21. B. A. Dubrovin, S. P. Novikov, and F. T. Fomenko, *Modern Geometry* (Nauka, Moscow, 1979).
22. A. M. Ignatov, J. Moscow Phys. Soc. **2**, 137 (1992).
23. D. E. Potter, *Computational Physics* (Wiley, New York, 1973; Mir, Moscow, 1975).
24. P. J. Morrison and D. Pfirsch, Phys. Fluids B **4**, 3038 (1992).
25. P. J. Morrison, Phys. Plasmas **1**, 1447 (1994).
26. A. M. Ignatov, Comm. Plasma Phys. Control. Fusion **12**, 205 (1989).

Translated by the author

Plasma Physics Reports, Vol. 30, No. 1, 2004, pp. 56–61. Translated from Fizika Plazmy, Vol. 30, No. 1, 2004, pp. 60–65.

PLASMA OSCILLATIONS AND WAVES

Amplification of Surface Waves in a Plasma Waveguide by a Straight Relativistic Electron Beam in a Finite Magnetic Field

I. N. Kartashov, M. V. Kuzelev, and A. A. Rukhadze

Prokhorov Institute of General Physics, Russian Academy of Sciences, ul. Vavilova 38, Moscow, 119991 Russia

Received May 12, 2003

Abstract—The problem of the excitation of electron waves in a thin-walled annular cold plasma in a cylindrical waveguide by a straight relativistic electron beam in a finite magnetic field is considered. The dispersion properties of a waveguide system with parameters close to the experimental ones are investigated. It is shown that the growth rate of the excited high-frequency plasma wave is comparable to that of the low-frequency wave, which is weakly sensitive to the strength of the longitudinal magnetic field. *© 2004 MAIK "Nauka/Interperiodica".*

In recent years, the excitation of surface plasma waves in beam–plasma systems has been actively studied both experimentally and theoretically [1–3]. In its simplest form, such a system is a circular metal waveguide of radius R in which there are a thin-walled annular plasma and a thin-walled annular beam with mean radii r_p and r_b, respectively. The thicknesses of the plasma and the beam, δ_p and δ_b, are much smaller than their radii. The system is usually placed in an external uniform longitudinal magnetic field in which the beam and plasma electrons become fully magnetized. The applicability condition of the corresponding approximation, in which the external magnetic field is assumed to be infinitely strong, is that the characteristic frequencies of the system (the radiation frequency and the electron Langmuir frequencies of the plasma and the beam, ω_p and ω_b) are low in comparison to the electron cyclotron frequency Ω_e. In actual experiments, the beam density is much lower than the plasma density, so that the condition for the beam electrons to be fully magnetized is, as a rule, satisfied with good accuracy. As for the plasma electrons, the corresponding condition is more stringent, especially in the range of short wavelengths.

An annular plasma of finite thickness is difficult to describe analytically even in the cold plasma approximation, because it is a system with an infinite number of degrees of freedom [4]. Under the assumptions that the plasma thickness is small and that the external magnetic field is infinitely strong, an annular plasma can be described as a tube with an infinitely thin wall, in which only one surface wave can propagate in the chosen direction. These assumptions make the system simple enough to be described analytically. For an external magnetic field of finite strength, the infinitely thin plasma approximation fails to hold because of the possible transverse plasma polarization.

In order to describe the surface waves of a thin-walled annular plasma in a longitudinal magnetic field of finite strength, one of us [5] proposed approximate boundary conditions at the plasma tube and showed that they can be successfully used in the theory of plasma microwave electronics. In the present paper, following [5], we derive a dispersion relation for a beam–plasma system in a longitudinal magnetic field of finite strength and determine the instability growth rate as a function of the system parameters.

In waveguide regions free of plasma, the electromagnetic field is described by the following set of equations for the longitudinal components of the electric and magnetic fields, $E_z, B_z \sim e^{-i\omega t + ik_z z}$:

$$\begin{aligned} \Delta_\perp E_z - \chi_0^2 E_z &= 0, \\ \Delta_\perp B_z - \chi_0^2 B_z &= 0. \end{aligned} \tag{1}$$

These equations, which describe azimuthally symmetric modes, are written in cylindrical coordinates with the Laplace operator $\Delta_\perp = \frac{1}{r}\frac{d}{dr}r\frac{d}{dr}$ and $\chi_0^2 = k_z^2 - \omega^2/c^2$ and are supplemented by the boundary conditions $E_z(R) = 0$ and $E_\varphi(R) \sim B_z(R) = 0$ at the metal waveguide surface and the conditions for the field to be finite at $r = 0$. If there is a plasma tube with the mean radius $r = r_p$ and thickness δ_p, then the corresponding equations should be written for the plasma region and the solutions obtained should be matched at the inner and outer boundaries of the plasma tube [6, 7]. In what follows, we will assume that the plasma tube is sufficiently thin, $k_z\delta_p \ll 1$.

1063-780X/04/3001-0056$26.00 © 2004 MAIK "Nauka/Interperiodica"

In the general case of a cold thin-walled annular plasma, there are two dispersion curves that describe surface waves: low-frequency and high-frequency (in the range $\omega < k_z c$) [4–6]. For strong magnetic fields such that $\Omega_e > \omega_p$, the low-frequency dispersion curve is analogous to that in the case of a fully magnetized plasma and, in the short-wavelength limit $k_z \longrightarrow \infty$, it asymptotically approaches ω_p. For large k_z values, the high-frequency branch of the dispersion curve is characterized by an anomalous dispersion and approaches the frequency Ω_e from above. The cutoff frequency of the high-frequency wave, ω ($k_z = 0$), is determined by the frequency ω_p and is independent of Ω_e. The highest frequency of this wave does not exceed the upper hybrid frequency $\Omega_h = \sqrt{\omega_p^2 + \Omega_e^2}$. In a weak magnetic field such that $\Omega_e < \omega_p$, the low-frequency dispersion curve in the short-wavelength limit approaches the frequency $\Omega_h/\sqrt{2}$ from below, while, in the same limit, the dispersion curve of the high-frequency wave approaches this frequency from above, indicating that the dispersion of the high-frequency wave is anomalous.

Based on an analysis of transverse structures of the electromagnetic field components, one of us [5] formulated approximate conditions at the plasma tube. With these boundary conditions, which differ between the low- and high-frequency waves, there is no need to solve the wave equation in the plasma region: the solution sought is derived by matching the solutions obtained for vacuum regions. Also, there is no need to distinguish between the cases of a weak and a strong longitudinal magnetic field. For the low-frequency branch, the matching conditions have the form

$$\{E_z(r_p)\} = 0,$$
$$\left\{\frac{dE_z}{dr}(r_p)\right\} = -\delta_p \chi_0^2 \frac{\omega_p^2}{\omega^2} E_z(r_p). \quad (2)$$

Here and below, we use the definition $\{X(x)\} = X(x+0) - X(x-0)$. Conditions (2) coincide with the exact matching conditions obtained in the limit of an infinitely strong magnetic field by integrating the wave equation over r in the vicinity of a plasma with a density profile such that $\omega_p^2 \longrightarrow \delta_p \omega_p^2 \delta(r - r_p)$ [8]. Consequently, the low-frequency branch is weakly sensitive to the strength of the external magnetic field. We can readily see that Eqs. (1) with boundary conditions (2) allow the wave field to be separated into **E** and **B** waves. The waves that are important for the purposes of plasma microwave electronics are those with a nonzero longitudinal electric-field component E_z (the **E** waves) and with phase velocities below the speed of light, $\omega/k_z < c$ [4, 8]. For such waves, the solution to Eqs. (1) supplemented with boundary conditions at $r = 0$ and $r = R$ has the form

$$E_z = \begin{cases} AI_0(\chi_0 r), & r < r_p, \\ B\left[I_0(\chi_0 r) - K_0(\chi_0 r)\dfrac{I_0(\chi_0 R)}{K_0(\chi_0 R)}\right], & r_p < r < R, \end{cases} \quad (3)$$

where I_0 and K_0 are zero-order modified Bessel functions. Substituting solution (3) into boundary conditions (2) and eliminating the constants A and B, we arrive at the following dispersion relation, which determines the dependence $\omega(k_z)$ at the lower branch of the dispersion curve:

$$r_p \delta_p \chi_0^2 \frac{\omega_p^2}{\omega^2} I_0^2(\chi_0 r_p)\left[\frac{K_0(\chi_0 r_p)}{I_0(\chi_0 r_p)} - \frac{K_0(\chi_0 R)}{I_0(\chi_0 R)}\right] = 1. \quad (4)$$

Dispersion relation (4) coincides with that for a plasma wave in an infinitely strong magnetic field. This reflects a fact that has already been mentioned, namely, that the low-frequency branch is weakly sensitive to the strength of the external magnetic field [5].

Unlike in the previous case, the high-frequency wave field cannot be separated into **E** and **B** waves. The matching conditions for the high-frequency branch are written in the form [5]

$$\left\{\frac{dE_z}{dr}(r_p)\right\} = 0, \quad \left\{\frac{dB_z}{dr}(r_p)\right\} = 0,$$
$$\{E_z(r_p)\} = \delta_p \frac{\chi^2}{\chi_0^2 \varepsilon_\perp}\frac{dE_z}{dr}(r_p) + ik_z \delta_p \frac{\omega}{c}\frac{g}{\chi_0^2 \varepsilon_\perp}\frac{dB_z}{dr}(r_p), \quad (5)$$
$$\{B_z(r_p)\} = \delta_p \frac{1}{\chi_0^2}\left(\chi^2 + \frac{g^2}{\varepsilon_\perp}\frac{\omega^2}{c^2}\right)\frac{dB_z}{dr}(r_p)$$
$$- ik_z \delta_p \frac{\omega}{c}\frac{g}{\chi_0^2 \varepsilon_\perp}\frac{dE_z}{dr}(r_p).$$

Here, $\chi^2 = k_z^2 - \varepsilon_\perp \omega^2/c^2$ and $\varepsilon_\perp$ and g are the elements of the dielectric tensor of a cold magnetized plasma [9],

$$\varepsilon_{ij} = \begin{pmatrix} \varepsilon_\perp & ig & 0 \\ -ig & \varepsilon_\perp & 0 \\ 0 & 0 & \varepsilon_\parallel \end{pmatrix}, \quad (6)$$

where

$$\varepsilon_\perp = 1 - \frac{\omega_p^2}{\omega^2 - \Omega_e^2}, \quad g = -\frac{\omega_p^2 \Omega_e}{\omega(\omega^2 - \Omega_e^2)},$$
$$\varepsilon_\parallel = 1 - \frac{\omega_p^2}{\omega^2}. \quad (7)$$

We insert solution (3) to the first of Eqs. (1) and the solution

$$B_z = \begin{cases} CI_0(\chi_0 r), & r < r_p \\ D\left[I_0(\chi_0 r) + K_0(\chi_0 r)\dfrac{I_1(\chi_0 R)}{K_1(\chi_0 R)}\right], & r_p < r < R, \end{cases} \quad (8)$$

to the second of the equations into the conditions relating the fields at the inner and outer surfaces of the plasma tube. As a result, we obtain a dispersion relation for the high-frequency wave:

$$\left[1 + \delta_p r_p \frac{\chi^2}{\varepsilon_\perp} G_E\right]\left[1 + \delta_p r_p \left(\chi^2 + \frac{g^2}{\varepsilon_\perp}\frac{\omega^2}{c^2}\right) G_B\right] = k_z^2 \delta_p^2 r_p^2 \frac{\omega^2}{c^2}\frac{g^2}{\varepsilon_\perp^2} G_E G_B. \quad (9)$$

Here, we have introduced the following notation for the geometric factors:

$$G_E = I_1^2(\chi_0 r_p)\left[\frac{K_1(\chi_0 r_p)}{I_1(\chi_0 r_p)} + \frac{K_0(\chi_0 R)}{I_0(\chi_0 R)}\right],$$
$$G_B = I_1^2(\chi_0 r_p)\left[\frac{K_1(\chi_0 r_p)}{I_1(\chi_0 r_p)} - \frac{K_1(\chi_0 R)}{I_1(\chi_0 R)}\right]. \quad (10)$$

The right-hand side of dispersion relation (9) is quadratic in the small parameter $k_z\delta_p \ll 1$ of a system with a thin-walled annular plasma. Consequently, to second order in this parameter, the dispersion relation for the high-frequency wave has the form [5]

$$1 + \delta_p r_p \frac{\chi^2}{\varepsilon_\perp} G_E = 0. \quad (11)$$

We now consider a plasma waveguide system with a beam that will be treated under the same assumptions as those which were made for the plasma. Specifically, we consider an annular thin-walled beam with thickness δ_b and mean radius $r_b < r_p$. In experiments [2, 3], the beam density is usually low enough for the beam electrons to be regarded as being fully magnetized and for their transverse motion to be ignored, in which case the beam can be assumed to be infinitely thin. In this approximation, the beam is described solely through the boundary conditions for matching the fields in the regions $r < r_b$ and $r > r_b$. These boundary conditions are well known [4, 8]:

$$\{E_z(r_b)\} = 0, \quad \left\{\frac{dE_z}{dr}(r_b)\right\} = -\delta_b \chi_0^2 \frac{\omega_b^2 \gamma^{-3}}{(\omega - k_z u)^2} E_z(r_b),$$
$$\{B_z(r_b)\} = 0, \quad \left\{\frac{dB_z}{dr}(r_b)\right\} = 0, \quad (12)$$

where $\gamma = (1 - u^2/c^2)^{-1/2}$ and u is the beam velocity. In describing the excitation of the low-frequency wave, it is sufficient to use only the first two of conditions (12), because this wave is essentially an E wave [5]. The plasma and beam divide the cylindrical waveguide into three regions, in which the equations for an E wave have the solutions

$$E_z = \begin{cases} AI_0(\chi_0 r), & r < r_b, \\ BI_0(\chi_0 r) + CK_0(\chi_0 r), & r_b < r < r_p, \\ DI_0(\chi_0 r) + EK_0(\chi_0 r), & r_p < r < R. \end{cases} \quad (13)$$

Using matching conditions (12) and (2) at the beam and plasma, respectively, and the condition that the field component E_z vanishes at the metal waveguide wall and eliminating the arbitrary constants, we arrive at a dispersion relation describing the excitation of the low-frequency wave by the beam:

$$\left[1 - \delta_p r_p \chi_0^2 \frac{\omega_p^2}{\omega^2} G_p\right]\left[1 - \delta_b r_b \chi_0^2 \frac{\omega_b^2 \gamma^{-3}}{(\omega - k_z u)^2} G_b\right] = \delta_p r_p \delta_b r_b \chi_0^4 \frac{\omega_p^2}{\omega^2}\frac{\omega_b^2 \gamma^{-3}}{(\omega - k_z u)^2}\frac{I_0^2(\chi_0 r_b)}{I_0^2(\chi_0 r_p)} G_p^2, \quad (14)$$

where the geometric factors of the beam and the plasma have the form

$$G_{p,b} = I_0^2(\chi_0 r_{p,b})\left[\frac{K_0(\chi_0 r_{p,b})}{I_0(\chi_0 r_{p,b})} - \frac{K_0(\chi_0 R)}{I_0(\chi_0 R)}\right]. \quad (15)$$

In order to derive the dispersion relation for the high-frequency wave, we substitute expressions (13) for E_z and the analogous expressions for B_z into conditions (5) and (12) and the boundary conditions at the metal waveguide wall. Then, after some laborious manipulations, we obtain

$$\left[1 + \delta_p r_p \frac{\chi^2}{\varepsilon_\perp} G_E\right]\left[1 - \delta_b r_b \chi_0^2 \frac{\omega_b^2 \gamma^{-3}}{(\omega - k_z u)^2} G_b\right] = \delta_p r_p \frac{\chi^2}{\varepsilon_\perp} \delta_b r_b \chi_0^2 \frac{\omega_b^2 \gamma^{-3}}{(\omega - k_z u)^2}\frac{I_0^2(\chi_0 r_b)}{I_0^2(\chi_0 r_p)} G_E^2. \quad (16)$$

We convert Eqs. (14) and (16) into a form more convenient for our analysis:

$$(\omega^2 - \Omega_{p\downarrow}^2)((\omega - k_z u)^2 - \Omega_b^2) = \Theta_\downarrow \Omega_{p\downarrow}^2 \Omega_b^2$$
for a low-frequency wave and
$$(\omega^2 - \Omega_h^2 + \Omega_{p\uparrow}^2)((\omega - k_z u)^2 - \Omega_b^2) = \Theta_\uparrow \Omega_{p\uparrow}^2 \Omega_b^2 \quad (17)$$
for a high-frequency wave.

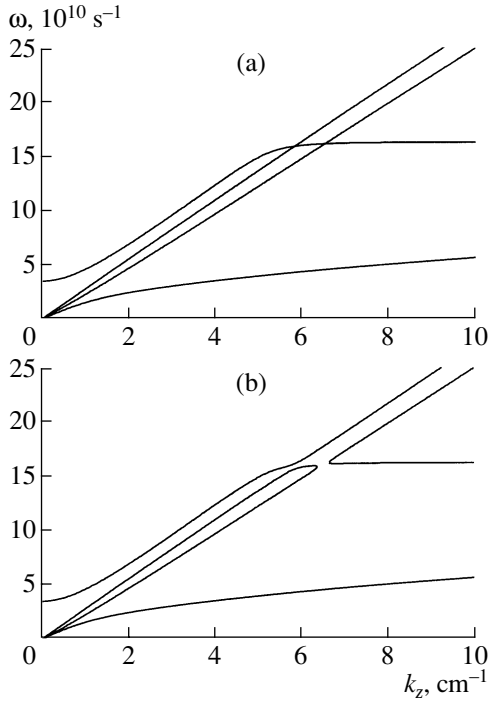

Fig. 1. Dispersion curves of a beam–plasma system ($\omega_p = 8 \times 10^{10}$ s^{-1}, $\Omega_e = 15 \times 10^{10}$ s^{-1}) in a strong magnetic field (a) without and (b) with allowance for the beam–plasma interaction.

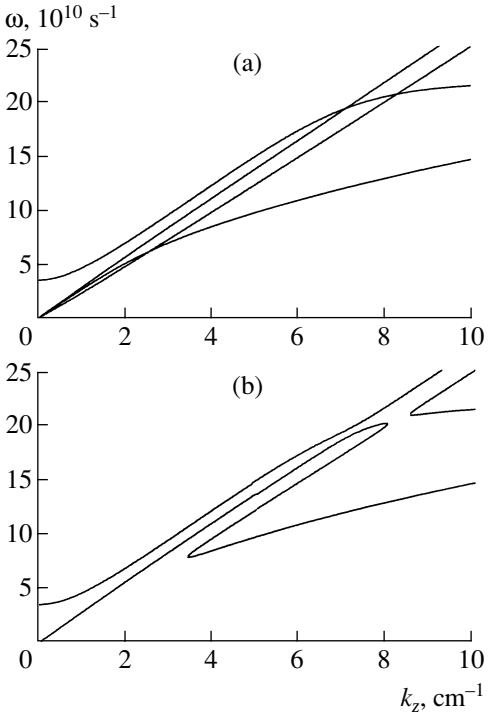

Fig. 2. Dispersion curves of a beam–plasma system ($\omega_p = 22 \times 10^{10}$ s^{-1}, $\Omega_e = 15 \times 10^{10}$ s^{-1}) in a weak magnetic field (a) without and (b) with allowance for the beam–plasma interaction.

Here, we have introduced the notation

$$\Omega_{p\downarrow}^2 = \delta_p r_p \chi_0^2 \omega_p^2 G_p, \quad \Omega_{p\uparrow}^2 = \delta_p r_p \chi^2 (\omega^2 - \Omega_e^2) G_E,$$
$$\Omega_b^2 = \delta_b r_b \chi_0^2 \omega_b^2 \gamma^{-3} G_b,$$
$$\Theta_\downarrow = \frac{\dfrac{K_0(\chi_0 r_p)}{I_0(\chi_0 r_p)} - \dfrac{K_0(\chi_0 R)}{I_0(\chi_0 R)}}{\dfrac{K_0(\chi_0 r_b)}{I_0(\chi_0 r_b)} - \dfrac{K_0(\chi_0 R)}{I_0(\chi_0 R)}}, \qquad (18)$$
$$\Theta_\uparrow = \frac{\dfrac{K_1(\chi_0 r_p)}{I_1(\chi_0 r_p)} + \dfrac{K_0(\chi_0 R)}{I_0(\chi_0 R)}}{\dfrac{K_0(\chi_0 r_b)}{I_0(\chi_0 r_b)} - \dfrac{K_0(\chi_0 R)}{I_0(\chi_0 R)}}.$$

Each of Eqs. (17) describes a system of two coupled oscillators. If we formally set the coupling coefficients $\Theta_\downarrow$ and $\Theta_\uparrow$ equal to zero, then we can see that the oscillators in each of the systems are decoupled and can be described by independent equations. In the absence of a beam, the dispersion relations take the form

$$\omega^2 - \Omega_{p\downarrow}^2 = 0$$
for a low-frequency wave and
$$\omega^2 - \Omega_h^2 + \Omega_{p\uparrow}^2 = 0 \qquad (19)$$
for a high-frequency wave.

These relations implicitly describe the dispersion properties of a plasma waveguide in a magnetic field of finite strength.

The dispersion relations obtained were analyzed numerically for the parameters of a beam–plasma system that were close to those adopted in actual experiments [2, 3]: the waveguide radius was $R = 2$ cm; the mean radii of the plasma and beam tubes were $r_p = 1.05$ cm and $r_b = 0.65$ cm, respectively; the thicknesses of the plasma and beam were $\delta_p = \delta_b = 0.1$ cm, the beam current was $i_b = 1.7$ kA, and the beam velocity corresponded to the relativistic factor $\gamma = 2$. The cyclotron frequency was taken to be $\Omega_e = 15 \times 10^{10}$ s^{-1}, and the plasma frequency was varied within the interval $\omega_p = (8–22) \times 10^{10}$ s^{-1}. Figures 1a and 2a show the dispersion curves obtained by numerically solving dispersion relations (19) for a plasma waveguide in a longitudinal magnetic field of finite strength at $\omega_p = 8 \times 10^{10}$ s^{-1} and 22×10^{10} s^{-1}, respectively. These figures also show two dispersion curves calculated for a plasma waveguide with a beam. The dispersion curve in Fig. 1a differs from a traditional dispersion curve in the limit of an infinitely strong longitudinal magnetic field in that it has an upper branch. For large k_z values, this branch is characterized by an anomalous dispersion; however, for the above parameter values, its existence is incompatible with the above assumption that the plasma tube is thin-walled. As the magnetic field increases, the upper

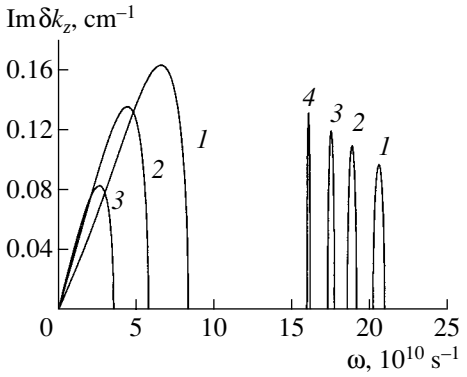

Fig. 3. Frequency dependence of the spatial growth rate for ω_p = (*1*) 22×10^{10}, (*2*) 17×10^{10}, (*3*) 13×10^{10}, and (*4*) 8×10^{10} s^{-1}.

branch is displaced toward higher frequencies. In the case at hand, the parameter values are chosen so that the low-frequency plasma wave does not resonate with the beam and the high-frequency plasma wave is excited at a frequency of $\omega \approx 16.1 \times 10^{10}$ s^{-1} ($k_z \approx 6.5$ cm^{-1}). Figure 2a refers to a waveguide in a weak magnetic field ($\Omega_e < \omega_p$). We can see that there are two points of resonant interaction: the point $\omega \approx 6.2 \times 10^{10}$ s^{-1}, $k_z \approx 2.6$ cm^{-1} and the point $\omega \approx 20.6 \times 10^{10}$ s^{-1}, $k_z \approx 8.3$ cm^{-1}, which are the intersections of the lower branch of the beam dispersion curve with the plasma dispersion curves. Figures 1b and 2b show the solutions to Eqs. (17), i.e., the dispersion curves calculated with allowance for the interaction between the beam waves and the plasma waves. In a strong magnetic field (Fig. 1b), there is only one instability region, which is fairly narrow and is associated with the excitation of the high-frequency mode of the plasma waves. In Fig. 2b, Cherenkov resonance conditions for both high-frequency and low-frequency waves are satisfied in two instability regions. From these figures we can see that all the instabilities under consideration are of a convective nature [10].

In order to determine the amplification coefficients δk_z of the waves (i.e., their spatial growth rates), we represent the wavenumber in the form $k_z = \omega/u + \delta k_z$. For a low-density beam, we have $\delta k_z \ll \omega/u$. We substitute the representation adopted for k_z into Eqs. (17), expand every term in the resulting equations in powers of δk_z, and retain only the lowest order (nonvanishing) terms in the expansions to obtain the following two cubic equations, which determine the spatial growth rates of each of the plasma waves:

$$\left(\omega^2 - \Omega_{p\downarrow}^2\left(\frac{\omega}{u}\right) - \frac{\partial \Omega_{p\downarrow}^2}{\partial k_z}\delta k_z\right)$$

$$\times\left(u^2\delta k_z^2 - \Omega_b^2\left(\frac{\omega}{u}\right) - \frac{\partial \Omega_b^2}{\partial k_z}\delta k_z\right)$$

$$= \Theta_\downarrow\left(\frac{\omega}{u}\right)\Omega_{p\downarrow}^2\left(\frac{\omega}{u}\right)\Omega_b^2\left(\frac{\omega}{u}\right) + \frac{\partial \Theta_\downarrow \Omega_{p\downarrow}^2 \Omega_b^2}{\partial k_z}\delta k_z$$

for a low-frequency wave and

$$\left(\omega^2 - \Omega_h^2 + \Omega_{p\uparrow}^2 + \frac{\partial \Omega_{p\uparrow}^2}{\partial k_z}\delta k_z\right) \quad (20)$$

$$\times\left(u^2\delta k_z^2 - \Omega_b^2\left(\frac{\omega}{u}\right) - \frac{\partial \Omega_b^2}{\partial k_z}\delta k_z\right)$$

$$= \Theta_\uparrow\left(\frac{\omega}{u}\right)\Omega_{p\uparrow}^2\left(\frac{\omega}{u}\right)\Omega_b^2\left(\frac{\omega}{u}\right) + \frac{\partial \Theta_\uparrow \Omega_{p\uparrow}^2 \Omega_b^2}{\partial k_z}\delta k_z$$

for a high-frequency wave.

Figure 3 shows the dependence of the growth rate $\mathrm{Im}\,\delta k_z$ on the frequency ω for the following values of the plasma frequency: ω_p = (*1*) 22×10^{10}, (*2*) 17×10^{10}, (*3*) 13×10^{10}, and (*4*) 8×10^{10} s^{-1}. As the plasma frequency decreases, the low-frequency plasma branch is displaced toward lower frequencies and, accordingly, the Cherenkov resonance frequency and the maximum growth rate both decrease. Below a certain critical frequency, there is no Cherenkov interaction at the lower branch and the spatial growth rate vanishes. For a high-frequency branch too, the instability region is displaced toward lower frequencies and narrows as the plasma density decreases. In this case, however, the spatial growth rate increases to about $\delta k_z \approx 0.12$ cm^{-1}, which is comparable to the growth rate in the range of low frequencies.

In this paper, we have investigated the dispersion properties of a beam–plasma waveguide system with typical experimental parameters in a longitudinal magnetic field of finite strength. We have determined how the spatial growth rates of the instability depend on the system parameters. We have shown that the amplification of high-frequency plasma waves in the linear stage is comparable to or may be even greater than the amplification of low-frequency waves, with which plasma microwave electronics is usually concerned.

ACKNOWLEDGMENTS

This work was supported in part by the Ministry of Education of the Russian Federation (project no. E02-3.2-447); the Russian Foundation for Basic Research (project no. 01-02-17265); and the Ministry of Industry, Science, and Technologies of the Russian Federation under the Program for Government Support of Leading Scientific Schools (project no. 1962.2003.2).

REFERENCES

1. M. V. Kuzelev and A. A. Rukhadze, Fiz. Plazmy **26**, 231 (2000) [Plasma Phys. Rep. **26**, 231 (2000)].

2. I. L. Bogdankevich, I. E. Ivanov, O. T. Loza, *et al.*, Fiz. Plazmy **28**, 748 (2002) [Plasma Phys. Rep. **28**, 690 (2002)].

3. P. S. Strelkov and D. K. Ul'yanov, Fiz. Plazmy **26**, 329 (2000) [Plasma Phys. Rep. **26**, 303 (2000)].

4. M. V. Kuzelev, A. A. Rukhadze, and P. S. Strelkov, *Plasma Relativistic Microwave Electronics* (Mosk. Gos. Tekhn. Univ. im. N. É. Baumana, Moscow, 2002).

5. M. V. Kuzelev, Fiz. Plazmy **28**, 544 (2002) [Plasma Phys. Rep. **28**, 501 (2002)].

6. M. V. Kuzelev, R. V. Romanov, I. A. Selivanov, *et al.*, Tr. Inst. Obshch. Fiz. Ross. Akad. Nauk **45**, 17 (1994).

7. M. V. Kuzelev, R. V. Romanov, and A. A. Rukhadze, Prikl. Fiz., No. 2, 100 (2001); No. 3, 103 (2001).

8. M. V. Kuzelev and A. A. Rukhadze, *Electrodynamics of Dense Electron Beams in Plasma* (Nauka, Moscow, 1990).

9. A. F. Aleksandrov, L. S. Bogdankevich, and A. A. Rukhadze, *Principles of Plasma Electrodynamics* (Vysshaya Shkola, Moscow, 1988; Springer-Verlag, Berlin, 1984).

10. *Plasma Electrodynamics*, Ed. by A. I. Akhiezer *et al.* (Nauka, Moscow, 1974; Pergamon, Oxford, 1975).

Translated by I.A. Kalabalyk

Plasma Physics Reports, Vol. 30, No. 1, 2004, pp. 62–68. Translated from Fizika Plazmy, Vol. 30, No. 1, 2004, pp. 66–72.

PLASMA ELECTRONICS

A 50-MW Broadband Plasma Microwave Amplifier

A. V. Ponomarev and P. S. Strelkov

Prokhorov Institute of General Physics, Russian Academy of Sciences, ul. Vavilova 38, Moscow, 119991 Russia

Received July 23, 2003

Abstract—A pure amplification regime (without accompanying generation) at two frequencies of 9.1 and 13 GHz is achieved in a plasma relativistic microwave amplifier. It is shown experimentally that an amplification regime with an output power of 40 MW can be achieved at both frequencies without changing the parameters of the system. This fact, along with the results of calculations, allows one to assert that the relative bandwidth of the amplifier is no less than 40%. It is shown experimentally that, by changing only one parameter, namely, the plasma density, the frequency corresponding to the maximum amplification can be varied from 9.1 to 13 GHz, which agrees with the results of calculations by a nonlinear model. At a frequency of 9.1 GHz, the maximum output power amounts to P = 40 MW, the efficiency is η = 4%, and the power gain is K_p = 800 (29 dB). At a frequency of 13 GHz, these parameters are P = 60 MW, η = 6%, and K_p = 1000 (30 dB). The measured plasma density range in which the amplification is observed agrees with calculations of the excitation of an E_{01} mode of a plasma waveguide. © *2004 MAIK "Nauka/Interperiodica".*

1. INTRODUCTION

One promising line of research on the creation of high-power microwave devices are the studies of the Cherenkov excitation of eigenmodes of a plasma waveguide by a high-current relativistic electron beam (REB). The plasma waveguide is a smooth cylindrical metal waveguide that is completely or partially filled with plasma. In the absence of plasma, the electron beam is stable because only fast modes with a phase velocity higher than the speed of light can exist in a metal tube with a constant radius. If a metal waveguide is filled with plasma, slow waves exist whose phase velocities are below the speed of light and depend on the plasma density. If the plasma density exceeds the threshold density at which the phase velocity of a slow wave becomes equal to the REB velocity, then the REB energy can be transferred to the electromagnetic wave, i.e., the wave is amplified [1].

The main advantage of plasma relativistic microwave devices over vacuum ones is that the frequency of output radiation can be tuned over a wide range by varying the plasma density. Figure 1 shows the calculated frequency dependence of the gain factor calculated by the linear theory at different plasma densities. The curves were calculated for the same geometry of an REB and plasma as was used in the experiment described in this paper. It can be seen from the figure that, as the plasma density increases from 10^{13} to 7×10^{13} cm^{-3}, the frequency at which the gain factor is maximum increases from 8 to 35 GHz. At the same time, the spectral width varies from 40% at low frequencies to 20% at high frequencies.

This conclusion is valid for both microwave amplifiers and noise masers. Experimental results were first obtained for masers. The first successful experiment in which microwaves were generated via the excitation of the eigenmodes of a plasma waveguide by an REB [2] demonstrated the main features of a plasma relativistic maser: a wide (~40%) emission band and the possibility of a twofold variation in the mean generation frequency. Later, a high-power (~250 MW) maser in which the frequency could be varied by a factor of more than 2 [3] and a maser in which the frequency could be tuned in the range 4–28 GHz at a power level of 30–50 MW [4] were created. In both cases, the relative width of the emission spectrum was no less than 20%. Around that time, the studies on the creation of plasma relativistic microwave amplifiers were started; however, the first successful results were obtained some what later, because the problem of the suppression of microwave generation accompanying the amplification turned out to be fairly complicated.

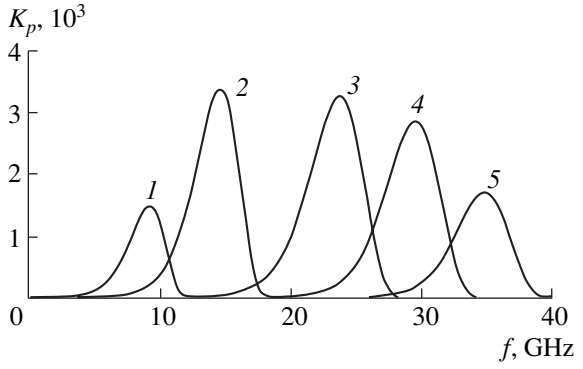

Fig. 1. Frequency dependences of the power gain calculated by the linear theory for an interaction length of 20 cm at different values of the plasma density: n_p = (*1*) 10^{13}, (*2*) 2×10^{13}, (*3*) 4×10^{13}, (*4*) 5.5×10^{13}, and (*5*) 7×10^{13} cm^{-3}.

1063-780X/04/3001-0062$26.00 © 2004 MAIK "Nauka/Interperiodica"

The experiment in [5] demonstrated the possibility of amplifying the input signal in a narrow interval of plasma densities near the threshold density. The amplification regime was rather unstable and was accompanied by generation at frequencies different from the input signal frequency. The use of a broadband absorber made it possible to improve the amplifier parameters [6]. In that experiment, the possibility of amplifying the input signal at both 9.1 and 12.9 GHz was demonstrated for the first time. Furthermore, there was a range of plasma densities within which the output radiation lay inside the 0.5-GHz band at an input frequency of 9.1 GHz. At the same time, there was generation at other plasma densities, which resulted in the broadening of the output spectrum. For the same reason, attempts to achieve stable amplification at an input frequency of 12.9 GHz did not met with success. A further modification of the experimental device, as well as the use of other types of microwave absorbers, made it possible to suppress generation over a wide range of plasma densities. As a result, it became possible to measure the main characteristics of the amplifier and optimize the system in terms of maximizing the output power. The results of this study are presented in the present paper.

We note that, at present, studies on high-power microwave amplifiers based on the effect of the slowing-down of waves in a vacuum (without plasma filling) corrugated waveguide are being carried out. Thus, in [7], an output power of 1 GW at a frequency of 9 GHz was achieved; however, the amplification bandwidth was lower than 1%. In [8], the amplification bandwidth was 20% (8.4–10.4 GHz), but the output power was as low as 1 MW. The microwave amplifier described in the present paper has an output power of ~50 MW and its amplification bandwidth attains 40% (9–13 GHz); i.e., it possesses a unique combination of parameters.

2. EXPERIMENTAL DEVICE

A schematic of the device is shown in Fig. 2. Annular plasma *1* with a mean radius of 8 mm and a thickness of 1 mm was created in smooth cylindrical waveguide *2* of radius 22 mm. The plasma was produced by an annular electron beam (with an electron energy of 600 eV and a current of 5–20 A) in xenon at a pressure of 2.5×10^{-4} torr over a time of about 30 μs [9]. The system was embedded in a strong uniform longitudinal magnetic field **B**. Annular REB *3* with a mean radius of 10 mm, a thickness of 1 mm, and an electron energy of 500 keV was injected into the system from a diode located on the left (not shown in the figure). The FWHM duration of the voltage pulse at the diode could be varied over a range of up to 120 ns. The REB current could also be varied. These experiments were carried out at currents of $I = 1$ and 2 kA. Microwave converter *4*, which converted the TE_{01} mode of a rectangular waveguide onto the TEM mode of the input coaxial waveguide, was placed at the entrance to the system.

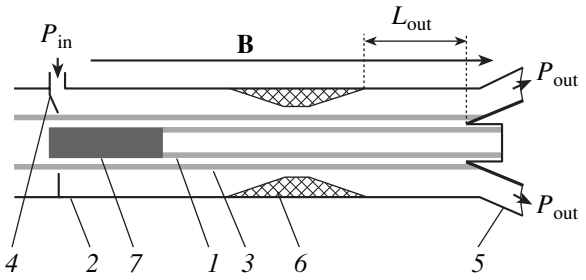

Fig. 2. Schematic of the relativistic microwave amplifier: (*1*) plasma, (*2*) metal waveguide, (*3*) REB, (*4*) amplifier input, (*5*) coaxial emitting horn, (*6*) microwave absorber, and (*7*) central conductor of the input coaxial waveguide.

The TEM wave was then converted into a slow plasma wave, amplified by the REB, and emitted by coaxial horn *5* with an inner diameter of 10 cm and outer diameter of 25 cm. To suppress microwave generation in the system, we used ceramic microwave absorber *6* of length 14 cm. The length L_{out} of the output part of the amplifier could be varied (Fig. 2). The maximum REB–plasma interaction length was 30 cm.

An input microwave signal with a duration on the order of several microseconds was generated by one of the two pulsed magnetrons operating at frequencies of 9.1 and 13.0 GHz. The output magnetron power could be varied within the range 20–60 kW by varying the magnetron anode voltage.

3. MEASUREMENT TECHNIQUE

Experiments of [4] showed that, in the case of microwave generation, the width of the output radiation spectrum was 20–40% of the mean frequency. In [10], it was shown that, in some time intervals, the spectrum of the generated microwave pulse was rather narrow ($\Delta f/f < 5\%$); however, the spectrum of the entire pulse was always wider than 20%. In the case of the amplification of a narrowband input signal, the output radiation should also be narrowband throughout the entire microwave pulse. In addition, the maser frequency depends on the plasma density, whereas the output frequency of a microwave amplifier is only determined by the frequency of the input signal and is independent of the plasma density within a wide density range. Hence, by measuring the spectral width of the output radiation, it is possible to distinguish the regimes of amplification and generation. To estimate the spectral width of the output radiation, we used a receiving transmission line consisting of two detectors and a narrowband filter (Fig. 3). One of the detectors (a broadband receiver) measured the total incident microwave power. At the input of the other detector (a narrowband receiver), we placed a narrowband filter ($\Delta f/f = 5\%$) that was tuned to the frequency of the input signal. The sensitivities of the detectors were chosen such that, in the case of a narrowband (<5%) signal at the input to the receiving line,

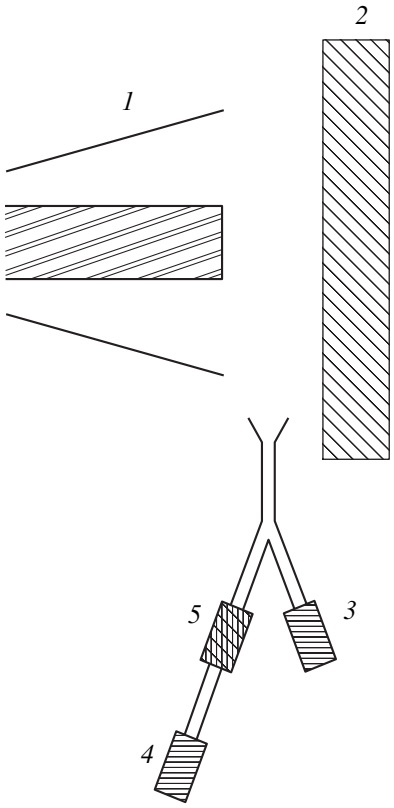

Fig. 3. Scheme of measurements: (*1*) coaxial emitting horn, (*2*) microwave calorimeter, (*3*, *4*) microwave detectors, and (*5*) narrowband microwave filter ($\Delta f/f = 5\%$).

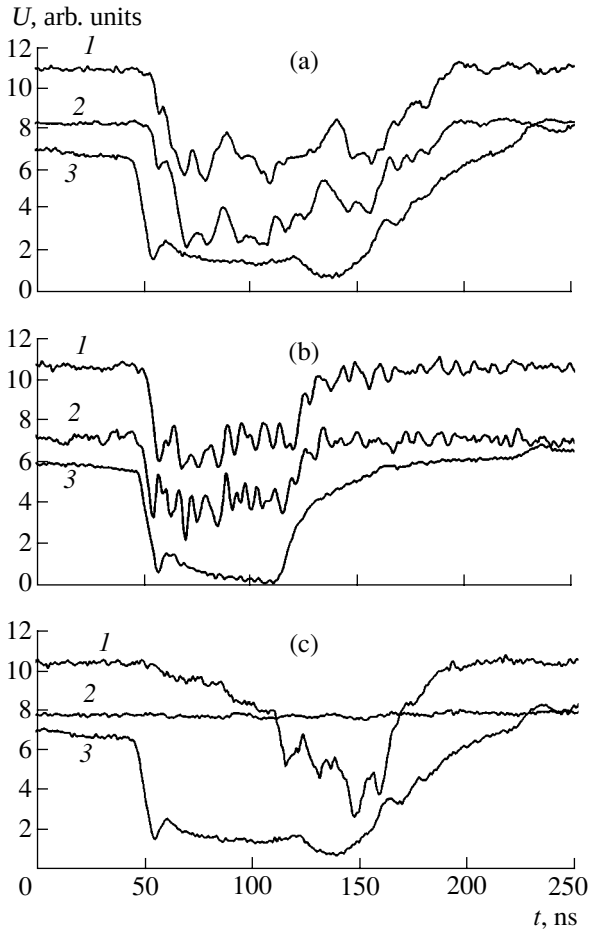

Fig. 4. Waveforms of the broadband (curves *1*) and narrowband (curves *2*) receiver signals and the diode voltage pulse (curve *3*) at input frequencies of (a) 9.1 and (b) 13.GHz and (c) in the absence of an input signal.

the signals from both detectors were identical in shape and amplitude. If the width of the radiation spectrum exceeded 5%, then the amplitude of the signal from the narrowband receiver was smaller than that from the broadband receiver. Thus, we could estimate the width of the spectrum of the output microwave radiation.

The total energy of the output microwave pulse was measured by a broadband large-area (30 cm in diameter) microwave calorimeter [11] (see Fig. 3). Knowing the energy of the microwave pulse and its envelope, we could calculate the power of the output microwave radiation.

4. EXPERIMENTAL RESULTS

The operation of the measuring system is illustrated by Fig. 4, which shows the waveforms of the broadband (curves *1*) and narrowband (curves *2*) receiver signals and the diode voltage pulse (curves *3*) for three different cases. Figures 4a and 4b correspond to input frequencies of 9.1 and 13 GHz, respectively, and Fig. 4c corresponds to the absence of an input signal. As was mentioned above, when the output radiation spectrum is narrower than the passband of the narrowband filter (5%), the signals from the broadband and narrowband receivers should be identical in shape and amplitude. It is just the case of Figs. 4a and 4b: the signals are identical to within pickups. This operating mode of the amplifier, in which the output radiation spectrum remains narrow throughout the entire pulse, we call the pure amplification regime (without accompanying generation).

It is important that the pure amplification regime was achieved at input powers of 20–60 kW throughout the entire plasma density range under study (5×10^{12}–5×10^{13} cm^{-3}), throughout the entire range of the lengths of the output part of the amplifier L_{out} (from –1 to +7 cm, Fig. 2), for both values of the REB current (1 and 2 kA), and at both frequencies (9.1 and 13 GHz). This result differs radically from the result described in our previous paper [6] and was obtained here for the first time.

By varying some parameters (e.g., by reducing the absorber volume), the pure amplification regime could be changed to the generation mode (Fig. 4c). In this case, the amplitude of the broadband receiver signal (*1*) was substantially larger than that of the narrowband

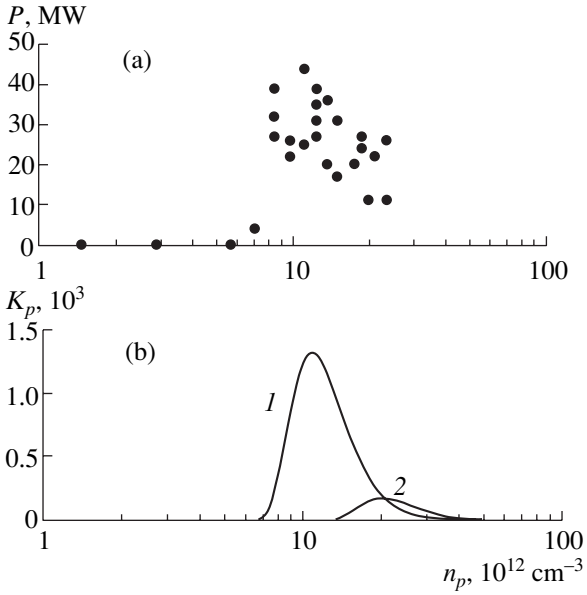

Fig. 5. (a) Measured output microwave power and (b) the gain factor calculated by the linear theory as functions of the plasma density at an input frequency of 9.1 GHz, L_{out} = 3 cm, and I = 2 kA. Curve *1* corresponds to the E_{01} mode, and curve *2* corresponds to the E_{11} mode.

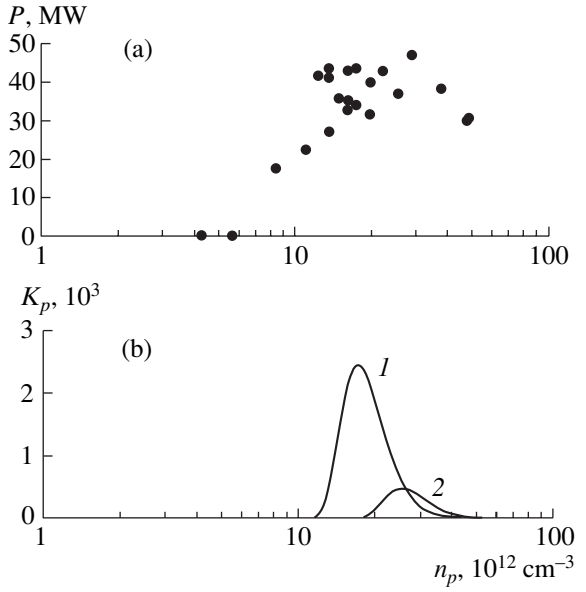

Fig. 6. The same as in Fig. 5, but for an input frequency of 13 GHz.

receiver signal (*2*) and the signal shapes differed from each other. This means that the output radiation spectrum was substantially wider than the filter passband.

As was mentioned above, the theory predicts that the frequency corresponding to the maximum amplification of the input signal in the Cherenkov plasma amplifier can be markedly varied by varying the plasma density (Fig. 1). In order to verify this prediction experimentally, it would be expedient to measure the amplifier output power as a function of the input signal frequency. However, since we did not have an appropriate microwave source with an output power on the order of several tens of kilowatts and a frequency tunable in the range from 8 to 30 GHz (to be fed to the amplifier input), we had to use a simplified measuring procedure: the measurements were performed at two input frequencies, 9.1 and 13 GHz.

Figures 5 and 6 show the measured output microwave power (Figs. 5a, 6a) and the gain factor calculated in accordance with the linear theory (Figs. 5b, 6b) as functions of the plasma density. The curves presented in Figs. 5b, 6b, 7, and 8 were calculated by M.V. Kuzelev. The calculations were performed for the three lowest modes of the plasma waveguide. Curve *1* corresponds to the azimuthally symmetric mode E_{01} with the lowest radial index, while curve *2* corresponds to the E_{11} mode. In addition, the calculations were performed for the E_{02} mode. For this mode, the plasma density at which the gain becomes nonzero is equal to 3×10^{14} cm^{-3}. Figures 5 and 6 corresponds to an input frequency of 9.1 and 13 GHz, respectively, all other parameters of the system being the same. It can be seen from Fig. 5 that the plasma density range in which the amplification at an input frequency of 9.1 GHz is observed (8×10^{12}–2.5×10^{13} cm^{-3}) agrees well with the calculated plasma density range for the E_{01} mode (Fig. 5b). For an input frequency of 13 GHz (Fig. 6), the operating plasma density range shifts toward higher densities (1.3×10^{13}–5×10^{13} cm^{-3}), which also agrees well with calculations (Fig. 6b).

A characteristic feature of the Cherenkov plasma microwave amplifier is a wide amplification band, i.e.,

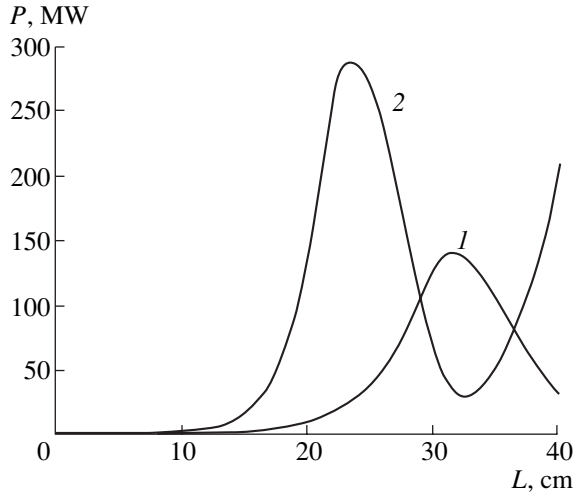

Fig. 7. Calculated power of the plasma wave (E_{01} mode) in the amplifier as a function of the interaction length at an input frequency of 9.1 GHz for REB currents of (*1*) 1 and (*2*) 2 kA.

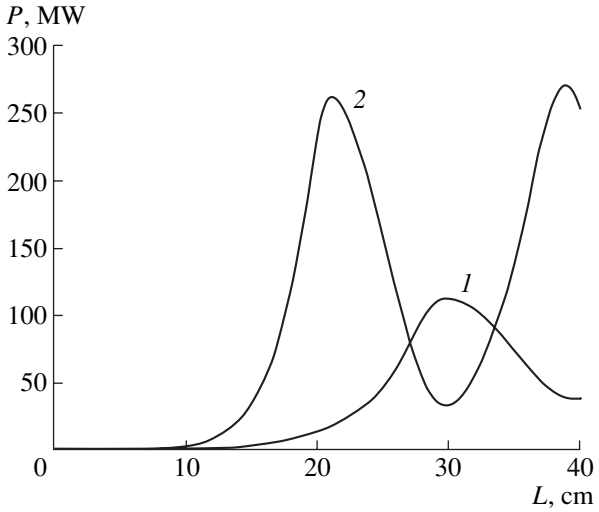

Fig. 8. The same as in Fig. 7, but for an input frequency of 13 GHz.

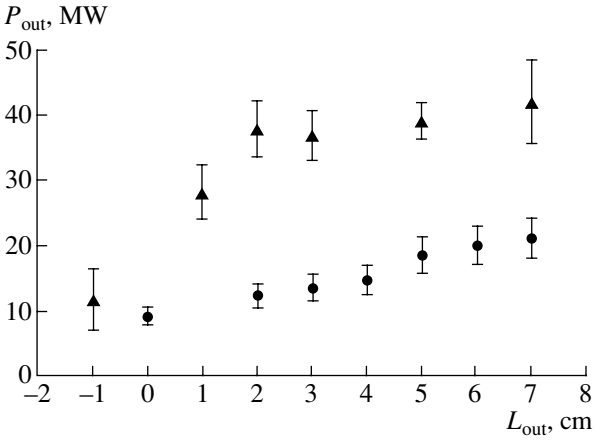

Fig. 9. Measured output microwave power as a function of the length of the output part of the amplifier at a frequency of 9.1 GHz for REB currents of 1 (circles) and 2 kA (triangles).

the possibility of amplifying input radiation over a wide frequency range without changing the system parameters. A comparison of Figs. 5 and 6 shows that, at a plasma density of 1.5×10^{13} cm^{-3}, amplification is observed at both frequencies of 9.1 and 13 GHz with an output power on the order of 40 MW. Correlating this fact with the calculated width of the amplification band (Fig. 1), we can assert that, at this plasma density, a signal at any frequency in the range 9.1–13 GHz will be amplified to a substantial output power; i.e., the width of the amplification band amounts to 40%.

Figures 7 and 8 show the calculated power of the plasma wave (E_{01} mode) in the amplifier as a function of the interaction length for frequencies of 9.1 and 13 GHz, respectively. Curves *1* and *2* correspond to REB currents of 1 and 2 kA, respectively. The signal power at the entrance to the amplifier ($L = 0$) was assumed to be 50 kW. It was also assumed in the calculations that the energy of the REB electrons is 511 keV, the plasma waveguide contains no microwave absorber, and reflections are absent (the approximation of an infinitely long waveguide). Under actual experimental conditions, the energy of the REB electrons varies during the pulse, an absorber is present in the plasma waveguide, and there are reflections from the waveguide ends. For this reason, one cannot directly compare these plots with the experimental results. Nevertheless, these plots provide an insight into the qualitative features of the system that can manifest themselves in the experiment.

Thus, under idealized conditions, for both input frequencies, the calculations predict the same amplification length L^* at which the output power is maximum. For a current of 1 kA, we have $L^* = 30$–31 cm. For a current of 2 kA, this length amounts to $L^* = 21$–23 cm. The power level P at both frequencies is nearly the same: $P = 120$–140 MW for a current of 1 kA, and $P = 270$–290 MW for a current of 2 kA.

In the experiment, the amplification length was varied by varying the length L_{out} of the output part of the amplifier (see Fig. 2), the total length being equal to $L = L_{out} + 23$ cm. The measurement results are shown in Figs. 9 and 10, which correspond to input frequencies of 9 and 13 GHz, respectively.

Each point in these figures represents the output radiation power averaged over 10–15 pulses, and the bars show the mean square deviation. All the parameters of the system (except for L_{out}) were fixed. We had to use this procedure because of the wide scatter in the output power in different pulses.

Returning to Figs. 9 and 10, we note that, in all cases, the optimum amplification length L^* (i.e., the length above which the output power does not increase with increasing length) was achieved. At a frequency of 9.1 GHz (Fig. 9), this length is $L^* = 28$–29 cm ($L_{out} = 5$–6 cm) for an REB current of 1 kA, and it is $L^* = 25$ cm ($L_{out} = 2$ cm) for a current of 2 kA. Hence, as the REB current increases, L^* decreases, which agrees qualitatively with calculations. For an input frequency of 13 GHz (Fig. 10), the optimum length for both currents is nearly the same, $L^* = 28$ cm ($L_{out} = 5$ cm), which contradicts the calculations. The maximum output powers are nearly the same for both frequencies: $P_{out} = 20$ MW for a current of 1 kA, and $P_{out} = 40$–60 MW for a current of 2 kA. This result agrees qualitatively with the calculated results, although the measured power is substantially lower than the calculated one.

Thus, the presence of a microwave absorber, reflections from the waveguide ends, and the pulsed character of the process lead to an appreciable discrepancy between the experimental and calculated results. This

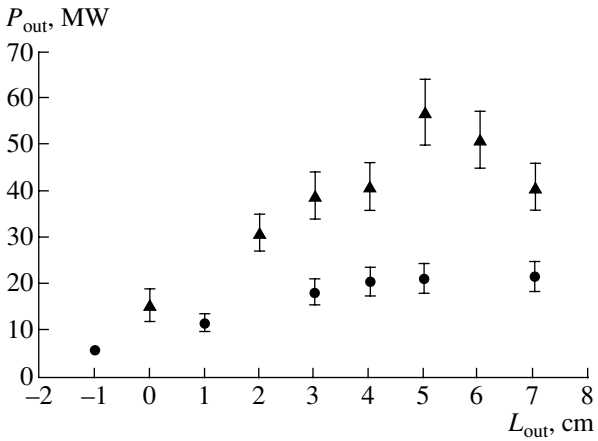

Fig. 10. The same as in Fig. 9, but for an input frequency of 13 GHz.

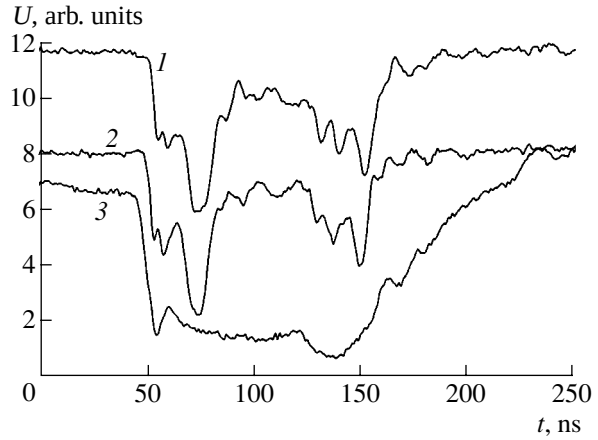

Fig. 11. Waveforms of the broadband (curve *1*) and narrowband (curve *2*) receivers signals and the diode voltage pulse (curve *3*) at an input frequency of 9.1 GHz, $I = 2$ kA, $n_p = 1.2 \times 10^{13}$ cm^{-3}, $P_{in} = 60$ kW, and $P_{out} = 47$ MW.

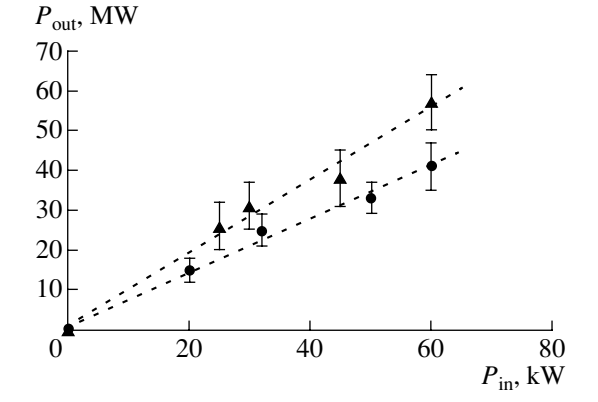

Fig. 12. Output amplifier power vs. input power at input frequencies of 9.1 (circles) and 13 GHz (triangles) for an REB current of $I = 2$ kA. The dashed lines show the straight-line fits.

means that it is necessary to carry out calculations using a more complicated model.

One remarkable result is that there is a configuration such that the maximum gain is achieved at both frequencies. Comparing Fig. 9 and Fig. 10, we can see that, for $L_{out} = 5$ cm and an REB current of 2 kA, amplification can be achieved at both a frequency of 9.1 GHz (to a power of ~40 MW) and a frequency of 13 GHz (to a power ~60 MW). The only parameter that should be changed to this end is the plasma density. If necessary, this parameter can be changed rapidly (in a time of ~10 μs) [9].

It can be seen from Figs. 9 and 10 that the maximum output power is 40 MW at a frequency of 9.1 GHz and 60 MW at a frequency of 13 GHz, which correspond to efficiencies of 4 and 6%, respectively. These values far exceed the efficiencies that were achieved in our previous study [6].

We recall that the above power values were obtained by averaging over a sequence of pulses; i.e., in some pulses, the power was even higher. Figure 11 shows waveforms of the broadband (curve *1*) and narrowband (curve *2*) receiver signals and the diode voltage pulse (curve *3*) at an input frequency of 9.1 GHz. The power in this pulse attained 47 MW.

Figure 12 shows the amplifier output power as a function of the input power for input frequencies of 9.1 GHz (circles) and 13 GHz (triangles). The dashed lines show the straight-line fits. For both input frequencies, a decrease in the input power results in a proportional decrease in the output power. In principle, it might be supposed that the amplifier under consideration is, in fact, a frequency-locked oscillator; i.e., the input power is merely an initial noise for exciting the oscillator. However, in this case, the output power would be independent of the input power and only the time during which the oscillation regime is established would change. Quite a different form of the dependences presented in Fig. 12 clearly shows that, in our case, amplification (rather than frequency-locked excitation) of microwave oscillations takes place.

It follows from Fig. 12 that the power gain is 800 (29 dB) for a frequency of 9.1 GHz, and it is 1000 (30 dB) for a frequency of 13 GHz.

5. CONCLUSIONS

(i) The regime of pure amplification (without accompanying generation) of a monochromatic microwave signal in a plasma relativistic microwave amplifier was achieved for the first time at frequencies of both 9.1 and 13 GHz. At both frequencies, the spectral width of the output radiation was no greater than 5% of the input signal frequency.

(ii) The coincidence of the measured plasma density ranges with the results of calculations allows us to conclude that an azimuthally-symmetric plasma waveguide mode with the lowest radial index is excited.

(iii) It was shown experimentally that an output power of 40 MW can be achieved by amplifying the input signal at a frequency of 9.1 or 13 GHz without changing the parameters of the system. This fact, along with the results of calculations, implies that the amplification bandwidth is no less than 40%.

(iv) The calculations show that the optimum length of the amplifier is almost the same for frequencies of 9.1 and 13 GHz. The measurements have shown that there is a length such that the maximum gain can be achieved at both 9.1 and 13 GHz by changing only one parameter, namely, the plasma density.

(v) The range of input powers was determined in which the amplifier operates in the linear regime at both frequencies.

(vi) At a frequency of 9.1 GHz, the maximum output power was $P = 40$ MW, the efficiency was $\eta = 4\%$, and the power gain was $K_p = 800$ (29 dB). At a frequency of 13 GHz, these parameters were $P = 60$ MW, $\eta = 6\%$, and $K_p = 1000$ (30 dB). At both frequencies, the length of the output section was $L_{out} = \text{const} = 5$ cm.

ACKNOWLEDGMENTS

We thank M.V. Kuzelev for performing the numerical calculations and A.A. Rukhadze and O.T. Loza for fruitful discussions. This work was supported in part by the Ministry of Industry, Science, and Technology of the Russian Federation under the Program for the Support of Unique Devices (registration no. 01-04), the Presidium of the Russian Academy of Sciences under the Complex Program "High-Power Nanosecond Relativistic Electronics" (Plasma Relativistic Broadband Maser Project), and the Russian Foundation for Basic Research (project no. 01-02-17265).

REFERENCES

1. L. S. Bogdankevich, M. V. Kuzelev, and A. A. Rukhadze, Usp. Fiz. Nauk **133**, 3 (1981) [Sov. Phys. Usp. **24**, 1 (1981)].
2. M. V. Kuzelev, F. Kh. Mukhametzyanov, M. S. Rabinovich, *et al.*, Zh. Éksp. Teor. Fiz. **83**, 1358 (1982) [Sov. Phys. JETP **56**, 780 (1982)]; Dokl. Akad. Nauk **267**, 829 (1982) [Sov. Phys. Dokl. **27**, 1030 (1982)].
3. A. G. Shkvarunets, A. A. Rukhadze, and P. S. Strelkov, Fiz. Plazmy **20**, 682 (1994) [Plasma Phys. Rep. **20**, 613 (1994)].
4. P. S. Strelkov and D. K. Ul'yanov, Fiz. Plazmy **26**, 329 (2000) [Plasma Phys. Rep. **26**, 303 (2000)].
5. A. V. Ponomarev, P. S. Strelkov, and A. G. Shkvarunets, Fiz. Plazmy **24**, 53 (1998) [Plasma Phys. Rep. **24**, 48 (1998)].
6. A. V. Ponomarev, P. S. Strelkov, and A. G. Shkvarunets, Fiz. Plazmy **26**, 633 (2000) [Plasma Phys. Rep. **26**, 592 (2000)].
7. E. B. Abubakirov, A. N. Denisenko, M. I. Fuks, *et al.*, IEEE Trans. Plasma Sci. **30**, 1041 (2002).
8. V. L. Bratman, A. W. Cross, G. G. Denisov, *et al.*, Phys. Rev. Lett. **84**, 2746 (2000).
9. O. T. Loza, A. V. Ponomarev, P. S. Strelkov, *et al.*, Fiz. Plazmy **23**, 222 (1997) [Plasma Phys. Rep. **23**, 201 (1997)].
10. I. L. Bogdankevich, I. E. Ivanov, O. T. Loza, *et al.*, Fiz. Plazmy **28**, 748 (2002) [Plasma Phys. Rep. **28**, 690 (2002)].
11. A. G. Shkvarunets, Prib. Tekh. Éksp., No. 4, 72 (1996).

Translated by N.F. Larionova

Plasma Physics Reports, Vol. 30, No. 1, 2004, pp. 69–75. Translated from Fizika Plazmy, Vol. 30, No. 1, 2004, pp. 73–79.

PLASMA ELECTRONICS

Classification of the Regimes of Cherenkov Beam Instabilities in Plasma Waveguides

Yu. V. Bobylev and M. V. Kuzelev

Prokhorov Institute of General Physics, Russian Academy of Sciences, ul. Vavilova 38, Moscow, 119991 Russia

Received May 12, 2003

Abstract—The regimes of the instabilities of an annular relativistic electron beam in a waveguide with an annular plasma are systematically analyzed and classified. The growth rates of the instabilities are calculated in different limiting cases, and the resonance conditions for the development of the instabilities are determined. The fastest growing instability of a high-current relativistic electron beam in a waveguide with a dense plasma is considered. The possible onset of a low-frequency instability of a beam in a waveguide with a low-density plasma is investigated. Typical examples of how the growth rates depend on the perturbation wavenumbers are presented for systems with parameters close to the experimental ones. © *2004 MAIK "Nauka/Interperiodica".*

It is well known that the way in which the instability of a straight electron beam develops in a plasma waveguide depends strongly on the beam and plasma densities and on their distributions over the waveguide cross section. In waveguides with high-current and ultrarelativistic beams, the well-studied single-particle and collective Cherenkov effects may manifest themselves in various forms. Although the mechanisms for the interaction between a beam and a plasma in a waveguide have been widely discussed in the literature [1, 2], we consider once again this problem because it is necessary to make some significant improvements and because some regimes of the beam–plasma instability have not yet been studied. The necessity for classifying the electromagnetic phenomena that occur in the beam–plasma interaction arises from the needs of relativistic plasma microwave electronics [3–5]—a branch of physics that is now being actively developed.

We start with the following dispersion relation, well known from the linear theory of beam–plasma instabilities [2, 5]:

$$(\omega^2 - \Omega_p^2)((\omega - k_z u)^2 - \Omega_b^2) = \Omega_p^2 \Omega_b^2 \tilde{q}^2. \quad (1)$$

Here,

$$\Omega_b^2 = \omega_b^2 \gamma^{-3} S_b \sum_{m=1}^{\infty} \frac{\chi^2}{k_{\perp m}^2 + \chi^2} \frac{\varphi_m^2(\mathbf{r}_b)}{\|\varphi_m\|^2},$$
$$\Omega_p^2 = \omega_p^2 S_p \sum_{m=1}^{\infty} \frac{\chi^2}{k_{\perp m}^2 + \chi^2} \frac{\varphi_m^2(\mathbf{r}_p)}{\|\varphi_m\|^2} \quad (2)$$

are the squared electron Langmuir frequencies of the beam and of the plasma,[1] $\chi^2 = k_z^2 - \omega^2/c^2$, ω and k_z are the wavelength of the wave and its longitudinal wavenumber, $\varphi_m(\mathbf{r}_\perp)$ is the eigenfunction in the transverse cross section of a waveguide without a plasma and beam, $k_{\perp m}^2$ is the corresponding eigenvalue, $\omega_{b,p}$ are the electron Langmuir frequencies of the beam and the plasma, $S_{b,p}$ are the cross-sectional areas of the beam and the plasma, u is the beam electron velocity, and $\gamma = (1 - u^2/c^2)^{-1/2}$ is the relativistic factor. Dispersion relation (1) also contains the coefficient of coupling between the plasma waves and electron-beam waves:

$$\tilde{q}^2 = \frac{\left(\sum_{m=1}^{\infty} \frac{1}{k_{\perp m}^2 + \chi^2} \frac{\varphi_m(\mathbf{r}_p)\varphi_m(\mathbf{r}_b)}{\|\varphi_m\|^2}\right)^2}{\left(\sum_{m=1}^{\infty} \frac{1}{k_{\perp m}^2 + \chi^2} \frac{\varphi_m^2(\mathbf{r}_p)}{\|\varphi_m\|^2}\right)\left(\sum_{m=1}^{\infty} \frac{1}{k_{\perp m}^2 + \chi^2} \frac{\varphi_m^2(\mathbf{r}_b)}{\|\varphi_m\|^2}\right)}, \quad (3)$$

where $\mathbf{r}_{b,p}$ are the radii of the beam and the plasma. Recall that dispersion relation (1) and formulas (2) and (3) were obtained for a waveguide with an arbitrary cross section in which there are a thin-walled annular plasma and a thin-walled annular electron beam in a strong longitudinal magnetic field. In a recent paper [6], it was shown that, in the frequency range $\omega \ll \omega_p$, dispersion relation (1) and formulas (2) and (3) are valid for waveguides with magnetic fields of arbitrary strength, in particular, for a waveguide with no magnetic field present.

In order to simplify transcendental equation (1), we represent the frequency ω in the form

$$\omega = k_z u(1 + \delta), \quad (|\delta| \ll 1), \quad (4)$$

where δ is the dimensionless growth rate of the Cherenkov beam instability. Substituting representation (4) into dispersion relation (1) and expanding the quantities

[1] The frequencies $\omega(k_z)$ of Langmuir waves in the beam and the plasma are implicitly determined from the relationships $\omega = k_z u \pm \Omega_b(\chi^2)$ and $\omega = \pm\Omega_p(\chi^2)$.

Ω_p^2, Ω_b^2, and $\tilde{q}^2$ in powers of δ (the power series expansions are valid under the inequality $k_{\perp 1}^2 + k_z^2\gamma^{-2} \gg 2k_z^2(u^2/c^2)\delta$), we rewrite the dispersion relation as

$$\begin{aligned}&\left(\eta_0 - \left(\frac{2}{\sigma\alpha_p} + 1 + \frac{k_z}{2}\frac{d\ln k_{\perp p}^{-2}}{dk_z}\right)\delta\right)\\ &\times\left(\delta^2 - \alpha_b\left(1 - \sigma\left(1 + \frac{k_z}{2}\frac{d\ln k_{\perp b}^{-2}}{dk_z}\right)\delta\right)\right)\\ &= -\frac{\tilde{\alpha}\alpha_b}{\sigma}\left(1 - \sigma\left(1 + \frac{k_z}{2}\frac{d\ln G}{dk_z}\right)\delta\right)^2,\end{aligned} \tag{5}$$

where we have introduced the notation

$$\begin{aligned}&\alpha_p = \frac{\omega_p^2}{k_{\perp p}^2 u^2\gamma^2}, \quad \alpha_b = \frac{\omega_b^2\gamma^{-3}}{k_{\perp b}^2 u^2\gamma^2}, \quad \tilde{\alpha} = k_{\perp p}^2 k_{\perp b}^2 S_p G^2,\\ &\sigma = 2\frac{u^2}{c^2}\gamma^2, \quad \eta_0 = \frac{1}{\sigma}\left(1 - \frac{1}{\alpha_p}\right),\\ &k_{\perp\alpha}^2 = \left(S_\alpha\sum_{m=1}^{\infty}\frac{1}{k_{\perp m}^2 + k_z^2\gamma^{-2}}\frac{\varphi_m^2(\mathbf{r}_\alpha)}{\|\varphi_m\|^2}\right)^{-1}, \quad \alpha = b, p,\\ &G = \sum_{m=1}^{\infty}\frac{1}{k_{\perp m}^2 + k_z^2\gamma^{-2}}\frac{\varphi_m(\mathbf{r}_b)\varphi_m(\mathbf{r}_p)}{\|\varphi_m\|^2}.\end{aligned} \tag{6}$$

The quantities $k_{\perp b}$ and $k_{\perp p}$ in formulas (6) are transverse wavenumbers of the low-frequency E-type surface eigenmodes of a thin-walled annular beam and a thin-walled annular plasma in a waveguide [5]. The parameter $\tilde{\alpha}$ is the coefficient of coupling between these waves. It coincides with the coupling coefficient in formula (3), in which χ^2 is replaced with $k_z^2\gamma^{-2}$. It is easy to see that the parameter $\tilde{\alpha}$ satisfies the inequalities $0 < \tilde{\alpha} \le 1$, in which the equality sign refers only to the case $\mathbf{r}_b = \mathbf{r}_p$.[2]

In numerical analysis, some results of which will be presented below, we retained all of the terms in dispersion relation (5). In analytical study, we simplify the fairly complicated expressions by discarding the correction terms in dispersion relation (5),

$$\frac{k_z}{2}\frac{d\ln k_{\perp b,\,p}^{-2}}{dk_z} \quad \text{and} \quad \frac{k_z}{2}\frac{d\ln G}{dk_z},$$

which can be neglected in the range of small wavenumbers k_z. We also restrict ourselves to the case of a dense plasma, $\sigma\alpha_p \gg 1$ and write dispersion relation (5) in the form

$$(\delta - \delta^{(1)})(\delta - \delta^{(2)})(\eta_0 - \delta) = -\tilde{\alpha}\frac{\alpha_b}{\sigma}(1 - \sigma\delta)^2, \tag{7}$$

where the quantities

$$\begin{aligned}\delta &= \delta^{(1)} \equiv -\frac{1}{2}\alpha_b\sigma\left(1 + \sqrt{1 + \frac{4}{\alpha_b\sigma^2}}\right),\\ \delta &= \delta^{(2)} \equiv -\frac{1}{2}\alpha_b\sigma\left(1 - \sqrt{1 + \frac{4}{\alpha_b\sigma^2}}\right),\end{aligned} \tag{8}$$

with allowance for representation (4), determine the spectra of the slow and fast beam waves, respectively, and the quantity $\delta = \delta^{(0)} \equiv \eta_0$ gives the spectrum of the plasma wave. The wavenumbers k_z corresponding to the single-particle and collective Cherenkov resonances between the electron beam and the plasma wave are calculated from the equations

$$\eta_0 = 0 \quad \text{and} \quad \eta_0 = \delta^{(1)} \tag{9}$$

by using formulas (6). The instability growth rates are usually maximum under any of resonance conditions (9). Below, we will show that this is not always the case.

Depending on the values of the parameters σ, $\tilde{\alpha}$, α_b, α_p, and η_0 in dispersion relation (7), the instability may proceed by different mechanisms, which we are going to analyze and classify below. To begin, we assume that the following inequality is satisfied:

$$\sigma|\delta| \ll 1, \tag{10}$$

As will be clear later, this inequality implies that the electron beam density is low.

The condition $\tilde{\alpha} \approx 1$ corresponds to a strong coupling between the plasma and the beam and holds when the beam and plasma radii are close to one another ($r_b \approx r_p$). In this case, under any of resonance conditions (9) and under inequality (10), the growth rate δ is described by the expression

$$\delta = \frac{-1 + i\sqrt{3}}{2}\left(\frac{\tilde{\alpha}\alpha_b}{\sigma}\right)^{\frac{1}{3}} \approx \frac{-1 + i\sqrt{3}}{2}\left(\frac{\alpha_b}{\sigma}\right)^{\frac{1}{3}}. \tag{11}$$

The instability with this growth rate originates from the stimulated single-particle Cherenkov effect. Using expression (11), we rewrite inequality (10) as $(\tilde{\alpha}\sigma^2\alpha_b)^{1/3} \ll 1$. In what follows, we will write such inequalities by neglecting constant factors on the order of unity and omitting power indices. So, inequality (10), which is the condition of the single-particle Cherenkov effect and under which the instability growth rate is described by expression (11), takes the form

$$\alpha_b\sigma^2 \ll 1. \tag{12}$$

[2] The expressions for quantities (2), (3), and (6) in cylindrical geometry can be found in [3, 5].

As was shown in [7], inequality (12) implies that the beam current is low in comparison with the limiting vacuum current in the waveguide under consideration [8].

Now, assuming, as before, that inequality (10) is satisfied, we consider the condition $\tilde{\alpha} \ll 1$, which corresponds to a weak coupling between the plasma and beam waves and holds when the beam and the plasma are separated in space ($\mathbf{r}_b \neq \mathbf{r}_p$). We also assume that inequality (12) is met. In this situation, the spectrum of the slow wave of the electron beam is determined by the formula $\delta^{(1)} = -\sqrt{\alpha_b}$ [see expressions (8)] and the instability growth rate is maximum when the plasma wave and the slow beam wave are in resonance, i.e., when

$$\eta_0 = \delta^{(1)} = -\sqrt{\alpha_b}. \tag{13}$$

In this case, dispersion relation (6) has the solution

$$\delta = -\sqrt{\alpha_b} + \tilde{\delta}, \quad \tilde{\delta} = i\left(\frac{\tilde{\alpha}\sqrt{\alpha_b}}{2\sigma}\right)^{\frac{1}{2}}. \tag{14}$$

Since $|\tilde{\delta}| < \sqrt{\alpha_b}$, we can readily see that inequality (10) again reduces to condition (12), which was used to derive solution (14). The instability with growth rate (14) results from the stimulated collective Cherenkov effect in a waveguide with a low-density electron beam.

We now consider the inequality opposite to inequality (10), i.e.,

$$\sigma|\delta| \gg 1. \tag{15}$$

Under this inequality, dispersion relation (7) reduces to the following form, which is valid for any value of $\tilde{\alpha}$:

$$(\delta + \alpha_b\sigma)(\eta_0 - \delta) = -\tilde{\alpha}\alpha_b(-2 + \sigma\delta). \tag{16}$$

One of the solutions to this dispersion relation is

$$\delta = \frac{1}{2}(\eta_0 - (1-\tilde{\alpha})\alpha_b\sigma + \sqrt{(\eta_0 - (1-\tilde{\alpha})\alpha_b\sigma)^2 + 4(\eta_0\alpha_b\sigma - 2\tilde{\alpha}\alpha_b)}). \tag{17}$$

Let us analyze solution (17) in different limiting cases under the inequality opposite to inequality (12), namely,

$$\alpha_b\sigma^2 \gg 1. \tag{18}$$

To do this, we use the fact that, under inequality (18), the spectrum of the slow beam wave is given by the formula $\delta^{(1)} = -\alpha_b\sigma$ [see expressions (8)].

If $\tilde{\alpha} \approx 1$, then, for a zero detuning ($\eta_0 = 0$), solution (17) becomes

$$\delta = i\sqrt{2\tilde{\alpha}\alpha_b} \approx i\sqrt{2\alpha_b}. \tag{19}$$

The instability with growth rate (19) stems from the negative permittivity of the plasma. In the literature, this instability is sometimes called the negative-mass instability [7, 9]. Under the conditions $\tilde{\alpha} \approx 1$ and

$$\eta_0 = \delta^{(1)} = -\alpha_b\sigma, \tag{20}$$

i.e., when the slow beam wave and the plasma wave are in resonance, the instability growth rate is determined by the formula

$$\delta = -\alpha_b\sigma\left(1 - \frac{\tilde{\alpha}}{2} - i\sqrt{\tilde{\alpha}\left(1 - \frac{\tilde{\alpha}}{4}\right)}\right) \approx \frac{1}{2}(-1 + i\sqrt{3})\alpha_b\sigma. \tag{21}$$

Although growth rates (19) and (21) are obtained at the resonance points $\eta_0 = 0$ and $\eta_0 = \delta^{(1)}$, they are not maximum: by virtue of inequality (18), growth rate (21) is faster than growth rate (19). From solution (17), it follows that the maximum instability growth rate is given by the expression

$$\delta = -\alpha_b\sigma(1 - i\sqrt{\tilde{\alpha}}) \approx (-1 + i)\alpha_b\sigma \tag{22}$$

and is reached under the condition

$$\eta_0 = -\alpha_b\sigma - \tilde{\alpha}\alpha_b\sigma \approx -2\alpha_b\sigma. \tag{23}$$

The instabilities with growth rates (21) and (22) stem from the negative plasma permittivity and from the strong coupling between the slow beam wave and the plasma wave.

Using expressions (19), (21), and (22), we can see that inequality (15) reduces to inequality (18), which was employed to obtain dispersion relation (16) and is opposite to condition (12). Inequality (18) implies that the electron beam current is high.

We now assume that inequality (15) is satisfied and consider the condition $\tilde{\alpha} \ll 1$ of a weak coupling between the slow beam waves and the plasma wave. In this case, according to solution (17), the maximum growth rate

$$\delta = \alpha_b\sigma(-1 + i\sqrt{\tilde{\alpha}}) \tag{24}$$

is achieved under condition (20), i.e., at resonance between the slow beam wave and the plasma wave. The instability with growth rate (24) originates from the stimulated collective Cherenkov effect in a waveguide with a high-density electron beam. It is easy to see that the condition for the applicability of solution (24) reduces to inequality (18).

Finally, in the case of a single-particle Cherenkov resonance ($\eta_0 = 0$ and $\tilde{\alpha} \ll 1$), the imaginary part of solution (17) vanishes regardless of the value of the electron beam density; this indicates that the beam–plasma system is stable.

The above results of an approximate analytical solution of dispersion relation (5) are systematized in the table (in which the factors on the order of unity in the expressions for the growth rates, inequalities, and resonance conditions are omitted).

Table

Effect	Restrictions on the parameters	Resonance condition	Complex growth rate
Stimulated single-particle Cherenkov effect	$\alpha_b\sigma^2 \ll 1$, $\tilde{\alpha} \approx 1$	$\eta_0 = 0$, $\eta_0 = -\sqrt{\alpha_b}$	$\delta = \frac{-1 + i\sqrt{3}}{2}\left(\frac{\alpha_b}{\sigma}\right)^{\frac{1}{3}}$
Stimulated collective Cherenkov effect for a low-density beam	$\alpha_b\sigma^2 \ll 1$, $\tilde{\alpha} \ll 1$	$\eta_0 = -\sqrt{\alpha_b}$	$\delta = -\sqrt{\alpha_b} + i\left(\frac{\tilde{\alpha}\sqrt{\alpha_b}}{2\sigma}\right)^{\frac{1}{2}}$
Stability of the system	$\alpha_b\sigma^2 \ll 1$, $\tilde{\alpha} \ll 1$	$\eta_0 = 0$	$\mathrm{Im}\delta = 0$
Negative-mass instability	$\alpha_b\sigma^2 > 1$, $\tilde{\alpha} \approx 1$	$\eta_0 = 0$	$\delta = i\sqrt{2\alpha_b}$
Negative-mass instability + collective Cherenkov effect	$\alpha_b\sigma^2 > 1$, $\tilde{\alpha} \approx 1$	$\eta_0 = -\alpha_b\sigma$	$\delta = \frac{1}{2}(-1 + i\sqrt{3})\alpha_b\sigma$
Instability with the maximum growth rate	$\alpha_b\sigma^2 > 1$, $\tilde{\alpha} \approx 1$	$\eta_0 = -\alpha_b\sigma(1 + \tilde{\alpha})$	$\delta = (-1 + i)\alpha_b\sigma$
Stimulated collective Cherenkov effect for a high-density beam	$\alpha_b\sigma^2 > 1$, $\tilde{\alpha} \ll 1$	$\eta_0 = -\alpha_b\sigma$	$\delta = \alpha_b\sigma(-1 + i\sqrt{\tilde{\alpha}})$
Stability of the system	$\alpha_b\sigma^2 > 1$, $\tilde{\alpha} \ll 1$	$\eta_0 = 0$	$\mathrm{Im}\delta = 0$

We now turn to an analysis of the beam instabilities in waveguides with a plasma of comparatively low density. It is well known that, in a beam–plasma waveguide, instability can occur only when the plasma density is higher than a certain minimum threshold value. Thus, in a waveguide with an electron beam of low (or, more precisely, infinitely low) density, the threshold plasma density is determined from the relationship $\eta_0(k_z \longrightarrow 0) \geq 0$ [3, 5], which, in accordance with formulas (6), reduces to the relationship

$$\alpha_p(k_z \longrightarrow 0) = 1 \quad (\alpha_b \longrightarrow 0). \tag{25}$$

Hence, in a waveguide with a beam of infinitely low density, instability occurs only when the plasma density exceeds the threshold value determined by formula (25). Let us analyze the situation with an electron beam of finite density. This way, we do not make the assumption used in deriving dispersion relation (7), namely, that the plasma density is high.

From dispersion relation (5) in which the parameter $\sigma\alpha_p$ is assumed to be arbitrary, we obtain, instead of dispersion relation (7), the relation

$$(\delta - \delta^{(1)})(\delta - \delta^{(2)})(\eta_0 - \beta_p\delta) = -\tilde{\alpha}\frac{\alpha_b}{\sigma}(1 - \sigma\delta)^2, \tag{26}$$

where the quantities $\delta^{(1)}$ and $\delta^{(2)}$ are given by expressions (8) and, in place of $\beta_p = 1$ in dispersion relation (7), we use the quantity $\beta_p = 1 + 2/(\sigma\alpha_p)$.

We are working under conditions corresponding to a low (but finite) beam density:

$$\sigma|\delta| \ll 1, \quad \alpha_b\sigma^2 \ll 1. \tag{27}$$

Under these conditions, dispersion relation (26) becomes

$$(\delta + \sqrt{\alpha_b})(\delta - \sqrt{\alpha_b})(\eta_0 - \beta_p\delta) = -\tilde{\alpha}\frac{\alpha_b}{\sigma}(1 - 2\sigma\delta). \tag{28}$$

Let us further assume that dispersion relation (28) has solutions of the form

$$\delta = -\sqrt{\alpha_b} + \tilde{\delta}; \quad |\tilde{\delta}| \ll \sqrt{\alpha_b}. \tag{29}$$

We substitute solution (29) into dispersion relation (28) and ignore the quantity $\tilde{\delta}$ in parentheses in the second factor on the left-hand side of the resulting relation to obtain the quadratic equation

$$\beta_p\tilde{\delta}^2 - (\eta_0 + (\beta_p + \tilde{\alpha})\sqrt{\alpha_b})\tilde{\delta} + \tilde{\alpha}\frac{\sqrt{\alpha_b}}{2\sigma} = 0, \tag{30}$$

one of whose roots is given by the formula

$$\tilde{\delta} = \frac{1}{2\beta_p}\left[\eta_0 + (\beta_p + \tilde{\alpha})\sqrt{\alpha_b} + \sqrt{(\eta_0 + (\beta_p + \tilde{\alpha})\sqrt{\alpha_b})^2 - \frac{2\tilde{\alpha}\beta_p\sqrt{\alpha_p}}{\sigma}}\right]. \tag{31}$$

The radicand in this expression is negative (which means that there is an instability) when

$$\eta_0 < \sqrt{\frac{2\tilde{\alpha}\beta_p\sqrt{\alpha_b}}{\sigma}} - (\beta_p + \tilde{\alpha})\sqrt{\alpha_b}. \tag{32}$$

The maximum instability growth rate is reached at

$$\eta_0 = -(\beta_p + \tilde{\alpha})\sqrt{\alpha_b} \quad (33)$$

and is equal to

$$\tilde{\delta} = i\sqrt{\frac{\tilde{\alpha}\sqrt{\alpha_b}}{2\sigma(1 + 2/(\sigma\alpha_p))}}. \quad (34)$$

In the case of a dense plasma such that the inequality $\alpha_p\sigma \gg 1$ is satisfied, expression (34) passes over to the growth rate (14) of a conventional instability driven by the collective Cherenkov effect in a waveguide with a low-density beam. In this case, to within terms on the order of $\tilde{\alpha}$, expression (33) coincides with formula (13). For small α_p values satisfying the condition $\alpha_p\sigma \ll 1$, maximum instability growth rate (34) becomes

$$\tilde{\delta} = \frac{i}{2}\sqrt{\tilde{\alpha}\alpha_p\sqrt{\alpha_b}}. \quad (35)$$

The dependence of growth rate (35) on α_p is qualitatively different: the growth rate is proportional to the plasma density.

By virtue of the inequality in solution (29), expression (34) for the growth rate is valid under the condition

$$\tilde{\alpha} \ll 2\sqrt{\alpha_b}\sigma(1 + 2/(\sigma\alpha_p)). \quad (36)$$

In the case of a dense plasma such that $\alpha_p\sigma \gg 1$, inequality (36) is satisfied only for $\tilde{\alpha} \ll 1$, by virtue of conditions (27). For $\alpha_p\sigma < 1$, inequality (36) can also hold when $\tilde{\alpha} \approx 1$, i.e., when the coupling between the beam wave and the plasma wave is strong. The latter case was considered in [10] for a waveguide filled uniformly with a beam and plasma. This case refers to the instability originating from the collective Cherenkov effect when there is a strong coupling between the slow beam wave and the plasma wave. Usually, this instability does not occur because, under conditions (27), it turns out to be overpowered by the instability resulting from the singe-particle Cherenkov effect [see expression (11) for the growth rate]. The instability in question, which can develop only when the plasma density is sufficiently low, may be of interest for creating plasma microwave emitters operating at wavelengths much larger than the transverse dimensions of the plasma waveguide.

The above analysis of the solutions to dispersion relation (5) in different limiting cases is interesting more from a theoretical than from a practical point of view. The reason is that the parameters of the new experimental beam–plasma systems that are currently under development [3, 4] lie in ranges intermediate to the limits under consideration. Thus, the beam current parameter $\alpha_b\sigma^2$ usually ranges from several tenths to several units (in which case the relativistic parameter σ is about several units). That is why, in order to illustrate the typical growth rates, frequencies, and instability ranges, we present some results of exact calculations carried out for an existing experimental system [3, 4] with the following parameters: the radius of the circular cross section of the waveguide is $R = 2$ cm; the radius of an annular beam is $r_b = 0.65$ cm; the beam thickness is $\Delta_b = 0.1$ cm; the relativistic factor of the beam is $\gamma = 2$ ($\sigma = 6$); the thickness of an annular plasma is $\Delta_p = 0.1$ cm; and the beam currents are $I_b = 1$, 2, and 3 kA. For this set of parameters, we consider several different values of the annular plasma radius r_p and several different values of the Langmuir frequency ω_p of the plasma electrons.

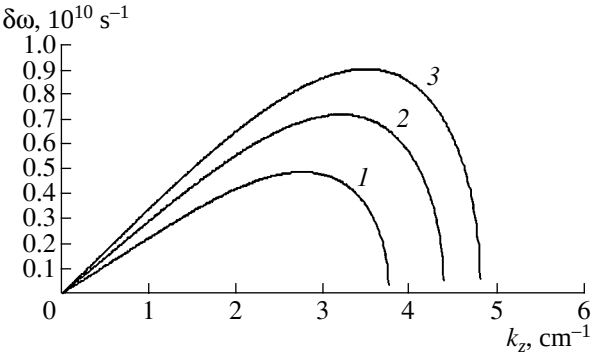

Fig. 1. Instability growth rates for $r_p = 0.65$ cm and $\omega_p = 2 \times 10^{11}$ s^{-1}. Here and in the subsequent figures, curves *1*, *2*, and *3* were obtained for beam currents of 1, 2, and 3 kA, respectively.

Figure 1 shows the dimensional growth rate $\delta\omega = \mathrm{Im}(k_z u\delta)$, calculated as a function of the wavenumber k_z for $r_p = 0.65$ cm, $\omega_p = 2 \times 10^{11}$ s^{-1}, and three different values of the electron beam current. In this and other figures, curves *1*, *2*, and *3* were obtained for beam currents of 1, 2, and 3 kA, respectively. In Fig. 1, the plasma and beam radii are the same, $r_p = r_b$, so that we have $\tilde{\alpha} = 1$. In this case, depending on the beam current, the instability may develop in one of the two limiting regimes: it may be driven by the stimulated single-particle Cherenkov effect and grow at maximum rate (11) or it may stem from the negative plasma permittivity and the strong coupling between the slow beam wave and the plasma wave and grow at maximum rate (22). From Fig. 1 we see that, as the beam current increases, the maximum growth rate becomes faster and is displaced toward longer wavelengths k_z and the wavelength range over which the instability occurs becomes wider. All three curves in Fig. 1 are similar in structure and are satisfactorily described by formula (17) with $\tilde{\alpha} = 1$; this indicates that the instability results from the negative plasma permittivity and the coupling between the beam wave and the plasma wave. As for the instability associated with the single-particle Cherenkov effect, it occurs at substantially lower beam cur-

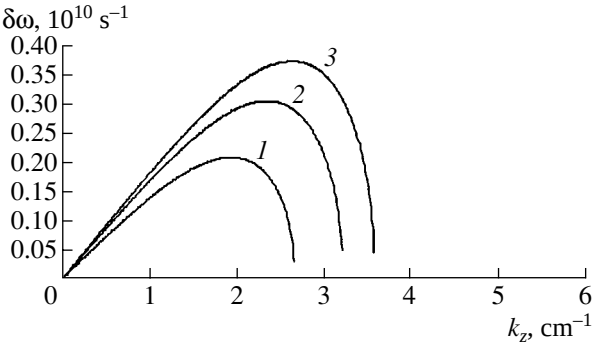

Fig. 2. Instability growth rates for $r_p = 1.2$ cm and $\omega_p = 2 \times 10^{11}$ s^{-1}.

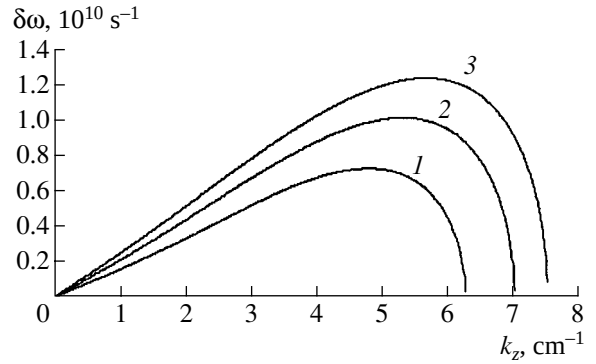

Fig. 3. Instability growth rates for $r_p = 0.65$ cm and $\omega_p = 3 \times 10^{11}$ s^{-1}.

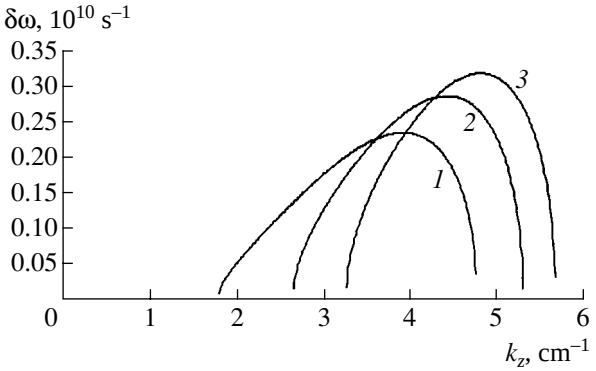

Fig. 4. Instability growth rates for $r_p = 1.2$ cm and $\omega_p = 3 \times 10^{11}$ s^{-1}.

rents, the remaining parameters of the system being the same.

In Fig. 2, the Langmuir frequency of the plasma electrons is taken to be the same as in Fig. 1, $\omega_p = 2 \times 10^{11}$ s^{-1}, but the plasma radius is increased to $r_p = 1.2$ cm, in which case the coupling coefficient is smaller than unity, $\tilde{\alpha} < 1$. However, the decrease in the coupling coefficient is insufficient to qualitatively change the shape of the curves. The only effect is that the growth rates become slower and the wavelength range over which the instability occurs becomes narrower. This effect stems from a slight decrease in $\tilde{\alpha}$.

In Fig. 3, the plasma radius is again equal to the beam radius, $r_p = 0.65$ cm $= r_b$, but the Langmuir frequency of the plasma electrons is increased to $\omega_p = 3 \times 10^{11}$ s^{-1}. In a sense, Fig. 3 is identical to Fig. 1 because $\tilde{\alpha} = 1$. The only difference is that, in Fig. 3, the growth rates are faster, their maxima are displaced to the right, and the range of k_z values over which the instability occurs becomes wider. This discrepancy is associated with an increase in the electron Langmuir frequency of the plasma. The increase in the growth rate stems from an increase in the resonance values of $k_z u$, while the dimensionless growth rate δ decreases as the electron Langmuir frequency of the plasma increases. Thus, in Fig. 1, the dimensionless growth rate is $\delta_{max} \approx 0.13$, while, in Fig. 3, we have $\delta_{max} \approx 0.1$. Note that, in all calculations, the maximum δ value was smaller than 0.14; this guarantees the validity of dispersion relation (5), which was obtained using the inequality in representation (4).

In Fig. 4, the Langmuir frequency of the plasma electrons is taken to be $\omega_p = 3 \times 10^{11}$ s^{-1} and the plasma radius is increased to $r_p = 1.2$ cm. In this case, the coefficient $\tilde{\alpha}$ decreases to a greater extent than that in Fig. 2 because the Langmuir frequency is higher. The consequences of such a significant decrease are clearly seen in Fig. 4: the growth rate becomes substantially slower and the instability range narrows. In particular, the instability does not occur in the range of small wavenumbers k_z. The curves in Fig. 4 are satisfactorily described by formula (17) with the corresponding $\tilde{\alpha}$ values. This allows us to conclude that Fig. 4 (at least at $I_b = 3$ kA) refers to the instability originating from the collective Cherenkov effect in a waveguide with a high-density beam.

We now consider the instabilities occurring at a low plasma density. Figure 5 shows the instability growth rates calculated for $\omega_p = 10^{11}$ s^{-1} and different plasma radii: r_p = (a) 0.65, (b) 0.8, and (c) 1.1 cm (at larger plasma radii, the instability does not occur). We can see that, at a high beam current, the growth rates are fast and are maximum at small wavenumbers k_z. Thus, for $r_p = 0.8$ cm and $I_b = 2$ kA, the maximum growth rate is about 2×10^9 s^{-1} and is reached at $k_z u \approx 3 \times 10^{10}$ s^{-1}. In a waveguide of radius 2 cm, this instability generates waves with wavelengths of $\lambda \approx 6$ cm.

In conclusion, note that, for beam–plasma systems with parameters close to those chosen for our analysis, the most typical instability is the one associated with both the interaction between the beam wave and the plasma wave and the negative (within the instability

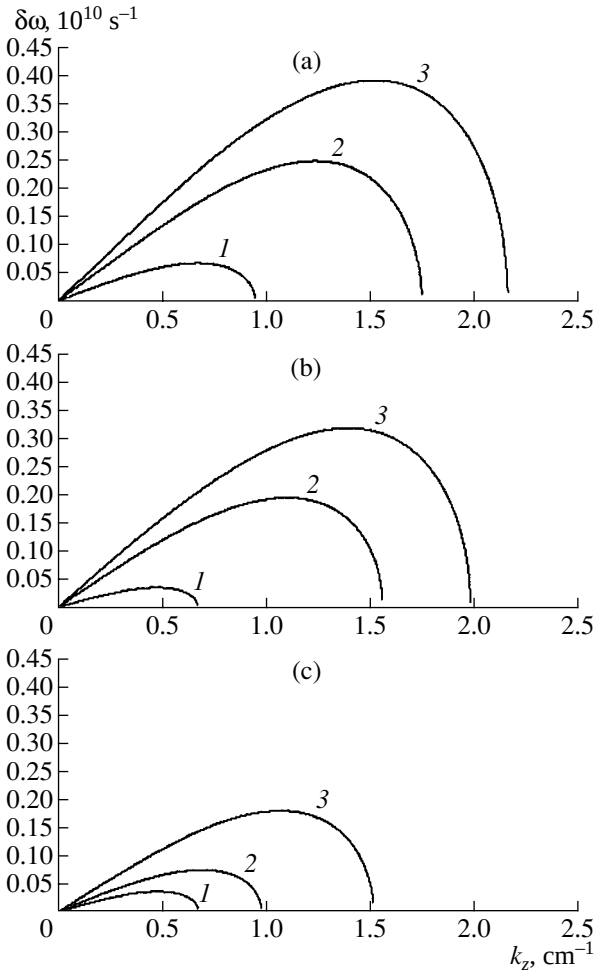

Fig. 5. Instability growth rates at a low plasma density (ω_p = 10^{11} s^{-1}) for different radii of the plasma tube: r_p = (a) 0.65, (b) 0.8, and (c) 1.1 cm.

range) permittivity of the plasma. Because of the hybrid nature of the instability, its growth rate is fast and the range of wave numbers over which it occurs is wide. As the electron Langmuir frequency of the plasma increases, the instability evolves to the regime of the collective Cherenkov effect in a waveguide with a high-density beam. As a result, the instability growth rate decreases and the instability range narrows (i.e., the resonant properties of the beam–plasma system become more pronounced). Otherwise, as the electron Langmuir frequency of the plasma decreases, the resonant properties of an unstable beam–plasma system become worse because of a decrease in the frequency $k_z u$ and growth rate δω.

ACKNOWLEDGMENTS

This work was supported in part by the Ministry of Education of the Russian Federation (project no. E02-3.2-447); the Russian Foundation for Basic Research (project no. 01-02-17265); and the Ministry of Industry, Science, and Technologies of the Russian Federation under the Program for Government Support of Leading Scientific Schools (project no. 1962.2003.2).

REFERENCES

1. A. F. Aleksandrov, M. V. Kuzelev, and A. N. Khalilov, Zh. Éksp. Teor. Fiz. **93**, 1714 (1987) [Sov. Phys. JETP **66**, 978 (1987)].
2. A. F. Aleksandrov, M. V. Kuzelev, V. A. Panin, *et al.*, Fiz. Plazmy **18**, 40 (1992) [Sov. J. Plasma Phys. **18**, 20 (1992)].
3. M. V. Kuzelev, O. T. Loza, A. A. Rukhadze, *et al.*, Fiz. Plazmy **27**, 710 (2001) [Plasma Phys. Rep. **27**, 669 (2001)].
4. P. S. Strelkov and D. K. Ul'yanov, Fiz. Plazmy **28**, 748 (2002) [Plasma Phys. Rep. **28**, 690 (2002)].
5. M. V. Kuzelev, A. A. Rukhadze, and P. S. Strelkov, *Plasma Relativistic Microwave Electronics* (Mosk. Gos. Tekhn. Univ. im. N. É. Baumana, Moscow, 2002).
6. M. V. Kuzelev, Fiz. Plazmy **28**, 544 (2002) [Plasma Phys. Rep. **28**, 501 (2002)].
7. M. V. Kuzelev and A. A. Rukhadze, *Electrodynamics of Dense Electron Beams in Plasma* (Nauka, Moscow, 1990).
8. L. S. Bogdankevich and A. A. Rukhadze, Usp. Fiz. Nauk **103**, 609 (1971) [Sov. Phys. Usp. **14**, 163 (1971)].
9. V. V. Bogdanov, M. V. Kuzelev, and A. A. Rukhadze, Fiz. Plazmy **10**, 548 (1984) [Sov. J. Plasma Phys. **10**, 319 (1984)].
10. Yu. P. Bliokh, V. I. Karas', M. G. Lyubarskiĭ, *et al.*, Dokl. Akad. Nauk **275**, 56 (1984) [Sov. Phys. Dokl. **29**, 205 (1984)].

Translated by I.A. Kalabalyk

Plasma Physics Reports, Vol. 30, No. 1, 2004, pp. 76–82. Translated from Fizika Plazmy, Vol. 30, No. 1, 2004, pp. 80–87.

PLASMA ELECTRONICS

Linear Theory of the Interaction of an Electron Beam with Electromagnetic Waves in the Ion Focus Regime in a Pasotron

D. I. Trubetskov and A. E. Khramov

"College" State Research and Education Center, Chernyshevsky Saratov State University, Astrakhanskaya ul. 83, Saratov, 410026 Russia

Received April 23, 2003

Abstract—A study is made of the interaction of an electron beam focused by a positive ion background with electromagnetic waves in a pasotron—a modern plasma microwave electronics device with long-term interaction in the ion focus regime. © *2004 MAIK "Nauka/Interperiodica".*

Pasotrons[1] constitute a new class of high-power plasma microwave oscillators and amplifiers [1–6] having two essential elements: (i) an electron gun with a plasma cathode for producing an intense electron beam and (ii) a gas-filled slow-wave electrodynamic structure in which a plasma channel is created through the ionization of gas atoms by the injected electron beam. In a pasotron, an electron beam passes through the interaction space in the ion focus regime, in which the plasma produced by ionizing a neutral gas (hydrogen, helium, or xenon) neutralizes the beam space charge and creates a fairly strong focusing force that compresses the beam injected into the interaction space.

Such a method of transporting an electron beam through the interaction space makes it possible to substantially reduce the weight and overall dimensions of high-power linear microwave sources in which electron beams should be focused in one way or another.[2]

Two types of experimental pasotrons are presently being developed: pasotrons operating as backward-wave tube oscillators (BWT pasotrons) and pasotrons operating as traveling-wave tube amplifiers (TWT pasotrons). Depending on the frequency range and output power, various periodic slow-wave electrodynamic structures (corrugated waveguides, helices, coupled-resonator chains, etc.) are used in these devices. This allows one to assign pasotrons to devices with long-term O-type interaction and ion focusing of the electron beam. As was mentioned above, the electron beam in a pasotron is generated using an electron gun with a plasma cathode [12–15]. This makes it possible to efficiently form an electron beam in systems in which the transportation and interaction regions are entirely filled with plasma.

The aim of this study is to analytically (in a linear approximation) investigate the interaction of a traveling electromagnetic wave with an electron beam focused by a positive ion space charge. The analysis is based on both the mathematical apparatus of the theory of the interaction of curved electron beams with electromagnetic waves [16, 17] and the results of theoretical studies of the nonmagnetic transportation of electron beams in the ion focus regime [7, 9–11].

Let us consider a simplified pasotron model in which an electron beam focused by the ion space charge propagates with a velocity v_0 along a slow-wave structure and interacts with the traveling electromagnetic waves in a transmission line under Cherenkov resonance conditions. It is assumed that the plasma channel through which the beam is transported has already been formed and the system has already relaxed to a steady state.

Let the beam electrons move along the z axis, which coincides with the symmetry axis of the interaction region of the system under study. With allowance for axial symmetry, the equations of motion of the beam electrons in the presence of a dense ion background can be written in the form

$$\frac{d^2r}{dt^2} = \eta(f_i + f_e + p_1), \tag{1}$$

$$\frac{d^2z}{dt^2} = 0. \tag{2}$$

Here, $z = v_0(t - t_1) = v_0\tau$ (i.e., it is assumed that the longitudinal electron velocity v_0 does not vary), f_i is the focusing force produced by the ions, f_e is the defocusing

[1] The term pasotron is derived from the words Plasma Assisted Slow Wave Oscillator.

[2] The idea of the ion focusing of electron beams in devices with long-term interaction was proposed and examined as early as the 1950s–1960s (see, e.g., [7–11]). However, this idea did not find wide practical application at that time and surfaced again only in the 1990s in connection with the development of high-power compact microwave amplifiers and oscillators with long-term interaction.

1063-780X/04/3001-0076$26.00 © 2004 MAIK "Nauka/Interperiodica"

force produced by the electron space charge, p_1 is the effective force related to the electron thermal motion,[3] and η is the specific electron charge.

We assume that the space charge density is uniform over the beam cross section and the axial wavelength of the beam surface perturbations is smaller than the beam diameter. Then, using Gauss's theorem and the adiabatic equation of state for the electron gas [7–9], we arrive at the following equation of motion of an electron beam in the ion focus regime:

$$\frac{d^2r}{dz^2} = -\frac{\pi\rho_i r}{V_0} + \frac{I_0}{rv_0V_0} + \frac{\varphi_T r_k^2}{V_0 r^3}, \quad (3)$$

where ρ_i is the mean ion density in a given transverse cross section of the beam; I_0 and V_0 are the beam current and potential, respectively; $\varphi_T = kT/e$, with k an T being the Boltzmann constant and the temperature of the electrons emitted from the cathode; and r_k is the radius characterizing the position of the electrons at the cathode.

We will assume that the amplitude of transverse fluctuations of the focused beam is small. The static radius of the beam can then be represented in the form

$$\bar{r}_i = r_0(1 + \tilde{r}), \quad |\tilde{r}| \ll r_0. \quad (4)$$

Here, r_0 is the equilibrium radius of the beam and $\tilde{r}$ is the perturbation of the beam radius. Under the adopted assumptions, the equation for the perturbation $\tilde{r}$ reduces to the linear equation

$$\frac{d^2\tilde{r}}{dz^2} + \delta^2\tilde{r} = 0, \quad (5)$$

where the quantity δ determines the axial wavelength $2\pi/\delta$ of the beam surface perturbations. In the case $(\rho_i - \rho_e)/\rho_e \ll 1$, which is of practical interest, the quantity δ is equal to [8]

$$\delta = 2sP\sqrt{m_i/m_e}. \quad (6)$$

Here, m_i and m_e are the ion and electron masses, respectively; s is the specific ionization; and P is the gas pressure.

The solution to Eq. (5) is

$$\tilde{r} = a\cos\delta z + b\sin\delta z, \quad (7)$$

where the coefficients a and b are determined by the boundary conditions at $z = 0$: $a = \tilde{r}|_{z=0}$ and $b = \left.\frac{d\tilde{r}}{dz}\right|_{z=0}$.

Let us now consider the problem of high-frequency beam oscillations in the one-dimensional approximation without allowance for the gradients of static fields and the high-frequency fields produced by the space charge of the beam. Assuming that all the perturbed quantities depend on time as $\exp(j\omega t)$, the equation for the bunched current in the high-frequency field of a traveling wave can be written in the form

$$\left(j\omega + \frac{\partial}{\partial\tau}\right)^2\tilde{i} = j\frac{\eta\beta_e I_0}{v_0^2}\tilde{E}(\bar{r}_i, \bar{z}_i, \tau). \quad (8)$$

Here, $\beta_e = \omega/v_0$, I_0 is the injected beam current, and the high-frequency field $\tilde{E}$ is equal to [17]

$$\tilde{E}(\bar{r}_i, \bar{z}_i, \tau) = E^0 e^{-j\beta_0 z} e^{-\beta_0\bar{r}_i} e^{-j\beta_0\bar{z}_i}, \quad (9)$$

where β_0 is the longitudinal wavenumber of an electromagnetic wave in the transmission line.

The equation for bunched current is more convenient to analyze in the integral (rather than in the differential) form. Taking into account that $z = v_0\tau$ (which implies that the amplitude of the high-frequency field $|\tilde{E}|$ is small), we transform differential equation (8) into the integral equation

$$\tilde{i} = j\frac{\beta_e I_0}{2V_0} e^{-j\beta_e z}\int_0^z \tilde{E}(\bar{r}_i(\xi), \bar{z}_i(\xi), \xi) e^{j\beta_e\xi}(z - \xi)d\xi, \quad (10)$$

where $V_0 = v_0^2/2\eta$ is the accelerating voltage.

We expand the exponential factor $\exp(-\beta_0\bar{r}_i)$ (where $\bar{r}_i$ is determined by formulas (4) and (7)) in expression (9) in a Fourier series and restrict ourselves to the terms with the numbers $k = 0$ and ± 1. We then obtain

$$\begin{aligned} &e^{-\beta_0\bar{r}_i} \\ &= -je^{-2j\delta z}((1 + e^{2j\delta z})I_1(a\beta_0 r_b) - e^{j\delta z}I_0(a\beta_0 r_b)) \\ &\quad\times((e^{2j\delta z} - 1)I_1(b\beta_0 r_b) - je^{j\delta z}I_0(b\beta_0 r_b)). \end{aligned} \quad (11)$$

Here, I_1 and I_0 are the first- and zero-order modified Bessel functions.

Let us consider the case $a \neq 0$ and $b = 0$, which corresponds to the boundary condition $d\tilde{r}/dz|_{z=0} = 0$. This boundary condition corresponds to a beam injected parallel with the system axis. Integrating Eq. (10) with this boundary condition, we find

$$\begin{aligned} \tilde{i}(z) &= j\frac{\beta_e I_0}{2V_0} e^{-j\beta_e z} e^{-\beta_0 r_b} \\ &\times [e^{jz(\beta_e - \beta_0 - 2\delta)}((\beta_e - \beta_0)^2 - 4\delta^2)^2 \\ &\times (e^{-jz(\beta_e - 2\delta)}(-e^{j\beta_e z} + e^{j\beta_0 z}(1 + jz(\beta_e - \beta_0))) \\ &\times ((\beta_e - \beta_0)^2 - \delta^2)^2 I_0(a\beta_0 r_b) \end{aligned}$$

[3] It was shown in [7–9] that ignoring the transverse thermal electron motion in the ion focus regime leads to significant errors in determining the parameters of the transported beam.

$$+(\beta_e-\beta_0)^2(e^{3j\delta z}(\delta-\beta_e+\beta_0)^2 + e^{j\delta z}(\delta+\beta_e-\beta_0)^2 + 2je^{j(2\delta-(\beta_e-\beta_0))z}(z\beta_0^3+j\beta_e^3-z\beta_e^3+\beta_0^2(j-3z\beta_e) + j\delta^2+z\beta_e\delta^2+\beta_0(3z\beta_e^2-2j\beta_e-z\delta^2)))\times I_1(a\beta_0 r_b))]/((\beta_e-\beta_0)^2(\delta^2-(\beta_e-\beta_0)^2)^2\times(4\delta^2-(\beta_e-\beta_0)^2)^2). \quad (12)$$

Expression (12) for bunched current shows that transverse beam dynamics (periodic oscillations with a spatial period of $2\pi/\delta$) substantially affects electron bunching. Let us consider this point in more detail. To this end, we will find the high-frequency field induced by the bunched current in the transmission line and, thus, the power transferred to the high-frequency field from the electron beam in the ion focus regime.

We will separately consider the interaction of the focused electron beam with a forward and a backward wave in a transmission line (a TWT and a BWT pasotrons, respectively).

Pasotron operating as a traveling-wave tube amplifier (TWT pasotron). We use expression (12) for bunched current and the time-independent integral equation describing the excitation of a forward wave by a curved beam in the transmission line [16, 18],

$$E(z) = E^0 e^{-j\beta_0 z} - \frac{\beta_0^2 K}{2}\int_0^z \tilde{i}(\xi)\varphi_\perp(\bar{r}_i)e^{-j\beta_0(z-\xi)}d\xi, \quad (13)$$

where $\varphi_\perp(r)$ is the transverse profile of high-frequency field (9) in the transmission line[4] and K is the coupling impedance. Taking into account that the amplitude of transverse beam oscillations is small ($|\tilde{r}| \ll r_0$), after not complicated but rather cumbersome algebra, we obtain the expression for the total field at the output of the waveguide system ($x = l$) in the ion focus regime,

$$E(l) = E^0 e^{-j\beta_0 l}e^{-\beta_0 r_i} \times [1-(2\pi CN)^3(F_a(\Phi_0,\varphi,\chi)+jF_r(\Phi_0,\varphi,\chi))], \quad (14)$$

where

$$F_a = \frac{I_0(\chi)(2(1-\cos\Phi_0)+\Phi_0\sin\Phi_0)}{\Phi_0^3} + \frac{4I_1(\chi)\Phi_0(\cos\Phi_0-\cos\varphi)}{(\Phi_0^2-\varphi^2)^2} + 2I_1(\chi)\sin\Phi_0, \quad (15)$$

$$F_r = \frac{I_0(\chi)(2\sin\Phi_0-\Phi_0(1-\cos\Phi_0))}{\Phi_0^3} + \frac{2I_1(\chi)((\Phi_0^2+\varphi^2)\sin\varphi+\varphi(\Phi_0^2-\varphi^2-2\Phi_0\sin\Phi_0))}{\varphi(\Phi_0^2-\varphi^2)^2}. \quad (16)$$

Here, $\Phi_0 = (\beta_e - \beta_0)l$ is the relative transit angle of an electron in the interaction region, $\varphi = \delta l$, $C^3 = \frac{I_0 K}{4V_0}\left(\frac{\beta_0}{\beta_e}\right)^2$, $\chi = a\beta_0 r_b$, and $N = \beta_e l/2\pi$ is the ratio of the tube length to the wavelength of the excited wave (the electric length of the tube).

The functions $F_a(\Phi_0, \varphi, \chi)$ and $F_r(\Phi_0, \varphi, \chi)$ describe the interaction of the focused electron beam with a traveling wave in a pasotron in the ion focus regime and are proportional to the active and reactive components of the electron interaction power P_e. The above expressions are valid when the transmission line is nondissipative; i.e., the wavenumber of the wave propagating in the transmission line is real.

We note that, in the limiting case of a constant beam cross section ($\chi \longrightarrow 0$, $\varphi \longrightarrow 0$), the above expressions for $F_a(\Phi_0, \varphi, \chi)$ and $F_r(\Phi_0, \varphi, \chi)$ transform into the well-known expressions describing beam bunching in conventional O-type devices [18, 19].

We also note that, when the resonance condition $\beta_e - \beta_0 = \pm\delta$ is satisfied, both F_a and F_r increase without bound, whereas the true solution must be finite at any relationship between β_e, β_0, and δ. This is related to the fact that we restricted our analysis to small perturbations of the static beam trajectory in the ion focus regime and a small number of the expansion terms. Hence, we will not further consider the case $\beta_e - \beta_0 = \pm\delta$. This is quite reasonable because the value of $|\varphi| = |\delta l|$ estimated by the data from pasotron experiments [3, 4] shows that the $|\delta l|$ value is fairly large and falls into the range $\Phi_0 = (\beta_e - \beta_0)l \in (-3\pi, 3\pi)$, which is of interest to us.

Figure 1 shows the function $F_a(\Phi_0, \varphi, \chi)$ versus the relative transit angle Φ_0 under the assumption that variations in this angle are caused by variations in the wave phase velocity at constant values of l, ω, and v_0. The curves are calculated at $\varphi = 20$ and different values of the parameter χ (which can be interpreted as different ion focus regimes in the pasotron). The curve $\chi = 0$ in Fig. 1 corresponds to the active component of the interaction power of electrons confined by an infinitely strong magnetic field (a conventional TWT amplifier) [18, 19].

It can be seen from Fig. 1 that, in the range of relative transit angles $-\pi < \Phi_0 < \pi$, the inequality $|F_a(\Phi_0, \varphi, \chi)| \le F_a(\Phi_0, 0, 0)|$ holds; i.e., the efficiency of the electron–wave interaction is increased in this range. It also follows from the figure that the larger the parameter χ (which can be interpreted as the amplitude of the trans-

[4] The function $\varphi_\perp(r)$ determines the value of the high-frequency field of the wave at the point r through which the beam (which is assumed to be thin) passes at a given instant.

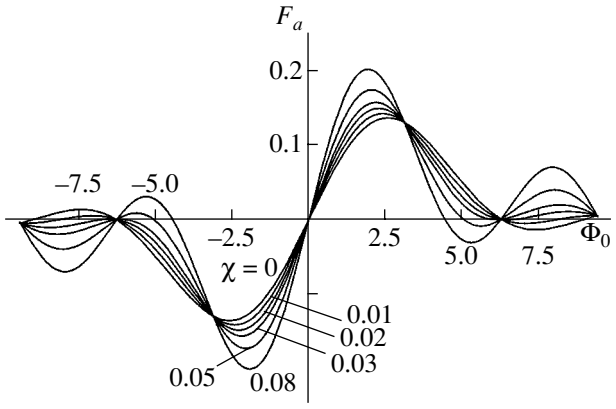

Fig. 1. Function $F_a(\Phi_0, \varphi, \chi)$ vs. relative transit angle Φ_0 for $\varphi = 20$ and different values of χ.

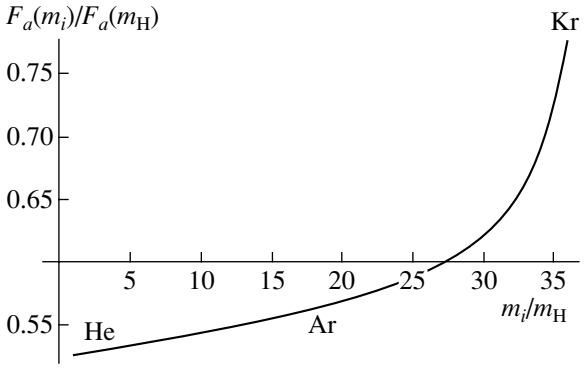

Fig. 2. $F_a(m_i)/F_a(m_H)$ ratio as a function of the ion-to-proton mass ratio for $\Phi_0 = -1.5\pi$, $\varphi = 20$, and $\chi = 0.05$.

verse oscillations of the electron bean in the ion focus regime), the larger the $|F_a|$ value. This is related to the increase in the effective coupling impedance of the pasotron slow-wave system with increasing beam radius. In the ranges $\Phi_0 > \pi$ and $\Phi_0 < -\pi$, the efficiency of the electron–wave interaction is lower than in a conventional TWT amplifier. The degree to which the interaction efficiency increases or decreases depends significantly on the parameters φ and χ, which characterize the ion focus regime.

Let us consider this point in more detail. In the experimental papers [2–4], particular attention was paid to the dependence of the pasotron characteristics (first all, the output power) on the parameters of the working gas, which is ionized when the beam is injected into the system.

Taking into account expression (6) for δ and formula (15) for F_a, we find the active interaction power as a function of the mass of the ions filling the interaction space. Figure 2 shows the normalized active interaction power $F_a(m_i)/F_a(m_H)$ versus the ion-to-proton mass ratio. In the figure, the points corresponding to the gases that are most frequently used in pasotron experiments (He, Ar, and Kr) are indicated. It is seen that the larger the mass of the ions that are used to focus the electron beam in a pasotron, the higher the active beam–wave interaction power; this is confirmed by the experimental results of [1, 4].

Another important pasotron characteristic is the power gain factor G, which is defined as

$$G\ [\text{dB}] = 10 \log(|E(l)/E(0)|^2),$$

where the field amplitude $E(l)$ at the output of the amplifier is determined by formula (14).

Figure 3 shows the pasotron power gain factor as a function of the parameter CN for different values of the ion-focusing parameter χ. These curves can be interpreted as the dependences of the power gain factor on the beam current ($CN \propto I_0^{1/3}$) or the interaction length ($CN \propto l$). It can be seen that, at small values of CN, the wave power varies insignificantly along the tube. This is related to the fact that, at small interaction lengths, the beam is yet almost unbunched and inefficiently interacts with the forward electromagnetic wave. As the parameter CN increases, the amplitudes of both the

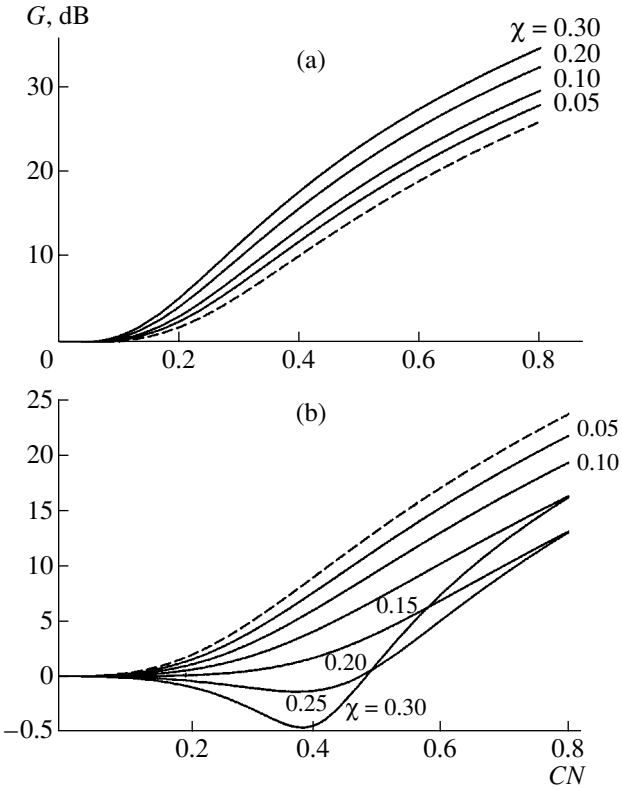

Fig. 3. Power gain factor G of a TWT pasotron amplifier vs. dimensionless tube length CN for $\varphi = 15$, $\Phi_0 =$ (a) -0.54π and (b) -1.2π, and different values of χ. The dashed lines correspond to the case of a TWT tube with an electron beam in an infinitely strong magnetic field ($\chi = 0$).

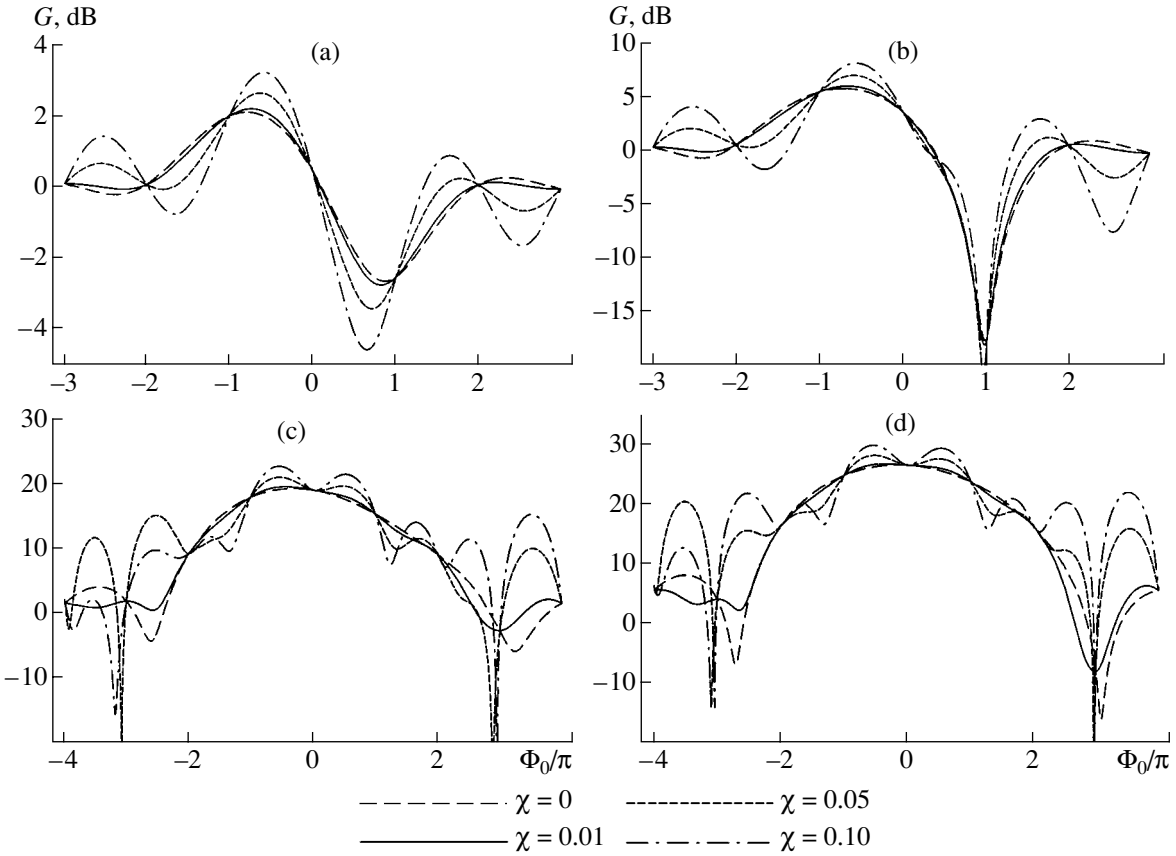

Fig. 4. Power gain factor G of a TWT pasotron amplifier vs. relative transit angle Φ_0 for $\varphi = 15$; dimensionless tube lengths of CN = (a) 0.2, (b) 0.3, (c) 0.6, and (d) 0.8; and different values of χ.

bunched current and the field in the tube increase, which results in a rapid increase in the power gain factor.

It can be seen in Fig. 3a, which is drawn for the relative transit angle $\Phi_0 > -\pi$, that the pasotron power gain factor increases with increasing parameter χ. As has already been pointed out, this is related to an increase in the effective beam–wave coupling impedance at $|\Phi_0| < \pi$ (see Fig. 1).

At $\Phi_0 < -\pi$ (Fig. 3b), the situation is the opposite. In this case, the power gain factor G decreases with increasing χ, which is related to the decrease in $|F_a|$ at $|\Phi_0| > \pi$. It can also be seen in Fig. 3b that, at large values of the ion-focusing parameter ($\chi > 0.22$), the dependence $G(CN)$ becomes nonmonotonic.

In order to examine in more detail the problem of signal amplification in a pasotron, we consider the dependence of the power gain factor on the relative transit angle Φ_0. Note that, at a fixed signal frequency ω, the relative transit angle characterizes the detuning from the "cold" beam–wave synchronism, i.e., the difference between the phase velocity v_{ph} of a "cold" wave in the transmission line and the electron beam velocity v_0. As follows from the definition of the relative transit angle, the case $v_0 > v_{ph}$ correspond to $\Phi_0 < 0$ and vice versa. Figure 4 shows the power gain factor G as a function of Φ_0 for different values of the parameter χ and the dimensionless pasotron length CN. The case $\chi = 0$ corresponds to the power gain factor of a conventional TWT amplifier calculated in the first order of the method of successive approximations (see [18, 19] for details), which is valid at $CN < 1.0$.

The transit-angle dependences of the power gain factor $G(\Phi_0)$ calculated at different dimensionless tube lengths CN (different beam currents) show that the shape of the dependence becomes more intricate as the parameter χ increases. Thus, at $\chi < 0.03$, the dependence of the power gain factor on the relative transit angle Φ_0 (or the wave frequency) is close to the corresponding curve calculated for a conventional TWT amplifier ($\chi = 0$). However, at $\chi > 0.03$, the shape of the function $G(\Phi_0, \chi)$ changes radically and the dependence $G(\Phi_0)$ becomes highly nonmonotonic as the parameter CN increases. The latter is a very adverse feature, because, in this case, a TWT pasotron will substantially distort a broadband signal even when operating in the linear regime.

A pasotron operating as a backward-wave tube amplifier or oscillator (BWT pasotron). Let us now

consider an electron beam interacting with a backward wave in the slow-wave structure of a pasotron. In this case, instead of integral equation (13), describing the amplification of a forward wave by a curved electron beam, one must use the following equation describing the excitation of a backward wave [18, 19]:

$$E(z) = E^0 e^{-j\beta_0(z-l)} - \frac{\beta_0^2 K}{2}\int_z^l \tilde{i}(\xi)\varphi_\perp(\bar{r}_i)e^{-j\beta_0(z-\xi)}d\xi. \quad (17)$$

After mathematical manipulations similar to those performed for the case of a TWT pasotron, we arrive at an expression for the total field at the output of the system ($x = 0$). In the first-order approximation, it has the form

$$E(0) = E^0 e^{j\beta_0 l} e^{-\beta_0 r_i} \times [1 + (2\pi CN)^3 (F_a(\Phi_0, \varphi, \chi) + jF_r(\Phi_0, \varphi, \chi))], \quad (18)$$

where the functions F_a and F_r are defined by formulas (15) and (16) and the other notation is the same as in formula (14).

By analogy to a TWT pasotron, we can introduce the power gain factor of a BWT pasotron:

$$G\ [\text{dB}] = 10\log(|E(0)/E(l)|^2),$$

where $E(l)$ is the amplitude of the input signal and $E(0)$ is the amplitude of the output signal, as described by expression (18).

Figure 5a shows the power gain factor of a BWT pasotron as a function of Φ_0 (the input signal frequency ω) for different values of the ion-focusing parameter χ and the same value of CN =0.3 (the same beam current). It can be seen from this figure that, at the same beam current (the parameter CN) and the optimum electron transit angle, the larger the parameter χ, the higher the power gain factor G and the narrower the amplification band $G(\Phi_0)$ (which is defined as the width of the $\Delta\Phi_0$ peak at a level of 3 dB). The relative amplification bandwidth $\Delta\omega/\omega$ is related to $\Delta\Phi_0$ by the formula $\Delta\omega/\omega \approx \Delta\Phi_0/2\pi N(1 - v_0/v_g)^{-1}$, where v_g is the wave group velocity in the transmission line [18]. We note that, as the parameter χ increases, the second amplification region appears at $\Phi_0 \approx -2.5\pi$.

The above is illustrated by Fig. 5b, which shows the maximum value of the power gain factor $G_{\max}$ and the amplification bandwidth $\Delta\omega$ as functions of the parameter χ at $\varphi = 15$. All the quantities are normalized to their values at $\chi = 0$. It can be seen that, in the framework of linear theory, the increase in the amplitude of the beam oscillations is accompanied by both the increase in the power gain factor from 16 to 24 dB and the narrowing of the relative amplification bandwidth. Such behavior of the power gain factor is related, as has already been pointed out, to an increase in the effective beam–wave coupling impedance in the transmission line with increasing ion-focusing parameter χ.

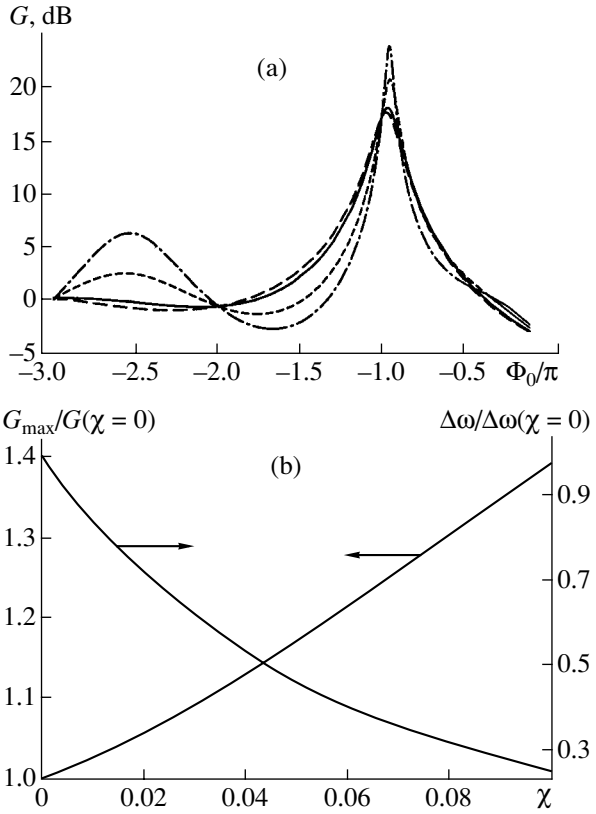

Fig. 5. (a) Power gain factor G of a BWT pasotron amplifier vs. relative transit angle Φ_0 for the same values of χ as in Fig. 4; (b) the maximum value of the power gain factor $G_{\max}$ and the amplification bandwidth $\Delta\omega$ as functions of χ at $\varphi = 15$.

We note that, in contrast to the TWT pasotron, we are now dealing with a regenerative amplification. Hence, at certain parameters of the system, the regime of backward-wave generation can be achieved. For such a BWT pasotron oscillator to be excited, it is necessary that either the gain factor tend to infinity or the field amplitude at the collector end of the tube vanish ($E(l) = 0$). Then, from expression (18) and formulas (15) and (16), we obtain the starting conditions for a BWT oscillator operating in the ion focus regime (BWT pasotron):

$$1 + (2\pi CN_s)^3 F_a(\Phi_{0s}, \varphi, \chi) = 0, \quad F_r(\Phi_{0s}, \varphi, \chi) = 0, \quad (19)$$

where the lower index s stands for the parameter values corresponding to the self-excitation of a BWT pasotron oscillator.

The solution of Eqs. (19) shows that the starting conditions for a pasotron oscillator depend weakly on the ion-focusing parameters and are close to those for an O-type BWT tube: $\Phi_{0s} \approx -\pi$ and $CN_s \approx 3.0$. It also follows from Eqs. (19) that the higher oscillation modes are easier to excite in a pasotron oscillator than in con-

ventional BWT oscillators; however, to determine the starting conditions for the excitation of these modes, it is necessary to use higher orders of the successive approximation method.

Therefore, in this study, we have analytically (in a linear approximation) investigated the interaction of an electron beam with a forward and a backward waves in a transmission line in the ion focus regime. The analysis is based on the method of successive approximations that was earlier used successfully in studying devices with long-term interaction. The results of the investigation of the interaction of an electron beam with slowed-down electromagnetic waves in the ion focus regime comply well with a simple qualitative picture of the physical processes in a pasotron.

ACKNOWLEDGMENTS

We are grateful to Prof. Yu.P. Bliokh (Technion, Israel) for fruitful discussions of pasotron physics. This study was supported in part by Russian Federal Program for Support of Leading Scientific Schools, the State Research and Education Center for Nonlinear Dynamics and Biophysics at the Chernyshevsky Saratov State University, and the U.S. Civilian Research and Development Foundation for the Independent States of the Former Soviet Union (grant no. REC-006).

REFERENCES

1. G. S. Nusinovich, Yu. Carmel, and T. M. Antonsen, IEEE Trans. Plasma Sci. **26**, 628 (1998).
2. D. M. Goebel, J. M. Butler, R. W. Schumacher, *et al.*, IEEE Trans. Plasma Sci. **22**, 547 (1994).
3. E. S. Ponti, D. M. Goebel, J. R. Feicht, and J. Santoru, Proc. SPIE **2557**, Paper 2557-09 (1995).
4. D. M. Goebel, E. S. Ponti, J. R. Feicht, and R. M. Watkins, Proc. SPIE **2843**, 69 (1996).
5. G. S. Nusinovich and Yu. P. Bliokh, Phys. Rev. E **62**, 2657 (2000).
6. Yu. P. Bliokh, G. S. Nusinovich, J. Felsteiner, and V. L. Granatstein, Phys. Rev. E **66**, 056503 (2002).
7. M. M. Bredov, in *Collection of Scientific Works Dedicated to the 70th Anniversary of Academician A. F. Ioffe* (Akad. Nauk SSSR, Moscow, 1950), p. 155.
8. B. I. Davydov and S. I. Braginskiĭ, in *Collection of Scientific Works Dedicated to the 70th Anniversary of Academician A. F. Ioffe* (Akad. Nauk SSSR, Moscow, 1950), p. 72.
9. Yu. D. Zharkov, Izv. Vyssh. Uchebn. Zaved. Radiofiz. **4**, 446 (1961).
10. L. É. Bakhrakh and Yu. D. Zharkov, Radiotekh. Élektron. (Moscow) **7**, 976 (1961).
11. B. S. Dmitriev, V. G. Medoks, and I. L. Sokolov, Élektron. Tekh., Ser. 1: Élektron. SVCh, No. 1, 61 (1966).
12. E. S. Ponti, D. M. Goebel, R. L. Poeschel, and R. M. Watkins, Proc. SPIE **2843**, 240 (1996).
13. D. M. Goebel, R. W. Schumacher, and R. M. Watkins, in *Proceedings of the 9th International Conference on High-Power Particle Beams, Washington, 1992*, Vol. 11, p. 1093.
14. D. M. Goebel and R. W. Schumacher, US Patent No. 5537005 (1996).
15. D. M. Goebel, Rev. Sci. Instrum. **67**, 3136 (1996).
16. A. V. Gaponov, Izv. Vyssh. Uchebn. Zaved., Radiofiz. **2**, 443 (1959).
17. A. V. Gaponov, Izv. Vyssh. Uchebn. Zaved., Radiofiz. **2**, 451 (1959).
18. V. N. Shevchik and D. I. Trubetskov, *Analytical Methods in Microwave Electronics* (Sov. Radio, Moscow, 1970).
19. D. I. Trubetskov and A. E. Khramov, *Lectures on Microwave Electronics for Physicists* (Nauka, Moscow, 2003), Vol. 1.

Translated by A.S. Sakharov

Plasma Physics Reports, Vol. 30, No. 1, 2004, pp. 83–90. Translated from Fizika Plazmy, Vol. 30, No. 1, 2004, pp. 88–95.

IONOSPHERIC PLASMA

On the Mechanism for the Generation of a Vortex Electric Field in the Ionospheric E-Region

A. G. Khantadze*, G. D. Aburjania, G. V. Jandieri**, and Kh. Z. Chargazia****

** Tbilisi State University, Chavchavadze ave. 1, Tbilisi, 380128 Georgia*

*** Vekua Institute of Applied Mathematics, Tbilisi State University, University str. 2, Tbilisi, 380043 Georgia*

Received May 15, 2002; in final form, January 15, 2003

Abstract—A mechanism is proposed for the generation of a vortex electric field in the ionospheric E-region. It is shown that long-scale (with a wavelength of $L > 10^3$ km) synoptically short-period (from several minutes to several hours) fast (with a propagation velocity higher than 1 km/s) processes excite a vortex electric field that may be much higher than the dynamo field generated in this region by ionospheric winds. © *2004 MAIK "Nauka/Interperiodica".*

1. INTRODUCTION

It is commonly accepted [1–3] that, in the E-region, ionospheric winds can only result in the excitation of an electrostatic polarization field via the dynamo mechanism: $\mathbf{E}_\Phi = -\nabla\Phi = -(\mathbf{V}_n \times \mathbf{H}_0)/c$, where $\mathbf{V}_n$ is the velocity of the neutral component (wind), $\mathbf{H}_0$ is the geomagnetic field, Φ is the electrostatic potential, and c is the speed of light. In this approach, only the currents $\mathbf{j}$ excited in the ionospheric E-region are usually considered, whereas the geomagnetic field perturbations $\mathbf{h}$ produced by these currents are ignored. It is clear, however, that the description of magnetohydrodynamic (MHD) waves (and, thus, a vortex electric field) is impossible in disregard of a vector equation for $\mathbf{h}$ ($\partial\mathbf{h}/\partial t = -c\nabla \times \mathbf{E}$).

Meanwhile, measurements performed with a global network of ionospheric and magnetic observatories [4–6] clearly show that, during earthquakes, major artificial explosions, and magnetic storms and substorms, long-scale (with a wavelength of $\lambda \cong 10^3$–10^4 km) electromagnetic perturbations are excited in the ionospheric E-region and propagate in the latitudinal direction around the Earth with relatively high (1–20 km/s) phase velocities. The characteristic period of such perturbations varies from several minutes to several hours, and their daytime and nighttime phase velocities differ by one order of magnitude.

We note that, in [7–9], theoretical models were proposed in which geomagnetic pulsations in the above frequency and phase-velocity ranges are interpreted as long-wavelength MHD perturbations. The maximum wavelength of these perturbations is less than 10^3 km (for longer perturbations with wavelengths of 10^3–10^4 km, it becomes necessary to take into account the inhomogeneity of the geomagnetic field and the angular velocity of the Earth's rotation). The phase velocity of MHD waves is proportional to the Alfvén velocity in terms of the neutral particle density [1–3, 9] (in contrast to fully ionized plasma, in which the Alfvén velocity is determined by the ion density). Therefore, the observed difference in the daytime and nighttime phase velocities of long-scale (10^3–10^4 km) electromagnetic ionospheric perturbations under consideration does not allow one to identify these perturbations as Alfvén, magnetosonic, or gyrotropic waves.

The existence of fast planetary electromagnetic waves in the ionospheric E-region was theoretically predicted by one of us in [10]. This approach was further developed in [11, 12]. In those papers, it was a priori assumed that both electrostatic and vortex electric fields are present in the E-region. It was shown that the electrostatic polarization field $\mathbf{E}_\Phi$ generates slow Rossby waves in the E-region that propagate in the latitudinal direction with a phase velocity on the order of the mean zonal wind velocity $C_{ph-} = \bar{V}_x - \eta e H_p(1 + 3\sin^2\theta')^{1/2}/(Mcr_0k_x^2)$, whereas the vortex electric field $\mathbf{E}_v = -c^{-1}\partial\mathbf{A}/\partial t$ generates fast planetary electromagnetic waves propagating in the latitudinal direction with the phase velocity $C_{ph+} = C_H = cH_p(1 + 3\sin^2\theta')^{1/2}/(4\pi eNr_0)$. Here, $\mathbf{A}$ is the vector potential; $C_{ph} = \omega/k_x$ is the wave phase velocity; ω is the wave frequency; $k_x = 2\pi/\lambda$ is the zonal wavenumber; $\bar{V}_x$ is the velocity of ionospheric zonal wind; $\eta = N/N_n$ is the degree of ionization; N and N_n are the electron and neutral-particle densities, respectively; $\theta' = 90° - \varphi'$ is the complement of the geomagnetic latitude; r_0 is the Earth's radius; e is the elementary charge; M is the mass of an ion (or a molecule); $H_p(1 + 3\sin^2\theta')^{1/2}/r_0 = (\beta_1^2 + \beta_2^2)^{1/2}$, $\beta_1 = \partial H_{0z}/\partial y$, $\beta_2 = \partial H_{0y}/\partial y$, $\partial/\partial y = -r_0^{-1}\partial/\partial\theta'$, $H_{0z} = -2H_p\cos\theta'$, $H_{0y} = -H_p\sin\theta'$; and $H_p = 3.2 \times 10^{-5}$ T is the magnetic field strength on the geomagnetic equator. Slow Rossby

1063-780X/04/3001-0083$26.00 © 2004 MAIK "Nauka/Interperiodica"

waves were theoretically predicted in [13, 14]. In contrast to ordinary Rossby waves, which propagate only at mid- and higher altitudes, these long-scale ionospheric waves are planetary in character and can propagate at any geomagnetic altitude. On the magnetic equator ($\varphi' = 0$), their phase velocity is maximum. These waves are, in fact, eigenmodes of the ionospheric E-region [10–12].

Observations of fast planetary electromagnetic waves [15–18] indicate the existence of a source generating a vortex electric field in the E-region.

In this paper, a mechanism for the generation of a vortex electric field in the E-region is proposed and the generated field is estimated. It is shown that the above slow and fast planetary waves play an important role in the generation of a vortex electric field.

2. PROBLEM FORMULATION AND BASIC DYNAMIC EQUATIONS

The ionospheric medium is a partially ionized three-component plasma. It can be described by quasi-hydrodynamic equations that are similar to hydrodynamic ones; the only difference is the presence in the former of friction terms related to collisions between particles of different species [1, 19, 20]. Quasi-hydrodynamic equations allow one to completely describe the electric current, particle flows, and diffusion processes in the ionospheric plasma. For the long-wavelength ($\lambda > 10^3$ km) ionospheric perturbations under consideration, atmosphere inhomogeneity, plasma compressibility, and diffusion processes are of minor importance. In this case, quasi-hydrodynamic equations can be substantially simplified and reduced to the following set of linearized equations [1, 9, 19, 20]:

$$\rho_n \frac{\partial \mathbf{V}_n}{\partial t} = \mathbf{F}_n - \rho_e \nu_{en}(\mathbf{V}_n - \mathbf{V}_e) - \rho_i \nu_{in}(\mathbf{V}_n - \mathbf{V}_i), \quad (1)$$

$$\rho_e \frac{\partial \mathbf{V}_e}{\partial t} = \mathbf{F}_e - \rho_e \nu_{ei}(\mathbf{V}_e - \mathbf{V}_i) - \rho_e \nu_{en}(\mathbf{V}_e - \mathbf{V}_n) - eN\mathbf{E} - \frac{eN}{c}\mathbf{V}_e \times \mathbf{H}_0, \quad (2)$$

$$\rho_i \frac{\partial \mathbf{V}_i}{\partial t} = \mathbf{F}_i - \rho_e \nu_{ei}(\mathbf{V}_i - \mathbf{V}_e) - \rho_i \nu_{in}(\mathbf{V}_i - \mathbf{V}_n) + eN\mathbf{E} + \frac{eN}{c}\mathbf{V}_i \times \mathbf{H}_0, \quad (3)$$

$$\nabla \cdot \mathbf{V}_n = 0, \quad \nabla \cdot \mathbf{V}_e = 0, \quad \nabla \cdot \mathbf{V}_i = 0. \quad (4)$$

Here, lower indices n, e, and i stand for the quantities related to the neutral, electron, and ion components, respectively; $\mathbf{V}$ is the hydrodynamic velocity; $\rho_n = MN_n$, $\rho_e = mN$, and $\rho_i = MN$ are the mass densities of the plasma components; m is the mass of an electron; ν_{ei}, ν_{en}, and ν_{in} are the electron–ion, electron–neutral, and ion–neutral collision frequencies, respectively; and $\mathbf{F}_n$, $\mathbf{F}_e$, and $\mathbf{F}_i$ are nonelectromagnetic forces that generally contain the gradients of the tensor of the momentum flux density for the corresponding plasma components.

Equations (1)–(4), along with Maxwell's equations and equations of state and heat transfer for each of the component, form a closed set, which can be further simplified using the results of observations of dynamic processes in the ionospheric E-region.

We note that the forces $\mathbf{F}_e$, $\mathbf{F}_i$, and $\mathbf{F}_n$ are proportional to the densities of the corresponding plasma components. The degree of ionization η of the ionospheric plasma at altitudes of 80–500 km varies from 10^{-9} to 10^{-4} [1–3, 9, 19, 20]. This means that the electron and ion inertia play a negligible role as compared to the inertia of the neutral component and, thus, can be ignored. Taking this into account and allowing for the fact that, at $\eta \ll 1$, the inequality $F_n \gg F_e, F_i$ is satisfied, we sum up Eqs. (1)–(3) to arrive at the following equation of motion for the ionospheric medium in the E-region:

$$\rho_n \frac{\partial \mathbf{V}_n}{\partial t} = \mathbf{F}_n + \frac{1}{c}\mathbf{j} \times \mathbf{H}_0, \quad (5)$$

where $\mathbf{j} = eN(\mathbf{V}_i - \mathbf{V}_e)$ is the current density. We also take into account that, in view of the inequality $\eta \ll 1$, the nonelectromagnetic forces $\mathbf{F}_e$ and $\mathbf{F}_i$ are too weak to excite appreciable ionospheric currents at altitudes of 80–500 km. Then, ignoring the electron inertia, Eqs. (2) and (3) can be written in the form

$$-\frac{\nu_{ei}}{\omega_e}(\mathbf{V}_e - \mathbf{V}_i) - \frac{\nu_{en}}{\omega_e}(\mathbf{V}_e - \mathbf{V}_n) + \mathbf{V}_D \times \mathbf{h}_0 = \mathbf{V}_e \times \mathbf{h}_0, \quad (6)$$

$$\frac{1}{\omega_i}\frac{\partial \mathbf{V}_i}{\partial t} = -\frac{\nu_{ei}}{\omega_e}(\mathbf{V}_i - \mathbf{V}_e) - \frac{\nu_{in}}{\omega_i}(\mathbf{V}_i - \mathbf{V}_n) + \mathbf{V}_i \times \mathbf{h}_0 - \mathbf{V}_D \times \mathbf{h}_0, \quad (7)$$

where $\mathbf{V}_D = c\mathbf{E} \times \mathbf{H}_0/H_0^2$ is the electric drift velocity, $\mathbf{h}_0 = \mathbf{H}_0/H_0$ is the unit vector directed along the geomagnetic field, and $\omega_\alpha = eH_0/(m_\alpha c)$, ($\alpha = e, i$) is the electron (ion) gyrofrequency. Taking into account that the electron and ion gyrofrequencies in the ionosphere are $\omega_e \approx 10^7$ s^{-1} and $\omega_i \approx (1.5–3) \times 10^2$ s^{-1}, respectively, and the collision frequencies at altitudes of 80–500 km reach their maximum values ($\nu_{en} \sim 10^5$ s^{-1}, $\nu_{in} \sim 10^4$ s^{-1}, and $\nu_{ei} \sim 10^4$ s^{-1}) in the lower layers and rapidly decrease with altitude, we obtain $\nu_{ei}/\omega_e \ll 1$ and $\nu_{en}/\omega_e \ll 1$; i.e., the electron component is always magnetized in this upper atmosphere region. Moreover, the frequency of the perturbations under study satisfies the inequalities $\omega \leq 10^{-2}$ s^{-1} and $\omega/\omega_i \leq 10^{-4} \ll 1$. With

allowance for the above inequalities, Eqs. (6) and (7) take the form

$$\mathbf{V}_D \times \mathbf{h}_0 = \mathbf{V}_e \times \mathbf{h}_0 \Rightarrow \mathbf{E} = -\frac{1}{c}\mathbf{V}_e \times \mathbf{h}_0, \quad (8)$$

$$\mathbf{V}_i = \mathbf{V}_n + \frac{\omega_i}{\nu_{in}}\mathbf{V}_i \times \mathbf{h}_0 - \frac{\omega_i}{\nu_{in}}\mathbf{V}_D \times \mathbf{h}_0. \quad (9)$$

It follows from Eq. (8) that the hydrodynamic velocity of the electron component is equal to the electric drift velocity ($\mathbf{V}_e = \mathbf{V}_D$) and the geomagnetic field $\mathbf{H}_0$ is always frozen in the electron flow ($\partial\mathbf{h}/\partial t = \nabla \times (\mathbf{V}_e \times \mathbf{H}_0)$). Taking the scalar product of Eq. (8) with $\mathbf{H}_0$, we obtain the important relationship $\mathbf{E} \cdot \mathbf{H}_0 = 0$, which shows that the generated electric field is orthogonal to the geomagnetic field $\mathbf{H}_0$.

As concerns Eq. (9) for ions, we note that, at altitudes of 80–150 km, the inequality $\omega_i/\nu_{in} \sim 10^{-2} \ll 1$ is satisfied. Hence, in this region, we can omit the two last terms on the right-hand side of Eq. (9), which is thus reduced to the equality

$$\mathbf{V}_i = \mathbf{V}_n; \quad (10)$$

i.e., the ion component in the E-region is completely entrained by the neutral wind. Indeed, numerous radiophysical observations of the motion of plasma inhomogeneities in the E-region [1, 2, 9], as well as observations of neutral winds with the help of artificial glowing clouds [2, 3, 19], clearly show that the ion component in this upper atmosphere region exactly follows the neutral wind.

The set of simplified motion equations (8), (10), and (5) for electrons, ions, and neutral particles, which is obtained from the general set of quasi-hydrodynamic equations (1)–(4), is traditionally used to describe the ionospheric plasma [1–3, 9].

Thus, in the ionospheric E-region, the electron component travels under the action of the internal electric field $\mathbf{E}$ with the electric drift velocity and the ion component is entrained by the dominant zonal neutral winds flowing with a velocity $\bar{V}_x$. This means that the generated internal electric field $\mathbf{E}$, which is orthogonal to the geomagnetic field, should have both the zonal and meridional components E_x and E_y. In this case, the electrons will travel in the meridional direction under the action of the electric field component E_y caused by the Lorentz force $F_y = -eV_xH_{0z}/c = -eE_y$ (the Hall effect) and the ions will move in the zonal direction. The direction of the total current depends on the relation between the Pedersen and Hall conductivities. Since the Hall conductivity σ_2 in this upper atmosphere region is much higher than the Pedersen conductivity σ_1, the net current should flow mainly in the meridional direction.

Note that the assumption of plasma quasineutrality in the ionospheric E-region does not mean that we ignore the charge separation effect. Charge separation is taken into account implicitly by introducing the internal electric field $\mathbf{E}$ caused largely by the Hall effect.

To close the set of Eqs. (4), (5), and (8), we will use Maxwell equations

$$\frac{\partial\mathbf{h}}{\partial t} = -c\nabla \times \mathbf{E}, \quad \mathbf{j} = \frac{c}{4\pi}\nabla \times \mathbf{h}, \quad (11)$$

where $\mathbf{E} = -\nabla\Phi - c^{-1}\partial\mathbf{A}/\partial t$ and $\mathbf{h} = \nabla \times \mathbf{A}$. Excluding $\mathbf{E}$ and $\mathbf{j}$ by means of Eq. (11) and omitting the lower index n by the neutral component velocity, we arrive at the following set of MHD equations for the ionospheric E-region:

$$\frac{\partial\mathbf{V}}{\partial t} = -\nabla\left(\frac{P}{\rho_n}\right) + \mathbf{V} \times 2\boldsymbol{\omega}_0 + \mathbf{g} + \frac{\mathbf{F}_A}{\rho_n}, \quad (12)$$

$$\frac{\partial\mathbf{h}}{\partial t} = \nabla \times (\mathbf{V} \times \mathbf{H}_0) - \alpha\rho_n\nabla \times \left(\frac{\mathbf{F}_A}{\rho_n}\right) = \nabla \times (\mathbf{V}_e \times \mathbf{H}_0), \quad (13)$$

$$\frac{\mathbf{F}_A}{\rho_n} = \frac{1}{\rho_n c}\mathbf{j} \times \mathbf{H}_0 = \frac{1}{4\pi\rho_n}(\nabla \times \mathbf{h}) \times \mathbf{H}_0 = \mathbf{V} \times 2\boldsymbol{\Omega}_i - \mathbf{V}_D \times 2\boldsymbol{\Omega}_i = \mathbf{U} \times 2\boldsymbol{\Omega}_i. \quad (14)$$

Here, P is the gas-kinetic pressure, $\boldsymbol{\omega}_0$ is the vector of the Earth's rotation rate, g is the free fall acceleration, $\mathbf{U} = \mathbf{V} - \mathbf{V}_D$, $2\boldsymbol{\Omega}_i = \eta e\mathbf{H}_0/(Mc) = \eta\omega_i$; $\alpha = c^2/(\sigma_2 H_0) = c^2/(eN)$ is the Hall parameter, and $\sigma_2 = e^2N/(m\omega_e)$ is the Hall conductivity. In Eq. (13), we also took account of the equality $\mathbf{V}_i = \mathbf{V}_n = \mathbf{V}$.

It follows from Eq. (14) that the Ampère force per unit mass $\mathbf{F}_A/\rho_n = \mathbf{U} \times 2\boldsymbol{\Omega}_i$ has exactly the same structure as the Coriolis acceleration $\mathbf{V} \times 2\boldsymbol{\Omega}_i$. Hence, the Ampère force should act on the ionospheric medium in the same way as the Coriolis force. It can be seen from Eq. (14) that this interaction is determined by both the ionospheric wind flowing with a velocity $\mathbf{V}$ and the electric fields ($\mathbf{V}_D \neq 0$) generated in this upper atmosphere region.

Later, we will be interested in long-wavelength ionospheric perturbations for which latitudinal variations in neither the Earth's rotation rate $\omega_0(\theta)$ (where θ is the complement of the geographic latitude) nor the geomagnetic field $\mathbf{H}_0(\theta')$ can be ignored. Therefore, like in dynamical meteorology, such large-scale perturbations are to be described by the Helmholtz equation for vorticity, which naturally incorporates the latitudinal variations in $\boldsymbol{\omega}_0$ and $\mathbf{H}_0$, rather than by equation of motion (12). The Helmholtz equation can be obtained by

applying the operator $\nabla\times$ to both sides of Eq. (12). Finally, MHD equations (12)–(14) take the form

$$\frac{\partial \nabla\times\mathbf{V}}{\partial t} = \nabla\times(\mathbf{V}, 2\boldsymbol{\omega}_0) + \nabla\times\left[\frac{1}{4\pi\rho_n}(\nabla\times\mathbf{h})\times\mathbf{H}_0\right], \quad (15)$$

$$\frac{\partial \mathbf{h}}{\partial t} = \nabla\times(\mathbf{V}\times\mathbf{H}_0) - \frac{c\rho_n}{eN}\nabla\times\left[\frac{1}{4\pi\rho_n}(\nabla\times\mathbf{h})\times\mathbf{H}_0\right]. \quad (16)$$

The closed set of Eqs. (15) and (16) yields six scalar equations for six unknowns V_x, V_y, V_z, h_x, h_y, and h_z. After finding **V** and **h** from this set, the pressure P can be expressed in quadratures using Eq. (12); the current density and the electric field are determined from Maxwell's equations (11); and the electron and ion velocities are found from the equalities $\mathbf{V}_e = \mathbf{V}_D$ and $\mathbf{V} = \mathbf{V}_i$, respectively. Thus, in the linear approximation, the problem of three-component plasma dynamics in the ionospheric E-region is solved completely, provided that the proper initial and boundary conditions are imposed.

Equations (15) and (16) (with allowance for the solenoidal character of the vectors **V** and **h**) are the basic ones in solving the problem of generating the vortex electric field $\mathbf{E}_v = -c^{-1}\partial\mathbf{A}/\partial t$.

When deriving Eqs. (15) and (16), it was assumed that the equilibrium densities of the charged and neutral components do not vary in space and time: N = const and N_n = const. Actually, the charged particle density in the E-region varies by almost one order of magnitude in mornings and evenings. With allowance for spatiotemporal variations of $N(\mathbf{r}, t)$ and $N_n(\mathbf{r}, t)$, Eqs. (15) and (16) become partial differential equations with variable coefficients and can hardly be solved analytically. For this reason, the further analysis of Eqs. (15) and (16) will be performed for near-midday and near-midnight hours, when it can be approximately assumed that N = const and N_n = const.

3. GENERATION OF A VORTEX ELECTRIC FIELD

Before studying the mechanism for the generation of a vortex electric field in the ionospheric E-region, let us briefly analyze the excitation of large-scale weather-forming solitary vortices (cyclones and anticyclones) in the Earth's troposphere by planetary Rossby waves.

Since the wavelengths of planetary waves is comparable to the Earth's radius r_0, it is natural to use spherical coordinates when solving the problem of generating large-scale vortices in the Earth's atmosphere. However, the difficulties that arise in analytically studying the equations obtained cause us to consider the problem of vortex generation in a "standard" coordinate system [21]. This is a local Cartesian system in which the x axis is directed eastward (along a parallel), the y axis is directed northward (along a meridian), and the z axis is directed upward. The differentials dx, dy, and dz are related to the spherical coordinates λ, θ, and r by the approximate formulas $dx = r_0\sin\theta d\lambda$, $dy = -r_0 d\theta$, and $dz = dr$. The velocity components are related as follows: $V_x = V_\lambda$, $V_y = -V_\theta$, and $V_z = V_r$. Here, θ is the complement to the geographic latitude, λ is the longitude, and the radial coordinate r is counted from the Earth's center. The above coordinate system is not equivalent to an ordinary Cartesian system because the directions of the axes vary when passing from one spatial point to another. However, when considering large-scale processes, the terms that appear in the equations of atmosphere hydrodynamics due to variations in the directions of the coordinate axes can be ignored in the first approximation (see [21, 22]); as a result, the equations of motion in spherical coordinates (with allowance for the above relationships between the coordinates) take the same form as in Cartesian coordinates. Such a procedure significantly simplifies the investigation of large-scale processes in the atmosphere [21].

Below, we will also use the so-called method of "freezing" the coefficients in dynamic equations—the method known in meteorology as the β-approximation method [21]. In this approximation, the parameters $2\omega_{0z} = 2\omega_0\cos\theta_0$ and $\beta = \partial\omega_{0z}/\partial y = 2\omega_0\sin\theta_0/r_0$ are assumed to be constant when integrating the Helmholtz vorticity equation. Here, θ_0 is an average value of the complement of the geographic latitude φ_0 in the vicinity of which the problem is solved. In this case, the Helmholtz equation transforms into an equation with constant coefficients, which can then be investigated using an expansion in plane waves. The β-approximation (or β-plane) method provides relatively simple results that nevertheless allow one to reveal the distinctive features of hydrodynamic motion on a rotating sphere as compared to motion on a rotating plane. Rossby was the first to show that large-scale weather-forming planetary waves in the troposphere are horizontal–transverse waves ($\partial V_x/\partial x + \partial V_y/\partial y = 0$, $V_z = 0$). In these waves, the atmosphere particles oscillate in the meridional direction, whereas the wave itself propagates in the latitudinal direction (eastward or westward, depending on the wavelength). In planetary waves, the particle motion is characterized by a nonzero vorticity, $\nabla\times\mathbf{V} \neq 0$. Vertical tropospheric vortices (cyclones or anticyclones) are generated due to the β effect [21]:

$$\frac{\partial(\nabla\times\mathbf{V})_z}{\partial t} = -\beta V_y, \quad (17)$$

i.e., by meridional winds (V_y) and variations in the vector of the Earth's rotation rate (β). At present, this concept of generating weather-forming vortices (cyclones and anticyclones) is commonly accepted in dynamic meteorology. Along with the baroclinic effect and the

relief effect of the underlying surface, the β effect is considered one of the main mechanisms for generating vortices in the Earth's troposphere.

Below, this important mechanism for generating vortices in the rotating ionosphere will be used in solving the problem of the excitation of a vortex electric field in the E-region.

We employ Eq. (8) to exclude the term $\nabla \times \left[\frac{1}{4\pi\rho_n}(\nabla \times \mathbf{h}) \times \mathbf{H}_0\right]$ from Eq. (16) and introduce the vector potential $\mathbf{A}$ via the formula $\mathbf{h} = \nabla \times \mathbf{A}$. As a result, we obtain the following equation:

$$\frac{\partial \nabla \times \mathbf{A}}{\partial t} = \nabla \times (\mathbf{V} \times \mathbf{H}_0) + \alpha\rho_n \nabla \times (\mathbf{V} \times 2\boldsymbol{\omega}_0) - \alpha\rho_n \frac{\partial \nabla \times \mathbf{V}}{\partial t}, \quad (18)$$

which will be used to determine the vortex electric field.

At high and temperate latitudes (where $\mathbf{H}_0 = H_{0z}(\theta')\mathbf{e}_z$, $\boldsymbol{\omega}_0 = \omega_{0z}\mathbf{e}_z$, and $\mathbf{A} = A_y(x, t)\mathbf{e}_y$, with $\mathbf{e}_y$ and $\mathbf{e}_z$ being the unit vectors directed along the y and z axes, respectively), the vertical component of Eq. (18) has the form

$$\frac{\partial (\nabla \times \mathbf{A})_z}{\partial t} = -\beta' V_y - \alpha\rho_n \frac{\partial (\nabla \times \mathbf{V})_z}{\partial t}. \quad (19)$$

Here, $\beta' = \beta_1 + \beta\alpha\rho_n$ and $\beta_1 = \partial H_{0z}/\partial y = -2H_p \sin\theta_0'/r_0$ is the magnetic Rossby parameter (later, we will assume that the geographic and geomagnetic latitudes coincide: $\varphi' = \varphi$ and $\theta' = \theta$).

If a wave perturbation propagates in the latitudinal direction ($V_y(x, t) \sim \exp\{i(k_x x - \omega t)\}$), then from Eq. (19) we obtain an expression similar to Eq. (17):

$$\frac{\partial (\nabla \times \mathbf{A})_z}{\partial t} = -\beta'\left(1 - \frac{C_{ph}}{C_{ph-}}\right)V_y, \quad (20)$$

where $C_{ph} = \omega/k_x$ is the phase velocity of the perturbation and $C_{ph-} = -\beta'/(\alpha\rho_n k_x^2)$ is the phase velocity of a slow planetary Rossby wave, which is on the order of the local wind velocity, $C_{ph-} = C_p' \approx 100$–$300$ m/s. The perturbation wavelength is $\lambda \sim 10^3$–10^4 km and the period varies from one day to two weeks (or even longer) [12, 19, 21].

It follows from Eq. (20) that, similarly to the generation of large-scale tropospheric vortices (cyclones and anticyclones) due to the β effect [see Eq. (17)], the vortex component of the internal electric field $\mathbf{E}_v = -c^{-1}\partial\mathbf{A}/\partial t$ should be generated in the E-region due to the latitudinal inhomogeneity of the geomagnetic field (β_1), meridional winds (V_y), and the effect related to the finite propagation velocity of an ionospheric wave perturbation ($C_{ph} \neq 0$).

Let us estimate the vortex electric field generated by fast long-wavelength ($\lambda \sim 10^3$–10^4 km) perturbations and compare it with the dynamo field $\mathbf{E}_d = \mathbf{V} \times \mathbf{H}_0/c$ generated by the meridional wind. To this end, we rewrite expression (20) in the form

$$(\nabla \times \mathbf{E}_v)_z = \frac{\beta'}{c}\left(1 - \frac{C_{ph}}{C_{ph-}}\right)V_y. \quad (21)$$

Taking into account that $C_{ph} = C_H$, $C_H/C_{ph} \gg 1$, and $\beta' \sim \beta_1 \approx H_{0z}/r_0$ and introducing the characteristic scale length of the perturbation along the x axis, $L = \lambda/2\pi$, we obtain from Eq. (21) the following estimate for the ratio of the vortex field $E_{v,y}$ to the dynamo field $E_{d,x} = -V_y H_{0z}/c$:

$$\frac{E_{v,y}}{E_{d,x}} \approx \frac{L}{r_0}\frac{C_H}{C_{ph-}} = \frac{\lambda}{2\pi r_0}\frac{C_H}{C_{ph-}}. \quad (22)$$

For $\lambda = 3000$ km, $C_H = 2$ km/s, and $C_{ph-} = 100$ m/s, we have $E_{v,y}/E_{d,x} \approx 1.5$; for $\lambda = 6000$ km, we have $E_{v,y}/E_{d,x} \approx 3$; for $\lambda = 10^4$ km, we have $E_{v,y}/E_{d,x} \approx 5$; and for $C_H = 20$ km/s and $\lambda = 3000$ km, we have $E_{v,y}/E_{d,x} \approx 15$. It can be seen from these estimates that, in the case of fast planetary ionospheric perturbations, the generated vortex electric field should play a decisive role in the electrodynamic processes occurring in the E-region.

We note that parameters of a wave perturbation (in particular, the electric field amplitude) propagating in the ionospheric layer under study (the Hall layer) also depend on the Pedersen conductivity σ_1. This problem was considered in [23], in which the Pedersen and Hall conductivities, both of the components of the geomagnetic field (H_{0y} and H_{0z}), and the four gradients of the geomagnetic field ($\beta_1 = \partial H_{0z}/\partial y$, $\beta_2 = \partial H_{0y}/\partial y$, $\beta_3 = \partial H_{0z}/\partial z$, and $\beta_4 = \partial H_{0y}/\partial z$) were taken into account. It was shown that, in the upper layers of the E-region (at altitudes of 100–150 km), fast waves with a wavelength of 2000 km are significantly damped due to the Pedersen conductivity. However, longer waves are damped weakly. For example, at an altitude of 120 km, the ratio between the damping rates γ of waves with the wavelengths $\lambda_1 = 2000$ km and $\lambda_2 = 10^4$ km is $\gamma_1/\gamma_2 \approx 20$–$50$. It was also shown that the longer the wavelength of fast electromagnetic waves, the wider the layer in which the damping rate related to the Pedersen conductivity is low. Therefore, in this paper, in considering long-wavelength perturbations with $\lambda \sim 10^4$ km, we neglect for the sake of simplicity the Pedersen conductivity in the Hall layer, assuming that $\mathbf{H}_0 = H_{0z}\mathbf{e}_z$.

4. CONDITION FOR THE GEOMAGNETIC FIELD TO BE FROZEN IN THE PLASMA IN THE IONOSPHERIC E-REGION

To reveal the specific features of the mechanism for generating an internal electric field $\mathbf{E}$, we will consider

the condition for the geomagnetic field to be frozen in the plasma in the ionospheric E-region. To this end, we rewrite Helmholtz vorticity equation (15) and Maxwell's equation (16) in the form

$$\frac{\partial \nabla \times \mathbf{V}}{\partial t} = \nabla \times (\mathbf{V} \times 2(\boldsymbol{\omega}_0 + \boldsymbol{\Omega}_i)) - \nabla \times (\mathbf{V}_D \times 2\boldsymbol{\Omega}_i), \quad (23)$$

$$\frac{\partial \mathbf{h}}{\partial t} = \nabla \times (\mathbf{V}_c \times \mathbf{H}_0) = \alpha\rho \nabla \times (\mathbf{V}_D \times 2\boldsymbol{\Omega}_i). \quad (24)$$

To obtain these equations, we use expression (14) for the Ampére force and the equality $\mathbf{V}_e = \mathbf{V}_D$.

It follows from Eq. (24) that, in the ionospheric E-region, the geomagnetic field is completely frozen in the electron component, whereas the ion component is frozen in only partially. Indeed, using the equality $\mathbf{V}_e = \mathbf{V}_i - \mathbf{j}/eN$, we exclude the electron velocity from Eq. (24) to obtain the equation for the partially frozen-in ion component:

$$\frac{\partial \mathbf{h}}{\partial t} = \nabla \times (\mathbf{V}_i \times \mathbf{H}_0) - \alpha \nabla \times \left(\frac{1}{c}\mathbf{j} \times \mathbf{H}_0\right). \quad (25)$$

In the β-plane approximation, for high and temperate latitudes (where $\mathbf{H}_0 = H_{0z}(\varphi')\mathbf{e}_z$ and $\mathbf{V}_e = V_{ey}\mathbf{e}_y$), we obtain from Eq. (24) the conservation condition for the total magnetic field $\mathbf{H} = \mathbf{H}_0 + \mathbf{h}$:

$$\frac{d}{dt}(h_z + H_{0z}) = 0, \quad (26)$$

where $d/dt = \partial/\partial t + V_{ey}\partial/\partial y$.

It follows from Eq. (26) that there is an invariant:

$$h_z + H_{0z} = h_z - 2H_p \sin\varphi' = \text{const}. \quad (27)$$

From Eq. (27) we find that, in the absence of a meridional electron flow ($V_{ey} = 0$), $-2H_p\sin\varphi' = \text{const}$. In the case of a northward meridional electron flow, $\sin\varphi'$ increases and, for condition (27) to hold, a positive perturbation of the geomagnetic field h_z should be generated. In the case of a southward electron flow, $\sin\varphi'$ decreases and the generated perturbation of the geomagnetic field should be negative ($h_z = -|h_z|$). If the electron component is perturbed by a horizontal–transverse planetary wave, then the generated magnetic field oscillates with the wave frequency. For fast planetary waves, as was shown above, the time derivative $\partial\mathbf{h}/\partial t$ gives rise to a significant vortex electric field. When the electron component oscillates with a period of slow horizontal–transverse waves (from one day to longer than two weeks), the time derivative $\partial\mathbf{h}/\partial t$ is negligibly small and no vortex electric field is excited in the ionospheric E-region.

Since the equality $V_e = V_D$ holds in the E-region, the electrodynamic interaction caused by the Ampére force $\mathbf{F}_A/\rho_n = (\mathbf{V} - \mathbf{V}_D) \times 2\boldsymbol{\Omega}_i$ is determined by the value of the electric drift velocity.

1. For $V_D \gg V = V_i$, the ion and neutral components of the ionospheric plasma can be considered immovable as compared to the electron component ($V_e = V_D$). Then, from the expression $\mathbf{j} = eN(\mathbf{V}_i - \mathbf{V}_e)$ we obtain the approximate equality $\mathbf{V}_e \approx -\mathbf{j}/eN$, and the electrodynamic problem of the generation of a vortex electric field reduces to one induction equation,

$$\frac{\partial \mathbf{h}}{\partial t} = -\nabla \times \left(\frac{1}{eN}(\mathbf{j} \times \mathbf{H}_0)\right) = -\frac{c}{4\pi eN}\nabla \times (\nabla \times \mathbf{h} \times \mathbf{H}_0), \quad (28)$$

from which, in the β-plane approximation, we obtain (assuming that $\mathbf{H}_0 = H_{0z}(\theta')\mathbf{e}_z$ and $h_z = h_z(x, t)$) the equation for fast planetary waves:

$$\frac{\partial h_z}{\partial t} = -\frac{c\beta_1}{4\pi eN}\frac{\partial h_z}{\partial x} \quad \text{or} \quad \frac{\partial V_{ey}}{\partial t} = -\frac{c\beta_1}{4\pi eN}\frac{\partial V_{ey}}{\partial x}. \quad (29)$$

For h_z, $V_y \sim \exp\{i(k_x x - \omega t)\}$, we find that the wave phase velocity is

$$C_{ph-} = \frac{\omega}{k_x} = C_H = \frac{c}{4\pi eN}\frac{\partial H_{0z}}{\partial y}. \quad (30)$$

Therefore, fast waves in the ionospheric E-region propagate against a practically immovable ion–neutral background. It is only the electron component with the frozen-in geomagnetic field that oscillates, thus giving rise to the induced magnetic field $\mathbf{h}$ and the vortex electric field ($\nabla \times \mathbf{E} \neq 0$). In fact, introducing the electron displacement $\xi_e(V_{ey} = d\xi_e/dt)$, from frozen-in condition (26) we have $h_z = -\beta_1\xi_y$. Then, using the second equation in (29), we arrive at the linear-oscillator equation $d^2\xi_y/dt^2 + \omega_0^2\xi_y = 0$ with the eigenfrequency $\omega = \omega_0 = k_x c\beta_1/(4\pi eN)$. A comparison of expression (30) with the phase velocity of short-wavelength whistling atmospherics (helicons) [24] $C_h = cH_{0z}k_z/4\pi eN$ shows that both types of waves are of the same physical nature and represent oscillations of the electron component frozen in the geomagnetic field. The only difference is that, for whistling atmospherics, the phase velocity depends on the vertical component of the geomagnetic field H_{0z} and the vertical component of the wavenumber k_z, whereas for C_H waves, it depends on the magnetic field gradient $\partial H_{0z}/\partial y$, which naturally determines the large-scale nature of C_H waves. Hence, at $V_D \gg V = V_i$, the electromagnetic interaction of the internal electric field $\mathbf{E}$ with the plasma in the ionospheric E-region is associated with fast planetary perturbations and the method for determining the eigenfrequencies of these perturbations may be called the inductive MHD approximation.

2. For $V_D = V = V_i$, electrodynamic processes in the E-region result in slow perturbations propagating with the local wind velocity. Since, in this case, both of the charged ionospheric plasma components are completely entrained by the wind, the electric current den-

sity $\mathbf{j} = eN(\mathbf{V}_i - \mathbf{V}_e)$ vanishes and dynamic equations (23) and (24) take the form

$$\frac{\partial \nabla \times \mathbf{V}}{\partial t} = \nabla \times (\mathbf{V} \times 2\boldsymbol{\omega}_0), \quad (31)$$

$$\frac{\partial \mathbf{h}}{\partial t} = \nabla \times (\mathbf{V} \times \mathbf{H}_0). \quad (32)$$

In view of the fact that slow planetary Rossby waves (with the phase velocity $C_{ph-} = -\beta/k_x^2$ and a period from one day to longer than two weeks) are exact solutions to Eq. (31), we can ignore the time derivative $\partial\mathbf{h}/\partial t$ in Maxwell's equation. This means that, for slow long-wavelength perturbations, the internal field is potential: $\nabla \times \mathbf{E} = 0$. This condition, along with the equation $\nabla \times (\mathbf{V}, \mathbf{H}_0) = 0$, allows us to unambiguously determine the polarization electric field generated in the ionospheric E-region by the neutral wind:

$$\mathbf{E}_\Phi = -\nabla\Phi = -\frac{1}{c}\mathbf{V} \times \mathbf{H}_0. \quad (33)$$

This approximation, as was mentioned above, may be referred to as the noninductive MHD approximation [19, 20].

3. The case $V_D \ll V = V_i$ corresponds to ultraslow electrodynamic processes in which the electron component, in view of the equality $V_e = V_D$, can be considered almost immovable, so that the current $\mathbf{j}$ is mainly produced by the ion component. It follows from Eq. (8) that, in this case, $\mathbf{E} \approx 0$. Then, from Maxwell's equation $\partial\mathbf{h}/\partial t = -c\nabla \times \mathbf{E}$, we have $\partial\mathbf{h}/\partial t = 0$. Therefore, ultraslow processes in the E-region do not lead to the generation of an internal electric field. If an electric field is, nevertheless, present in such slow ionospheric processes, then one may conclude that this field is produced due to certain external effects (e.g., the penetration of electric fields from the magnetosphere and auroral regions). In this case, Eqs. (23) and (24) can be reduced to one closed Helmholtz equation

$$\frac{\partial \nabla \times \mathbf{V}}{\partial t} = \nabla \times [\mathbf{V} \times 2(\boldsymbol{\omega}_0 + \boldsymbol{\Omega}_i)]. \quad (34)$$

Exact solutions to this equation are ultraslow planetary Rossby waves propagating in the E-region with the phase velocity $C_{ph-} = -(\beta + \beta_H)/k_x^2$, where $\beta = \partial 2\omega_{0z}/\partial y$ and $\beta_H = \partial 2\Omega_{iz}/\partial y = (eN/(N_n Mc))\partial H_{0z}/\partial y$. Since ω_{0z} and H_{0z} are opposite in sign ($\omega_{0z} > 0$ and $H_{0z} < 0$), the phase velocity of ultraslow planetary waves is lower than the phase velocity of ordinary Rossby waves, which are described by Eq. (31). Numerical results show that, in the nighttime, the quantity $\beta + \beta_H$ vanishes at an altitude of 150 km, and in the daytime, it vanishes at an altitude of 115 km. Accordingly, ultraslow planetary wave should not exist at these altitudes in the corresponding periods of time [12].

5. CONCLUSIONS

A physical mechanism for the generation of an internal electric field by long-wavelength ($\lambda \sim 10^3$–10^4 km) perturbations in the ionospheric E-region has been investigated using a three-fluid model of the ionospheric plasma.

It is shown that the electrostatic polarization field $\mathbf{E}_\Phi = -\nabla\Phi$ is generated by slow planetary hydrodynamic waves with a period from one day to two weeks (or even longer). Such long-period processes are described by MHD equations in the noninductive approximation. In this case, the electrostatic field $\mathbf{E}_\Phi$ is generated due to the dynamo effect. Diurnal tidal motions (thermal tide) and the accompanying slow planetary waves are the main source for the generation of S_q currents in the ionospheric E-region [1–3]. It has been found that ultraslow planetary Rossby waves are not accompanied by the generation of internal electric fields in the E-region. If an electric field is, nevertheless, present in such slow (almost stationary) ionospheric processes, then one may conclude that this field is produced due to certain external effects.

It has been shown that fast planetary waves in the ionospheric E-region perturb only the electron component and the geomagnetic field frozen in it. In this case, an internal vortex electric field is naturally generated. It has been found that the vortex electric field is several times higher than the polarization field generated due to the dynamo effect. It has been shown that fast ionospheric processes can be adequately described in the inductive approximation. A formula has been derived [see Eq. (21)] that allows one to unambiguously determine the character (potential or vortex) of the generated internal field from the measured phase velocity of large-scale wave perturbations in the ionospheric E-region.

REFERENCES

1. B. I. Gershman, *Dynamics of the Ionospheric Plasma* (Nauka, Moscow, 1974), p. 163.
2. É. S. Kazimirovskiĭ and V. D. Kokourov, *Ionospheric Motions* (Nauka, Novosibirsk, 1979), p. 34.
3. V. M. Polyakov, L. A. Shepkin, É. S. Kazimirovskiĭ, and V. D. Kokourov, *Ionospheric Processes* (Nauka, Novosibirsk, 1968), p. 288.
4. V. A. Liperovskiĭ, O. A. Pokhotelov, and S. A. Shalimov, *Ionospheric Precursors of Earthquaks* (Nauka, Moscow, 1992).
5. V. I. Drobzhev, G. R. Moloetov, Z. S. Sharadze, *et al.*, Ionosfer. Issled., No. 39, 61 (1986).
6. L. A. Haykowicz, Planet. Space Sci. **39**, 583 (1991).
7. V. I. Sorokin, Geomagn. Aeron. **26**, 640 (1986); **28**, 490 (1988).
8. N. D. Borisov, Geomagn. Aeron. **28**, 469 (1988); **29**, 614 (1989).
9. V. M. Sorokin and G. V. Fedorovich, *Physics of Slow MHD Waves in Ionospheric Plasma* (Énergoizdat, Mos-

cow, 1982); Izv. Vyssh. Uchebn. Zaved. Radiofiz. **25**, 490 (1982).
10. A. G. Khantadze, Soobshch. Akad. Nauk Gruz. SSR, No. 1, 69 (1986).
11. A. G. Khantadze, Dokl. Akad. Nauk **376**, 703 (2001).
12. G. D. Aburjania and A. G. Khantadze, Geomagn. Aéron. **42**, 1 (2002).
13. I. Tolstoy, J. Geophys. Res. **7**, 1435 (1967).
14. A. G. Khantadze, Tr. Inst. Geofiz. Akad. Nauk Gruz. SSR **28**, 112 (1967).
15. Z. S. Sharadze, G. A. Dzhaparidze, and G. B. Kikvilashvili, Geomagn. Aéron. **28**, 797 (1988).
16. L. S. Al'perovich, V. N. Drobzhev, V. M. Sorokin, *et al.*, Geomagn. Aéron. **22**, 797 (1982).
17. W. Baumjohann, R. A. Treumann, T. Labelle, *et al.*, J. Geophys. Res. **94** (A11), 221 (1989).
18. T. M. Bauer, W. Baumjohann, R. A. Treumann, *et al.*, J. Geophys. Res. **100** (A6), 9605 (1995).
19. A. G. Khantadze, *Some Problems of the Dynamics of a Conducting Atmosphere* (Nauka, Tbilisi, 1973), p. 88.
20. S. I. Braginskiĭ, Zh. Éksp. Teor. Fiz. **37**, 1417 (1959) [Sov. Phys. JETP **10**, 1005 (1959)].
21. L. S. Gandin, D. L. Laĭkhtman, L. T. Matveev, and M. I. Yudin, *Fundamentals of Dynamic Meteorology* (Gidrometizdat, Leningrad, 1955), p. 62.
22. P. D. Thompson, *Numerical Weather Analysis and Prediction* (McMillan, New York, 1961; Inostrannaya Literatura, Moscow, 1962).
23. Z. L. Kobaladze and A. G. Khantadze, Soobshch. Akad. Nauk Gruz. SSR **134** (1), 97 (1989).
24. B. B. Kadomtsev, *Collective Phenomena in Plasma* (Nauka, Moscow, 1988).

Translated by A.S. Sakharov

Plasma Physics Reports, Vol. 30, No. 1, 2004, pp. 9–17. Translated from Fizika Plazmy, Vol. 30, No. 1, 2004, pp. 11–20.

MAGNETIC CONFINEMENT SYSTEMS

Experimental Study of the Evaporation and Expansion of a Solid Pellet in a Plasma Heated by an Electron Beam

R. Yu. Akent'ev, A. V. Arzhannikov, V. T. Astrelin, A. V. Burdakov, I. A. Ivanov, V. S. Koĭdan, K. I. Mekler, S. V. Polosatkin, V. V. Postupaev, A. F. Rovenskikh, and S. L. Sinitskiĭ

Budker Institute of Nuclear Physics, Russian Academy of Sciences, Siberian Division, pr. Akademika Lavrent'eva 11, Novosibirsk, 630090 Russia

Received February 4, 2003; in final form, June 3, 2003

Abstract—Results are presented from experiments on the injection of solid pellets into a plasma heated by an electron beam in the GOL-3 device. For this purpose, two pellet injectors were installed in the device. The target plasma with a density of ~10^{15} cm^{-3} was produced in a solenoid with a field of 4.8 T and was heated by a high-power electron beam with an electron energy of ~1 MeV, a duration of ~7 μs, and a total energy of 120–150 kJ. Before heating, the pellet was injected into the center of the plasma column transversely to the magnetic field. The injection point was located at a distance of 6.5 or 2 m from the input magnetic mirror. Polyethylene pellets with a mass of 0.1–1 mg and lithium-deuteride pellets with a mass of 0.02–0.5 mg were used. A few microseconds after the electron beam starts to be injected into the plasma, a dense plasma bunch is formed. In the initial stage of expansion, the plasma bunch remains spherically symmetric. The plasma at the periphery of the bunch is then heated and becomes magnetized. Next, the dense plasma expands along the magnetic field with a velocity on the order of 300 km/s. A comparison of the measured parameters with calculations by a hydrodynamic model shows that, in order to provide such a high expansion velocity, the total energy density deposited in the pellet must be ~1 kJ/cm^2. This value substantially exceeds the energy density yielded by the target plasma; i.e., the energy is concentrated across the magnetic field onto a dense plasma bunch produced from the evaporated particle.

1. INTRODUCTION

One of the alternative magnetic fusion devices is the so-called multimirror system, in which an increase in the plasma confinement time is achieved due to a corrugated configuration of the magnetic field [1]. The concept of multimirror confinement implies that the ion mean free path should be much shorter than the full length of the device. Hence, in order to achieve reactor parameters at reasonable device dimensions, the plasma density should be ~10^{17} cm^{-3} and, accordingly, the β value should be larger than unity (see [2] for details). The problem of producing such a plasma is still unsolved.

Experiments in the GOL-3 device are primarily aimed at studying the physics of the production and confinement of a hot dense plasma in a multimirror system [3]. The experimental layout is shown in Fig. 1. A hydrogen or deuterium plasma with a density of 10^{14} to 10^{16} cm^{-3} is produced by a special linear discharge in the longitudinal magnetic field. Typical parameters of the pellet-injection experiments under consideration are as follows. The length and diameter of the plasma column are ~12 m and 7 cm, respectively (the diameter is given for a magnetic field of 4.8 T). The magnetic field is produced by a solenoid. The magnetic induction in the region where the field is uniform and in the end magnetic mirrors is 4.8 and 9 T, respectively. Near each of the solenoid ends, ten magnetic cells are formed. The length of each cell is 22 cm, and the minimum magnetic induction in each cell is 3.3 T. Thus, two end sections with a corrugated magnetic field are created. The plasma is heated by a relativistic electron beam with a maximum electron energy of ~1 MeV, maximum current of ~30 kA, full duration of ~7 μs, total energy of 120–150 kJ, and diameter of 6 cm (for a magnetic field of 4.8 T).

Let us briefly consider the physics of plasma heating by an injected beam under the conditions of our experiment (see [3–6]). Due to the collective beam–plasma interaction, resonant plasma oscillations are excited to which the beam transfers a fraction of its energy. The nonlinear relaxation of these oscillations leads to the heating of the plasma electrons. It was shown experimentally that the beam can lose up to 30–40% of its energy as it passes through the 12-m-long plasma column. During the beam injection, the electron temperature increases, and, at a plasma density of 10^{15} cm^{-3}, it can reach 2 keV. The ion temperature remains relatively low because of the short lifetime of the hot plasma.

As the plasma density increases, the efficiency of beam relaxation degrades and the maximum electron temperature decreases. On the other hand, the concept of multimirror confinement requires a high-temperature plasma with a density of ~10^{17} cm^{-3}. Such a density is too high for efficient beam relaxation due to collective effects. In order to achieve a high-temperature in

1063-780X/04/3001-0009$26.00

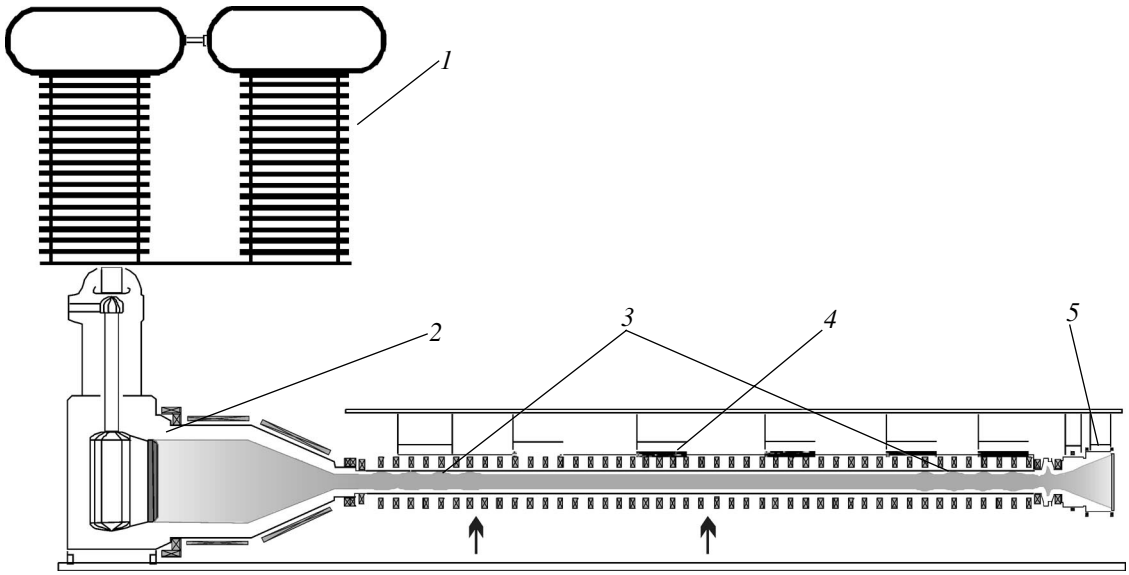

Fig. 1. Schematic of the GOL-3 device: (*1*) U-2 electron beam generator, (*2*) system for generating the electron beam (the ribbon diode and the beam magnetic-compression region), (*3*) sections with a corrugated field, (*4*) solenoid, and (*5*) exit unit (system for generating the target plasma and the beam receiver). Arrows indicate the locations of the two pellet injectors.

the dense plasma, the so-called method of the two-stage heating of a dense plasma was implemented for the first time in the GOL-3 device [7]. The method implies that a short plasma bunch with a density of 10^{17}–10^{18} cm^{-3} is produced in a long plasma column with a density of ~10^{15} cm^{-3}. The target plasma is heated due to electron beam relaxation, and the temperatures of the bunch and the target plasma are then equalized due to binary collisions.

Experiments by this scheme were conducted using gas puffing in order to form the required plasma density profile along the device. The plasma pressure increased by a factor of up to 3 as compared to the pressure of a uniform plasma with the density optimum for beam relaxation. The ion temperature in dense plasma bunches was close to the electron one (the measured ion temperature was up to 150 eV at a density higher than 5×10^{15} cm^{-3} [5]). A further increase in the temperature of the dense plasma bunch was limited by longitudinal heat conduction and the rapid longitudinal expansion of the bunch.

The experiments demonstrated the feasibility of the scheme for the two-stage heating of a dense plasma. At the same time, the method for producing dense plasma bunches by gas puffing has a number of limitations:

(i) The dense gas fills the entire cross section of the chamber, rather than only the region occupied by the plasma column. The presence of the dense gas at the periphery of the plasma column increases charge-exchange and ionization losses and leads to the cooling of the peripheral plasma.

(ii) The presence of the dense cold peripheral plasma hampers (or even makes impossible) the use of conventional diagnostics, such as the analysis of charge-exchange neutrals and measurements of the intensity and profiles of spectral lines.

(iii) The increase in the gas cloud density promotes the onset of kink instability. The reason for this is that the initial degree of gas ionization becomes too low as the density increases above a certain level. This leads to the deterioration of the conditions for beam current neutralization in the plasma. The high unneutralized beam current causes the loss of the macroscopic stability of the beam when the Kruskal–Shafranov limit is exceeded.

(iv) The element composition of gases introduced into the plasma is limited.

In this paper, we describe experiments on the production of dense plasma bunches by injecting solid pellets. A pellet consisting of about 10^{20} atoms is injected at a certain point of the plasma column. The pellet is rapidly destroyed and evaporated under the action of the high-energy electron beam, and its material is then ionized. The dense, weakly ionized vapor can expand over a distance of ~1 cm across the magnetic field. After the ionization of the pellet material is completed, the produced dense plasma becomes magnetized and its further heating proceeds in the same way as in the two-stage scheme described above. This scenario of the production of a dense plasma bunch is free of the above disadvantages of pulsed gas puffing. In addition to the production of a dense high-pressure plasma bunch, the proposed technology can be used to solve the following physical problems: local diagnostics of the plasma parameters (together with optical methods), creation of a bright source of line emission from multiply charged

ions with a given element composition, and study of material ablation in a high-temperature plasma.

The method for injecting solid pellets into plasma is well known and is used in a number of devices for diagnostic purposes, to fuel the plasma, and to control the plasma density profile (see, e.g., [8–10]). The range of physical parameters typical of the GOL-3 device allows us to use a nontraditional method of pellet injection and to significantly simplify and cheapen the required equipment. The plasma lifetime is fairly short; therefore, the pellet can be injected at the required point before the onset of the discharge. This allows us to avoid the passage of the pellet through the high-temperature plasma (in this case, the initial injection velocity can be decreased and the evaporation of the outer layers of the pellet at the plasma periphery is precluded). In this stage of an experiment, radiative losses from the plasma can be ignored even at a relatively high impurity concentration; hence, we used pellets made of hydrogen-containing materials (polymers, lithium hydride, etc.). Diagnostic pellets can have any chemical composition.

2. EXPERIMENTAL AND DIAGNOSTIC TECHNIQUES

The pellet injector was designed according to an electrodynamic scheme. The parameters of the injector were chosen to satisfy by the following technical requirements: (i) the system operation should be independent of the material and weight (within the range 0.1–10 mg) of the pellet, (ii) the injector should provide five pulses without vacuum failure in the device, and (iii) the injector should be exactly synchronized with the other systems of the device. The electrodynamic system of the injector consists of a plane coil and a driver disk adjacent to the coil. The current flowing through the coil induces the eddy currents in the driver disk. The latter is accelerated and knocks the injector striker containing a pellet in its central hollowing. A scheme with the hard stopping of the striker was chosen in order to guarantee the detachment of the pellet from the striker. The pellet is injected from bottom to top.

The current pulse in the injector coil is produced by a source consisting of a 160-μF, 500-V MBGV capacitor and a thyristor switch. The electric-circuit parameters are chosen such that the current pulse duration is on the order of the penetration time of the magnetic field into the driver disk. The current amplitude at a capacitor voltage of 350 V amounts to ~1.5 kA. The duration of the current pulse is ~75 μs. The exact positioning of the pellet in the chamber at the instant of beam injection is provided by choosing the operating voltage at a fixed triggering time of the thyristor switch (13 530 μs before the start of the beam, i.e., somewhat earlier than the magnetic system is switched on). The initial velocity of the pellet varies in the range 10–25 m/s as the supply voltage varies from 200 to 350 V. The scatter in the pellet positions from shot to shot is ~2 cm around the center of the plasma chamber.

Two injectors were fabricated and installed in the device. The first injector was placed at the diagnostic port located between the 59th and 60th coils, nearly at the center of the GOL-3 solenoid (at a distance of Z = 662 cm from the center of the input magnetic mirror, taken as the coordinate origin). The second pellet injector was placed at Z = 219 cm (between the 19th and 20th coils).

Several methods were used to diagnose the parameters of the dense plasma. At the location of the first (central) injector, the dense plasma bunch was photographed with the help of a digital photographic camera and a digital VUV pinhole camera with a frame duration of ~1 μs (the radiation fell directly on the surface of the microchannel plate). The visible emission from the dense plasma bunch was recorded by a digital spectrograph with spatial resolution. The electron density in the bunch was measured by the broadening of the hydrogen H_α line with the help of a digital spectral system consisting of two components: a high-resolution spectrometer (a detector based on a photodiode array) with a frame duration of ~1 μs and a system with a moderate spectral resolution, which scanned the line profile with a period of 5–20 μs. The light was fed to this diagnostics through a fiber whose receiving end could be placed at different distances from the pellet injector. The plasma density at a distance of ~1.9 m from the injector was measured using a Michelson interferometer operating at a wavelength of 1.15 μm. Another similar interferometer was placed at Z = 84 cm. The temperature profile across the plasma bunch was assessed from the intensity ratio of the spectral lines of ions in different ionization states. For this purpose, we used a frame VUV spectrograph with spatial resolution and a frame duration of ~1 μs. VUV plasma emission was also measured by several vacuum photodiodes positioned at different distances from the pellet injector. We also used other conventional diagnostics.

At the location of the second injector (Z = 219 cm), we used different diagnostic equipment providing us with additional information on the parameters of the dense plasma bunch. Immediately at the injection point, an optical spectrometer with spatial resolution and a sixteen-channel VUV pinhole camera with aluminum photocathodes were installed. A Thomson scattering system (a ruby laser, 694.3 nm, 5 J) that was located 33 cm from the injection point measured the electron temperature and density immediately inside the plasma bunch. Between the injector and Thomson scattering system, there were three detectors measuring plasma diamagnetism. On the other side, detectors of soft X-ray plasma emission (one covered with an 8-μm beryllium foil with a cutoff energy of 0.8 keV and the other with a 100-μm beryllium foil with a cutoff energy

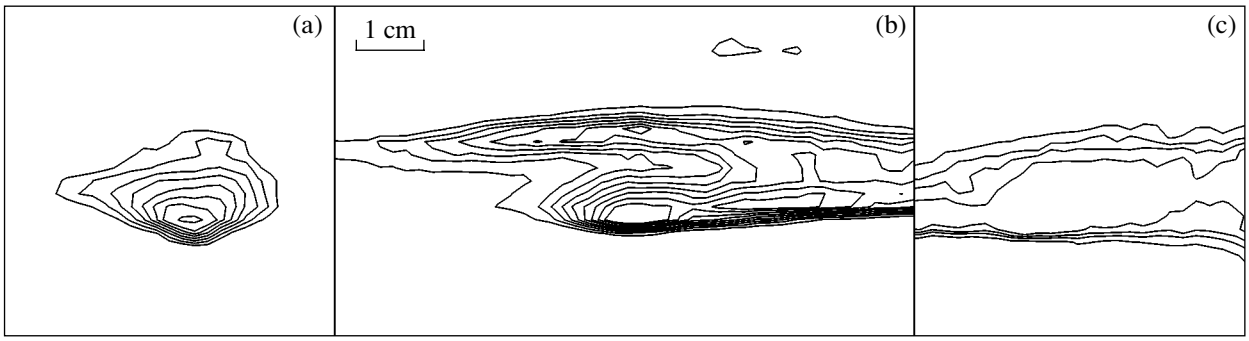

Fig. 2. Intensity of VUV emission from dense plasma in different stages of the plasma bunch formation: (a) 2 μs from the beginning of the beam injection (the formation of a spherical bunch and 3D expansion), (b) 4 μs (the transition to the magnetization regime), and (c) 6 μs (1D expansion). The contours lines of the intensity with a level exceeding the emission intensity of the surrounding target plasma are shown. The exposure time is 1 μs. The spatial scale is the same for all the frames.

of 2.2 keV) were installed at a distance of 22 cm from the injection point.

3. GENERAL PATTERN OF THE FORMATION AND EXPANSION OF A DENSE PLASMOID

A preliminary (target) plasma in the GOL-3 device was produced by a special linear discharge. The chamber was filled with hydrogen with the help of pulsed valves. By the instant when the discharge began, the gas had filled a part of the vacuum system of the device (from the compression region of the electron beam to the location of the annular cathode of the linear discharge [6]). The generation region of the electron beam and the region of the beam receiver remained at working vacuum. Due to creating the target plasma in this way, the plasma density is nonuniform along the system. In experiments with pellets, the initial density of the target plasma in the central part of the chamber (at the location of the first injector) was $\sim 10^{15}$ cm^{-3}. Toward the solenoid ends, the initial density decreased by a factor of 2–3.

On the whole, the formation of a dense plasma bunch and its expansion proceed as was described in the Introduction. The dynamics of pellet expansion can be seen in brightness maps (Fig. 2) obtained with the help of the VUV pinhole camera with an exposure of 1 μs. In these experiments, we used a 0.15-mg polyethylene pellets. Before the beam injection (when the pellet moves through the neutral gas or through the low-temperature target plasma of the linear discharge), no signs of pellet evaporation are seen.

The pellet starts to evaporate just after the beginning of the electron beam injection, when the temperature of the surrounding plasma is still rather low. Under our experimental conditions, the solid pellet is destroyed in an explosive manner due to volumetric energy deposition by the fast beam electrons (see [11]). In this stage, the expansion of the dense plasma bunch is spherically symmetric (see Fig. 2a). A characteristic feature of the GOL-3 experiments is a wide electron energy spectrum, which is a result of the collective relaxation of the beam in the plasma (see [5]). Under these conditions, the spectrum of fast electrons (within measurement accuracy) decreases monotonically toward higher energies. Electrons with energies of up to 1.3–1.5 MeV were detected, which far exceeds the energy of the injected beam electrons. Estimates show that the energy deposited in the pellet in the first stage of the process is primarily associated with fast electrons with energies from ~1 MeV (the mean free path of such electrons is much longer than the effective thickness of the plasma bunch) down to ~10 keV. As the cross section of the plasma bunch grows, the power deposited in the pellet plasma increases because of the growing contribution from electrons with relatively low energies (i.e., from electrons whose mean free path in the dense plasma bunch is comparable to its effective thickness, which decreases as the bunch diameter increases).

For some time, the center of the bunch remains cold. In experiments with a relatively massive 1-mg polyethylene pellet, the central bunch temperature calculated from the intensity ratio of the CIII 57.4-nm and CIV 154.8-nm lines at the time interval 4–6 μs from the beginning of the beam injection was found to be ~2.5 eV. The estimated ion plasma density at this time is 3×10^{18} cm^{-3}, while the electron density is nearly two times higher. Under our experimental conditions, the plasma begins to be magnetized approximately at $nT^{-3/2} \sim 10^{16}$ cm^{-3} eV$^{-3/2}$. The above parameters of the dense plasma in the time interval 4–6 μs do not satisfy this condition; i.e., the dense plasma still remains unmagnetized at this time.

As the bunch expands, its density decreases, whereas the heating power per particle and the temperature increase. For this reason, the plasma bunch fairly rapidly becomes completely magnetized. After the diameter of the bunch reaches ~1.5 cm, the transverse expansion comes to an end (see Fig. 2b).

One-dimensional expansion of the dense plasma along the magnetic field then begins (Fig. 2c). An important factor affecting the character of expansion of the dense plasma bunch in this stage is the heat transport along the magnetic field. Let us recall that, under conditions of nonlinear beam relaxation, the thermal conductivity of a strongly turbulent hot plasma is anomalously low because the longitudinal-transport coefficients are suppressed by a factor of 10^2–10^3 in comparison to their classical values [12]. By the end of the beam pulse, when the plasma electron temperature is on the order of 1 keV and the heating power begins to decrease, the anomalous thermal conductivity disappears and the transport coefficients rapidly restore to their classical values. Over a time on the order of a few microseconds, the thermal energy that is stored in the 12-m plasma column within the magnetic flux tube filled with the pellet material is transferred to the dense plasma bunch and is rapidly thermalized. In this case, a local peak of the plasma pressure appears for a short time at the point of pellet injection.

The time evolution of the dense plasma bunch can be analyzed using a simple hydrodynamic model proposed in [13]. In this model, the expansion of a dense plasma bunch into vacuum is considered in the local thermodynamic equilibrium approach. For some interesting practical profiles of energy deposition in the plasma (e.g., a uniform or parabolic profile), this model gives analytic solutions for the size and expansion rate of the dense plasma bunch. In this case, the asymptotic expansion rate of the bunch, v_{max}, turns out to be related to the deposited energy density through a simple expression

$$v_{max} = \sqrt{6Q_0/\mu},$$

where Q_0 is the total energy deposited per unit transverse area of the bunch from external heating sources and μ is the mass per unit area of the bunch. The resultant expansion rate v_{max} is approximately equal to the ion-sound velocity. Thus, using the simple models described above, the energy transferred from the target plasma to the pellet material can be determined from the measured time evolution of the bunch density (below, such measurements will be discussed in detail).

Let us briefly consider the problem of stability of a plasma column with a long higher density plasma filament at its axis. The experiments show that the presence of a pellet in the target plasma only slightly affects the operation of the linear discharge producing this plasma. The injection and transport of the relativistic beam also have no considerable impact on the target plasma, in contrast to the previously used pulsed gas puffing. We note that, in special experiments with the second injector, special conditions were produced for the occurrence of disruptions related to the appearance of a low-temperature dense plasma occupying the entire cross section of the plasma column (this situation is typical of experiments in which dense plasma is produced by pulsed gas puffing). An example of device operation in such a regime is shown in Fig. 3. We injected ~1 mg of fine lithium deuteride powder into the vacuum chamber. After the evaporation of the powder, a region occupied by dense plasma was formed. This region spanned almost the entire cross section of the plasma column. After the end of beam injection, the plasma pressure (which is determined from diamagnetic measurements) rapidly fell to zero. At the same time, the signal from a wall calorimeter located a distance of 66 cm from the injector increased by a factor of 3 and NaI (a doublet of 589.0 and 598.6 nm) and SiII (595.8 and 597.9 nm) lines appeared in the plasma emission spectrum, which indicates the evaporation of the surface of a Zerodur-like protection of the diamagnetic coils.

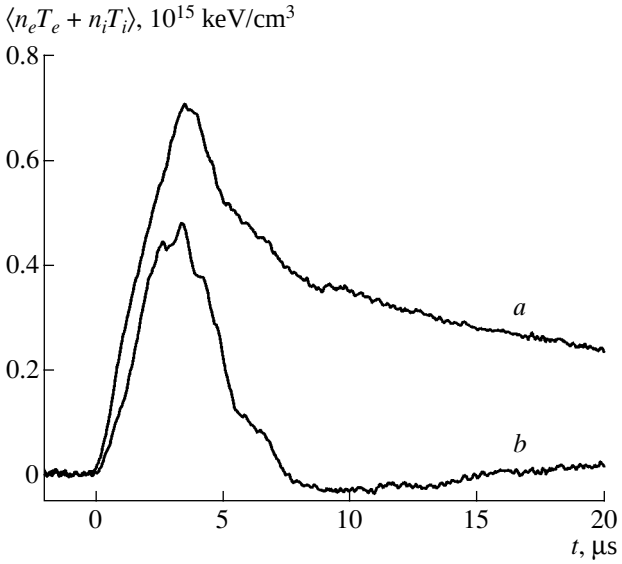

Fig. 3. Disruption of the discharge with injection of a LiD powder into the chamber: (*a*) a 0.3-mg LiD pellet is injected and (*b*) ~1 mg of fine LiD powder is injected. Signals from a diamagnetic coil located at Z = 209 cm (10 cm from the pellet injector) are shown.

4. PARAMETERS OF THE DENSE PLASMA BUNCH

The first series of experiments was performed with an injector located at Z = 662 cm. We mainly used polyethylene pellets with a mass of 0.1 to 1 mg. Time-resolved measurements of the plasma density evolution at the injection point were performed by measuring the Stark broadening of the H_α line. The brightness of the surrounding target plasma was several orders of magnitude lower and did not influence the line profile. The measured full width of the line profile exceeded 10 nm (approximately 500 measured points with a step of 0.03 nm, see Fig. 4). In this profile, a structure corresponding to the first several even harmonics of the cyclotron frequency is clearly seen; there is probably

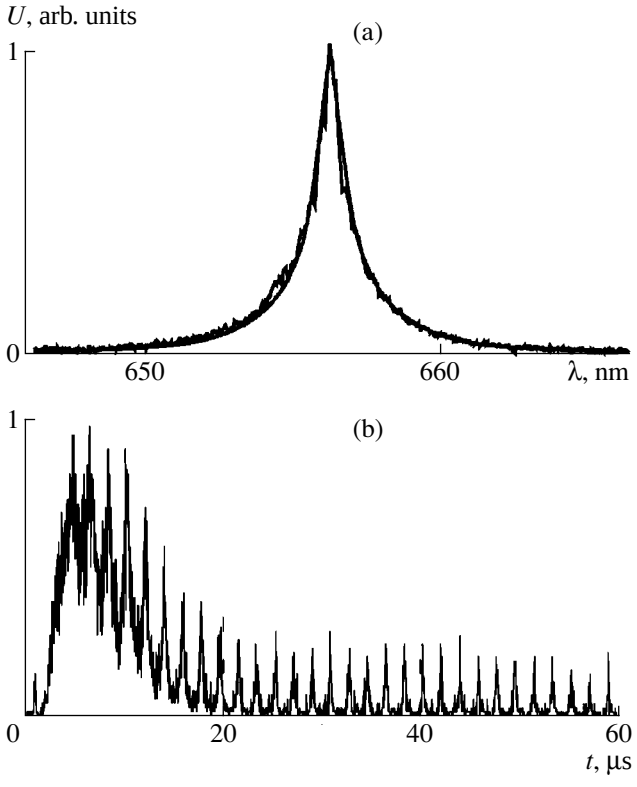

Fig. 4. Typical H_α line profile measured in the pellet injection experiments: (a) the line profile obtained using a system with a high spectral resolution (the calculated line profile for $n_e = 1.7 \times 10^{17}$ cm^{-3} and $T_e = 4$ eV is also shown) and (b) a signal from the system for scanning the line profile with 10-ns discretization (the emission intensity is measured at a distance of ~50 cm from the injector).

some contribution from the CII 657.8-nm and CII 658.3-nm lines.

In the course of one-dimensional expansion of the magnetized plasma, its density decreases from 10^{18} to 10^{16} cm^{-3} over ~30 μs (Fig. 5). The rate at which the plasma density decreases within this time interval is determined by the longitudinal bunch expansion velocity. The measured time dependence of the plasma density agrees well with the prediction of the above simple one-dimensional gasdynamic model of the expansion of a dense plasma bunch under energy deposition conditions typical of the GOL-3 experiments, in which the heating power grows linearly during the beam injection. A comparison with the experiment shows that, to fit the observed time evolution of the plasma density, the bunch expansion rate (which is two times the front velocity) should be about 6.2×10^7 cm/s. This corresponds to a directed kinetic energy of hydrogen ions at the bunch front of ~0.5 keV, which is substantially higher than the temperature of the dense plasma at the point of pellet injection. The model calculations were fitted to the experimental data by varying a single free parameter, namely, the energy deposited in the dense plasma, which turned out to be ~1 kJ/cm^2. The other parameters of the model are the known pellet mass per unit area of the bunch and the mean ion charge in the bunch, i.e., the ratio between the electron and ion densities. For a dense plasma, these parameters can be estimated with sufficient accuracy from the measured temperature.

The second injection point, located at $Z = 219$ cm, is of interest for several reasons. A principal difference in the physics of plasma bunch formation here is that this point is located close to the boundary of the region of maximum heating (the electron temperature here is twice as high as that at the location of the first injector and is substantially nonuniform in the longitudinal direction, whereas the first injector is located in the region with a low temperature gradient). In addition, there is a 2.2-m-long section with a corrugated magnetic field between the input magnetic mirror and this point. In the classical scheme of multimirror confinement, the plasma ions can undergo the action of a sort of frictional force exerted by the corrugated field, which decreases the longitudinal expansion rate. This theory implies a sufficiently long system in which the distribution function is close to isotropic and differs markedly from the case with a high-velocity directed plasma flow. However, in our case, we also could expect some effect related to the field corrugation.

The experiments at this point were carried out with 0.15- to 0.4-mg polyethylene pellets and 0.02- to 0.5-mg lithium-deuteride pellets. Some experiments were conducted with the simultaneous injection of several pellets, including some made of different materials. On the whole, the character of pellet evaporation and the initial expansion of the dense plasma was the same as described above. The time evolution of the plasma density at the injection point almost coincides with the data obtained for the first injector (see Fig. 5). The same figure shows the data obtained with a 0.1-mg LiD pellet and a receiving fiber located at $Z = 350$ cm. It can be seen that, in this case, the local density increases by a factor of more than 2 within the time interval 40–120 μs. Most likely, this is due to the deceleration of the expanding bunch in the target plasma (which is ignored in the model).

In the model calculations, we also used data on the transverse dimensions of the dense plasma bunch at the injection point; these were measured with the help of a VUV pinhole camera. Figure 6 shows typical waveforms of signals from several channels of the pinhole camera and the brightness map of the injection region, which was constructed using the nine central channels. It can be seen that VUV emission appears just after the beginning of beam injection; however, the signal level remains relatively low for several microseconds. A bright VUV burst is seen to appear by the end of the electron beam pulse. Such signal behavior may be related to the disappearance of the anomalous longitudinal electron thermal conductivity and the abrupt dep-

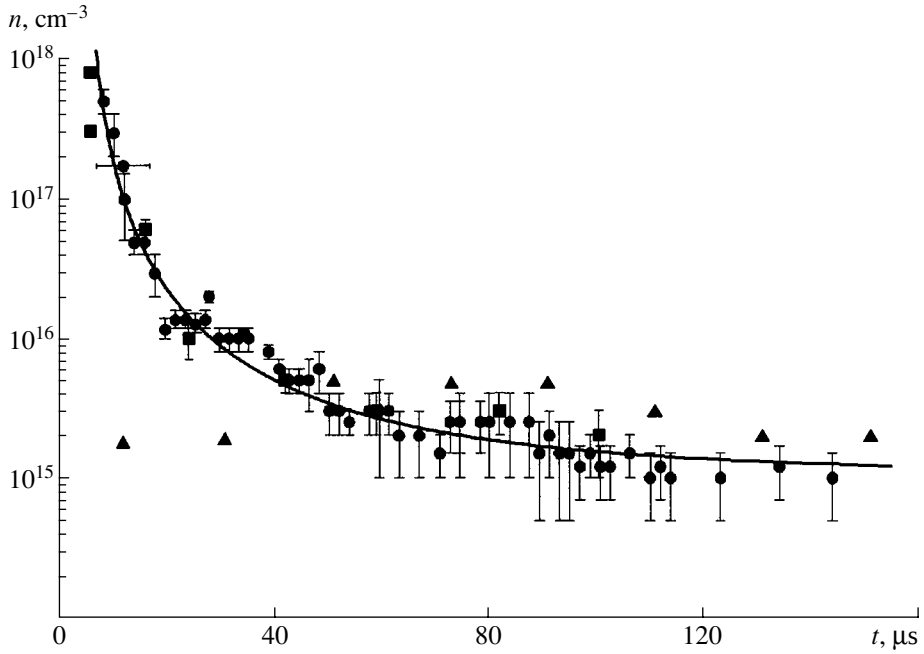

Fig. 5. Time evolution of the plasma bunch density by the data from spectroscopic measurements. The circles correspond to the injector located at $Z = 662$ cm; the observations are made at the injection point. The squares and triangles correspond to the injector located at $Z = 219$ cm; the observations are made at the injection point and at a distance of 1.4 m along the beam propagation direction (the measurement accuracy in the latter case is higher because of a smaller change in the signal level).

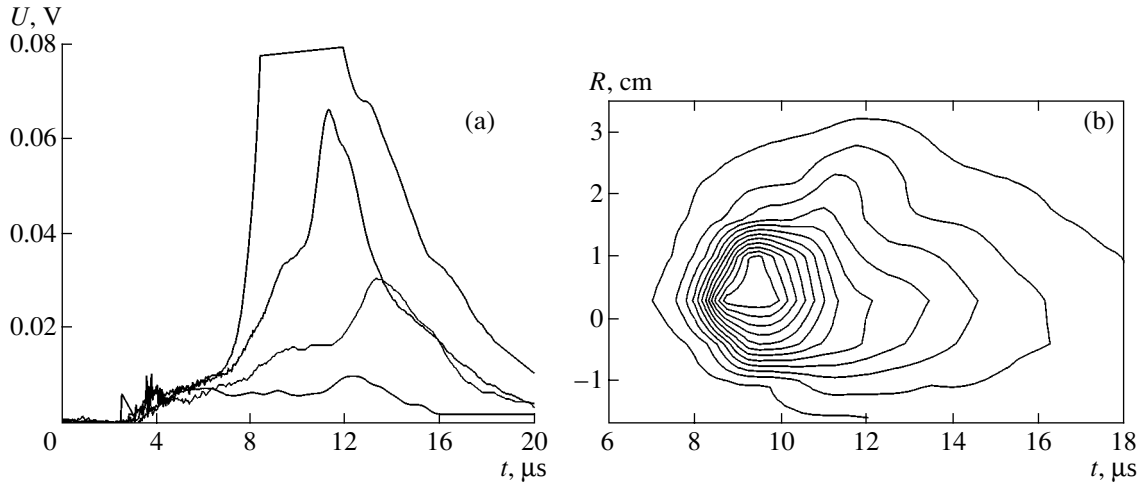

Fig. 6. Time evolution of the intensity of VUV emission from the dense plasma bunch: (a) signals from the channels of the VUV pinhole camera with lines of sights passing at distances from the pellet center of 0.5, 1.7, 2.1, and 2.9 cm (from top to bottom) and (b) contour lines of the signal magnitude (the distance between contour lines is 0.02 V; the coordinate is counted from the chamber axis). The beam injection begins at 2.5 μs.

osition of a relatively high energy in the dense plasma bunch.

In addition to the time evolution of the plasma bunch density, the model calculations also give the change in the dense plasma temperature. The same change was also measured experimentally (from precise measurements of the time evolution of the H_α line profile). Figure 7 shows the time evolution of the plasma pressure in the bunch (by the data from the injector located at $Z = 662$ cm). The axial magnetic field at the injection point amounts to 3.8 T. Hence, in the initial stage of pellet expansion, the measured β value is at least a few tens of percent (with respect to the vacuum field). Formally, the model allows one to extrapo-

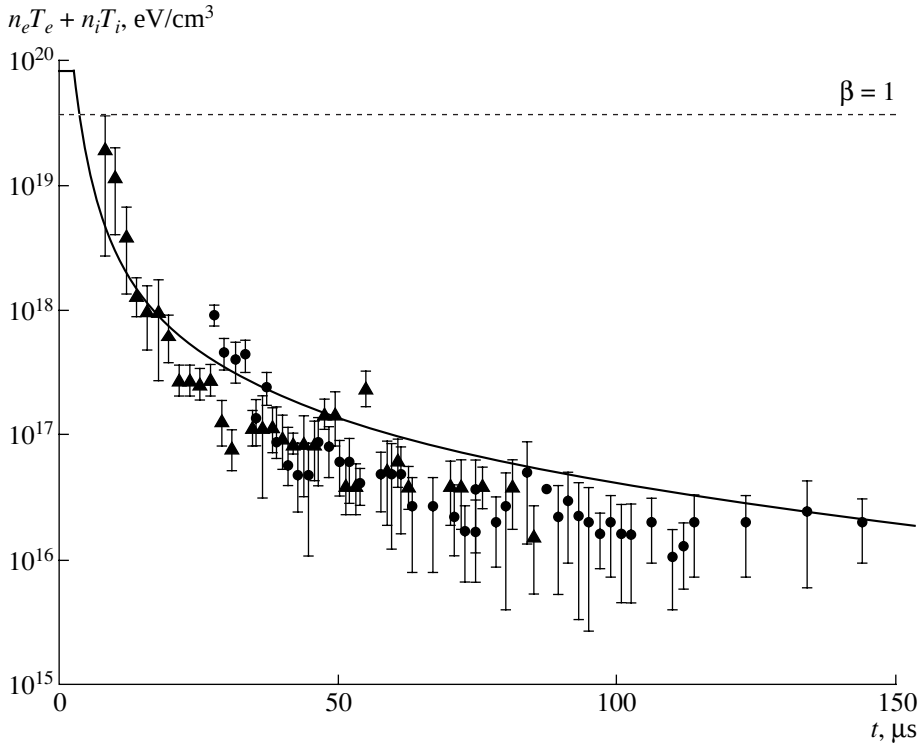

Fig. 7. Time evolution of the dense plasma pressure at the injection point. The circles and triangles show the data from two shots with the first injector, the solid line shows the results of model calculations, and the dashed line shows the level of the magnetic pressure at the injection point (3.8 T).

late β to values exceeding unity; however, for a dense, weakly magnetized plasma, such an extrapolation seems to make no physical sense.

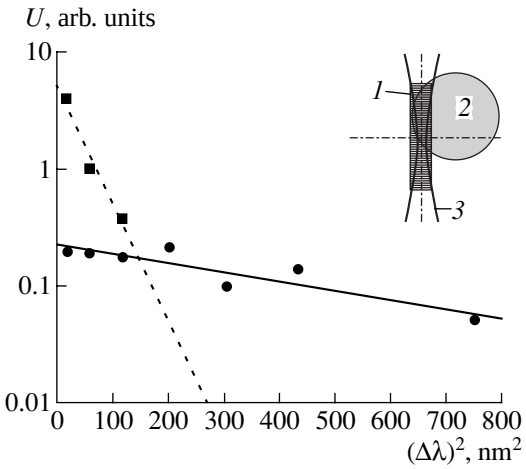

Fig. 8. Thomson scattering diagnostics in the pellet injection experiments: (*1*) projection of the entrance slit of the spectrograph (the slit is widened for a clearer illustration), (*2*) cross section of a dense plasma bunch, and (*3*) focused laser beam. The circles and squares show the measured scattered spectrum for two different shots. The solid line shows the fit with $n_e = (0.37 \pm 0.05) \times 10^{15}$ cm^{-3} and $T_e = 150 \pm 30$ eV, and the dashed line shows the fit with $n_e = (2.4 \pm 1) \times 10^{15}$ cm^{-3} and $T_e = 11 \pm 3$ eV.

When operating with the injector located at Z = 219 cm, the parameters of the dense plasma bunch were measured for the first time with the help of Thomson scattering diagnostics. Since the observation point was located a distance of 33 cm from the pellet injection point, it was decided to perform laser measurements at a fixed time of 15 μs after the beginning of beam injection (by this time, the brightness of the bunch emission decreases and becomes acceptable for measuring scattered light). A specific feature of these measurements is the approximate equality of the three values: the diameter of the dense plasma filament (about 1.5–2 cm), the scatter in the pellet positions in the chamber (~2 cm), and the dimension of the light-collection region of the Thomson scattering system (2 cm). For this reason, the laser beam in every experiment passed at a certain distance from the bunch center. The measured temperature varied in the range from 170 eV at a density of 0.7×10^{15} cm^{-3} to 10 eV at a density of 2.4×10^{15} cm^{-3} (typical scattering spectra are presented in Fig. 8). These results are in fair agreement with the above data from spectroscopic and other measurements.

In the experiments on pellet injection, we also measured plasma diamagnetism at different distances from the injection point (altogether, there were 25 diamagnetic coils). Unfortunately, we cannot unambiguously conclude that the diamagnetism changed in the presence of a pellet. The fact is that, even at high specific parameters of the dense plasma (e.g., at β ~ 1), its rela-

tive contribution to the total diamagnetic signal does not exceed 5–20% because of the small cross-sectional area of the dense bunch. The scatter in the plasma energy lifetime leads to similar variations in the time behavior of diamagnetic signals, thus masking the effects associated with the presence of the pellet.

5. CONCLUSION

On the whole the experiments on pellet injection in the GOL-3 device confirm our notion of the character of the formation and expansion of a dense plasma bunch produced by the explosive (volumetric) evaporation of a pellet. With 0.3-mg pellets, the measured expansion rate of the dense plasma corresponds to a maximum proton energy of ~500 eV, which means that the energy density deposited in the pellet attains ~1 kJ/cm^2. This value substantially exceeds the averaged energy density that can be provided by the ambient plasma (the total plasma energy at the maximum temperature amounts to 5–10 kJ, and the plasma cross-sectional area is ~30 cm^2 in the region where the magnetic field produced by the solenoid is uniform). This difference can be attributed to the transverse energy transport (the concentration of energy in the dense plasma bunch) by both fast electrons and heat conduction.

We plan to further improve the method for producing dense plasma bunches and to carry out experiments on the injection of pellets in the region with a corrugated magnetic field. We are also considering the possibility of injecting cryogenic hydrogen pellets.

ACKNOWLEDGMENTS

We thank S.S. Garifov, V.G. Ivanenko, A.V. Kutovenko, E.V. Mostipanov, and V.A. Rastoropov for their assistance in preparing and carrying out experiments. This work was supported in part by the Russian Foundation for Basic Research (project no. 99-02-16728).

REFERENCES

1. G. I. Budker, V. V. Mirnov, and D. D. Ryutov, Pis'ma Zh. Éksp. Teor. Fiz. **14**, 320 (1971) [JETP Lett. **14**, 212 (1971)].
2. A. J. Lichtenberg and V. V. Mirnov, in *Reviews of Plasma Physics*, Ed. by B. B. Kadomtsev (Consultants Bureau, New York, 1996), Vol. 19.
3. M. A. Agafonov, A. V. Arzhannikov, V. T. Astrelin, *et al.*, Plasma Phys. Controlled Fusion **38**, A93 (1996).
4. A. V. Burdakov, S. G. Voropaev, V. S. Koĭdan, *et al.*, Zh. Éksp. Teor. Fiz. **109**, 1128 (1996) [JETP **82**, 1120 (1996)].
5. A. V. Arzhannikov, V. T. Astrelin, A. V. Burdakov, *et al.*, Trans. Fusion Technol. **35** (1T), 112 (1999).
6. A. V. Arzhannikov, V. T. Astrelin, A. V. Burdakov, *et al.*, Trans. Fusion Technol. **39** (1T), 17 (2001).
7. V. T. Astrelin, A. V. Burdakov, V. S. Koĭdan, *et al.*, Zh. Éksp. Teor. Fiz. **113**, 897 (1998) [JETP **86**, 489 (1998)].
8. S. K. Combs, Rev. Sci. Instrum. **67**, 1679 (1993).
9. S. L. Milora, W. A. Houlberg, L. L. Lengyel, and V. Mertens, Nucl. Fusion **35**, 657 (1995).
10. B. V. Kuteev, Zh. Tekh. Fiz. **69** (9), 63 (1999) [Tech. Phys. **44**, 1058 (1999)].
11. V. T. Astrelin, A. V. Burdakov, P. Z. Chebotaev, *et al.*, Nucl. Fusion **37**, 1541 (1997).
12. V. T. Astrelin, A. V. Burdakov, and V. V. Postupaev, Fiz. Plazmy **24**, 450 (1998) [Plasma Phys. Rep. **24**, 414 (1998)].
13. D. D. Ryutov, Preprint No. 90-143 (Budker Institute of Nuclear Physics, Siberian Division, Acad. Sci. USSR, Novosibirsk, 1990).

Translated by N.F. Larionova

Plasma Physics Reports, Vol. 30, No. 1, 2004, pp. 91–98. Translated from Fizika Plazmy, Vol. 30, No. 1, 2004, pp. 96–103.

LOW-TEMPERATURE PLASMA

Spectroscopic Measurements and Numerical Simulations of the Electrode Plasma of an Electrode Microwave Discharge in Hydrogen

Yu. A. Lebedev, M. V. Mokeev, A. V. Tatarinov, and I. L. Epsteĭn

Topchiev Institute of Petrochemical Synthesis, Russian Academy of Sciences, Leninskiĭ pr. 29, Moscow, 119991 Russia

Received April 9, 2003; in final form, June 5, 2003

Abstract—The structure of an electrode microwave discharge in hydrogen at pressures of 1–8 torr and incident powers of 20–100 W is studied using optical spectroscopy. A two-dimensional computer code is developed for self-consistently simulating a self-sustained steady-sate electrode microwave discharge ignited at the end of the inner conductor of a coaxial line. The model is based on simultaneously solving time-dependent Maxwell's equations, the balance equations for charged particles, and a homogeneous Boltzmann equation. The numerical results referring to the electrode region of the discharge are in fair agreement with the experimental data. This confirms the early suggestion (inferred from experimental data) of the combined "self-sustained–non-self-sustained" character of the electrode discharge. It is shown that the self-sustained discharge domain is located in the electrode region of the discharge. © *2004 MAIK "Nauka/Interperiodica".*

1. INTRODUCTION

Low-pressure microwave discharges existing near an electrode through which energy is supplied under conditions such that the plasma domain is much less than the discharge chamber are a striking example of plasma structurization. Experimental data on the properties of such discharges and the physical processes occurring inside them have been accumulated since the late 1990s [1–5]. Discharges in molecular gases consist of a thin bright electrode sheath and a less bright spherical region surrounding the electrode and separated by a sharp interface from the dark outer space. In [6], based on the measurements of the electron density and electric field in plasma, it was suggested that the electrode microwave discharge consisted of the three regions: a self-sustained discharge (electrode sheath), a non-self-sustained discharge (spherical region), and an afterglow region separated from the discharge by an electric double layer.

This study is aimed at investigating the electrode region of the discharge. In [3], the degree of dissociation in the electrode plasma of an electrode microwave discharge was studied using optical spectroscopy. It was shown that the degree of dissociation was low and the excitation of the emitting states of hydrogen molecules and atoms, as well as their ionization, proceeded from the ground state via direct electron impacts.

In this paper, we present the results of spectroscopic measurements of the structure of the electrode region of an electrode microwave discharge in hydrogen and the results of self-consistent two-dimensional computer simulations of a diffuse discharge in an nonregular coaxial system. An example of such a system is the discharge section used in our experiments, in which the discharge is produced at the end of the inner conductor of a coaxial line. A comparison of the numerical results with the experimental data allows us to come to a number of conclusions about the physical processes occurring in the electrode region of the discharge.

2. EXPERIMENTAL SETUP

The experiments were carried out with a hydrogen discharge at a pressure of 1–8 torr and an incident microwave power of 20–90 W, the absorbed power being 2–12 W. The microwave oscillator with a maximum output power of 170 W operated at a frequency of 2.45 GHz. The discharge chamber was a metal cylinder 8.5 cm in diameter (see [1–3] for details). The microwave antenna (a cylindrical stainless-steel tube 6 mm in diameter) was inserted in the chamber through its end via a vacuum joint. The antenna was a part of a coaxial-to-waveguide converter, which was adjusted with the help of a shorting plunger. The experiments were carried out in a gas flow. The gas was supplied through a channel in the upper wall of the discharge chamber and pumped out through a channel in the lower wall. The working gas was hydrogen with a 5% admixture of argon. Argon was added for diagnostic purposes and had virtually no effect on the properties of the hydrogen plasma.

The discharge was ignited around the antenna (the exciting electrode). The discharge dimensions were much less than the chamber diameter and the distance from the lower end of the chamber. The discharge emission was output through a window on the side wall of the discharge chamber. The spatial resolution of the measurements was about 0.5 mm. Plasma emission in

1063-780X/04/3001-0091$26.00 © 2004 MAIK "Nauka/Interperiodica"

the spectral range 400–800 nm was studied using an MDR-23 monochromator. An FEU-79 photomultiplier was used as an emission detector. The optical system was calibrated with the help of an SI-8-200 tungsten band lamp.

3. MODEL

To study the processes in a nonequilibrium plasma of an electrode microwave discharge, we developed a self-consistent model based on simultaneously solving time-dependent Maxwell's equations and balance equations for charged particles. The local plasma electron parameters needed to solve these equations were obtained by numerically solving a homogeneous Boltzmann equation [7].

3.1. Computation of the Electromagnetic Field in an Nonregular Coaxial System Partially Filled with Plasma

To study the distributions of the electric field and microwave energy density in a plasma-filled chamber with a given configuration, we developed a computer code for solving Maxwell's equations in a dispersive medium. The electromagnetic fields inside the plasma reactor were described by time-dependent Maxwell's equations

$$\nabla \times \mathbf{E} = -\frac{1}{c}\frac{\partial \mathbf{H}}{\partial t}, \quad (1)$$

$$\nabla \times \mathbf{H} = \frac{1}{c}\frac{\partial \mathbf{D}}{\partial t}. \quad (2)$$

The permittivity ε is a function of the frequency ω,

$$\varepsilon = 1 - \frac{\omega_p^2}{\omega^2 + \nu^2} + i\frac{\omega_p^2}{\omega^2 + \nu^2}\frac{\nu}{\omega} = 1 - \frac{\omega_p^2}{\omega^2 + i\nu\omega}, \quad (3)$$

where $\omega_p = \sqrt{4\pi e^2 n_e/m}$ is the electron plasma frequency, ω is the circular microwave frequency, ν is the collision frequency of electrons with heavy particles, and n_e is the electron density.

Equations (1) and (2) were solved in the ($\mathbf{r}$, t) coordinates (rather than in the ($\mathbf{k}$, ω) coordinates). Hence, a conventional constitutive equation

$$\varepsilon(\omega) = \frac{D(\omega)}{E(\omega)} \quad (4)$$

should be transformed into an equation relating $D(t)$ and $E(t)$. Following [8], we substitute ε in form (3) into Eq. (4) for the complex permittivity to obtain

$$(\omega^2 + i\nu\omega - \omega_p^2)E(\omega) = (\omega^2 + i\nu\omega)D(\omega). \quad (5)$$

Applying the inverse Fourier transformation

$$f(t) = \int_{-\infty}^{+\infty} f(\omega)\exp(-i\omega t)dt, \quad (6)$$

to Eq. (5), we obtain the second-order differential equation relating $D(t)$ and $E(t)$:

$$\frac{\partial^2 E}{\partial t^2} + \nu\frac{\partial E}{\partial t} + \omega_p^2 E = \frac{\partial^2 D}{\partial t^2} + \nu\frac{\partial D}{\partial t}. \quad (7)$$

Equations (1), (2), and (7) comprise a complete set of equations describing the propagation of electromagnetic waves in dispersive media. The numerical algorithm is arranged as a three-stage successive procedure of calculating the electromagnetic fields. The algorithm is based on an explicit finite-difference scheme of integrating Maxwell's equations, which was originally applied to nondispersive media [9].

The equations are written in cylindrical coordinates (r, φ, z) under the assumption of axial symmetry: $\partial/\partial\varphi = 0$. We used a square mesh with dimensions $h_z = h_r = h$. We represent the vector equations in finite differences and use the leap-frog scheme of second order accuracy [10]:

$$(H_r)_{k-1/2,\,i}^{n+1/2} = (H_r)_{k-1/2,\,i}^{n-1/2} + \frac{\tau}{h_z}((E_\varphi)_{k,\,i}^n - (E_\varphi)_{k-1,\,i}^n), \quad (8)$$

$$(H_z)_{k,\,i-1/2}^{n+1/2} = (H_z)_{k,\,i-1/2}^{n-1/2} + \frac{\tau}{r_{i-1/2}h_z}(r_i(E_\varphi)_{k,\,i}^n - r_{i-1}(E_\varphi)_{k-1,\,i}^n), \quad (9)$$

$$(H_\varphi)_{k-1/2,\,i-1/2}^{n+1/2} = (H_\varphi)_{k-1/2,\,i-1/2}^{n-1/2} - \frac{\tau}{h_z}((E_r)_{k,\,i-1/2}^n - (E_r)_{k-1,\,i-1/2}^n) + \frac{\tau}{h_r}((E_z)_{k-1/2,\,i}^n - (E_z)_{k-1/2,\,i-1}^n), \quad (10)$$

$$(D_r)_{k,\,i-1/2}^{n+1} = (D_r)_{k,\,i-1/2}^n - \frac{\tau}{h_z}((H_\varphi)_{k+1/2,\,i-1/2}^{n+1/2} - (H_\varphi)_{k-1/2,\,i-1/2}^{n+1/2}), \quad (11)$$

$$(D_z)_{k-1/2,\,i}^{n+1} = (D_z)_{k-1/2,\,i}^n + \frac{\tau}{h_r r_i}(r_{i+1/2}(H_\varphi)_{k+1/2,\,i+1/2}^{n+1/2} - r_{i-1/2}(H_\varphi)_{k-1/2,\,i-1/2}^{n+1/2}), \quad (12)$$

$$(D_\varphi)_{k,\,i}^{n+1} = (D_\varphi)_{k,\,i}^n + \frac{\tau}{h_z}((H_r)_{k+1/2,\,i}^{n+1/2} - (H_r)_{k-1/2,\,i}^{n+1/2}) - \frac{\tau}{h_r}((H_z)_{k,\,i+1/2}^{n+1/2} - (H_z)_{k,\,i-1/2}^{n+1/2}). \quad (13)$$

The new E^{n+1} value is calculated from Eq. (7) represented in finite differences by using the known values

of E^n, D^{n+1}, and D^n, as well as the values of E^{n-1} and D^{n-1}, calculated at the preceding time step:

$$\begin{aligned}(E_{r,z,\varphi})^{n+1} &= (\omega_p^2\tau^2 + \nu\tau + 2)^{-1} \\ \times\{&-(\omega_p^2\tau^2 + \nu\tau + 2)(E_{r,z,\varphi})^{n-1} + 4(E_{r,z,\varphi})^n \\ &+ (-\nu\tau + 2)(D_{r,z,\varphi})^{n-1} - 4(D_{r,z,\varphi})^n \\ &+ (\nu\tau + 2)(D_{r,z,\varphi})^{n+1}\}.\end{aligned} \quad (14)$$

Here, τ is the time step; k and i are the mesh cell numbers along the z and r axes, respectively; and n is the time step number. The variables in Eqs. (8)–(14) are normalized as follows:

$$\begin{aligned}r \longrightarrow \frac{r}{R};\quad t \longrightarrow t\frac{c}{R};\quad E \longrightarrow \frac{eR}{mc^2}E; \\ D \longrightarrow \frac{eR}{mc^2}D;\quad H \longrightarrow \frac{eR}{mc^2}H;\end{aligned} \quad (15)$$

where the characteristic size of the system is chosen to be $R = 1$ cm.

The boundary conditions for the fields on a perfectly conducting metal wall are $E_\tau|_S = 0$ and $H_n|_S = 0$. The subscripts τ and n stand for the tangential and normal components of the fields at the metal surfaces of the chamber and the central electrode.

3.2. Balance Equation for Charged Particles

The distribution of the charged particle densities in the discharge chamber are found by solving the charged particle balance equation that accounts for diffusion, ionization, and volume recombination:

$$\begin{aligned}\frac{\partial n}{\partial t} &= \frac{1}{r}\frac{\partial}{\partial r}\left(D_a(\bar{E})r\frac{\partial n}{\partial r}\right) \\ &+ \frac{\partial}{\partial z}\left(D_a(\bar{E})\frac{\partial n}{\partial z}\right) + \nu_i(\bar{E})n - \alpha_r(\bar{E})n^2.\end{aligned} \quad (16)$$

It is assumed that the plasma is quasineutral and the diffusive losses of charged particles are governed by ambipolar diffusion with the diffusion coefficient D_a. In the plasma of an electrode discharge in hydrogen, the working-gas particles are excited and ionized from the ground state via electron impacts [3]. The charged particles are recombined via the volumetric dissociative recombination of H_3^+ ions (the cross section is taken from [11]). To calculate the local values of $D_a(\bar{E})$, $\nu_i(\bar{E})$, and $\alpha_r(\bar{E})$, we used the electron energy distribution functions (EEDFs) obtained by solving a homogeneous Boltzmann equation with a self-consistent set of cross sections for hydrogen taken from [12]. The mean electric field $\bar{E}$, which is needed to solve the Boltzmann equation, is found by solving Maxwell's equations. The gas temperature is assumed to be spatially uniform and equal to 300 K.

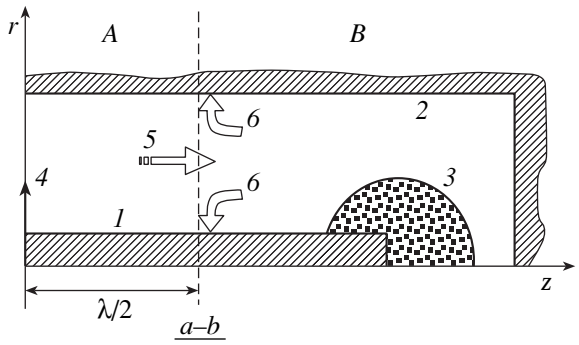

Fig. 1. Schematic diagram of the discharge chamber used in the calculations: (*1*) central electrode, (*2*) cylindrical discharge chamber, (*3*) plasma, (*4*) wave excitation plane (TEM-wave generator), (*5*) wave propagating from region *A* to region *B*, and (*6*) reflected wave disappearing at the *a*–*b* plane.

3.3. Computation Procedure

A schematic diagram of the discharge chamber used in the calculations is shown in Fig. 1. The computation region (the *rz* half-plane) is divided into two parts. The incident-wave generator lies at the very left of region *A*. It generates a 2.45-GHz TEM wave propagating to the right. The wave traverses empty region *A* of length $\lambda/2$ and enters region *B* (the discharge chamber). It is assumed that the reflected wave (which propagates to the left) vanishes at the left boundary of region *B* and does not interact with the incident wave arriving from region *A*. Thus, there is a TEM wave propagating to the right in region *A* and a standing wave in region *B*. The computation time t should be sufficiently long for a steady-state field distribution to be established in a working chamber partially filled with plasma (generally, $t > 3L/c$, where L is the total length of the computation region and c is the speed of light).

At each time step, all the electromagnetic wave components (H, D, and E) are calculated by formulas(8)–(14) at each point of the *rz* half-plane: first, in region *A* and, then, in region *B*. The length of region *A* was chosen such that easy comparison of the amplitudes and phases of the reference and established waves in the chamber was possible.

In the calculations, the total length of the system was 28 cm, the diameter of the working chamber was 8 cm, and the diameter of the inner core was 0.6 cm. The distance between the end of the central electrode and the chamber bottom was 4 cm. These dimensions were identical to the experimental ones. The mesh size was 0.03 cm. The parameters of the problem were the incident-wave power and the gas pressure in the discharge chamber.

The computation procedure was as follows:

First, an arbitrary distribution of the electron density in the discharge chamber is specified. A microwave wave then enters the chamber. It is partially absorbed by and reflected from the plasma. Relaxation to an equilibrium steady-state field distribution generally takes a few microwave periods. In this stage, the electrodynamic part of the problem is solved.

Next, based on the average calculated fields and using the Boltzmann equation, the coefficients are determined that are necessary to solve the balance equation for charged particles at each point of the spatial mesh in the discharge chamber. A new steady-state solution $n(r, z)$ to the balance equation for charged particles with given coefficients is found by the Gauss–Zeidel method.

The above two-stage procedure is repeated for a new distribution of the electron density. The process is repeated until it converges to a steady-state to within a given accuracy, i.e., until steady-state spatial distributions of the densities and fields are reached.

Let us analyze in more detail the applicability range of the model.

The procedure of solving a set of Maxwell's equations allows one to calculate the time-resolved structure of electromagnetic fields in any dissipative system ($\nu \neq 0$). The charged particle distribution is obtained from the balance equation. The parameters of the plasma electron component are calculated using a homogeneous Boltzmann equation in the local two-term approximation for the steady-state isotropic part of the EEDF. It is the use of the Boltzmann equation in such a form that determines the applicability range of the model.

It is well known that the nonlocal character of the EEDF manifests itself when the characteristic electron energy relaxation length λ_ε exceeds the characteristic plasma scale length Λ [13]. For the diffuse discharge under consideration, we have $\lambda_\varepsilon \sim (D_a\tau_\varepsilon)^{1/2}$ and $\tau_\varepsilon = 1/\nu_\varepsilon \sim 1/\delta\nu_{ef}$, where D_a is the ambipolar diffusion coefficient, δ is the average fraction of the electron energy transferred to heavy particles in one collision event, and ν_{ef} is the effective collision frequency of electrons with heavy particles. For hydrogen at a pressure of 1 torr, we have $\nu_{ef} \sim 10^9$ s^{-1}, $\delta \geq 10^{-2}$, $D_a \sim 10^4$ cm^2/s, and $\lambda_\varepsilon <$ 1 mm. At a characteristic discharge scale length of $\Lambda \sim$ 10 mm, we obtain $\lambda_\varepsilon \ll \Lambda$. This is certainly the case at higher pressures. Hence, for any molecular gas, the nonlocal character of the EEDF can be ignored at pressures higher than 1 torr. For noble gases, the lowest pressure at which the nonlocal character of the EEDF can be ignored shifts toward higher pressures because of the larger energy relaxation length.

These estimates also show that the EEDF becomes isotropic at scale lengths much shorter than 1 mm, which validates the use of the two-term expansion of the EEDF in spherical harmonics.

It is known that, in a quasi-homogeneous alternating field, an electron acquires energy only in collisions with heavy particles (Joule heating). This mechanism is characteristic of moderate- and high-pressures plasmas.

In a low-pressure plasma ($\omega \gg \nu_{ef}$), there are narrow localized plasma resonance regions (with a characteristic size of Δ) in which the electric field can be very high. In a strongly nonuniform field, there is an extra mechanism for the acceleration (heating) of electrons—the so-called "stochastic heating." This process enriches the high-energy part of the EEDF as compared to a homogeneous plasma. Such an effect has been observed experimentally; however, it disappears at pressures higher than 50 mtorr [14, 15]. Hence, under the conditions concerned, stochastic heating and, consequently, the emergence of fast electrons is of minor importance.

Thus, a pressure of 0.5–1 torr is the lowest pressure at which the model adequately describes the experiment.

At high pressures, the limitation of our model is related to the violation of the steady-state character of the EEDF isotropic part. At low pressures, when $\omega \gg \nu_{ef}$, the EEDF is certainly steady-state. At pressures of 15–20 torr, we have $\nu_{ef} \sim \omega \ll 1/\tau_\varepsilon$, and the isotropic part of the EEDF becomes non-steady-state at high energies. At these pressures, the modeling can be inadequate, so that it is necessary to use a time-dependent Boltzmann equation. At $\nu_{ef} \gg \omega$ (which corresponds to pressures of 50–100 torr), the EEDF is in equilibrium with the microwave field; hence, to calculate the EEDF, one can use a time-independent Boltzmann equation and the instant values of the fields obtained by solving the electrodynamic problem.

4. RESULTS AND DISCUSSION

The experiments show that the bright electrode sheath of an electrode microwave discharge is highly inhomogeneous.

When viewed from the electrode end, the electrode sheath is a glowing toroid. The intensities of the line and band emission sharply increase inside the toroid. The emission intensity is maximum near the sharp edge of the electrode end.

It is well known that the electric field increases in the vicinity of sharp inhomogeneities (like corners and points). Our modeling of the field structure in a plasma-filled coaxial system showed that, inside the electrode sheath, where the emission intensity is maximum, the microwave field is enhanced. The field is maximum on the bisectrix of the right-angle electrode edge and sharply decreases with distance from the electrode. The maximum electric field is two to three times higher than that in a uniform coaxial line. Such an increase is in good agreement with the calculated field in the near-field zone of an isolated antenna [16].

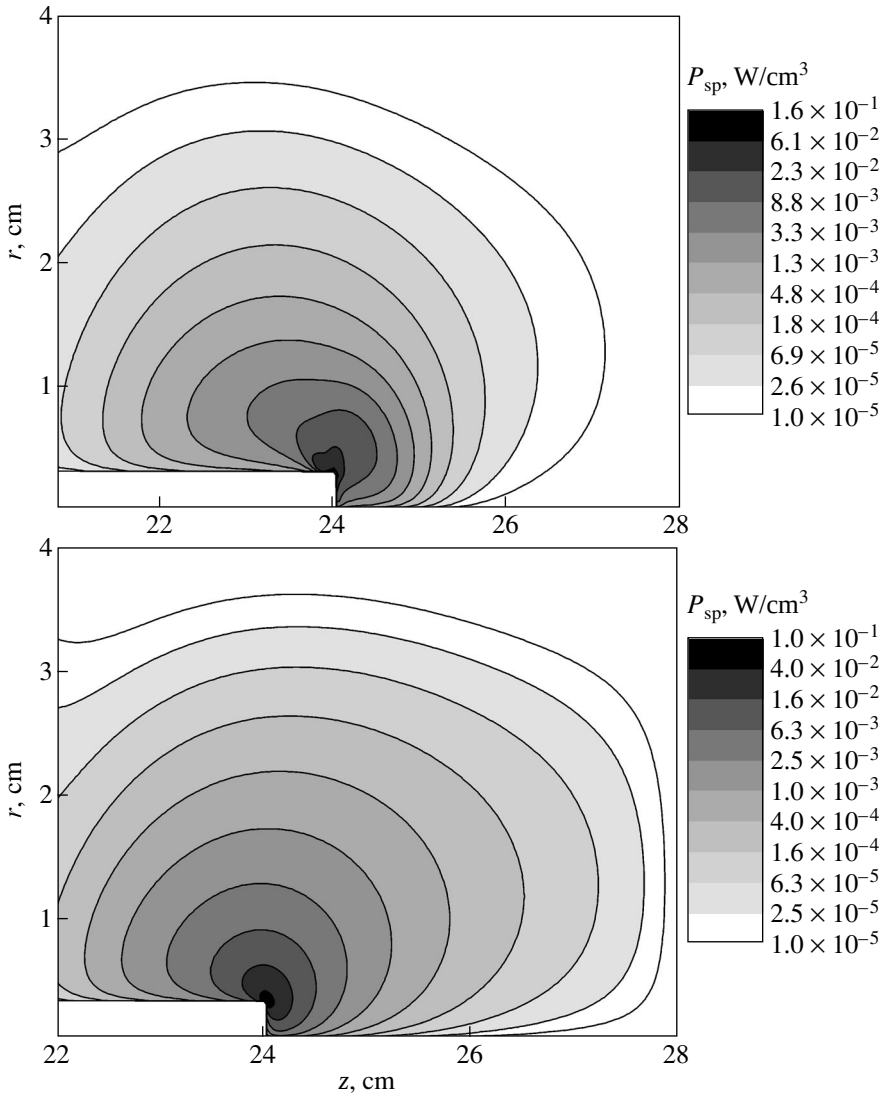

Fig. 2. Self-consistently calculated distributions of the specific energy deposition in the plasma for (a) a pressure of 1 torr, an incident power of 30 W, and an absorbed power of 18 W and (b) a pressure of 8 torr, an incident power of 30 W, and an absorbed power of 20 W.

The increase in the electric field near the end of the central electrode shows that this region plays an important role in igniting and sustaining the discharge.

Figure 2 shows the distribution of the specific energy deposition in plasma calculated using the self-consistent model. One can see a toroidal region of the maximum energy deposition near the edge of the electrode end. Since the energy deposition and the plasma emission intensity behave in the same manner, the results of the calculations agree with the experimental data.

Figure 3 shows the radial profiles of the density of the excited hydrogen atoms responsible for H_β line emission near the electrode end for different incident powers and pressures. It can be seen that the profiles are nonmonotonic: there is a maximum near the edge of the electrode end (about 3 mm from the axis). The maximum is caused by the enhanced electric field in this region. At higher distances from the axis, a kind of plateau is seen, which shrinks with increasing pressure.

The closer to the system axis, the lower the density of the excited particles and the H_β line emission intensity. It is shown experimentally that this effect is more pronounced in cross sections closer to the electrode edge. At large distances, the density has a maximum on the discharge axis. The experiments also showed that the higher the emission excitation threshold, the more pronounced this effect. The observed distribution of the emission intensity can be explained by the specific features of the electric field distribution in the electrode sheath.

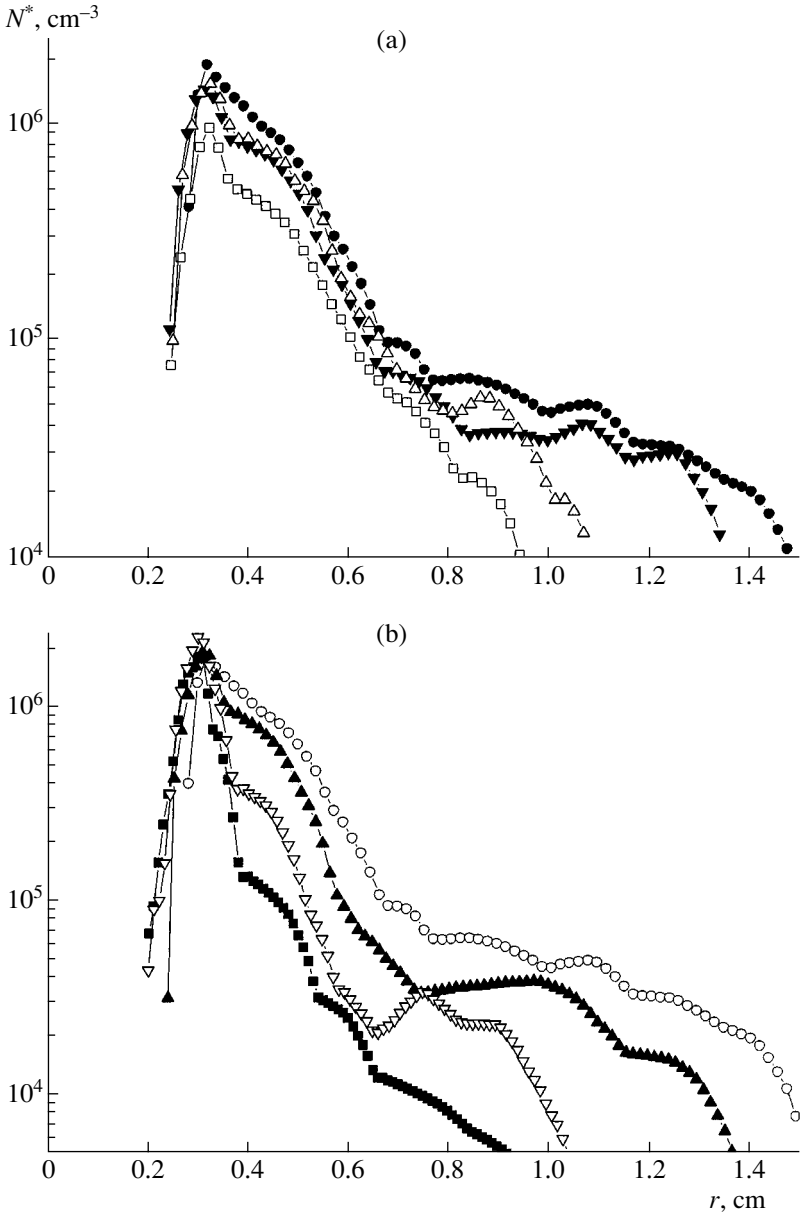

Fig. 3. Radial profiles of the densities of the excited hydrogen atoms (in the $n = 4$ state) determined from the emission intensity in the Balmer-series H_β 486.1-nm line in a plane located 0.16 cm below the tube electrode end for (a) a pressure of 1 torr and incident powers of $W_{inc} = 80$ (circles), 60 (closed triangles), 40 (open triangles), and 20 W (squares) and (b) an incident power of 80 W and pressures of 1 (circles), 2 (closed triangles), 4 (open triangles), and 8 torr (squares).

The calculated radial profiles of the specific energy deposition at different distances from the electrode end are shown in Fig. 4. It can be seen that the calculated profiles are in fair agreement with those shown in Fig. 3. The maximum electron density in the electrode sheath is slightly higher than 10^{11} cm^{-3}, which also agrees with the experimental value. Thus, at low pressures, there is a region with a supercritical plasma density in the electrode sheath (at a frequency of 2.45 GHz and $\nu/\omega \ll 1$, we have $n_{cr} \approx 7.6 \times 10^{10}$ cm^{-3}). Hence, the observed plateau on the profile of the specific energy deposition can be attributed to the effect of the plasma resonance. At high pressures, collisions reduce this effect and the shapes of the profiles depend only slightly on the ratio between the electron density and n_{cr} (at a frequency of 2.45 GHz and pressure of 8 torr, we have $n_{cr} \approx 3 \times 10^{11}$ cm^{-3}). In this pressure range, the maximum electron density increases proportionally to the power absorbed in the plasma. Another characteristic feature is that, over the entire pressure range under study, the specific energy deposition is maximum at a distance of ~3 mm from the axis. This fact indicates

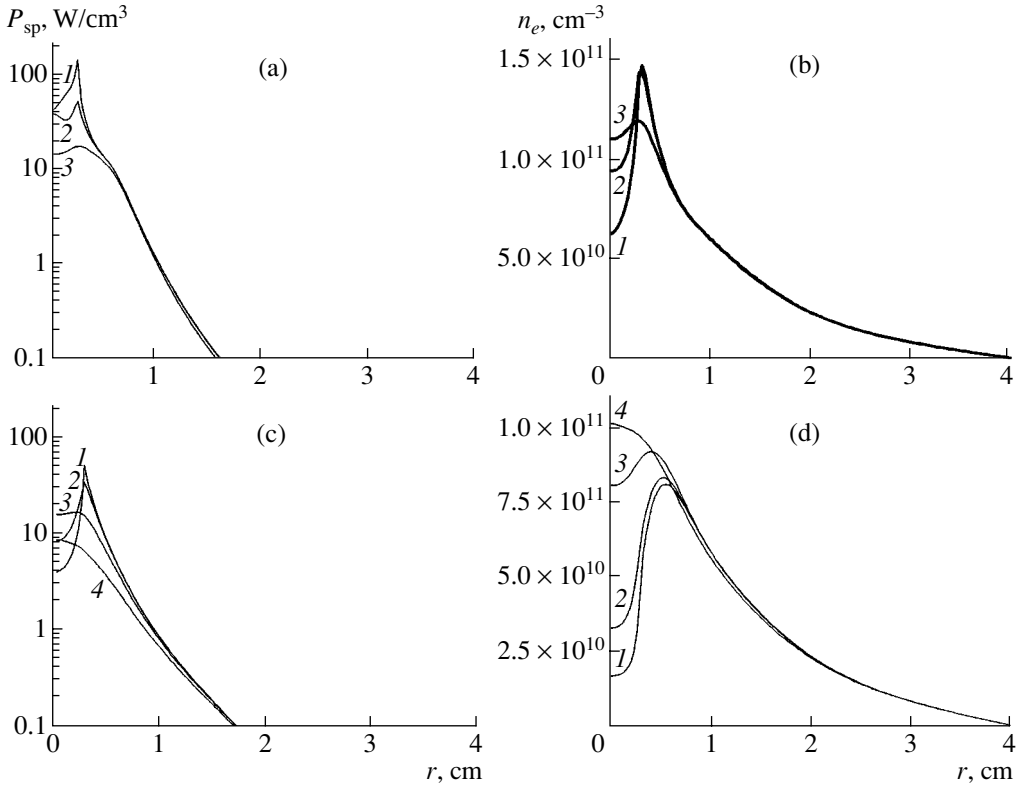

Fig. 4. Calculated radial profiles of the (a, c) specific energy deposition and (b, d) electron density at different distances Δz from the electrode end: (*1*) 0.03, (*2*) 0.06, (*3*) 0.18, and (*4*) 0.36 cm. The incident power is 30 W. The pressure and the absorbed power are (a, b) 1 torr and 18 W and (c, d) 8 torr and 20 W.

that it is the presence of a sharp edge at the electrode end that causes the increase in the electric field.

Thus, the numerical simulations of a self-sustained diffuse microwave discharge satisfactorily describe the electrode plasma of an electrode microwave discharge in hydrogen. This confirms the assumption of [6] that the electrode plasma is a region of a self-sustained discharge.

5. CONCLUSIONS

A two-dimensional computer code has been developed for self-consistently simulating a self-sustained steady-state electrode microwave discharge operating at the end of the inner conductor of a coaxial line. The parameters of a diffuse discharge in hydrogen at pressures of 1–8 torr and incident powers of 20–100 W have been calculated. The discharge structure has been studied using optical spectroscopy. The numerical results referring to the electrode region of the discharge are in fair agreement with the experimental data. This confirms the early suggestion (inferred from experimental data) about the combined "self-sustained–non-self-sustained" character of the electrode discharge. It has been shown that the self-sustained discharge domain is located in the electrode region of the discharge.

ACKNOWLEDGMENTS

This study was supported in part by the Russian Foundation for Basic Research (project no. 02-02-16021) and the Interaction of Plasmas with High-Speed Gas Flows Fundamental Research Program of the Presidium of the Russian Academy of Sciences.

REFERENCES

1. L. Bardos and Yu. A. Lebedev, Zh. Tekh. Fiz. **68** (12), 29 (1998) [Tech. Phys. **43**, 1428 (1998)].
2. Yu. A. Lebedev, M. V. Mokeev, and A. V. Tatarinov, Fiz. Plazmy **26**, 293 (2000) [Plasma Phys. Rep. **26**, 272 (2000)].
3. Yu. A. Lebedev and M. V. Mokeev, Fiz. Plazmy **27**, 443 (2001) [Plasma Phys. Rep. **27**, 418 (2001)].
4. Yu. A. Lebedev, M. V. Mokeev, A. V. Tatarinov, and I. L. Epstein, in *Proceedings of the 4th International Workshop on Microwave Discharges: Fundamentals and Applications, Zvenigorod, 2000* (Yanus-K, Moscow, 2001), p. 187.
5. Yu. A. Lebedev, A. V. Tatarinov, and I. L. Epstein, Plasma Sources Sci. Technol. **11**, 146 (2002).
6. Yu. A. Lebedev, M. V. Mokeev, and A. V. Tatarinov, in *Proceedings of the 30th Conference on Plasma Physics and Controlled Fusion, Zvenigorod, 2003*, Abstract of Papers, p. 165.

7. Yu. A. Lebedev and I. L. Epstein, J. Moscow Phys. Soc. **5** (1), 103 (1995).
8. J. D. Jackson, *Classical Electrodynamics* (Wiley, New York, 1975), p. 331.
9. R. M. Joseph, S. C. Hagness, and A. Taflove, Opt. Lett. **16**, 1412 (1991).
10. C. K. Birdsall and A. B. Langdon, *Plasma Physics via Computer Simulations* (McGraw-Hill, New-York, 1985).
11. H. Tawara, Y. Itikawa, H. Nishimura, and M. Yoshino, J. Phys. Chem. Ref. Data **19**, 617 (1990).
12. V. E. Gal'tsev, A. V. Dem'yanov, I. V. Kochetov, *et al.*, Preprint No. 3156 (Kurchatov Institute of Atomic Energy, Moscow, 1979), p. 19.
13. V. I. Demidov, N. B. Kolokolov, and A. A. Kudryavtsev, *Probe Methods for Studying Low-Temperature Plasmas* (Énergoatomizdat, Moscow, 1996).
14. T. A. Grotjohn, in *Proceedings of the 4th International Workshop on Microwave Discharges: Fundamentals and Applications, Zvenigorod, 2000* (Yanus-K, Moscow, 2001), p. 25.
15. J. Kudela, T. Terebessy, and M. Kando, in *Proceedings of the 4th International Workshop on Microwave Discharges: Fundamentals and Applications, Zvenigorod, 2000* (Yanus-K, Moscow, 2001), p. 63.
16. E. N. Vasil'ev and A. P. Seregina, Radiotekh. Élektron. (Moscow), No. 6, 929 (1971).

Translated by N.N. Ustinovskiĭ